Resonant Spatial Light Modulation: Optical Programming and Sensing at the Fundamental Limit

by

Christopher L. Panuski

B.S., United States Naval Academy (2017)
S.M., Massachusetts Institute of Technology (2019)

Submitted to the Department of Electrical Engineering and Computer Science in partial fulfillment of the requirements for the degree of

Doctor of Philosophy

at the

MASSACHUSETTS INSTITUTE OF TECHNOLOGY

May 2022

Author . . . .
Department of Electrical Engineering and Computer Science
May 13, 2022

Certified by . . . .
Dirk R. Englund
Associate Professor of Electrical Engineering and Computer Science
Thesis Supervisor

Accepted by . . . .
Leslie A. Kolodziejski
Professor of Electrical Engineering and Computer Science
Chair, Department Committee on Graduate Students

Resonant Spatial Light Modulation: Optical Programming and Sensing at the Fundamental Limit

by

Christopher L. Panuski

Submitted to the Department of Electrical Engineering and Computer Science
on May 13, 2022, in partial fulfillment of the
requirements for the degree of
Doctor of Philosophy

Abstract

Fast, energy-efficient, and compact manipulation of multimode optical signals is required for technologies ranging from brain imaging to quantum control, yet remains an open goal for present-day spatial light modulators (SLMs), active metasurfaces, and optical phased arrays. Here, we develop wavelength-scale, high-finesse photonic crystal cavity arrays as a solution to this problem.

Specifically, we demonstrate nanosecond- and femtojoule-order spatial light modulation enabled by four key advances: (i) near-unity vertical coupling to high-finesse microcavities through inverse design, (ii) scalable fabrication of photonic crystal circuits by optimized, 300 mm full-wafer processing, (iii) picometer-precision resonance alignment using automated, closed-loop "holographic trimming", and (iv) out-of-plane cavity control via a high-speed μLED display. Combining each, our approach weds the latest advances in incoherent and coherent optics to open a previously inaccessible regime of programmability: near-complete spatiotemporal control with a >MHz modulation bandwidth per diffraction-limited mode. Simultaneously operating wavelength-scale modes near the space- and time-bandwidth limits, this work approaches the fundamental limits of multimode optical control.

In developing this technology, we also analyze the fundamental limits of light-matter interaction in these remarkable optical microcavities that continue to drive modern science. Operated in reverse, our device constitutes a high-spatial-resolution focal plane array. Surprisingly, we discover that the fundamental limits of these sensors are ultimately dictated by refractive index variations induced by statistical temperature fluctuations. We present the first theoretical and experimental characterization of the associated thermal noise limits in wavelength-scale microcavities, develop a new class of optical sensors operating at this fundamental limit, and analyze noise cancellation techniques to enable continued development in quantum optical measurement, precision sensing, and low-noise integrated photonics.

Thesis Supervisor: Dirk R. Englund
Title: Associate Professor of Electrical Engineering and Computer Science

Fair Winds and Following Seas

> If you want to build a ship, don't drum up the men to gather wood, divide the work and give orders. Instead, teach them to yearn for the vast and endless sea.
>
> Antoine de Saint-Exupéry

The advances described in this thesis would not have been possible without the assistance of an international collaboration of researchers built over the duration of my graduate studies. While the extent of their efforts is innumerable, I have attempted to recognize their contributions in footnotes throughout the following chapters.

Over the past five years, the members of the Quantum Photonics Group at MIT have become my colleagues, friends, and mentors. Ian Christen was instrumental to the experimental efforts detailed in this thesis; his unique ability to out-run and out-swim me after out-smarting me in the lab pushed me towards excellence in my daily endeavors. I was also fortunate enough to work with Cole Brabec, Sivan Trajtenberg-Mills, Thomas Propson, and Mohamed ElKabbash as part of the lab's "*qp-slm*" subgroup that spun out of the spatial light modulation (SLM) work described in this thesis. The other thermal noise work described here was enabled by the support and infinite wisdom of a talented research scientist in our group: Ryan Hamerly. Academic collaborations aside, I am thankful to my office-mates over the years (Mihika Prabhu, Cheng Peng, Valeria Saggio, and Darius Bunandar) whose positive attitudes, joking, and encouragement helped me through challenging times. Lukas Mennel, a visiting student, made our group the "bee's knees" while he was here; his contagious enthusiasm during our squash games was always worth the (seemingly inevitable) blunt force trauma.

These lasting friendships and collaborations would not have been possible in the first place without the Hertz Foundation — and specifically the Fantone family — who funded my graduate experience and helped me to navigate graduate school with a military career. The freedom afforded by the Hertz Fellowship requires an equally flexible advisor — I was fortunate to find Professor Dirk Englund to fill that role. Those who have worked with Dirk will often cite his relentless drive and innovative mindset; however, beyond those characteristics, I found Dirk's ability to *trust* his group members truly remarkable. Shortly after our initial discussion on avenues towards the "ideal" spatial light modulator, I wrote an internal research proposal to focus my thoughts. To my amazement, Dirk suggested that we submit it as a grant proposal. The grant was funded shortly thereafter, and Dirk allowed me to help run the program. So beyond the technical development expected from any graduate program, Dirk helped me to grow as a leader. Professors Isaac Chuang (a fellow

Hertz Fellow) and Jim Fujimoto, the other members of my thesis committee, were similarly flexible: Prof. Fujimoto let me lead lectures and develop new content as a teaching assistant for the 6.631 graduate optics course; Prof. Chuang led me towards challenging problems of importance and continually encouraged me to broaden the scope of my investigations. Thank you all for showing me the "vast and endless sea".

Outside of the lab, the eternal support of my friends and family made my long work days a joy. From snowboarding with Matt Johnson, Josh Perozek, Wammie Hill, and Shan McBurney-Lin to backcountry flying with my father Louis, mother Rebecca, and two brothers Patrick and Benjamin, I always had something to look forward too. Thank you, Mom and Dad, for teaching me to be an explorer, to take pride in my work, and to stay positive. Finally, I would like to recognize and thank my Naval Academy classmates and the rest of our uniformed services for "having the watch" while I pursued this research. I look forward to rejoining you to help solve national security's increasingly technical challenges.

Contents

It is a triumph more glorious, because far more useful to mankind, than was ever won by conqueror on the field of battle.

President James Buchanan (1858)

1

Introduction

At ten minutes-per-word [1], President Buchanan's short message of congratulation to Queen Victoria on the world's first transatlantic telegraph cable would have taken roughly four hours to transmit to the United Kingdom. By contrast, today's international communications constitute (on average) some two hundred trillion bits-per-second (∼200 Tbps) with a total network capacity sufficient to transmit this entire thesis in merely a billionth of a second [2]. Yet despite the seemingly endless social, cultural, and ideological connectivity of this interface, its physical cross section — a collection of less than 500 undersea fiber optic cables mapped in Fig. 1-1 — is remarkably small. The single cable highlighted in green in Fig. 1-1 (Google's "Dunant" cable), for example, houses only twelve pairs of optical fiber — each passing light through a single, ∼10 μm-diameter spatial mode — but could itself support the mean bandwidth of *all* international data [3]. This *spatial* simplicity is enabled by *temporal* complexity: each fiber supports $\mathcal{O}(100)$ independent wavelength channels modulated at $\mathcal{O}(100)$ GBps.

In principle, the high carrier frequencies ω_0 of optical fields ($\sim 2\pi \times 10^{14}$ Hz) *also* enable extreme spatial density (the diffraction-limited with of a single optical mode scales as $1/\omega_0$). For example, combining the cores of *every* undersea optical fiber would form a mere mm^2-area glass aperture. Converting to a free-space aperture with diffraction-limited spatial modes (or, equivalently, increasing each fiber's numerical aperture from ∼0.1 to unity) would further shrink this size by a factor of ∼100 to the cross-sectional area of *a single human hair*[1].

But why can we not manipulate the spatial degrees-of-freedom of these optical fields at the wavelength scale? After all, each undersea cable is terminated with a fiber

---

[1] What a fragile world it would be!

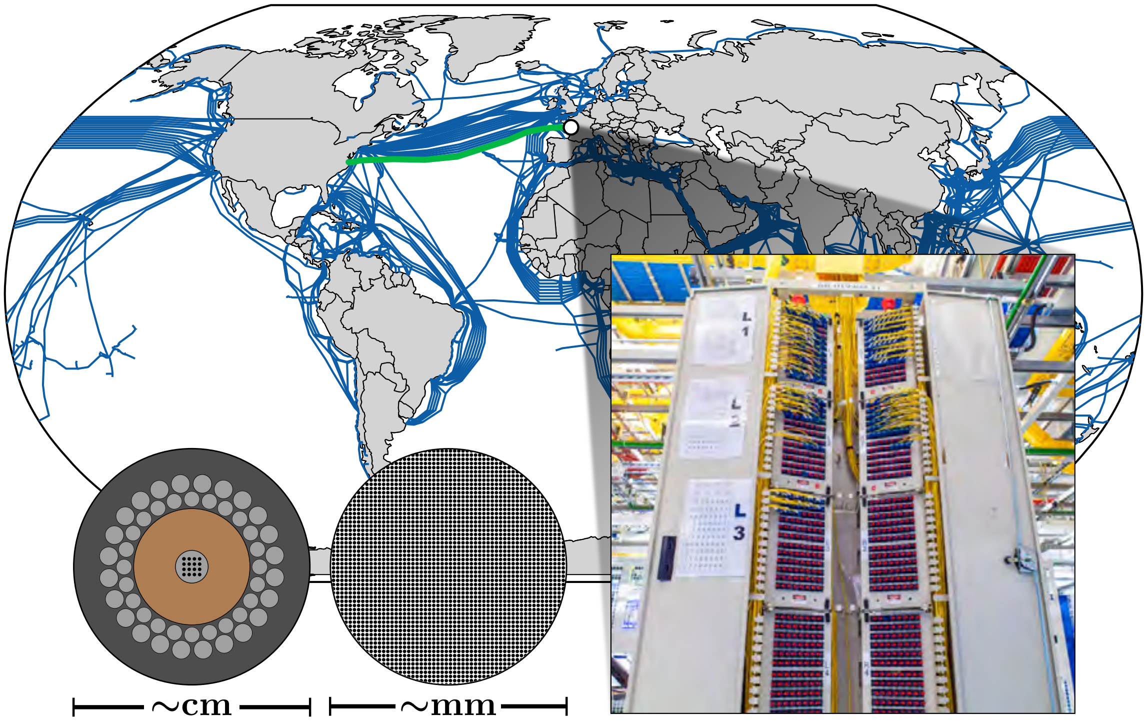

Figure 1-1: Map of undersea fiber optic cables (blue). A single cable (green), housing $\mathcal{O}(10)$ pairs of optical fiber as illustrated by the inset cross-section (left), is capable of supporting the mean bandwidth of all international data. The *temporal* complexity such cables comes at the cost of *spatial* sparsity: while the cores of *all* undersea fibers could fit through a mm^2-area aperture (center cross-section), each data channel is instead separated and manipulated by telecommunications equipment at length-scales orders of magnitude larger than the wavelength of light (as illustrated by the optical distribution frame at a fiber landing station). Photocredit: *arsTechnica* [4].

landing station (inset photograph in Fig. 1-1) as required to distribute and manipulate the individual wavelength channels on each fiber using macroscopic (i.e. “server rack”-scale) telecommunications equipment. The answer, in short, is a recurring tradeoff between spatial and temporal control in optical systems. The ultimate goal of this thesis is to improve the joint *spatiotemporal* control of optical fields — to combine the high-speed modulation characteristic of modern computing and telecommunication systems with wavelength-scale spatial control.[2]

---

[2] Our manuscript describing these central efforts, which spanned the five year duration of my doctoral studies, is currently under review; a pre-print is currently available online [5].

1.1 Spatiotemporal Control with SLMs

This quest to improve spatiotemporal control is motivated by the fundamental importance of programmable optical transformations across science and engineering, from adaptive optics in astronomy [6] and neuroscience [7, 8] to dynamic matrix operations in machine learning [9–11] and quantum computing [12, 13]. Advances in nanotechnology have only recently (within the past 50 years) led to the development of wavelength-scale two-dimensional optical modulator arrays known as "spatial light modulators" (SLMs), yet these devices have become ubiquitous in optical science. Within the past year alone, SLMs has enabled us to engineer and measure our surrounding physical world at length scales spanning orders-of-magnitude: from the creation of arbitrary geometry, two-dimensional Rydberg atom lattices [13] to volumetric three-dimensional laser printing at centimeter-scale [14], all while imaging between micron-scale neural circuits [15] and the light-year-scale "cosmic abyss"[3]. *Despite this importance, the fast, energy-efficient, and compact manipulation of multimode optical systems — the core objective of SLMs — remains an open challenge* [16, 17].

Figure 1-2a summarizes the limitations of current SLMs, which typically comprise a two-dimensional (2D), Λ-pitch array of tunable pixels (subscript p) emitting at wavelength λ into the solid angle Ω_p with a system (subscript s) modulation bandwidth ω_s. Given these parameters, each "spatiotemporal" degree-of-freedom (DoF) simultaneously satisfying the minimum-uncertainty space- and time-bandwidth relations ($\delta A/\lambda^2 \cdot \delta\Omega = 1$ and $\delta t \cdot \delta\omega = 1$, respectively) can be illustrated as a real-space voxel with area λ^2/Ω_p and time duration $1/\omega_p$ for pixel bandwidth ω_p. The optical-delay-limited pixel bandwidth $\omega_p \approx (\Delta\epsilon_p/\epsilon)ck$ can be approximated as a function of the pixels' achievable permittivity swing $\Delta\epsilon_p$ (for the speed of light c) using first-order perturbation theory [18] or similarly derived from linear scattering theorems [19].

Integrating over the switching interval $T = 1/\omega_s$ and aperture area A then gives the total DoF count [20] [4]

$$F = \int_{A,\Omega_p} \frac{\mathrm{d}A}{\lambda^2} \cdot \mathrm{d}\Omega \int_{T,\omega_p} \mathrm{d}t \cdot \mathrm{d}\omega. \tag{1.1}$$

By comparison, the same switching period contains $N = A/\Lambda^2 \leq F$ *controllable* modes, each confined to the pixel area Λ^2 and time window T (shaded box in Fig. 1-2a). Complete spatiotemporal control with $N = F$ is only achieved under the follow-

---

[3] The James Webb Space Telescope (JWST), featuring a 132 degree-of-freedom adaptive optics system, launched during the final year of this thesis. I thank JWST Senior Project Scientist and Hertz Fellow Dr. John Mather for discussing the requirements of these systems with me.

[4] Note that the exact coefficient of proportionality in Eqn. 1.1 depends on the number of polarizations, the complex amplitude and phase controllability of each mode, and the exact definition of distinguishability when defining the Fourier uncertainty relations. For simplicity, we have omitted these $\mathcal{O}(1)$ coefficients.

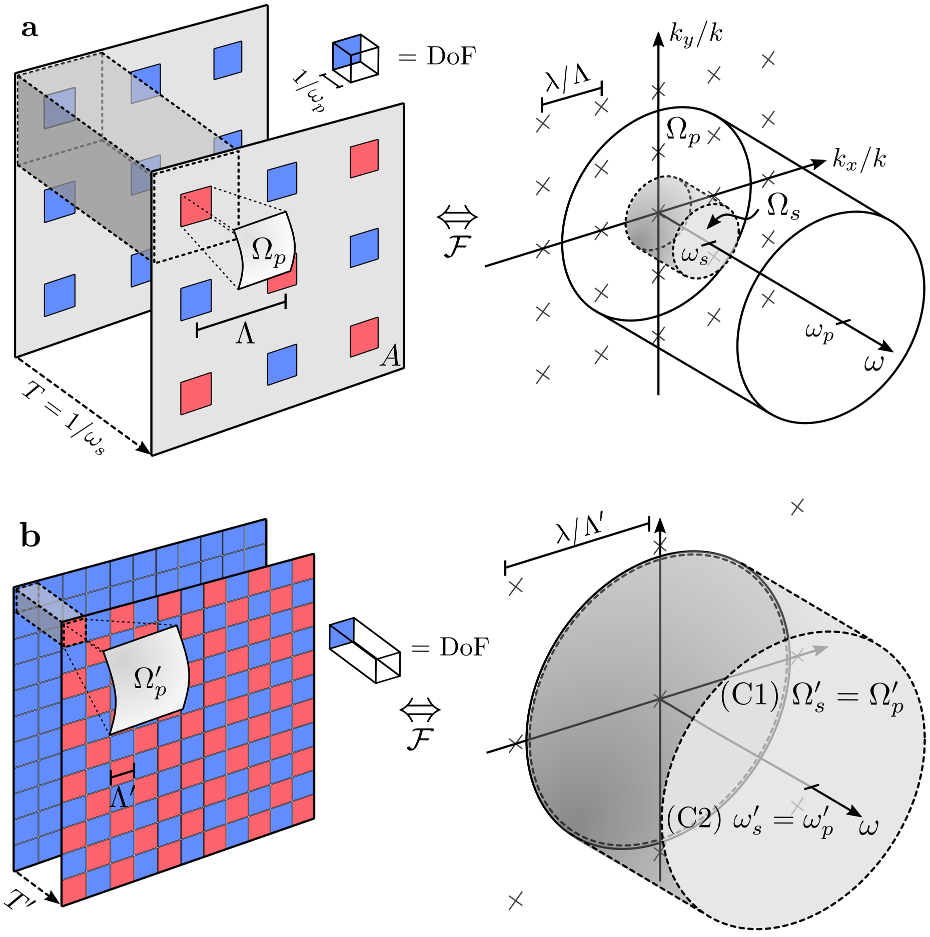

Figure 1-2: Full degree-of-freedom (DoF) spatiotemporal optical programming. A traditional spatial light modulator (a) operating at wavenumber $k = 2\pi/\lambda$ (frequency ω_0) features a 2D array of Λ-pitch pixels within an aperture area A. Each pixel radiates into the solid angle Ω_p and can be switched (as depicted by the blue ↔ red color change) over the timescale $T = 1/\omega_s$ (given a modulation bandwidth ω_s) with a large but slow fractional permittivity perturbation $\Delta\epsilon_p/\epsilon$ (e.g. liquid crystal rotation). The shaded volume indicates the smallest controllable near-field spatiotemporal mode. In the far-field (right), the corresponding shaded spatiotemporal bandwidth $\nu = \Omega_s\omega_s = (\lambda/\Lambda)^2\omega_s$ counts the controllable DoF per unit area and time in a single diffraction order. Since $\Omega_s \ll \Omega_p$ and $\omega_s \ll \omega_p \sim \omega_0\Delta\epsilon_p/\epsilon$, the delay-limited system bandwidth, spatiotemporal control is limited and scattering into undesired diffraction orders (grey ×s) reduces the achievable diffraction efficiency. Alternatively, a fully-filled array of wavelength-scale resonant apertures (b) emitting into the solid angle Ω'_p can enhance the effect of fast (modulation frequency ω'_s), low-energy perturbations $\Delta\epsilon'_p \ll \epsilon$ to simultaneously achieve space- and time-bandwidth limits (C1 and C2, respectively), yielding near-complete spatiotemporal control with $\nu' \approx \Omega'_p\omega'_p$.

ing criteria: (C1) emitters fully "fill" the near-field aperture such that Ω_p matches the field-of-view $\Omega_s = (\lambda/\Lambda)^2$ of a single array diffraction order; and (C2) $\omega_s = \omega_p$. In the Fourier domain, the system's "spatiotemporal bandwidth" $\nu = \Omega_s \omega_s$ counts the controllable DoF per unit area and time within a single far-field diffraction order. As illustrated by the shaded pillbox in Fig. 1-2a, (C1) and (C2) are both satisfied when ν matches the accessible pixel bandwidth $\Omega_p \omega_p$.

Practical constraints have prevented present-day SLM technology from achieving this bound. In general, commercial devices satisfy (C1) at the expense of (C2). Specifically, they offer excellent near-field fill-factor across megapixel-scale apertures but require large $\mathcal{O}(\epsilon)$, slow index perturbations. Liquid crystal SLMs, for example, are limited to $\omega_s \sim 2\pi \times 10^3$ Hz $\ll \omega_p$ modulation rates by the slow rotation of viscous, anisotropic molecules that modulate the medium's phase delay [21, 22]. Digital micromirror-based SLMs offer moderately faster ($\sim 10^5$ Hz) binary amplitude modulation by electrically displacing a mechanical reflector, but at the expense of diffraction efficiency [23]. Mechanical phase shifters [24–28] improve this efficiency but still require design trade-offs between pixel size, response time, and drive energy.

Recent research has focused on surmounting the speed limitations of commercial SLMs with integrated photonic phased arrays [33, 42–44] and active metasurfaces comprised of thermally [45–47], mechanically [27, 48], or electrically [40, 41, 49–51] actuated elements. In most of these approaches, (C1) is not satisfied. Silicon photonics in particular has attracted significant interest due to its fabrication scalability; however, the combination of standard routing waveguides, high-power ($\sim$ mW/π phase shift) thermal phase shifters, and vertical grating couplers in each pixel reduces the fill-factor of emitters, yielding $\Omega_p \gg (\lambda/\Lambda)^2$ [33]. Scattering into the numerous diffraction orders within Ω_p then reduces the achievable zero-order and overall diffraction efficiencies (η_0 and η, respectively). For this reason, η_0 is a useful measure of near-field fill.

Various workarounds, including 1D phased arrays with transverse transverse wavelength tunability [42, 52, 53], sparse antenna arrays [32], and switched arrays [37, 54] improve steering performance but restrict the spatiotemporal basis (i.e. limit F). Alternative nanophotonics-based approaches, often limited to 1D modulation, have their drawbacks as well: phase change materials [45–47] have slow crystallization rates and large switching energies, while electro-optic devices [38, 40, 41, 50, 51, 55, 56], to date, have primarily relied on large-area grating-based resonators to achieve appreciable modulation.

Figure 1-3 compares the performance of these and other experimentally-demonstrated, active, 2D SLMs as a function of spatiotemporal bandwidth's two components: modulation bandwidth ω_s and field-of-view Ω_s. Controllability aside, the evident trade-off between these parameters illustrates the difficulty of creating fast, compact modulator arrays with high ν. Thus, in addition to satisfying the complete control criteria (C1) and (C2), an "ideal" SLM would: (C3) maximize ν by combining wavelength-scale pitches (for full-field $\Omega_s \rightarrow 2\pi$ beamforming) with gigahertz (GHz)-order bandwidths

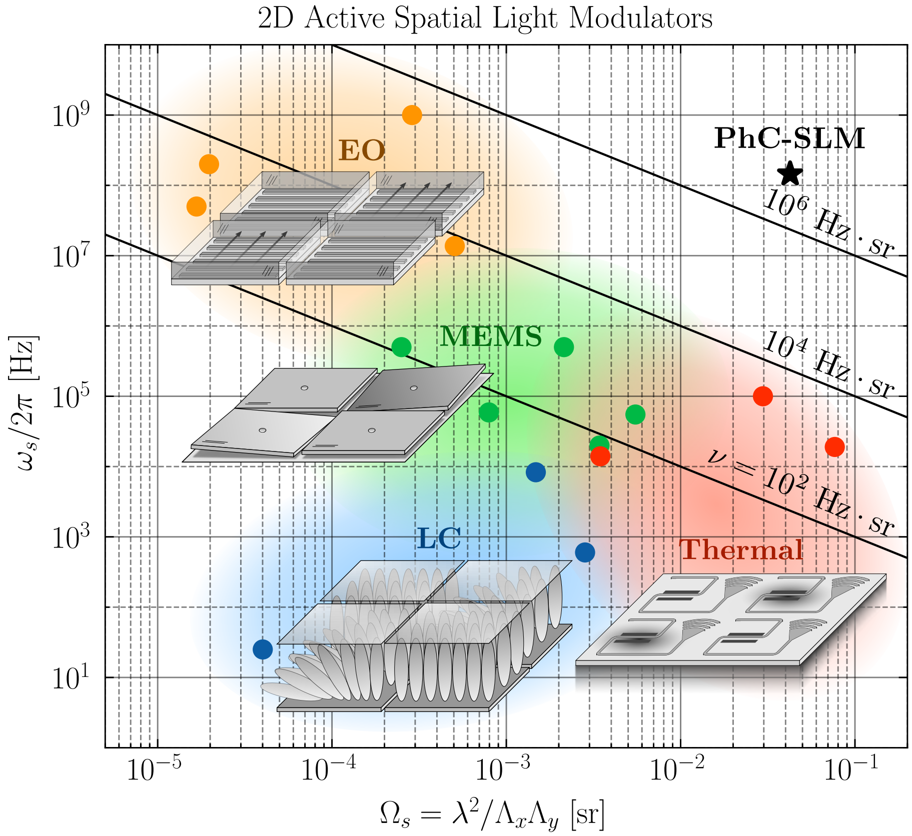

Figure 1-3: A graphical review of previous liquid crystal- (LC) [29–31], thermal- [32–34], micro-electro-mechanical system- (MEMS) [26, 27, 35–37], and electro-optic-driven (EO) [38–41] SLMs reveals an observed tradeoff between modulation bandwidth ω_s and the controllable field-of-view $\Omega_s = \lambda^2/\Lambda_x\Lambda_y$ (i.e. a single diffraction order for $\Lambda_x \times \Lambda_y$ pitch pixels at wavelength λ). The void of compact, high-speed modulator arrays limits demonstrated spatiotemporal bandwidths to $\nu = \Omega_s\omega_s \sim 2\pi \times 10^5$ Hz·sr. This thesis demonstrates a novel photonic crystal spatial light modulator (PhC-SLM) that offers near-complete control over an order-of-magnitude larger ν that previous techniques.

ω_s competitive with electronic processors; (C4) support femtojoule (fJ)-order switching energies as desired for information processing applications [57]; and (C5) have scalability to state-of-the-art megapixel-scale apertures.

These criteria, summarized in Table 1.1, motivate the resonant architecture in Fig. 1-2c. Here, (C3) and (C4) are achieved by switching a fully-filled array of wavelength-scale resonant optical antennas with fast, fJ-order perturbations $\Delta\epsilon_p/\epsilon \ll 1$. Each resonator's far-field scattering and quality factor Q can then be tuned to achieve (C1) and (C2), respectively. Specifically, for any given $\Delta\epsilon_p$ (dictated by system energy constraints, for example), the resonant quality factor Q can be adjusted

Criteria	Description	PhC-SLM
C1	Space-bandwidth limited (full fill)	$\Omega_s/\Omega_p \approx 1$
C2	Time/delay-bandwidth limited	$\omega_s/\omega_p > 0.1$
C3	Maximize spatiotemporal bandwidth	$\nu >$ MHz · sr
C4	fJ-order switching energy (E_{switch})	$E_{\text{switch}} \approx 5$ fJ
C5	Scalable foundry fabrication	300 mm wafer

Table 1.1: Design criteria for an "ideal" spatial light modulator. The performance metrics of the PhC-SLM demonstrated in this thesis are provided for comparison.

to efficiently control each mode at the time-bandwidth limit $\omega_s = \omega_p$. Surprisingly, we also show that proper far-field engineering simultaneously enables operation at the space-bandwidth limit $\Omega_s = \Omega_p$ despite the complex near-field profiles characteristic of confined microcavity modes. *Combined, this resonant SLM architecture enables complete, efficient control of the large spatiotemporal bandwidth supported by its constituent pixels.*

1.2 Photonic Crystals: Ideal Pixels, Poor Systems

Figure 1-4 illustrates our specific implementation of this optimal programmable surface: the photonic crystal spatial light modulator (PhC-SLM) [58]. Coherent signal light is reflected off a semiconductor slab (permmitivity ϵ) hosting a 2D array of semiconductor PhC cavities with instantaneous resonant frequency $\omega_0 + \Delta_{mn}(t)$. A short-wavelength incoherent control plane imaged onto the cavity array controls each resonator's detuning $\Delta(t) \approx -\Delta\epsilon(t)/2\epsilon$ via the permmitivity change $\Delta\epsilon_p(t)$ induced by photo-excited free carriers [59, 60]. We optimize the resonator bandwidth $\Gamma \approx \omega_s \approx 2\pi \times \text{GHz}$ (corresponding to a quality factor $Q = \omega_0/\Gamma \sim 10^5$) to maximize the linewidth-normalized detuning Δ/Γ without significantly attenuating the cavity's response at the carrier lifetime (τ)-limited modulation rate $\omega_s = 1/\tau$. Under these conditions, free carrier dispersion efficiently modulates the complex cavity reflectivity $r(\Delta)$ to enable fast ($>$ 100 MHz given a $\sim$ns free carrier lifetime [61]), low-energy (fJ-order) conversion of incoherent control light into a dense array of coherent, modulated signal modes.

This out-of-plane, all-optical switching approach is motivated by the recent development of high-speed, record-brightness µLED displays [63, 64] integrated with complementary metal-oxide-semiconductor (CMOS) drive electronics for consumer displays [65, 66] and visible light communication [67, 68]. In particular, gallium nitride µLED displays with record GHz-order modulation bandwidths [68, 69], submicron pixel pitches [50], and large pixel counts [70] have been demonstrated within the past few years. Re-purposing these displays for reconfigurable, "wireless" all-

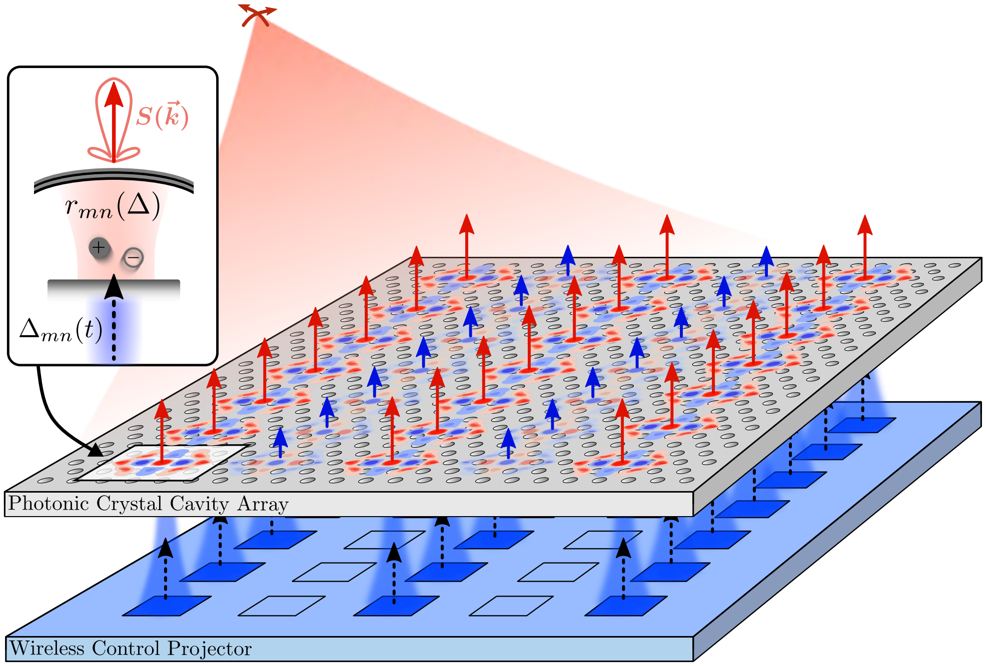

Figure 1-4: Overview of the resonant photonic crystal spatial light modulator (PhC-SLM). We overcome the limitations of previous SLMs by modulating an array of wavelength-scale, high-finesse microcavities with a high-speed incoherent μLED display. Absorbed μLED pulses control the detuning Δ of resonant pixels — each comprising a high-quality-factor ($Q > 10^5$), small-mode-volume ($V < 0.1\lambda^3$) silicon PhC cavity — via free carrier dispersion, which efficiently modulates the amplitude and phase (illustrated by the length and color of emission arrows at each cell, respectively) of the pixel's complex reflection coefficient $r(\Delta)$. Despite the sub-wavelength near-field confinement of each resonator mode (c.f. inset simulated mode profile overlaid on a SEM micrograph of an $L4/3$-type cavity [62]), inverse design focuses its far-field scattering $S(\vec{k})$ into the ideal diffraction-limited field-of-view $\Omega_p = \lambda^2/\Lambda_x\Lambda_y$ for $\Lambda_x \times \Lambda_y$ pitch pixels. The array emission (c.f. inset far-field profile) is thus limited to the zeroth diffraction order (marked by ×s), corresponding to efficient vertical coupling and near-unity "fill factor" of the radiating aperture. Combining the scattering from each resonant "antenna" in a large-scale aperture, fabricated via optimized 300 mm wafer-scale processing (inset photograph), enables efficient, high-speed optical beamforming.

optical cavity control eliminates the need for electronic tuning elements at each pixel. These controls induce excess optical loss, limit pixel pitches, and even impose a fundamental scaling limit for single-layer architectures: as aperture area A grows, $\mathcal{O}(A)$ pixel controls eventually cannot be routed through the $\mathcal{O}(\sqrt{A})$ perimeter [71].

Free of these constraints, we designed high-finesse, vertically-coupled microcavities offering coupling efficiencies $> 90\%$, phase-dominant reflection spectra [34, 73],

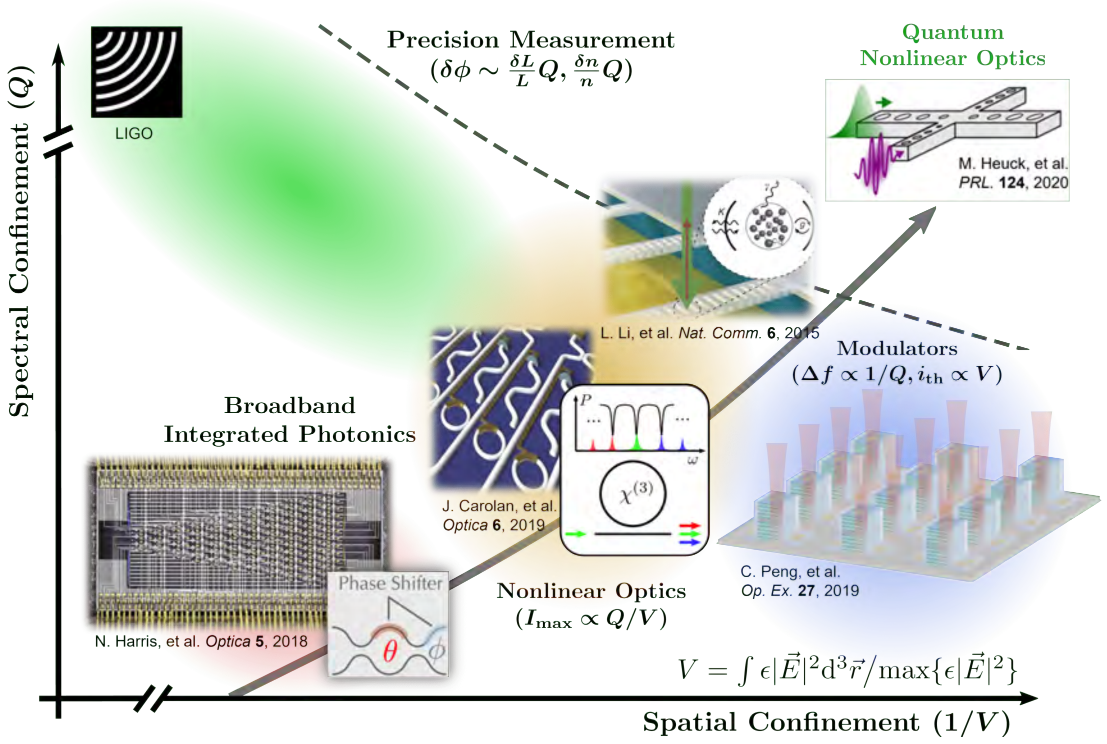

Figure 1-5: Characterization of integrated optical devices based on their spectral and spatial confinement, quantified by the quality factor Q and inverse mode volume $1/V$, respectively. Tradeoffs between these two figures-of-merit are weighed for various applications: precision measurement favors high-Q to magnify the phase shift $\delta\phi$ produced by a fraction length $\delta L/L$ or index perturbation $\delta n/n$; modulators and active devices reduce V (at the expense of Q) to improve bandwidth, reduce threshold currents i_{th}, etc.; and nonlinear optics seeks the best possible tradeoff between Q and V to maximize the intensity enhancement $I_{\max} \propto Q/V$ of any input field. Combining high-Q/V photonic crystal cavities — offering best-n-class and continually improving performance for both metrics — with the scalable fabrication characteristic of traditional broadband integrated photonic circuits (such as the illustrated interferometer mesh), unveils new applications such as photon-level (i.e. quantum) nonlinear optics. Our beamforming application harnesses these high-Q/V devices for efficient, compact switching. We note that the exact form of V varies per application; I have listed the Purcell mode volume — a weighted average of electric field energy density normalized its peak value in the device, which serves as a proxy for the more fundamental local density of states quantity [72] — based on its prevalence in the field.

and directional emission $\Omega_p \approx \Omega_s$ for high-efficiency beamforming (Chapter 2). Optimized, wafer-scale processing enables these “resonant antennas" to be fabricated in arrays with mean quality factors $\langle Q \rangle > 10^6$ and sub-nm resonant wavelength stan-

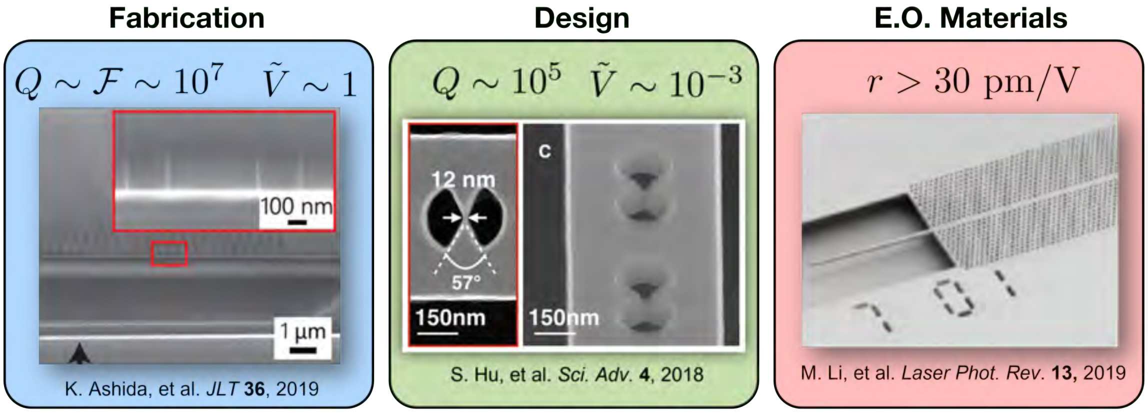
Fabrication

$Q \sim \mathcal{F} \sim 10^7 \quad \tilde{V} \sim 1$

K. Ashida, et al. *JLT* **36**, 2019

Design

$Q \sim 10^5 \quad \tilde{V} \sim 10^{-3}$

S. Hu, et al. *Sci. Adv.* **4**, 2018

E.O. Materials

$r > 30$ pm/V

M. Li, et al. *Laser Phot. Rev.* **13,** 2019

Figure 1-6: Summary of recent developments in PhC cavity performance. Improved fabrication (left) offers record quality factors $Q > 10^7$ in normalized mode volumes $\tilde{V}$ approaching a single cubic wavelength in the confining medium [76]. Engineering dielectric boundary conditions shrinks $\tilde{V} \ll 1$ [77, 78] (for the Purcell mode volume V). Combining both advances in novel electro-optic (E.O.) materials such as thin-film lithium niobate (with Pockels coefficient $r > 30$ pm/V) enables efficient modulation and control [79–82].

dard deviation (Chapter 3). Automated, parallel laser-assisted thermal oxidation [74, 75] then trims 8×8 cavity arrays to picometer-order uniformity [74, 75] (Chapter 6), enabling high-speed spatial light modulation with fJ-order switching energies and $\omega_s > 2\pi \times 100$ MHz (Chapter 7). Compared to the previous devices surveyed in Fig. 1-3, our SLM offers near-complete control over an order-of-magnitude larger spatiotemporal bandwidth.

Returning to this sections title, why do we focus on photonic crystals? Fig. 1-2 demonstrates that the achievable system spatiotemporal bandwidth is ultimately limited to that of its constituent pixels. Wavelength-scale PhC cavity pixels therefore maximize ν by supporting Purcell mode volumes V below a cubic wavelength in the confining dielectric with tunable quality factors (up to record values $Q \sim 10^7$ [76]) to meet design criteria (C2). Among all integrated photonic resonators, PhC cavities offer the best-in-class combination of spectral and spatial confinement (Fig. 1-5).

For this reason, these high-Q/V microcavities are a backbone of physical science: they improve sensitivity, enhance atom-photon interactions, and shape optical modes. Ongoing theory, design, and fabrication advances (Fig. 1-6) continue to improve their performance towards the requirements of “holy grail” goals in optics such as photon-level nonlinearities. This recurring improvement, recently enabling experimental demonstrations of devices with quality factor to normalized mode volume ratios $Q/\tilde{V}$ in excess of 10^7, led us to reconsider potential applications of these devices. One of those investigations led to my master’s thesis on the photodetection scheme illustrated in Fig. 1-7 [83]. There, we showed that single absorbed photons could lead to linewidth-order resonant frequency shifts via free-carrier-dispersion given devices with $Q/\tilde{V} \sim 10^8$ [60]. This possibility of efficient, few-photon switching at wavelength-scales ultimately motivated us to develop PhC cavities for beamforming applications.

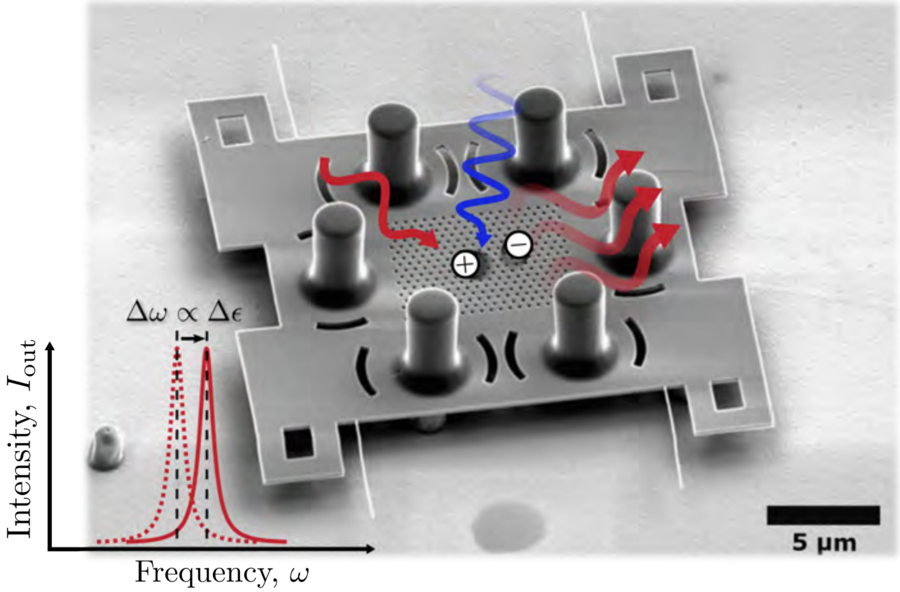

Figure 1-7: Concept for photon-level switching via free-carrier dispersion in a high-Q/V microcavity [60]. Absorbed visible photons (blue) generate a permmitivity change $\Delta\epsilon$ by photoexciting free carriers. The resulting change in resonant frequency $\Delta\omega$ produces a "photomultiplication" effect since the number of photons in the scattered probe field can exceed that of the absorbed pump. The micrograph depicts a thermally isolated PhC cavity for bolometry as described in Chapter 8 [84].

Unfortunately, photonic crystals are plagued with a number of problems that prevent translation of these excellent per-pixel figures-of-merit to the system:

1. Optimizing the Q of small-V PhC cavities cancels radiative leakage, yielding broad far-field patterns $\Omega_p \gg \Omega_s$ that violate (C1) and reduce coupling, effectively isolating the device from external inputs

2. nm-scale fabrication fluctuations produce nm-scale resonant wavelength variations, preventing efficient simultaneous switching at a common resonant frequency; (C4) is therefore restricted

3. Few-100 nm feature sizes and nm-scale wavelength variations favor serial direct write fabrication techniques such as electron-beam lithography, negating (C5)

To date, these complications have prevented the simultaneous, coherent operation high-Q resonant systems.

1.3 The Road Ahead

This thesis demonstrates that these problems are not fundamental. The coming chapters, outlined in Fig. 1-8 will detail how we overcame each hurdle to achieve the "ideal" SLM of Table 1.1. Along the way, our engineering pursuit also led to fundamental scientific insight. Namely, the ability to fabricate optical microcavities near-record finesse raised the question: how far can can we increase $Q/\tilde{V}$? The surprising results described in Chapter 4 show that, similar to well-studied macroscopic optical cavities present in graviational wave interferometers (e.g. LIGO), microcavity performance is fundamentally limited by thermal noise. This has immediate implications to recently-proposed room temperature optical quantum computing proposals, which we specifically explore. It's not all "gloom and doom" though — Chapter 5 shows how proper characterization of thermal noise enables novel cancellation to surmount the demonstrated noise-volume tradeoff.

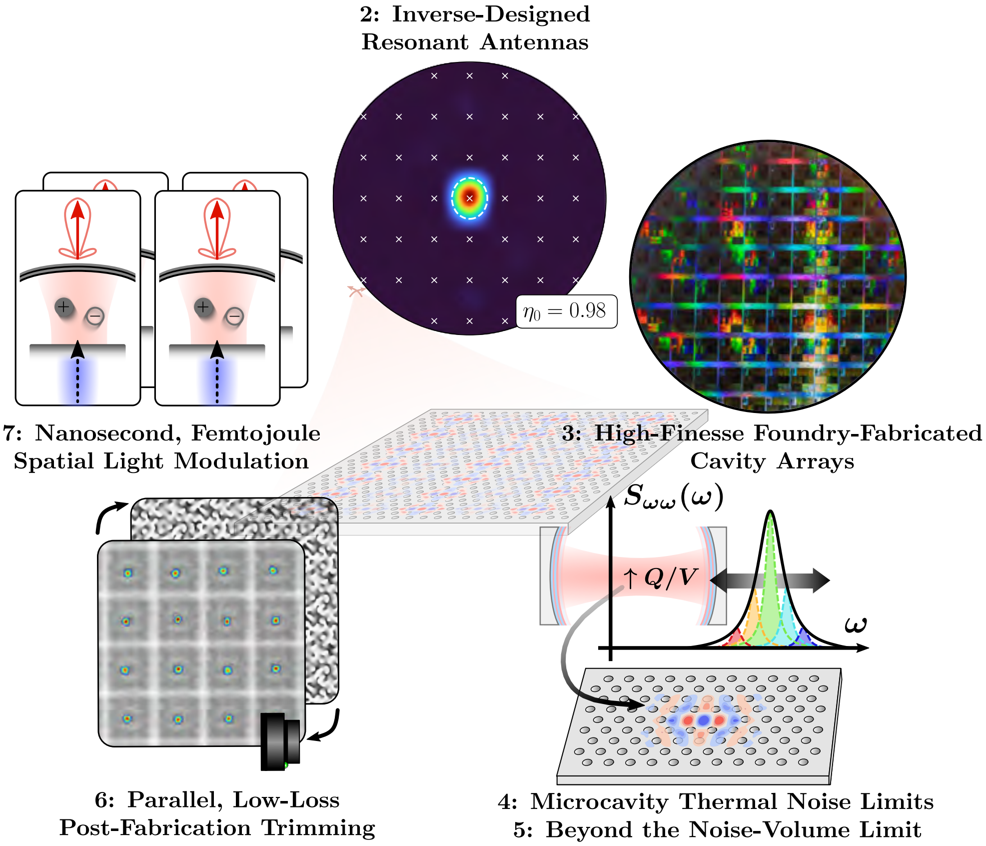

Figure 1-8: Outline of thesis chapters. Chapters 2-3 and 6-7 focus on designing, fabricating, and controlling scalable resonant photonic crystal circuits. The more fundamental investigations in Chapters 4-5, which describe thermal noise limits and noise cancellation techniques in high-finesse microcavities, were motivated by the engineering advances required to develop the PhC-SLM (background image).

Like killing a fly with an atomic bomb.

Dr. John Kolena (1947-2020)

2

Microcavity Beamforming

Abstract

We introduce an efficient inverse-design method that allowed us to discover a new generation of optical microcavities for diffraction-limited beamforming with 10× improvement in directivity over existing designs. This technique avoids solves a recurring issue with optical resonators: storing light requires emission to be eliminated, which effectively decouples the device from free-space optical fields. Our optimized photonic crystal cavities, however, act as resonant "optical antennas" with near perfect free-space coupling into a diffraction-limited vertical beam. This cavity design breaks a paradigm in nanophotonic cavities that small mode volume (V) must come with large beam divergence: we show that high-Q, small-V, and low beam divergence are all simultaneously possible. The resulting space-bandwidth-limited emission satisfies a key requirement for complete degree-of-freedom spatiotemporal control (criteria C1) and enables high performance resonant beamforming.

2.1 The Bandwidth-Efficiency Trade-off

In many regards, optical microcavities constitute the "ideal" spatial light modulator pixels described in Chapter 1. Beyond maximizing the the pixel's accessible spatiotemporal bandwidth, they are also well suited for low-power switching: any small index change $\Delta\epsilon$ applied across the small mode volume V can be resonantly enhanced to yield linewidth-order frequency shifts [85]. Two-dimensional PhC cavities — which isolate a mode by vertical index guiding and lateral Bragg reflection in a periodically patterned dielectric slab — extend this spatial and spectral confinement to the extreme with sub-wavelength (i.e. normalized volume $\tilde{V} = V/(\lambda/n)^3 < 1$ relative to a cubic wavelength in the confining dielectric of refractive index n) modes supporting quality factors in excess of 10^7 [76, 78]. This record experimental performance continues to evolve, and pushing both metrics towards their fundamental limits remains an active field of research [77, 86, 87] that we will further explore in Chapters 4 and 5. Unfortunately, the near-ideal resonant characteristics of traditional PhC designs are optimized at the expense of out-of-plane coupling, rendering them ill-suited for beamforming applications.

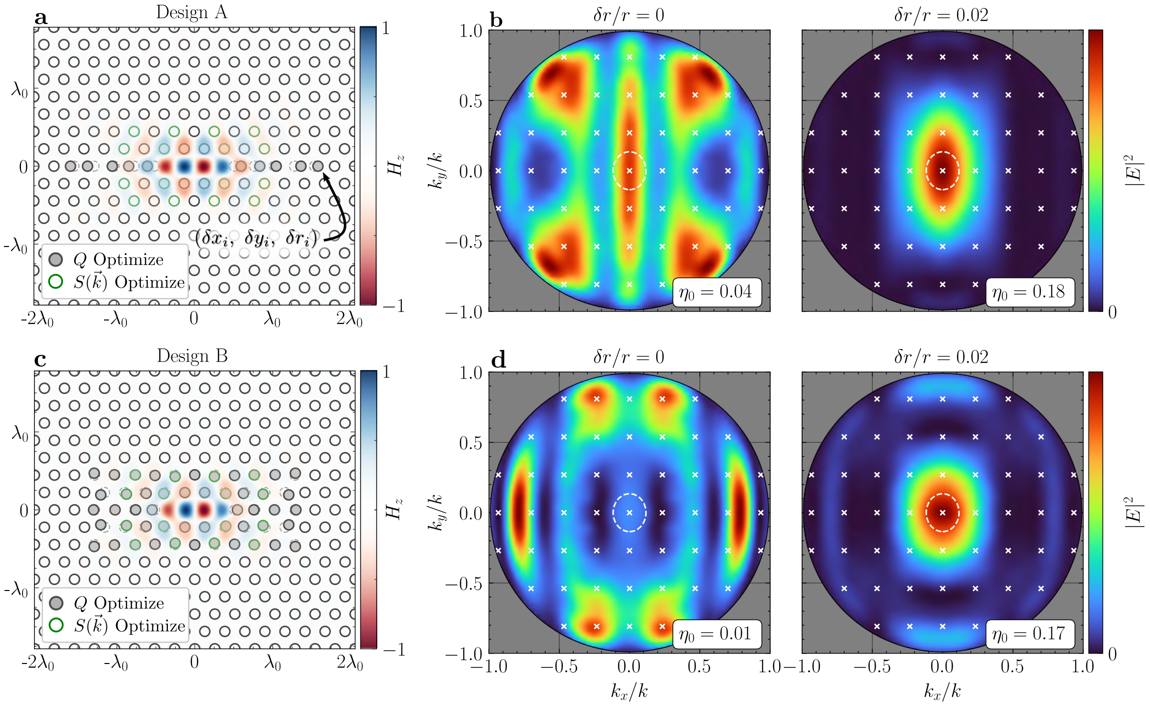

Figure 2-1: Silicon $L3$ slab defect cavity designs (hexagonal lattice constant $a = 0.4$ µm; hole radius $r/a = 0.25$; slab thickness $t = 220$ nm) with overlaid midplane magnetic field profile H_z after Q optimization by displacing $(\delta x_i,\ \delta y_i)$ and resizing (δr_i) the shaded holes in the $16a \times 16(\sqrt{3}/2)a$ periodic unit cell. Hole shifts are magnified by 3× for visualization. Design A (panel a) [88] offers $Q \approx 5 \times 10^6$ at a resonant wavelength $\lambda_0 = 1544$ nm, whereas Design B (panel c) features $(\lambda_0, Q) \approx (1560\text{ nm},\ 3 \times 10^7)$ [89]. Both optimizations produce well-confined modes that radiate into broad, complex far-field profiles $S(\vec{k})$ (left panels of b, d, respectively), yielding poor coupling to a and zero-order diffraction efficiency $\eta_0 \ll 1$. The state-of-the art technique for improving directionality is to superimpose a grating perturbation (via a hole size increase $\delta r/r$ at the holes outlined in green) to vertically scatter band-edge energy at the expense of Q. The resulting far-field profiles for $\delta r/r = 0.02$ are shown in the right-hand panels; the Q of both designs is reduced to $\sim 8 \times 10^5$ for a modest zero-order efficiency improvement.

To illustrate this point, consider the common Q-optimized "L3" PhC cavity designs in Fig. 2-1 [88, 89]. Removing three holes from a hexagonal lattice confines a defect mode in a silicon PhC slab. A few holes are then displaced by $(\delta x_i, \delta y_i)$ and possibly resized by δr_i to minimize radiative leakage in the light cone (transverse wavenumber $k_{||} = |\vec{k}| = \sqrt{k_x^2 + k_y^2}$ smaller than the resonant wavenumber $k = 2\pi/\lambda$), thereby maximizing Q. The exact displacement parameters are typically numerically optimized in computationally expensive full-wave electromagnetics simulations (finite difference time domain, or FDTD, for example), which ultimately limits the number of free parameters. In contrast with the ideal fully filled array of uniform apertures in Fig. 1-2b, the resulting unit cells house small, confined, and spatially complex modes. The consequences of these nonidealities are immediately apparent in each mode's far-field intensity profile (Fig. 2-1b, d): 1) the Q optimization forces radiative leakage to high numerical apertures ($k_{||}/k \approx 1$); and 2) multiple grating orders of the array lie within this broad emission profile since $\Omega_p \gg \Omega_s$. Complete spatiotemporal control is thus impossible due to the low zero-order diffraction efficiency $\eta_0 \ll 0.1$.

Fortunately, these limitations are not fundamental: the effective scattering aperture $A_0 = \lambda^2/\Omega_p$ of a resonant mode can extend beyond its $1/e$ decay area A_e. This apparent space-bandwidth violation $(A_e/\lambda^2) \cdot \Omega_p = A_e/A_0 < 1$ is enabled by resonant scattering [1]: permittivity perturbations further into the mode's evanescent tail (i.e. further from the central cavity defect) can become a dominant scattering source as Q increases. The question then becomes: how should scatterers be arranged to produce a desired far-field emission pattern?

One intuitive (and in this case, the state-of-the-art) answer is a harmonic $2a$-period grating perturbation (shown in Fig. 2-1) that "folds" energy concentrated at the band-edge $k_x = \pi/a$ back to $k_{||} = 0$, yielding vertical radiation at the expense of reduced Q [92–94]. In the perturbative regime, the far-field scattering profile exactly images the broad band-edge mode. Magnifying the perturbation thus reduces Q without any significant directivity improvement, demonstrating the constraints imposed by a fixed-geometry design. The right-hand panels of Fig. 2-1 show the narrowed far-field profile produced by a $\delta r_i/r \approx 0.02$ grating perturbation, which balances the reduced $Q \approx 8 \times 10^5$ and a modest diffraction efficiency improvement ($\eta_0 < 0.2$).

2.2 Inverse-Design Technique

Since the perturbative grating coupler is applied after the single-objective Q optimization is complete, this approach sacrifices Q for directivity. Ideally, the near- and far-field cavity confinement would instead be simultaneously optimized to maximize Q and η_0. This open goal in integrated photonics — the ability to efficiently couple free-space light into the high-Q resonant modes of small-volume microcavities — was

---

[1] Resonant electrical antennas feature similar characteristics, leading to well-studied relationships between antenna Q and super-directivity [90, 91].

a recurring theme in my research group. The specific applications varied, but a common objective was to efficiently collect the Purcell-enhanced emission from quantum (i.e. single photon) emitters into single-mode fiber, where it could then be manipulated with other instruments over long distances. Unfortunately, the optimization approaches for this objective were akin to the quote at the beginning of this chapter from my late physics professor Dr. John Kolena. Specifically, they relied on iteratively optimizing FDTD simulation outputs with gradient-free algorithms [95, 96]. For me, the harrowing process of simply verifying the resonant properties of a high-Q optical microcavity with a single FDTD simulation — an hours long process on our computational cluster depending on the desired accuracy — was enough to motivate a search for better solutions.

A review of semi-analytic methods eventually led me to the seminal work on "guided mode expansion" (GME) [97], which effectively reduces three-dimensional photonic crystal simulations to 2D using an optimized basis set of guided modes as opposed to a complete basis set (plane waves, for example). The technique is inherently approximate as a result, but the close correspondence between GME results in the literature and first-principles FDTD or plane-wave-expansion simulations gave promise for its applicability to my beamforming application. Idea turned to action when Momchil Minkov, a photonic crystal optimization expert at Stanford, released an open-source GME package with integrated inverse design functionality via automatic differentiation [98]. Within a week of contacting Momchil, we were able to show that: 1) GME could accurately predict the far-field profiles of PhC cavities; and 2) that we could optimize designs to achieve the ideal directivity of the planar apertures in Fig. 1-2b for any desired quality factor (below the maximum achievable metrics of Q-only optimizations). Before fully unveiling the technique in the coming sections, I will first review the fundamentals of GME.

2.2.1 Guided Mode Expansion for PhC Slabs

To better understand the applicability of GME, we will consider the bandstructure (i.e. the discrete eigenfrequency spectrum of localized eigenmodes as a function of in plane wave vector $\vec{k}$) of a $t = 0.55a$ nm-thick silicon ($n \approx 3.48$ at the design wavelength $\lambda \sim 1550$ nm) slab with a hexagonal lattice of varying normalized radius r/a holes for the lattice constant a (Fig. 2-2).[2] Since the finite-thickness slab lacks vertical translational symmetry, the modes are not purely polarized (except in the midplane of the slab) but can instead be classified as even or odd with respect to reflection

---

[2] Despite the incomplete bandgaps supported by these "PhC slabs" — broken translational symmetry in the vertical direction allows modes with frequencies above the light line ($\omega = |\vec{k}|/n_{\text{clad}}$ for a cladding index n_{clad} and in-plane wave vector $\vec{k}$) to couple to the continuum of unbound propagating modes in free space — the feasibility of fabricating these structures has led to their widespread adoption in resonant biosensors [99, 100], high-Q optical cavities [76], efficient optical switches [101], coupled-cavity delay lines [102], polarization converters [103], and more.

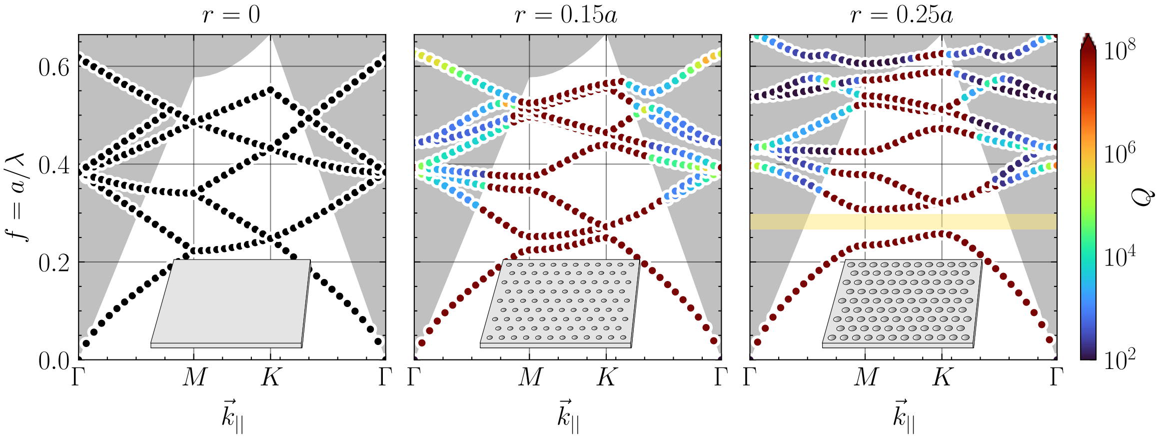

Figure 2-2: GME-computed bandstructure — frequency of eigenmodes in normalized units $f = a/\lambda$ as a function of in plane wavevector $\vec{k}$ at points around the independent Brillouin zone (IBZ) boundary — for a photonic crystal slab ($n = 3.48$) with a hexagonal lattice of variable air holes ($r/a \in [0, 0.15, 0.25]$ from left to right), lattice constant a, and normalized thickness $t/a = 0.55$. The parameters are chosen to match the high-Q . Only even (with respect to vertical reflection symmetry about the slab midplane; also known as "TE-like" for low-frequency bands [18]) are computed by restricting the GME basis set to even slab waveguide modes. The light cone is shaded in gray. The color of each eigenmode corresponds to its associated radiative quality factor, which is computed analytically through perturbation theory. Below the light cone, the true guided modes have infinite quality factor, whereas the majority of guided resonances above the light line have finite quality factor due to coupling with continuum modes. For sufficiently large r/a, an incomplete bandgap (shaded in yellow) is present.

about the midplane bisecting the slab due to the permittivity profile's reflection symmetry in that plane.[3] Here, we consider only the even-symmetry modes to match the permittivity profile symmetry of the symmetrically-clad PhC membranes of interest.

The unpatterned slab in the left-hand panel of Fig. 2-2 has continuous lateral translational symmetry, so $\vec{k}$ is conserved. Thus, while the artificial imposition of a reduced Brillouin zone produces states lying above the light line, all of the bound modes are *true* guided modes with infinite radiative quality factor. Since this approximate bandstructure is computed using a basis set of confined waveguide modes, these bound states are the *only* computed eigenmodes. This is not true in general, but rather a feature of GME's restricted basis set of true guided modes in an "effective" unpatterned photonic crystal slab. For any general computational implementation, the

---

[3] The low-lying even and odd bands are "TE-like" ($\sim H_z$ polarized) and "TM-like" ($\sim E_z$ polarized), respectively. This relationship breaks down for sufficiently high eigenfrequencies, as the emergence of nodal planes along the vertical direction can switch the mode's symmetry [104].

eigenmodes $\vec{H}(\vec{r}) = \sum_j a_j \vec{H}_j(\vec{r})$ are expanded in a truncated basis set of known eigenmodes $\vec{H}_j$, allowing the expansion coefficients a_j to be solved as a finite-dimensional Hermitian eigenproblem. Using an alternative plane-wave basis (i.e. the set of $\vec{H}_j$ computed from the uniform permittivity $\epsilon(\vec{r}) = 1$ Maxwell eigenproblem), for example, would produce bands consisting of bound states as well as unbound propagating modes. As a result, bands above the light cone in 3D plane-wave expansion (PWE) simulations [105] must be interpreted with great care.

The center and right panels of Fig. 2-2 illustrate the evolution of bandstructure as the radius r of holes in the hexagonal lattice increase. The modes of the patterned slabs closely resemble the guided modes of the unpatterned slab with two notable differences: 1) states above the light line become lossy guided resonances due to scattering from the patterned holes (or, alternatively, due to coupling to the radiative continuum above the light line since $\vec{k}$ is no longer conserved), and 2) the same patterning effectively couples the original guided modes, leading to the observed band splittings. This close relationship between the unpatterned and patterned modes is the essence of guided mode expansion. In the GME formalism [98], the patterned slab is seen as a structural perturbation of an "effective" unpatterned slab with an permittivity $\epsilon_{\text{eff}} = \int_\Omega \epsilon(\vec{r})\ \mathrm{d}^2\vec{r}/A_\Omega$ averaged over the unit cell Ω with area A_Ω. Intuitively, the reduced effective permittivity shifts the unpatterned bands to higher frequencies, producing bands qualitatively co-located with the center of the split bands in the patterned bandstructure.

Whereas PWE imposes artificial periodic boundary conditions in the vertical direction of a 3D unit cell, GME's incomplete basis set of true guided modes is computed for an arbitrary multi-layer slab structure from transfer matrix theory [98] which analytically accounts for the boundary conditions between layers and effectively reduces the problem to 2D. Finally, first-order perturbation theory can be used to calculate the coupling between guided resonances above the light line and continuum states of the unpatterned slab, thereby yielding the approximate radiative quality factorrs shown for the patterned slabs in Fig. 2-2. However, these advantages of GME are not without an associated cost: the incomplete basis set of GME fundamentally implies that the technique is approximate. This is contrary to PWE, where the only approximation is a required truncation of the complete plane-wave basis set. Despite this main drawback, we will show that GME is an efficient, accurate method for computing the frequencies, Bloch modes, and radiative quality factors of highly confined slab PhC cavity modes. Combining these benefits of GME with inverse-design then allows us to produce "ideal" resonant pixels for beamforming.

2.2.2 Efficient Simulation Meets Efficient Optimization

Compared to the fixed-geometry, grating-coupled cavity designs, an ideal cavity would make use of *all* design parameters to maximize η_0 (and thereby the effective near-field fill factor) for any desired Q. With hundreds of tunable hole parameters per

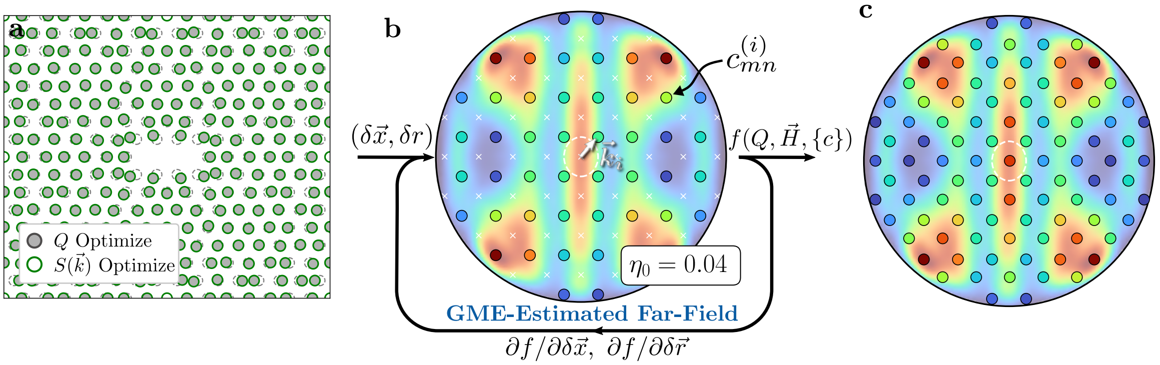

Figure 2-3: Combining GME with inverse-design enables joint optimization of a cavity's Q and far-field scattering profile $S(\vec{k})$ with respect to the position and size of *every* hole in its unit cell (a). The unit cell parameters match those of Fig. 2-1. Guided mode expansion (GME) approximates the mode's Q *and* far-field profile by sampling the losses $\{c\}$ at the array's diffraction orders (white ×s) displaced by Bloch boundary conditions $\vec{k}_i$ (i.e. at the colored dots in b). An objective function f that maximizes Q, confines $\vec{H}$, and minimizes $\{c\}$ at any non-zero diffraction order can then be efficiently optimized with respect to *all* hole parameters using reverse-mode automatic differentiation (b). Aggregating the losses from simulations at multiple $\vec{k}_i$ increases the resolution of the GME-estimated far-field profile (c).

unit cell, the 2D PhC cavities under consideration are ideal candidates for this goal. We therefore developed the simulation framework in Fig. 2-3, which combines semi-analytic guided mode expansion (GME) simulations with automatic differentiation to simultaneously optimize the cavity's near- and far-field confinement using efficient gradient-based optimization. In each iteration, GME approximates the eigenmode of a cavity unit cell (Fig. 2-3a) using the incomplete basis set of waveguide modes in an "effective" unpatterned slab [97], effectively transforming the 3D eigenproblem to 2D as described in Sec. 2.2.1. Although radiative plane waves are excluded from this basis set, we compute the loss rate $c_{mn}^{(i)} = -\mathrm{Im}\{\omega_0|_{\vec{k}_i,\vec{G}_{mn}}\}$ at each reciprocal lattice vector G_{mn} offset by the Bloch periodic boundary conditions $\vec{k}_i$ using time-dependent perturbation theory based on the overlap between the cavity mode and the radiative continuum. *Critically, we discovered that these coupling coefficients coarsely sample and accurately approximate the cavity's far-field emission* (Fig. 2-3b). Scanning $\vec{k}_i$ over the irreducible Brillouin zone of the rectangular cavity array improves the sampling resolution (Fig. 2-3c), and an overall Q can be estimated by averaging the total loss rates $\Gamma^{(i)} = \sum_{mn} c_{mn}^{(i)}$ in each simulation.

The gradient of any arbitrary function of these GME simulation outputs can then be efficiently computed with respect to *all* input parameters using reverse-mode automatic differentiation. Whereas numerical gradient computation time scales with the number of input parameters (hundreds), the cost of this backpropagation generally scales with the number of simulation outputs — a single scalar figure-of-merit (f) in our case. Whereas $f = Q$ has been the target metric for most GME-based cavity optimization [62, 88] to date, here we simultaneously optimize the cavity's approximated far-field emission with an objective function

$$f = \frac{1}{N} \sum_{i=1}^{N} \frac{c_{00}^{(i)}}{\Gamma^{(i)}} \arctan\left(\frac{Q}{Q_0}\right) |E_0|^2 \tag{2.1}$$

targeting three main goals: 1) increase Q to a design value Q_0; 2) force the associated radiative loss into the zeroth diffraction order of the array for efficient vertical coupling; and 3) minimize the Purcell mode volume V by maximizing $|E_0|$, the electric-field magnitude at the center of the unit cell.

2.3 Simulation Results

We implement the inverse design strategy in Fig. 2-11b using the open-source guided mode expansion (GME) package `Legume` [98]. During each optimization step, we aggregate the losses of the fundamental slab mode over four Bloch boundary conditions $\vec{k}_i$ at all wave vectors $\vec{g}_{mn} = \vec{k}_i + \vec{G}_{mn} = \vec{k}_i + 2\pi(\frac{m}{\Lambda_x}, \frac{n}{\Lambda_y})$ satisfying $|\vec{g}_{mn}| < g_{\max} = 2.5 \times 2\pi/a$ given the reciprocal lattice vectors $\vec{G}_{mn}$. The objective function Eqn. 2.1 converges within tens of iterations, and the resulting design is then verified with $g_{\max} = 3 \times 2\pi/a$ using a 3×3 $\vec{k}_i$ grid in the Brillouin zone of the rectangular lattice of unit cells.

The resulting designs support tunable-Q resonances with near-diffraction-limited ($\Omega_p \approx \Omega_s$) vertical beaming comparable to the ideal planar apertures of Fig. 1-2b. Two exemplary $L3$ cavity designs with different target quality factors Q_0 are shown in Fig. 2-4a,d. The GME-computed far-field profiles (Fig. 2-4b,e) are provided for comparison to those computed using near-to-far-field transformations of FDTD-simulated fields [106, 107] (Fig. 2-4c,f). The example design in Fig. 2-4d, for instance, maintains $Q \approx 8 \times 10^5$ (as with the grating-coupled designs in Fig. 2-1) but now with a $\sim$5× efficiency improvement to $\eta_0 \approx 0.8$ based on the simulated far-field profile in Fig. 2-4f. These results confirm that the perturbatively-computed GME coupling coefficients can be used to accurately estimate a cavity's resonant characteristics *and* far-field scattering profile.

Combining this accuracy with inverse-design approach breaks the existing trade-off between Q and directionality. The objective function (Eqn. 2.1) maximizes the directivity

$$D = 4\pi \frac{S(0)}{\int_\Omega S(\vec{k})\ \mathrm{d}\Omega} \tag{2.2}$$

of the emission profile $S(\vec{k})$ within the light cone Ω for *any* desired Q_0. The resulting

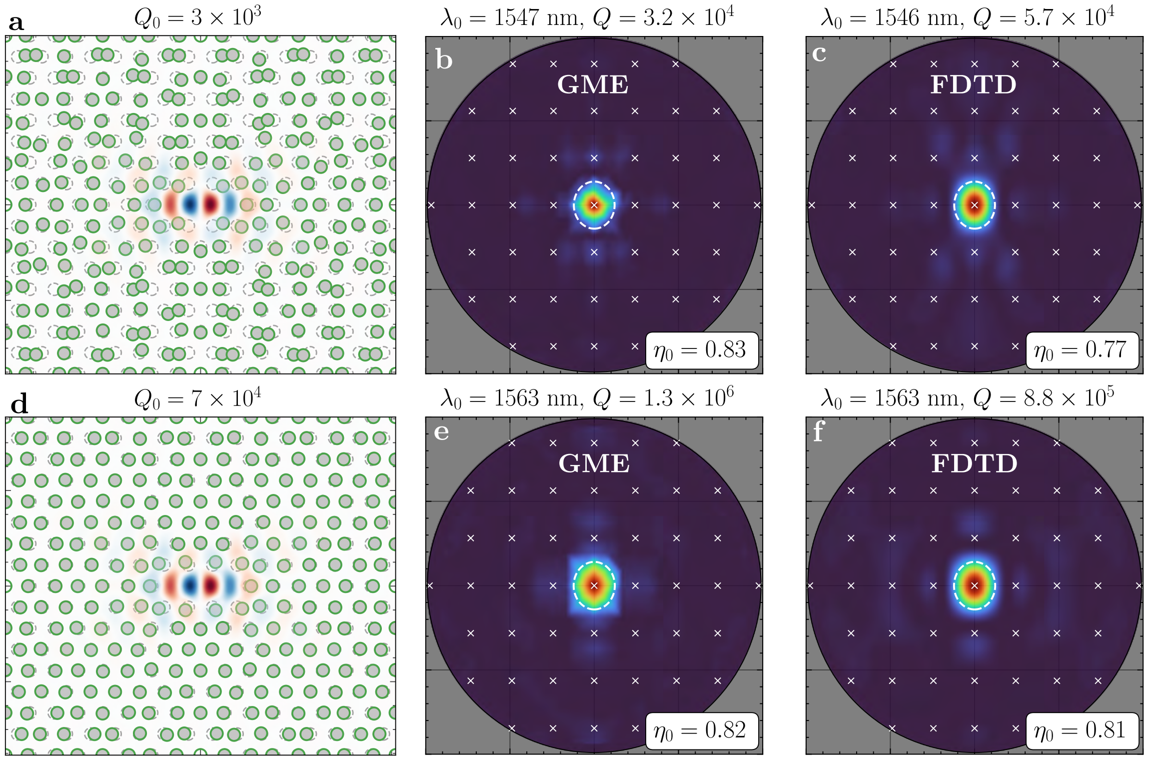

Figure 2-4: Directional emission from low-Q_0 (a-c) and high-Q_0 (d-f) inverse-designed microcavities. Hole shifts in each $\Lambda_x \times \Lambda_y$ unit cell (a, d) are magnified by 2× for visualization. The resonant wavelengths λ_0, quality factors Q, and far-field emission spectra $S(\vec{k})$ computed from GME (b, e) are in excellent agreement with FDTD simulations (c, f). The far-field profiles are confined within the ideal beamwidth of an ideal $\Lambda_x \times \Lambda_y$ uniform aperture (white dashed ellipse) and therefore primarily overlap with a single diffraction order (illustrated by white ×s), yielding near-unity zero-order diffraction efficiency η_0.

aperture efficiency

$$\eta_a = \frac{D_0}{\max D} = \frac{\lambda^2}{A} \frac{S(0)}{\int_\Omega S(\vec{k})\ \mathrm{d}\Omega} = \frac{A_0}{A} \tag{2.3}$$

compares D to the maximum directivity $4\pi A/\lambda^2$ of an area $A = \Lambda_x \Lambda_y$ aperture at wavelength λ, and can therefore be interpreted as the fill factor of light scattered from an effective area A_0. Fig. 2-5 compares η_a for grating-coupled and inverse-designed $L3$ cavities. For most inverse designs, $\eta_a \approx 1$ regardless of Q_0. Since GME assumes periodic boundary conditions (indicative of the true array design), scattering from neighboring unit cells enables designs with $\eta_a > 1$. However, this "super-directive" performance is undesirable since the steerable field-of-view is narrowed to $\Omega_p < \Omega_s$. Even near the maximum simulated $Q \approx 4 \times 10^6$, inverse-design enables near-unity

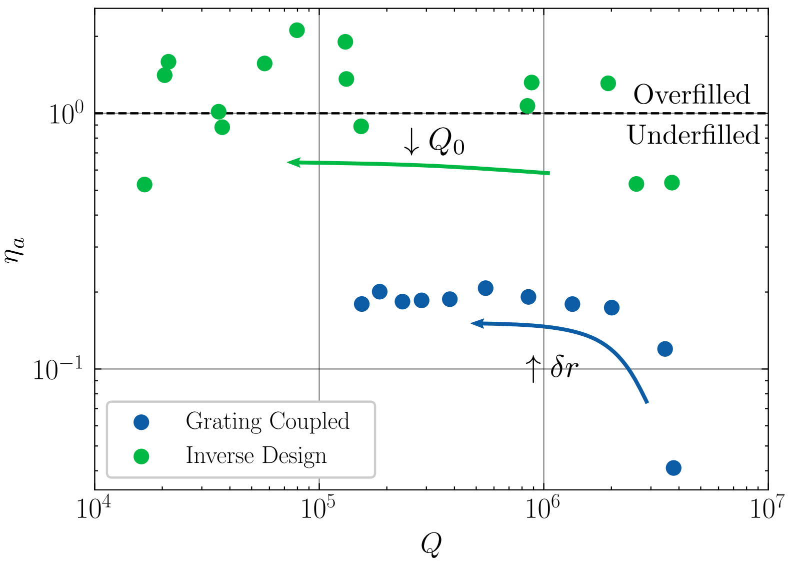

Figure 2-5: FDTD-computed aperture efficiency η_a of vertically coupled $L3$ cavities based on a grating perturbation $\delta r/r \in [0, 0.05]$ or an inverse-design target quality factor $Q_0 \in [10^2, 10^6]$. Inset arrows illustrate parameter trends.

aperture efficiencies — indicating a more than an order-of-magnitude directivity improvement over existing designs.

2.3.1 Optimal Gaussian Coupling

To this point we have only considered the far-field intensity profile $S(\vec{k})$, i.e. the power envelope that modulates the array factor in beamsteering applications. In other applications such as fiber coupling, the full complex amplitude emission profile must be considered. Here, we optimize the waist diameter of an input Gaussian beam to maximize its coupling to a localized PhC cavity mode. The far-field spatial overlap integral between the two modes [108]

$$O(w_0) = R^2 \iint_\Omega \vec{E}_c(\theta, \phi) \times \vec{H}_g^*(w_0, \theta, \phi) \sin\theta d\theta d\phi \tag{2.4}$$

over the hemisphere Ω at distance R yields the power coupling $|O(w_0)|^2$ between the cavity mode c and fundamental Gaussian beam g as a function of the Gaussian waist radius w_0. We compute the cavity electric field profile $\vec{E}_c(\theta, \phi)$ by applying a near-to-far field transformation to the FDTD-simulated cavity mode in a plane just above and parallel to the PhC slab [4]. The resulting far-field profile is finely discretized — relative to the diffraction-limited beamwidth $\lambda/\Lambda \approx 14°$ for typical cavity unit cell

---

[4] Flexcompute, Inc. Tidy3D. `https://simulation.cloud`

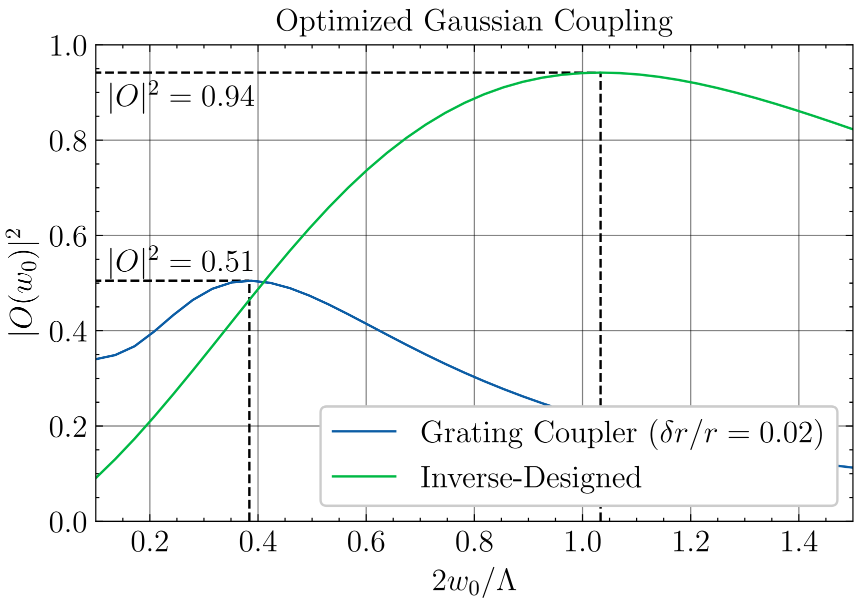

Figure 2-6: Comparison of coupling between a fundamental Gaussian beam with waist w_0 and two different cavity designs with maximum unit cell dimension Λ.

dimensions Λ and resonant wavelength λ — on a 1° grid in zenith and azimuth (θ and ϕ, respectively). For the co-polarized Gaussian mode, we instead convert the magnetic field [109]

$$\vec{H}(x,y,z) = \sqrt{\frac{\pi}{Z_0}}\frac{2w_0}{z+j\pi w_0^2}\exp\left\{\frac{-j2\pi(x^2+y^2)}{2(z+j\pi w_0^2)}\right\}\left[\hat{x}+\left(\frac{-xz-jx\pi w_0^2}{z^2+(\pi w_0^2)^2}\right)\hat{z}\right]e^{-j2\pi z} \tag{2.5}$$

derived from paraxial diffraction theory (for the free space impedance Z_0) to spherical coordinates at a far-field distance R. Both modes are normalized to carry unit power $\int_\Omega \mathrm{Re}\{\vec{E}\times\vec{H}^*\}/2$.

Fig. 2-6 compares the resulting power coupling as a function of normalized waist $2w_0/\Lambda$ for grating-coupled and inverse-designed cavity designs with maximum dimension Λ. In both cases, a backreflector is assumed for unidirectional emission into Ω. Besides the increase in maximum coupling to 94% (!), the optimized waist diameter $2w_0 \approx \Lambda$ indicates that the inverse-designed cavity's effective near-field scattering profile fully fills the design unit cell.

The power coupling $|O|^2_{\max}$ to a single desired free-space mode also allows us to compute that mode's amplitude reflection spectrum [109]

$$r(\tilde{\Delta}) = \frac{2|O|^2_{\max}/p - j\tilde{\Delta}}{1+j\tilde{\Delta}} \tag{2.6}$$

using temporal coupled mode theory assuming a normalized detuning $\tilde{\Delta} = \Delta/\Gamma$ from the cavity resonance and p-directional emission (i.e. $p = 1$ for unidirectional emission with a backreflector or $p = 2$ for symmetric emission). Fig. 2-10 plots these optimized spectra for comparison to our prototype devices described in Sec. 2.5. Whereas the grating-coupled cavity is undercoupled with an amplitude-dominant reflection spectrum, the inverse-designed cavity is phase-dominant as desired for high efficiency beamforming. These results provide yet another metric for comparing our design technique to existing approaches.

2.4 *Why* does it work?

The problem with inverse design [110] and machine learning-based design in general [111] is that the results do not necessarily yield any physical insight. This could certainly be argued for our design strategy, where we input a simple PhC structure into a “black-box" optimizer and a directive, high-Q cavity design comes out the other side. These designs offer excellent performance, but leave an open question: why does this approach work so well?[5] While a rigorous analytic description remains an open goal for future investigation, we can glean some intuition from the real- and Fourier-space permittivity profiles in Fig. 2-7.

To first order in the permittivity perturbation profile $\Delta\epsilon(\vec{r})$, each illustrated design can be represented by an effective current source $\vec{J} = j\omega\Delta\epsilon\vec{E}$. The Fourier transform of $\vec{J}$ — the far-field scattering profile — is therefore proportional to the Fourier-domain convolution of $\Delta\epsilon$ and $\vec{E}$. This result is inherently approximate due to the ill-defined product $\Delta\epsilon\vec{E}$ at high-index boundaries [112], but suffices for our qualitative analysis here.

The perturbative grating coupler in the top panel of Fig. 2-7, for example, is partially composed of Fourier components at $k_x = \pm\pi/2a$. Convolving these spatial frequencies with a band-edge mode (i.e. a mode at $k_x \approx \pm\pi/a$) in a one-dimensional photonic crystal (a distributed Bragg mirror stack, for example) shifts the induced current and associated far-field scattering to $k_x = 0$, recreating the previously introduced bandfolding argument. Fig. 2-1 demonstrates the applicability of this technique to our defect cavities despite a number of complications: 1) the deviation from a perfect sinusoidal index perturbation broadens the $k_x = \pi/a$ peak and therefore the induced current distribution; 2) other harmonics ($k_y \approx \pm\sqrt{3}/4a$, for example) are present in the Fourier spectrum; and 3) the the energy spectrum of the slab defect-type cavities is actually localized around the Brillouin zone boundary of the a two-dimensional hexagonal lattice.

Q optimization accounts for the last of these by arranging holes to minimize modal overlap with the light cone. As illustrated by the center panel of Fig. 2-1, the resulting index change profiles typically consist of a complex Fourier spectrum. Our inverse

---

[5] I thank Momchil Minkov and Professor Steven Johnson for insightful discussions on this question.

Grating Coupler

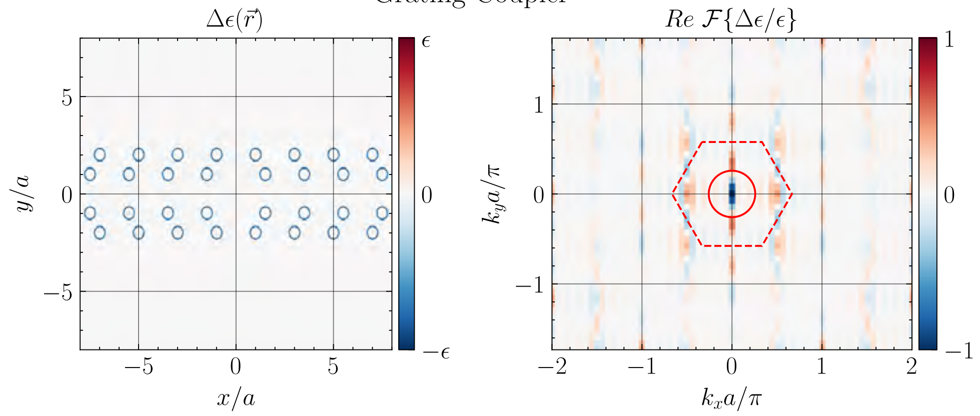

Q-optimized

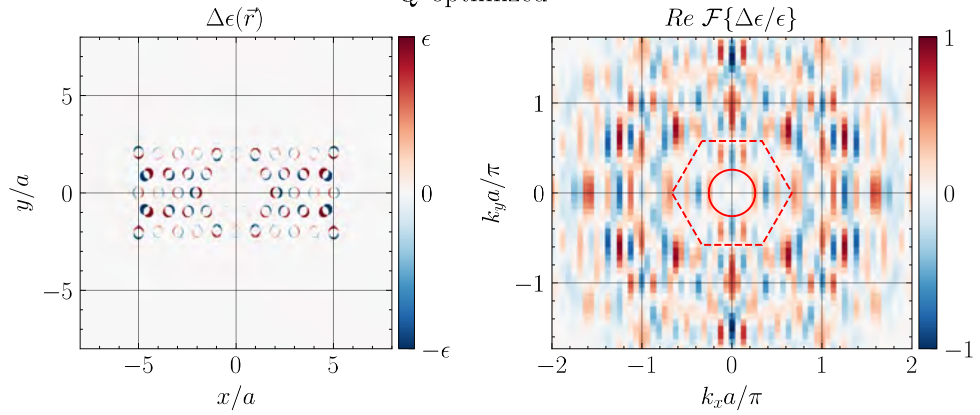

Inverse Design

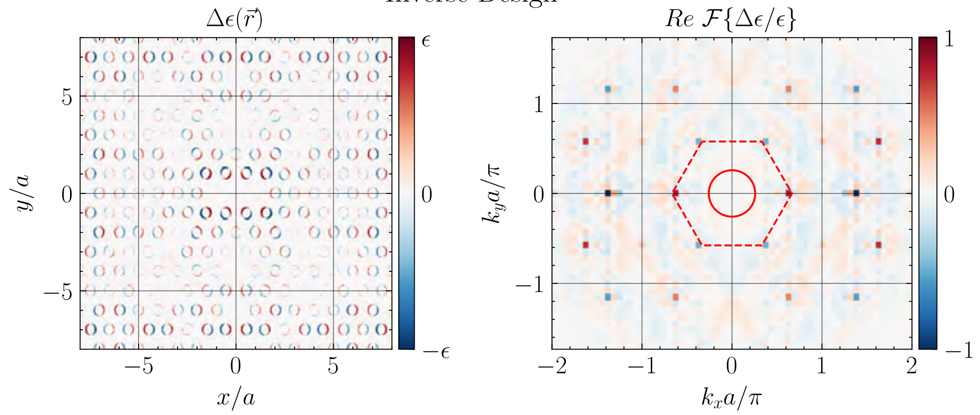

Figure 2-7: Real- (left) and normalized Fourier-space (right) permittivity difference ($\Delta\epsilon$) profiles between an unoptimized $L3$ lattice (in an slab with permittivity ϵ) and a grating coupled (top), Q-optimized (center, using Design B from Fig. 2-1 [89]), and inverse-designed (bottom, using the high-Q_0 design from Fig. 2-4) $L3$ cavities. Since $\Delta\epsilon$ is real and symmetric, we only show the real portion of its discrete Fourier transform.

design technique, by comparison, produces localized peaks in the Fourier spectrum located at the corners of the Brillouin zone (specifically the K point of the irreducible Brillouin zone). This configuration extends the 1D bandfolding argument to 2D. Once Q-optimized, coupling to the closest edge of the slab's incomplete bandgap dominates leakage. For our cavities with normalized resonant frequency $f = a/\lambda \approx 0.26$ nearest to the dielectric band below the gap (c.f. Fig. 2-2), this leakage occurs at the K point. The co-located Fourier components of the inverse-designed permittivity profile shifts this leakage to the Γ point at $k = 0$ for efficient vertical scattering.

2.5 Experimental Verification

To experimentally validate the simulated results discussed in the previous sections, we prototyped Q-optimized, grating coupled, and inverse designed cavities at a commercial electron beam lithography (EBL) foundry [6] before transitioning to the wafer-scale foundry process described in Chapter 3.

2.5.1 Measurement Setup

The wide-field, cross-polarized microscope in Fig. 2-8 allows us to simultaneously measure the near- and far-field reflection spectra of every cavity within a camera's field-of-view. A visible illumination path (not illustrated) is joined with collimated infrared light from a tunable laser with a dichroic mirror and focused onto the back-focal-plane (BFP) of an objective lens by lens L1. The angle-of-incidence and spot size of the infrared beam on the sample are therefore controlled by translating L1 and varying the collimated beam diameter, respectively. In our typical wide-field configuration, a 7.2 mm beam diameter focused to the center of a 40× objective's BFP yields a $\sim$150 µm waist-diameter, vertically-incident field that quasi-uniformly illuminates 10×10 PhC cavity arrays.

By orienting the input polarization at a 45° angle relative to the dominant cavity polarization axis (with a half-wave plate or by physically rotating the sample), light coupled into and reflected by the PhC cavity is polarization rotated and can be isolated from direct, specular reflections with a polarizing beamsplitter. A kHz-rate free-running, dual-band (visible and infrared) camera images this cross-polarized reflection signal through the tube lens L3. For each frame collected during a laser sweep, the wavelength is interpolated from the recorded camera and laser output triggers and each cavity's reflection is integrated over a fraction of pixels within its imaged unit cell boundary. We use the resulting high-contrast reflection spectra (across all devices within the field-of-view) to characterize device performance and monitor the cavity trimming process.

---

[6] Applied Nanotools, Inc. `https://www.appliednt.com/`

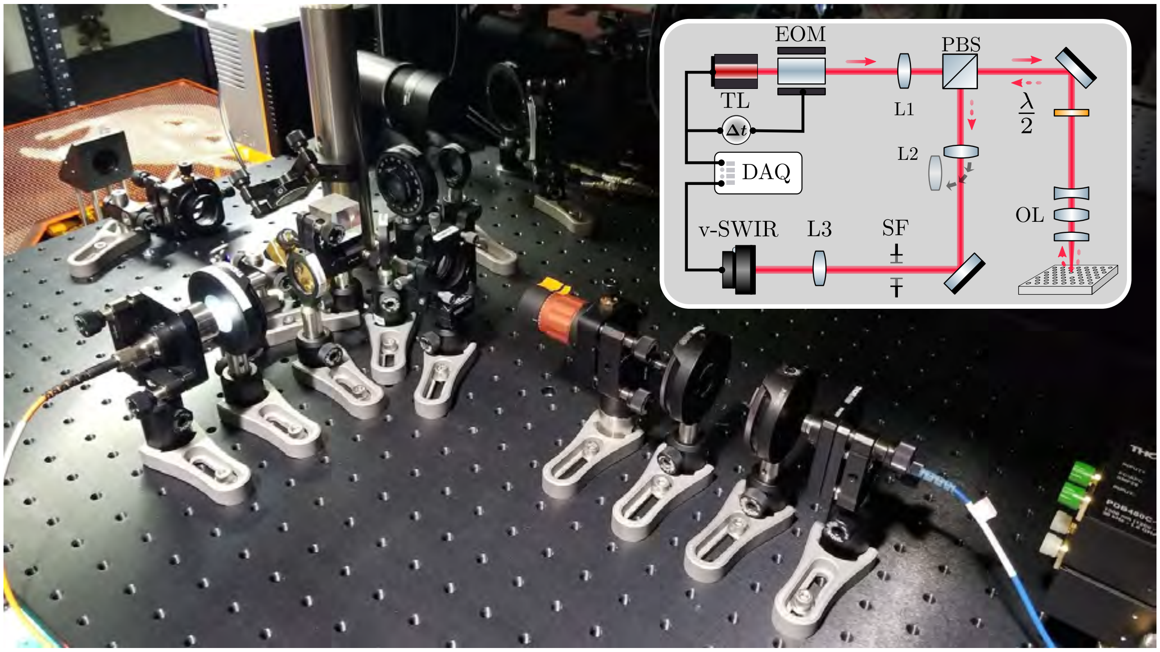

Figure 2-8: Photograph and simplified inset schematic of the cross-polarized microscopy setup used for near- and far-field characterization of photonic crystal cavity arrays. TL: tunable infrared laser (Santec TSL-710), EOM: electro-optic amplitude modulator; $\lambda/2$: half-wave plate, PBS: polarizing beamsplitter; L1: 250 mm back-focal-plane lens; DM: long-pass dichroic mirror; OL: objective lens (Nikon Plan Fluor 40×/0.60 NA or Nikon LU Plan 100×/0.95 NA), L2: 250 mm back-focal-plane lens; SF: spatial filter; L3: 200 mm tube lens; v-SWIR: visible-short wave infrared camera (Xenics Cheetah 640); DAQ: data acquisition unit (NI USB-6343); Δt: trigger delay generator (SRS DG645).

The sample mount below the objective (OL) is temperature stabilized to within 10 mK with a Peltier plate and feedback controller. For trimming experiments, the sample is placed in a high-pressure oxygen environment within a custom chamber offering in-situ optical access through a glass window.

2.5.2 Far-Field Scattering Profile Measurement Technique

Inserting a lens (L2) in the collection path one focal length from the objective BFP allows us to measure the far-field profile $S(\vec{k})$ of individual or multiple cavities using the same setup. We position an iris at the intermediate image plane — located with a removable lens (not shown) placed before L3 — to spatially filter the emission from desired devices. We also calibrate the BFP scale using a reflective reference grating with known pitch. Due to the cross-polarized configuration, only a single polarization $\tilde{S}(\vec{k})\big|_{\theta}$ is imaged for any cavity-input polarization angle difference θ. The complete

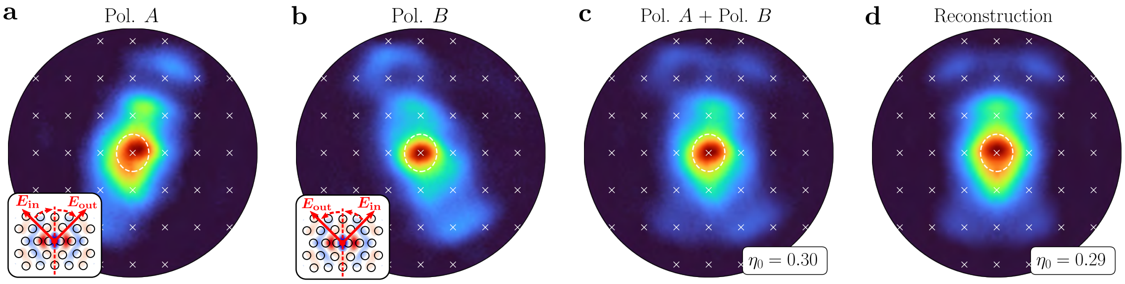

Figure 2-9: Cross-polarized back-focal-plane (BFP) imaging techniques for a grating-coupled $L3$ cavity. Two orthogonally polarized far-field profiles are imaged by orienting the input polarization E_{in} at a +45° (a) or −45° (b) angle from the dominant cavity polarization axis (dashed line in inset). The complete cavity emission profile $S(\vec{k})$ can be reconstructed by summing both images (c) or approximated from a single polarized image (d), yielding near-identical images with quantitative agreement between the extracted η_0.

cavity emission profile

$$S(\vec{k}) = \tilde{S}(\vec{k})\big|_{\theta} + \tilde{S}(\vec{k})\big|_{\theta \pm \pi/2} \tag{2.7}$$

an therefore be reconstructed by sequentially imaging both polarizations as in Figs. 2-9a-c for $\theta = 45°$. For maximum accuracy, we used this technique for the experimental results in Fig. 2-10.

Alternatively, the specific choice $\theta = 45°$ allows $S(\vec{k})$ to be reconstructed from a single measurement. Due to mirror symmetry about the cavity's principal polarization axis $\hat{y}$, Fig. 2-9a-b shows that $\hat{\sigma}_{\hat{y}}\{\tilde{S}(\vec{k})\big|_{\pm 45°}\} = \tilde{S}(\vec{k})\big|_{\mp 45°}$ for the reflection operator $\hat{\sigma}$. This alternative reconstruction

$$S(\vec{k}) = [1 + \hat{\sigma}_{\hat{y}}]\, S(\vec{k})\big|_{\pm 45°} \tag{2.8}$$

is demonstrated experimentally in Fig. 2-10d, yielding excellent agreement with Fig. 2-10c. This technique simplifies high-throughput far-field measurements across cavity arrays (Figs. 3-16 and 3-15, for example).

2.5.3 Single Cavity Characterization

Fig. 2-10a-c and Fig. 2-10d-f show the results for the grating coupled and inverse-designed cavities, respectively. The optimal grating coupled cavities offer $Q \sim 4 \times 10^5$ at $\lambda \approx 1553$ nm with a near-field resonant scattering profile well-centered on the cavity defect (Fig. 2-10c, inset). The mode mismatch between this wavelength-scale PhC mode and the wide-field input beam (Gaussian beam with ∼150 µm waist diameter for array-level excitation) is further evidenced by the small normalized reflection amplitude (relative to that of the inverse designed cavities) on resonance as well as the broad far-field profile (Fig. 2-10b) with $\eta_0 = 0.24$ in qualitative agreement with the corresponding simulation.

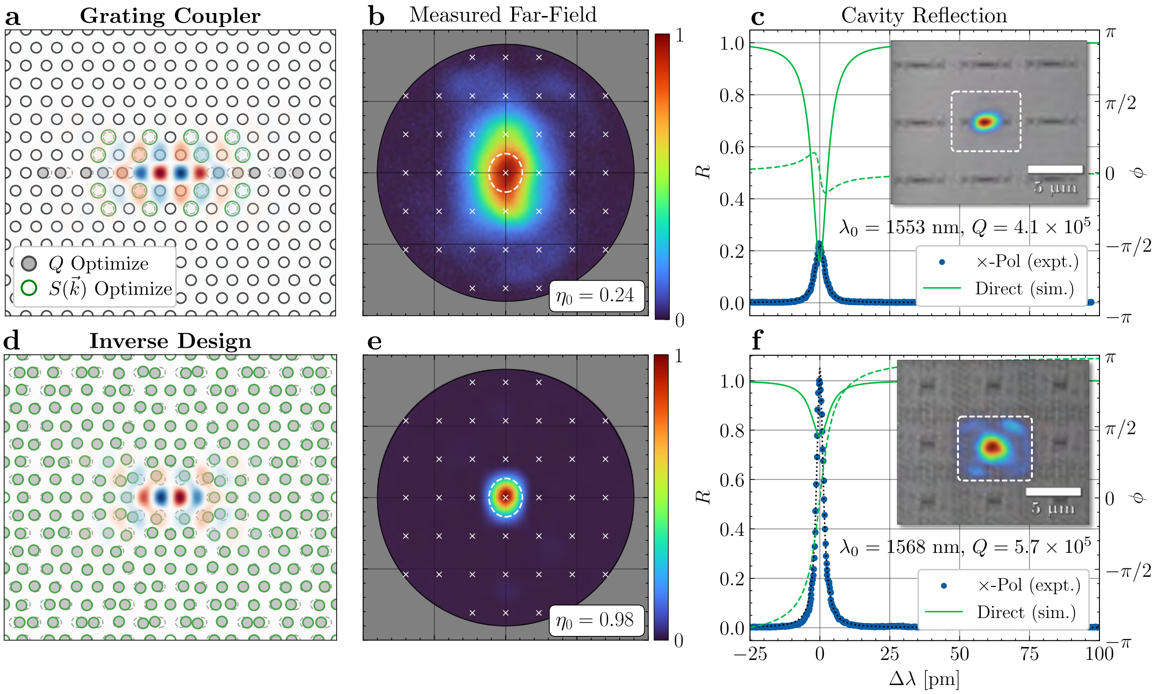

Figure 2-10: Experimental comparison of existing (a-c) and inverse-designed (d-f) PhC cavities with high-Q and near-diffraction-limited vertical beaming. Superimposing a grating perturbation (a, outlined in green) on the Q-optimized design of Fig. 2-11a improves vertical coupling at the expense of reduced Q, yielding the simulated far-field intensity profile in (b, left) with $\eta_0 = 0.18$. Our measured far-field profile (b, right), collected from a grating-coupled cavity using a cross-polarized imaging setup (Fig. 2-8), confirms the broad emission relative to the array field-of-view (dashed white line) Ω_s. This mismatch explains the low effective "fill factor" and poor coupling observed in our resonant imaging (c, inset) and near-field reflection spectra (c, blue), respectively. An input Gaussian beam (with waist matched to the unit cell dimensions) is undercoupled and exhibits an amplitude-dominant power reflectivity $R = |r|^2$ modulation (c, green solid curve) with minimal phase variation $\Delta\phi$ (c, green dashed curve). Our inverse designed cavities (d) overcome these issues by optimizing *every* hole in the unit cell to vertically scatter the loss associated with any target quality factor. This technique produces "ideal" resonant SLM pixels with: 1) near-diffraction limited simulated and measured far-field profiles (e) with $\eta_0 \sim 1$; 2) fully-filled near-field resonant scattering (f, inset); 3) a $\sim 5\times$ experimental resonance contrast and $> 94\%$ single-sided (i.e. assuming an ideal back-reflector described in Sec. 3.3) coupling to an input Gaussian beam with optimized waist (Sec. 2.3.1) for phase-dominant modulation (f).

In comparison, inverse design non-pertrubatively modifies the cavity mode (Fig. 2-10d) to produce the near-ideal measured far-field profile in Fig. 2-10e with $\Omega_0 \approx \Omega$ and $\eta_0 = 0.98$ while *simultaneously* increasing Q to 5.7×10^5. We attribute the slight increase in zero-order diffraction efficiency over the simulated value $\eta_0 = 0.86$ to the substrate-dependent effects described in Sec. 3.3. The fully-filled near-field resonant scattering image in Fig. 2-10f explains the close resemblance between this measured pattern and that of an ideal uniform aperture [90]. In addition, the narrowed emission profile $S(\vec{k})$ yields a $\sim$5× increase in cross-polarized reflection and the phase-dominant simulated direct reflection spectrum in Fig. 2-10f. The latter is achieved by near-perfect (94%) one-sided coupling to a Gaussian beam with optimized waist diameter derived in Sec. 2.3.1.

Combined, these results break the traditional coupling–Q tradeoff (offering an order-of-magnitude improvement in the figure-of-merit $Q \cdot \eta_0$ for the prototype devices in Fig. 2-10) to enable high-performance beamforming at the space-bandwidth limit.

2.6 Beamforming Comparison

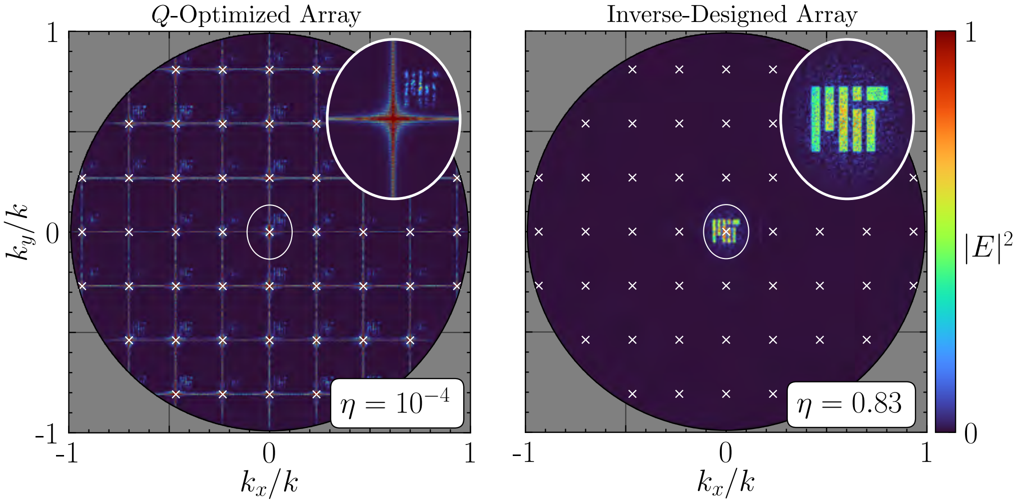

Figure 2-11: Optimized holography with inverse-designed, vertically-coupled microcavity arrays. Simulated trial holograms from a 64×64 array of Q-optimized (Design A in Fig. 2-1) cavities with optimized detunings have a near-zero overall diffraction efficiency η. By comparison, inverse-designed devices (right) with high-Q, efficient coupling, and directional emission enable high-performance ($\eta \sim 1$) resonant holography (d).

But how do these single-device performance metrics translate to beamforming? Simply put, the narrowed emission into a solid angle $\Omega_p \approx \Omega_s$ (corresponding to near-unity fill-factor of the radiating aperture) enables two features: 1) phase-dominant modulation via near-unity coupling to a free-space Gaussian beam (Fig. 2-6), and 2) near-unity zero-order diffraction efficiency by inhibiting emission into undesirable diffraction orders at high numerical aperture. Combined, these features enable high efficiency far-field steering as illustrated by Fig. 2-11.[7]

The left panel shows the far-field pattern formed by detuning each Q-optimized resonator in a 64×64 array to match a desired target image (the MIT logo). The low η_0 and non-ideal coupled amplitude-phase response of each pixel, a byproduct of poor coupling to an input Gaussian beam, produce a distorted pattern with near-zero overall diffraction efficiency η. An array of optimally detuned, inverse-designed cavities, however, forms the clear far-field image in the right-hand panel with a several order-of-magnitude improvement in overall diffraction efficiency ($\eta = 0.83$).

---

[7] I thank Cole Brabec for his work in developing algorithms to optimize diffraction efficiency in the presence of the coupled amplitude-phase response of microcavities in various coupling regimes (under-coupled, over-coupled, and critically-coupled). His work will be published externally, so I will defer detailed discussion of these algorithms to those reports.

3

Foundry-Fabricated Photonic Crystals

Abstract

Through a closed-loop process of theory, semiconductor foundry fabrication, and automated testing of hundreds of thousands of devices, we developed scalable manufacturing of photonic crystal systems. Our 300 mm, full-wafer foundry process is specifically optimized for fabricating arrays ultra-high-finesse photonic crystal microcavities. The resulting devices combine our cavity's record directivity with a normalized quality-to-mode-volume ratio $Q/V \approx 4 \times 10^6$ that is among the highest demonstrated for any optical cavity.

3.1 Motivation and Initial Attempts

Since nanometer-scale hole placement and sizing errors in typical silicon PhC cavities translate to $\mathcal{O}(\text{nm})$ resonant wavelength variations and $\mathcal{O}(10^6)$ disorder-limited Qs, electron-beam lithography (EBL) is well suited for prototyping the few-pixel devices used in Chapter 2 to validate our inverse design strategy [113, 114]. For these same reasons, record high-Q and small-V cavities have (to date) required the state-of-the-art resolution and accuracy characteristic of EBL [76, 78]. However, serial direct-write techniques are impractical for manufacturing the large-scale cavity arrays desired for our PhC-SLM. Field stitching issues and sample preparation aside, a single cm^2, megapixel-scale sample would require a full day of EBL write time alone. Modern photolithography tools, by contrast, expose hundreds of 300 mm-diameter wafers per hour and offer a direct avenue towards scalable fabrication. Recent studies have therefore investigated PhC fabrication via deep ultraviolet (DUV) photolithography,

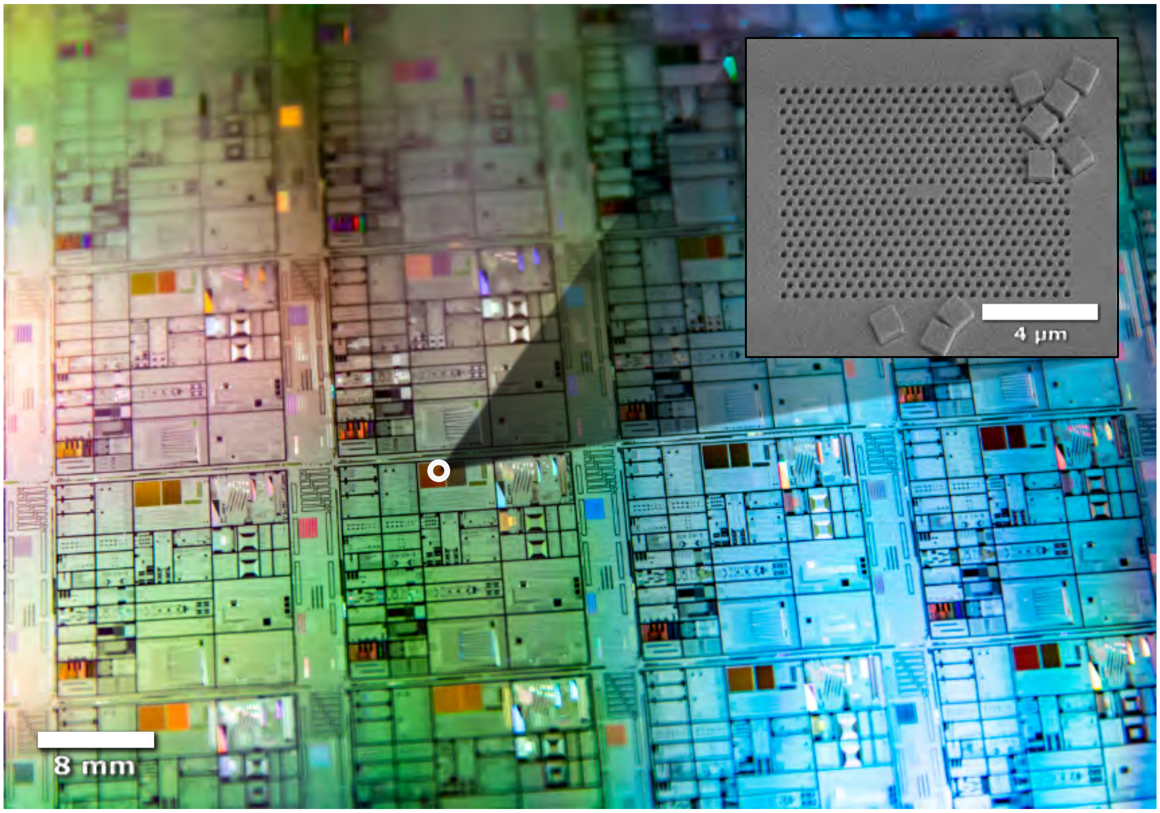

Figure 3-1: Optical photograph and inset helium ion microscope (HIM) micrograph of the initial PhC fabrication attempts via a multi-project wafer in the *AIM Photonics* foundry. The dark blocks are areas of single (e.g. the inset $L3$ cavity showing scattered silicon fill blocks following the oxide release process) and arrayed PhC cavities.

often focusing on long-correlation-length variability between few devices arranged across the wafer [115, 116] or maximizing the Q of fabrication-tolerant, large volume PhC heterostructure cavities [117, 118]. Table 3.1 summarizes the performance of these previous fabrication attempts.

Here, we extend these initial investigations by developing a full-wafer silicon photonics fabrication process specifically optimized for large-scale, wavelength-pitch arrays of high-Q/V PhC microcavities in the *AIM Photonics* foundry [125]. This work started through a collaboration with Dr. Michael Fanto (Air Force Research Laboratory's Informatics Directorate) and Professor Stefan Preble (Rochester Institute of Technology), who were developing an alternative low-loss process at *AIM* for quantum photonics applications when I started graduate school in 2017. Mike was gracious enough to let us prototype our PhC designs on the 2018 "Dr. Manhattan" run. Some photographs of this initial run are shown in Fig. 3-1.

We unfortunately found that the default *AIM* process yielded oblique, incomplete

Foundry	Cavity (Structure)	Q	$\tilde{V}$	$Q/\tilde{V}$	σ_λ [nm]	$\sigma_{1/Q}$	σ_h [nm]
AIM	***L*4/3 (Released)**	$\mathbf{1.2 \times 10^6}$	**0.3**	$\mathbf{4 \times 10^6}$	**1.1**	$\mathbf{3.3 \times 10^{-7}}$	**0.6**
AIM	***L*3 (Released)**	$\mathbf{1.6 \times 10^6}$	**0.9**	$\mathbf{2 \times 10^6}$	**0.6**	$\mathbf{2.5 \times 10^{-6}}$	**1.9**
IMEC [119]	1D Nanobeam (Released)	1.1×10^5	0.6	2×10^5	—	—	—
IMEC [120]	1D Nanobeam (Cladded)	7.8×10^5	—	—	—	—	—
IMEC [117]	2D heterostructure (Released)	1.2×10^6	—	—	—	—	5.8
IMEC [115]	2D heterostructure (Cladded)	6×10^5	2.2	3×10^5	1.5	5.9×10^{-7}	1.2
IMEC [121]	*L*3 (Released)	3×10^3	—	—	—	—	—
AIST [118]	*L*3 (Released)	3.1×10^4	—	—	0.4	—	0.79
AIST [118]	2D heterostructure (Released)	2.0×10^6	—	—	0.5	1.7×10^{-7}	0.79
AIST [116]	2D heterostructure (Released)	2.5×10^6	—	—	2.47	7.7×10^{-8}	0.57
Micron [122]	quasi-1D Nanobeam (Cladded)	5.8×10^4	0.8	7×10^4	—	—	$2.0^\dagger$
IBM [123]	1D Nanobeam (Cladded)	2×10^3	—	—	—	—	
IME [124]	2D line defect (Cladded)	2.2×10^5	1.7	1×10^5	0.16	—	$1.6^\dagger$

Table 3.1: Summary of foundry-fabricated silicon photonic crystal cavities. Q: quality factor; $\tilde{V}$: normalized Purcell mode volume; λ: resonant wavelength; h: hole parameters (size, position, etc.); σ: standard deviation.

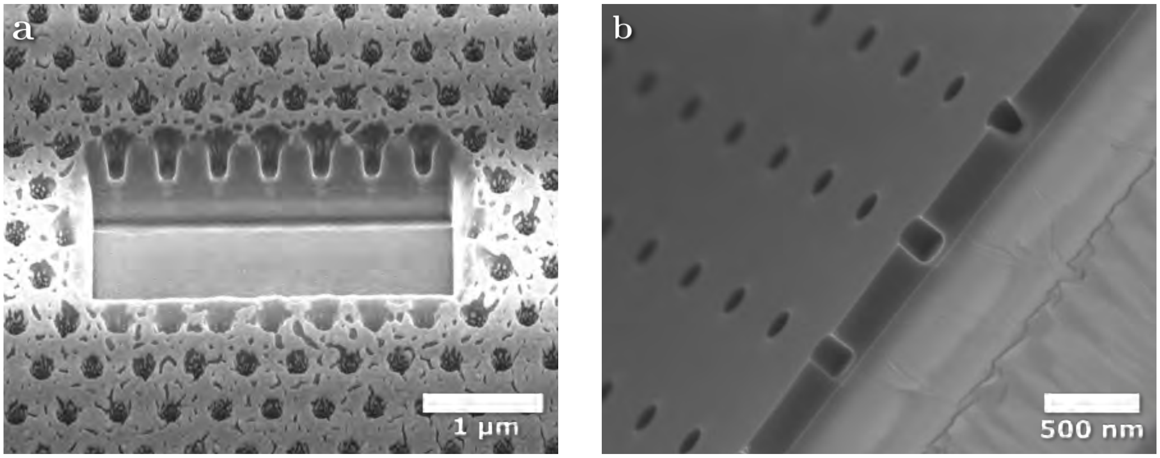

Figure 3-2: Focused ion beam (FIB, left) and cleaved (right) cross sections of PhC lattices fabricated in the AIM and ANT foundries, respectively. For both processes, the silicon etch was incomplete for ∼200 nm target hole diameters.

etches for the target ∼200 nm hole diameters (Fig. 3-2a)[1] and resorted to the Applied Nanotools (ANT) electron-beam (e-beam) foundry for further prototyping.[2] We converted the ANT process to a positive-tone resist to reduce write time and improve etch quality, yielding the improved (but still incomplete) etches shown in Fig. 3-2. A few subsequent process modifications eventually yielded the high-quality devices tested in Chap. 2.

These results motivated further optimization of the AIM process to fabricate high-Q/V microcavity arrays at scale. Analyzing the fabrication biases and trends (Fig. 3-3, for example) led us to identify a number of process improvements for future runs. Based on these results, we ultimately decided to develop a dedicated, full-wafer process optimized for the pattern densities and critical dimensions characteristic of telecom-band (i.e. $\lambda \sim 1550$ nm) photonic crystal circuits.

3.2 The "MONEV" Full-Wafer Process

The resulting "MONEV" process was optimized over numerous full-wafer runs between 2019 and 2021, and ultimately yielded the 300 mm PhC wafers illustrated in Fig. 3-4 comprising $\mathcal{O}(10^9)$ high-finesse cavities spread across 64 identical reticles. To briefly summarize the scale of this endeavor, the final designs required:

- $\sim 85,000$ core-hours of design optimization on Massachusetts's Green High Per-

---

[1] I thank Josh Perozek (MIT) for his assistance with focused ion beam cross-sections and for numerous insightful fabrication discussions.

[2] I owe a great deal of thanks to Cameron Hovarth (ANT) and Jocelyn Westood-Bachman for optimizing the ANT process for PhC fabrication.

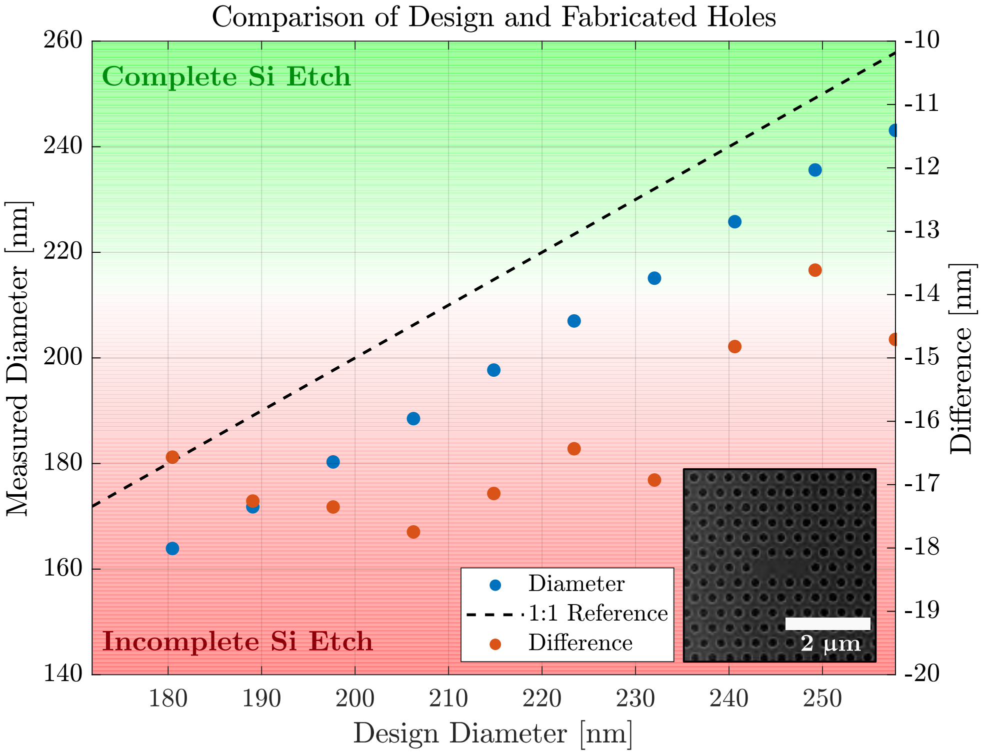

Figure 3-3: Hole biases in the default *AIM* process. HIM metrology of fabricated PhC cavities (inset micrograph) and lattices allowed us to compare the as-drawn and fabricated hole dimensions a. By observing which hole sizes were undercut by a wet release etch, we found that hole diameters larger than ∼220 nm for a lattice constant $a \sim 0.4$ µm yielded complete etches through the silicon layer.

formance Computing Center

- 30 GB of compiled `.gds` design files that were reduced to 400 MB compressed `.oas` files for dissemination between manufacturing facilities
- $\mathcal{O}(10^8)$ holes per die and $\mathcal{O}(10^{11})$ holes per wafer, corresponding to $\mathcal{O}(10^4)$ hours of equivalent e-beam write time[3]
- Photolithographically patterned feature sizes sizes down to ∼100 nm

Based on the initial fabrication described in Sec. 3.1, we determined that a central goal was to create a complete etch through the silicon membrane with vertical side-walls. The transmission electron microscope (TEM) cross-section in Fig. 3-5a

---

[3] Writing the reticle mask even became infeasible at this scale, as the write preparation and fracturing steps crashed the mask partner's (Toppan) systems. A laser mask writer (Applied Materials 4700DP) was thus required for mask fabrication, yielding a *scalable, fully lithographic* PhC process.

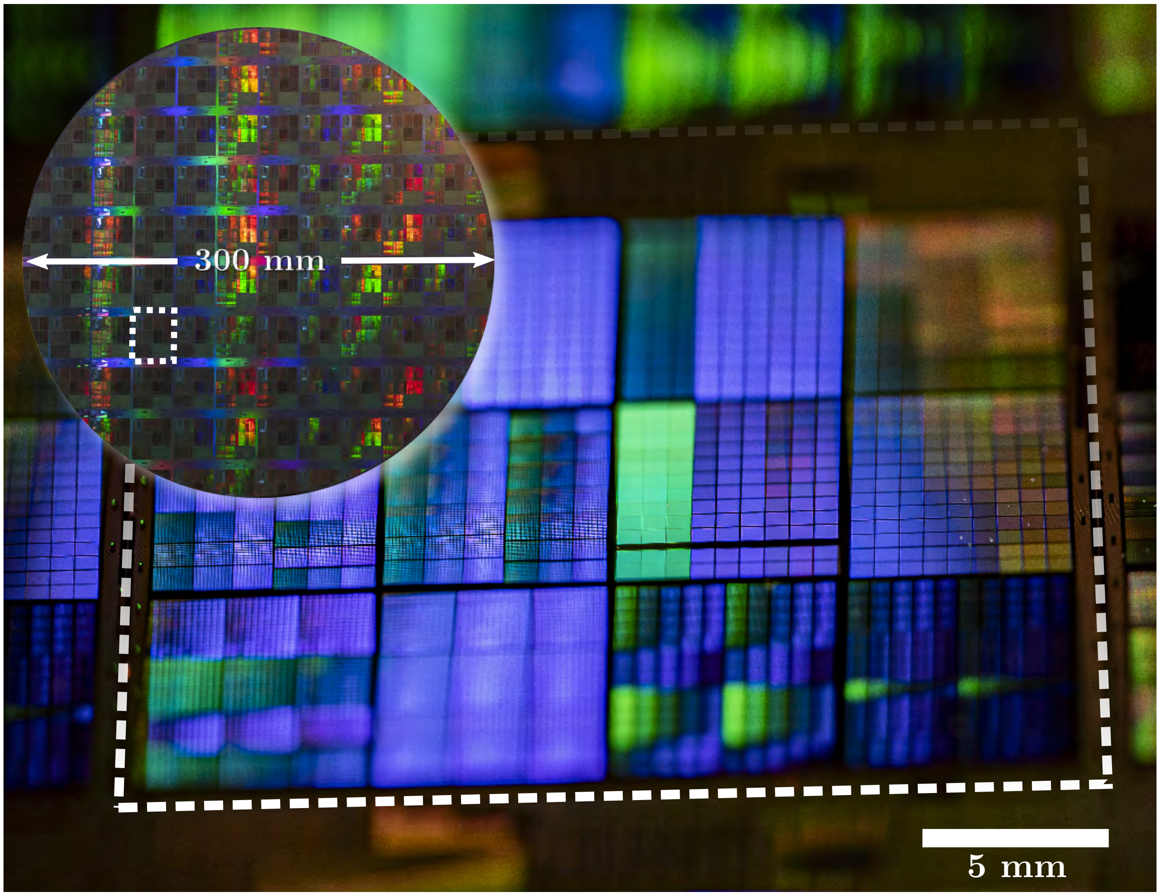

Figure 3-4: Full-wafer photonic crystal fabrication in an optimized 300 mm foundry process. A wafer (inset) contains 64 complete reticles (dashed white box) each comprising millions of inverse-designed PhC cavities.

shows that the default fabrication process (optimized for isolated waveguides) yielded an oblique (∼100°), incomplete etch through the silicon device layer for the target PhC lattice parameters. Both nonidealities erase the membrane's vertical reflection symmetry, leading to coupling between even- and odd- symmetry (about the slab midplane) modes that ultimately limits the achievable Q of bandgap-confined resonances [126]. Extending the etch time with a reverse (positive) tone lithography processes improved the etch angle but produced a "cupped" etch termination (Fig. 3-5b). By contrast, our revised fabrication process achieves near-vertical 91° sidewall angles with a vertical etch termination (Fig. 3-5c)[4], yielding high-quality PhC lattices for a range of hole diameters between the ∼100 nm critical-dimension (CD) and $2r \approx a$ (Fig. 3-6). Using TEM cross-sectioning and automated optical metrol-

---

[4] Note the slight but insignificant over-etch of the underlying oxide, which is ultimately removed with a subsequent wet etch as described in Sec. 3.3).

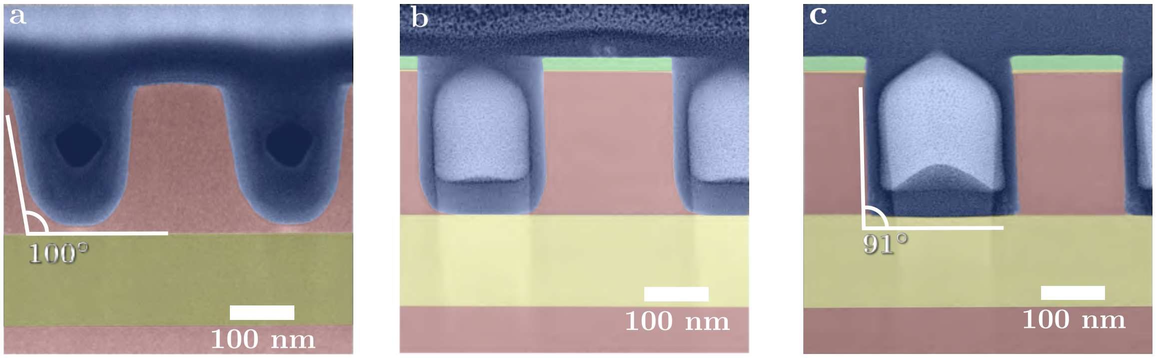

Figure 3-5: Initial (a), intermediate (b), and final (c) false-color (blue: metal fill; red: silicon; yellow: silicon dioxide; green: etch mask) transmission electron microscope cross-sections show how process optimization enables a near-vertical (90°), complete etch through the 220 nm thin-film silicon layer of a silicon-on-insulator die, yielding high-quality PhC lattices.

ogy as feedback over multiple 300 mm wafer runs in the *AIM Photonics* foundry's 193 nm DUV water-immersion lithography line, this new process relies on a combination of dose-optimized reverse (positive) tone lithography, high-accuracy laser written masks[5], and optimized etch termination. Hole statistics were collected via scanning electron microscopy-based metrology at each critical processing step to determine their influence on the final pattern accuracy.

3.3 Post-Processing

Following fabrication and dicing, we post-processed individual die with a backside silicon nitride anti-reflection coating and, as required, suspend the PhC membrane with a timed wet etch. Both processes are optimized to minimize reflections from the silicon substrate of the silicon-on-insultor (SOI) die.

3.3.1 SOI Woes: Stress and Reflection

Isolated slab PhC cavities feature symmetric, bi-directional emission due to vertical reflection symmetry about the slab midplane. When placed above a reflective substrate, however, interference between the (reflected) downwards and upwards emission paths alters the cavity's radiation pattern $S(\vec{k})$ and Q. Summing the direct emission path with the multiple membrane-substrate reflections yields an approximate vertical

---

[5] Laser writing a minimum-tolerance (0.6 µm minimum specable feature size, 0.3 µm minimum clear critical dimension (CD), 0.2 µm minimum dark CD, 25 nm 3σ CD uniformity) binary chrome-on-glass mask (Toppan) minimizes fabrication overhead while improving hole placement accuracy.

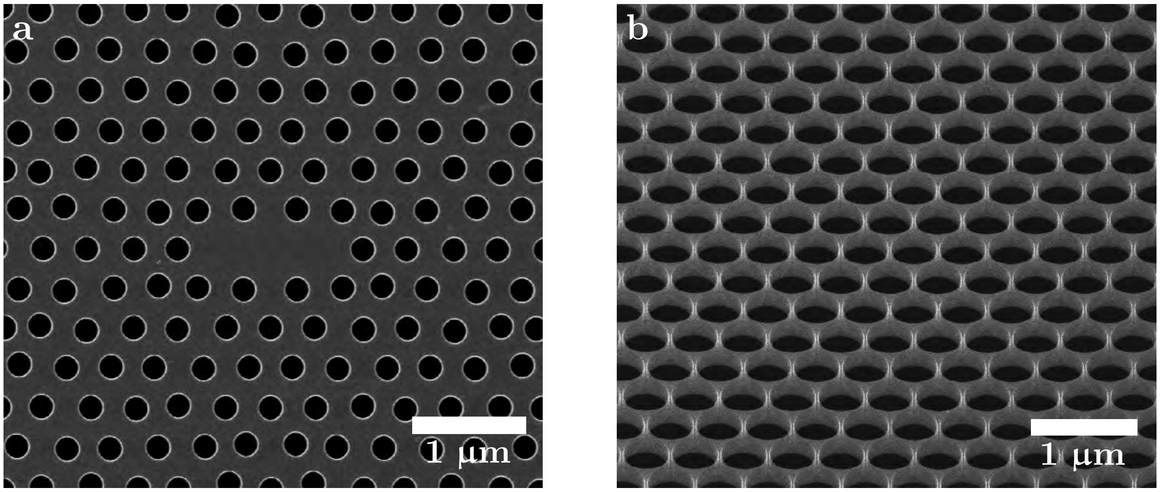

Figure 3-6: Top-down (a) and angled (b) helium-ion microscopy photos of released PhC lattices fabricated with the optimized *AIM* process. The vertical etch (Fig. 3-5c) enables narrow (10s of nm) silicon veins for hole radii $r \approx a/2$ (b).

enhancement factor [127]

$$S = \left| 1 + \frac{t^2 e^{ik_z d}}{(1 - r^2 e^{2ik_z d})(r - e^{-2ik_z d}) - rt^2 e^{2ik_z d}} \right|^2 \tag{3.1}$$

for the Fresnel amplitude reflection and transmission coefficients r and t, respectively, vertical wavenumber k_z, and the membrane-substrate gap spacing d. The results, analogous to the modified spontaneous emission from a quantum emitter placed above a mirror [128], are plotted in Fig. 3-7.

Fig. 3-7 also plots the FDTD-simulated quality factor trends of an inverse-designed $L3$ cavity as a function of d assuming a silicon substrate (with refractive index $n = 3.48$). Since the optical thickness of the PhC slab is approximately $\lambda/2$, constructive interference at $d \approx m\lambda/2$ ($m \in 1, 2, ...$) maximizes vertical emission and minimizes Q. Destructive interference at $d \approx (2m-1)\lambda/4$ has the opposite effects, leading to Q and vertical coupling trends that closely track the expected analytic result of Eqn. 3.1. The corresponding variation in η_0 explains the minor discrepancy between the simulated and measured $\vec{S}(k)$ in Sec. 2.5 (Fig. 2-10).

We first noticed these effects when releasing large-scale (∼mm × mm) cavity arrays (Fig. 3-8, center). Compressive stress in the SOI die buckles suspended cavity arrays (stress in the thermal oxide layer is transferred to the suspended PhC membrane after a sacrificial oxide release etch [129]), yielding variations in d — and therefore cavity reflectivity — across the membrane. The reflectivity variations (left-hand grayscale image in Fig. 3-8, for example) are qualitatively correlated with the expected Q variation (i.e. low-reflectivity dark regions host higher-Q cavities and vice versa),

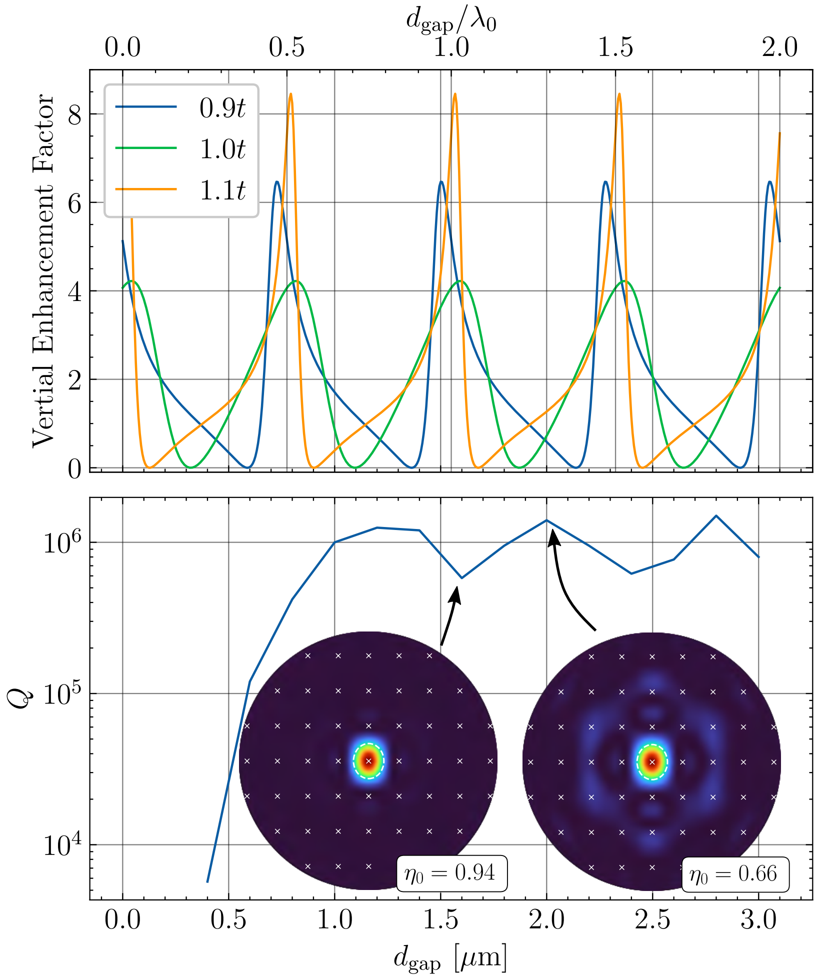

Figure 3-7: Simulated quality factor (Q) and analytic vertical enhancement factor (S) trends for an $L3$ PhC cavity (resonant wavelength λ_0) placed a distance d above a silicon back-reflector. Insets show the far-field emission pattern $S(\vec{k})$ at select points.

limiting the overall uniformity of the fabricated arrays.

We explored a number of methods to resolve this issue. The first was to deposit a thin (~10 nm) stress-compensating layer of silicon nitride directly onto the buckled membranes [130]. This approach was successful as illustrated by the flattened arrays in Fig. 3-8, but degraded the cavity Q and was unable to withstand the trimming process described in Chapter 6 (thermal annealing relaxed the high tensile stress in the silicon nitride layer). We also fabricated previously proposed stress-engineered support structures (Fig. 3-9) [131]; however, these devices often collapsed during the release process leading to stiction failure.

As a final alternative, we flattened the suspended arrays by mechanically bowing the die with a backside set pin in a custom sample mount (Fig. 3-10). This approach

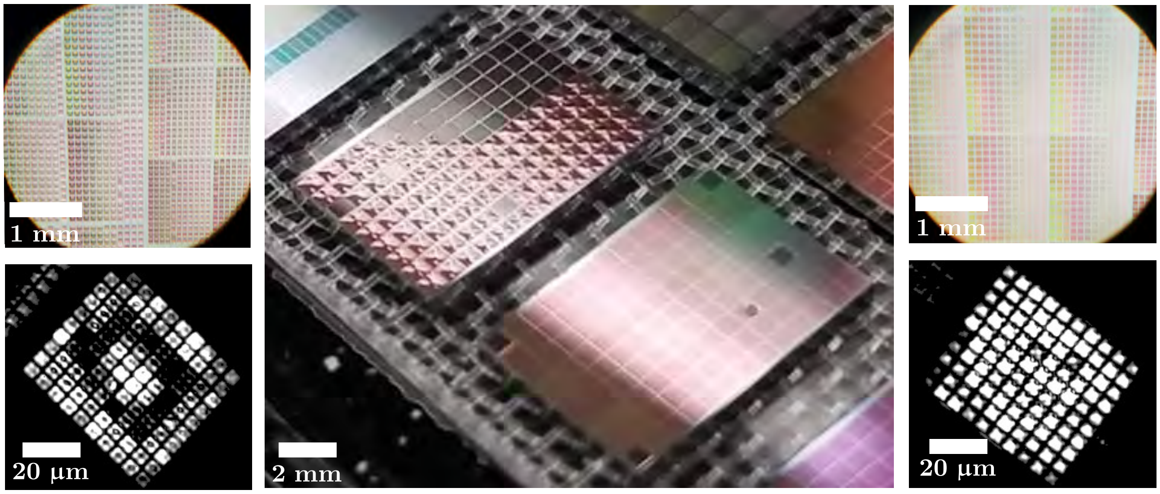

Figure 3-8: Millimeter-scale suspended PhC membranes (left) buckle when released due to compressive stress in the thermal oxide of SOI die but can be subsequently flattened (right) by depositing a 10 nm layer of high-tensile-stress silicon nitride. As a result, variations in the peak resonant reflectivity (grayscale images) are suppressed.

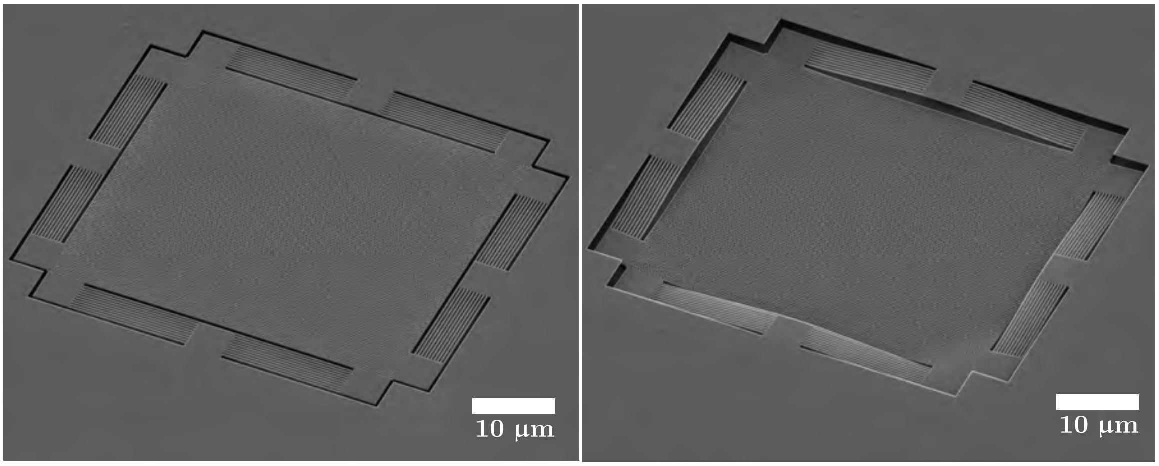

Figure 3-9: Suspended (left) and collapsed (right) PhC cavity arrays with stress-engineered suspension [131].

Figure 3-10: Sample mount with set pin to flatten stress-buckled suspended membranes.

flattened the membranes as desired; however, the resulting (uniform) gap spacing $d = 2$ μm minimized vertical coupling at the design wavelength $\lambda_0 = 1.55$ μm. We therefore added a back-side silicon nitride anti-reflection coating (ARC) on the substrate and timed the release etch to form a front-side ARC with the remaining oxide (Fig. 3-11). The combination of these optimized post-processing steps enabled uniform, high-reflectivity cavities arrayed across mm-scale suspended membranes.

3.4 High-Q/V at Wafer-Scale

The resulting die contain single and arrayed PhC cavities with swept dimensions to offset systematic fabrication biases. We chose Lm-type cavity designs — formed by removing m holes from the PhC lattice as demonstrated by the $L3$ unit cells in Fig. 2-10 — to host tunable-volume (via variable m), high-Q resonant modes with even reflection symmetry (about the unit cell axes) as required for vertical emission [107]. As evidenced by Fig. 3-12, the highest-performance measured devices feature $Q > 10^6$ with normalized volumes $\tilde{V} < 0.5$. With a joint spectral- and spatial-confinement (quantified by the figure-of-merit $Q/\tilde{V}$) $\approx 4 \times 10^6$, these devices are among the highest-finesse optical cavities ever fabricated in a foundry process.

Our optimized foundry processing extends this exceptional single-device performance (rivaling record EBL-fabricated devices) to large-scale cavity arrays. Compared to previous PhC experiments with few waveguide-coupled devices, we developed the fully-automated measurement system described in Sec. 2.5.1 to locate and characterize hundreds of cavities per second via parallel camera readout (Fig. 3-13a).

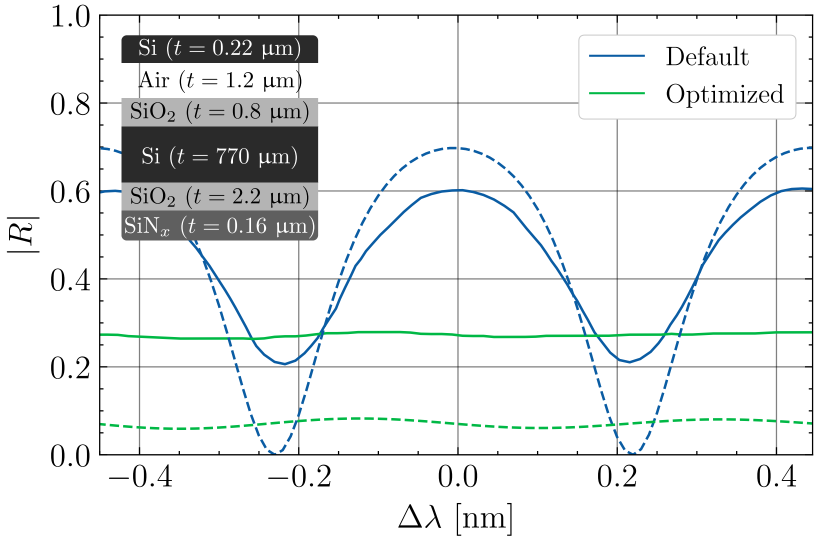

Figure 3-11: Comparison of simulated (dashed) and measured (solid) silicon-on-insulator (SOI) sample reflection before (blue) and after (green) anti-reflection optimization for normal incidence at $\lambda = 1550$ nm. Measured values were calibrated with a known reference mirror. The final layer stack of silicon (Si, $n = 3.48$), oxide (SiO$_2$, $n = 1.44$), and deposited silicon nitride (SiN$_x$, $n = 1.90$) is shown in the inset with optimized layers highlighted in green.

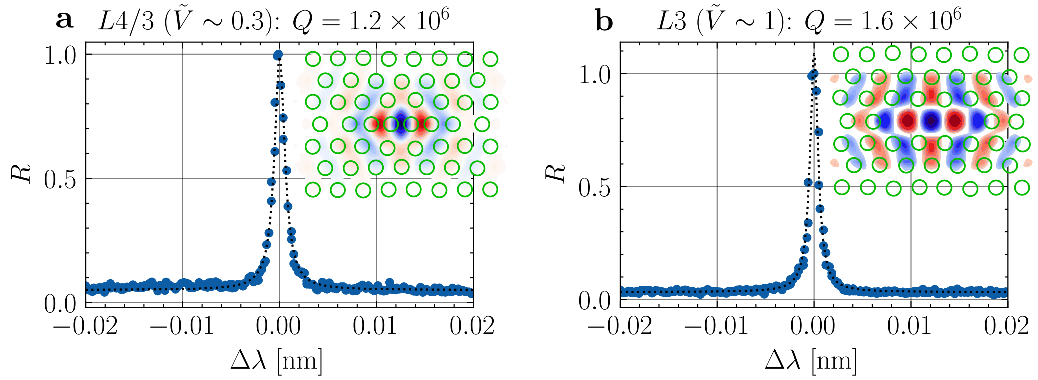

Figure 3-12: Single-device reflection spectra of $L4/3$ (a) and $L3$ (b) cavity designs with sub-wavelength mode volumes and $Q > 10^6$. Insets depict the hole arrangement of inverse-designed PhC lattices with superimposed electric field profiles in the slab midplane along the cavity's dominant polarization axis (E_y).

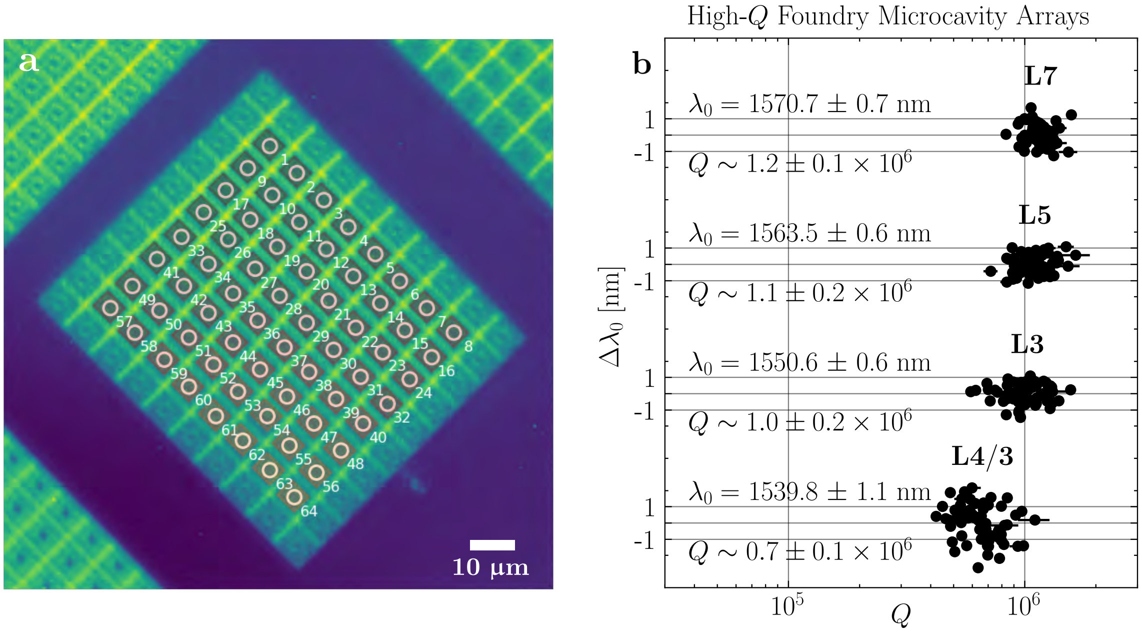

Figure 3-13: Simultaneous measurement of high-Q/V cavity arrays via widefield camera readout. A white-light image of any array of cavities within the camera's field of view (a) is processed to place integration bounds around each device (illustrated here by red boxes co-located with the white circles denoting the center of each numbered cavity). Processed camera frames synchronized to a tunable laser scan give reflection spectra for each cavity, which reveal Lm-type cavity arrays with $\langle Q \rangle > 10^6$ and sub-nanometer wavelength standard deviation (b).

The resulting data, extracted from hundreds of thousands of devices measured across the wafer, allow us to statistically analyze resonator performance and fabrication variability at the die, reticle, and wafer level. Fig. 3-13b, for example, shows resonant wavelength and Q variations within 8×8 arrays of four different cavity designs. Using camera readout of the reflected widefield excitation, each dataset is extracted from a single wavelength scan of a tunable laser. Besides the expected positive correlation between uniformity and mode volume [132], the data demonstrates — for the first time, to our knowledge — the ability to fabricate sub-wavelength ($\tilde{V} < 1$) microcavity arrays with $\langle Q \rangle > 10^6$ and sub-nanometer standard deviation in resonant wavelength.

This excellent wavelength uniformity can be partially attributed to the improved fabrication tolerance of our cavity designs, which we briefly studied using the Monte Carlo method. Assuming hole placement and size errors (with standard deviation σ_h) are the dominant fabrication variability leads to a proportional wavelength standard deviation σ_lambda and a [114] and an inverse Q standard deviation $\sigma_{1/Q} \propto \sigma_h^2$. The constants of proportionality for any cavity of interest can thus be approximated using Monte Carlo methods: for each design, variations with Gaussian distributed error patterns (with fixed σ_h) are randomly generated and simulated using GME. The

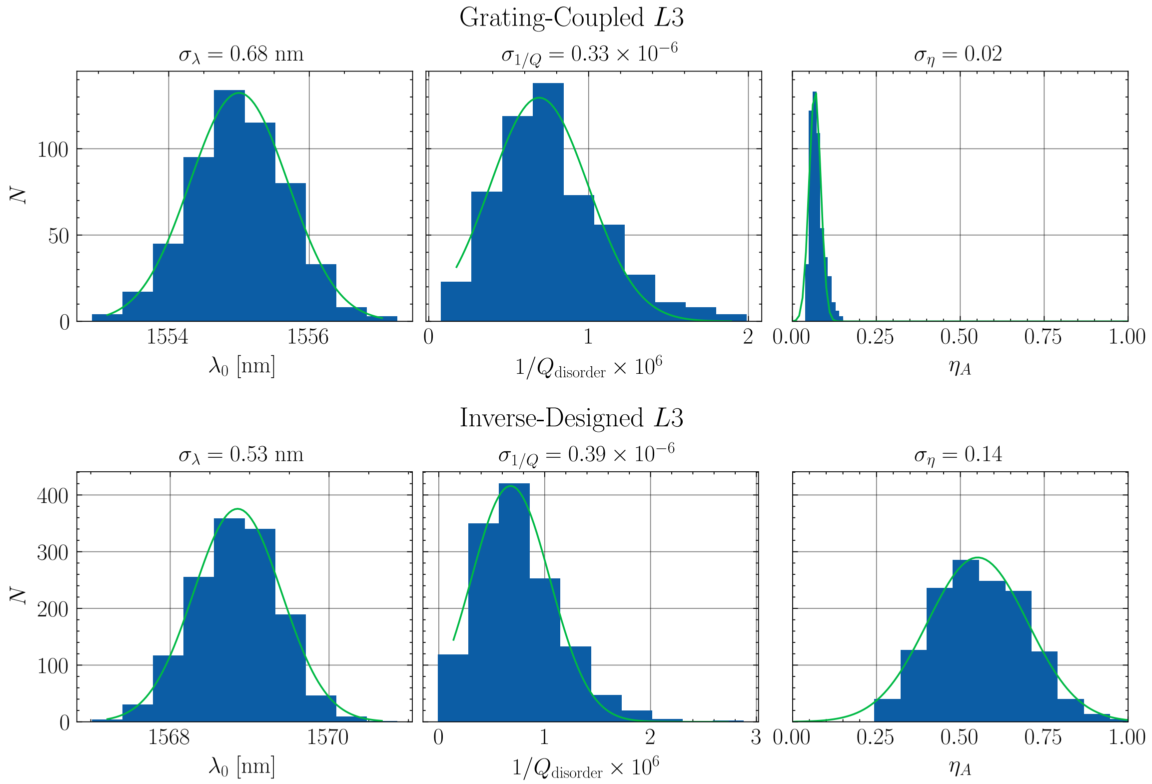

Grating-Coupled $L3$

$\sigma_\lambda = 0.68$ nm

$\sigma_{1/Q} = 0.33 \times 10^{-6}$

$\sigma_\eta = 0.02$

Inverse-Designed $L3$

$\sigma_\lambda = 0.53$ nm

$\sigma_{1/Q} = 0.39 \times 10^{-6}$

$\sigma_\eta = 0.14$

Figure 3-14: GME-simulated resonant wavelength λ_0, quality factor Q, and aperture efficiency η_A statistics for grating-coupled (top) and inverse-designed (bottom) $L3$ designs given a random, Gaussian distributed hole placement and size error with standard deviation $\sigma_h = 1$ nm.

aggregated statistics are then fitted to extract determine each design's fabrication tolerance. Fig. 3-14, for example, shows that the wavelength uniformity of the inverse-designed $L3$ cavity in Fig. 2-4b is reduced by 20% compared to the grating-coupled, Q optimized design in Fig. 2-1a. While these results mirror those of similar neural network-designed heterostructure cavities [133], we note that the improvement is not necessarily inherent: the fabrication tolerance varies by design.

Critically for beamforming, this state-of-the-art uniformity also extends to the far-field: Figs. 3-15 and Fig. 3-16 demonstrate the far-field uniformity characteristic of grating coupled and inverse-designed $L3$ cavity arrays, respectively. Averaged across the 8×8 arrays, the former offers a $\sim 3\times$ improvement in zero-order diffraction and aperture efficiencies ($\langle \eta_0 \rangle = 0.86$, $\langle \eta_a \rangle = 0.99$).

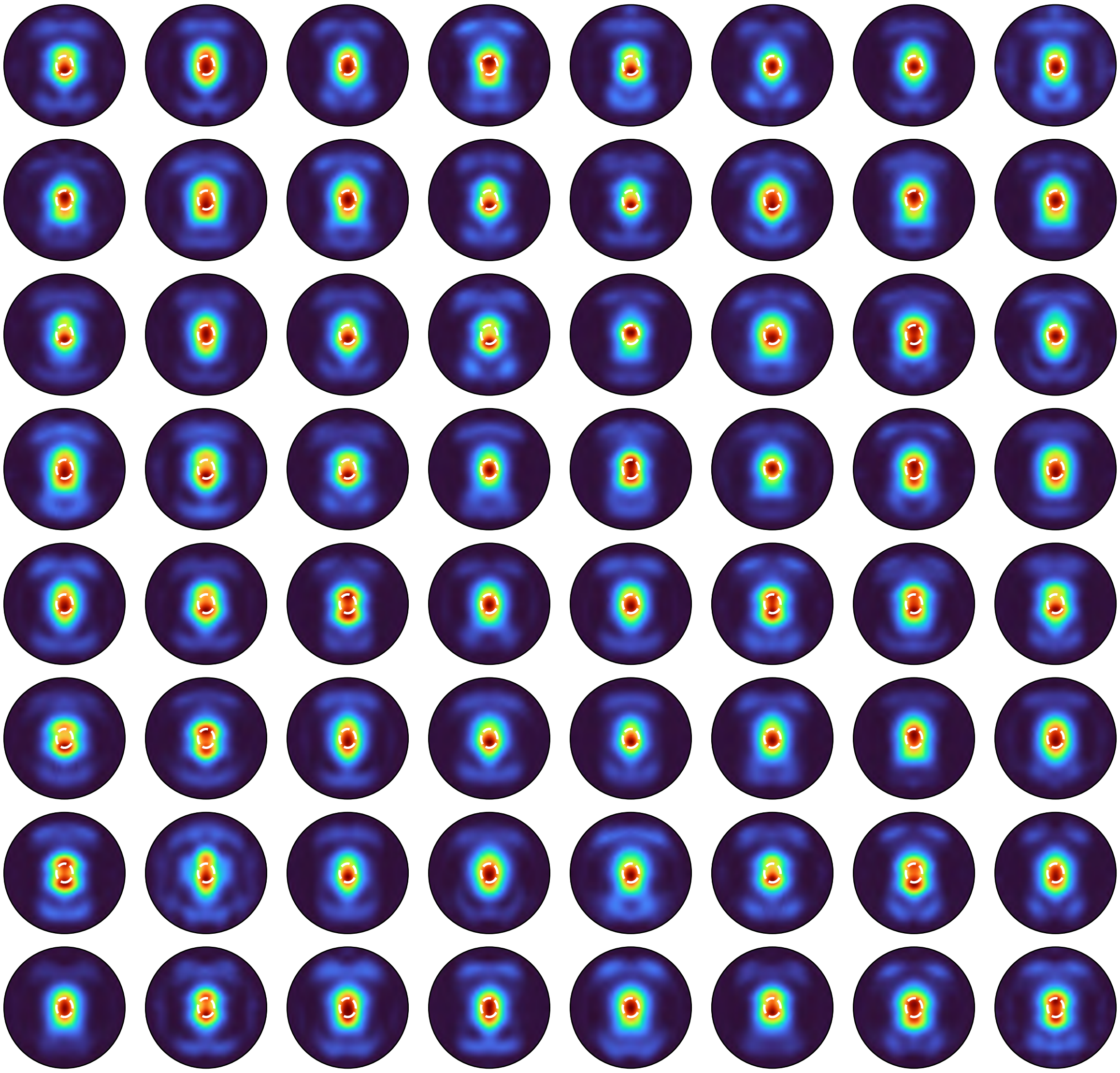

Figure 3-15: Imaged far-field profiles $S(\vec{k})$ (over a 0.9 numerical aperture) for each device in an 8×8 array of grating-coupled $L3$ PhC cavities, yielding $\eta_0 = 0.31 \pm 0.03$.

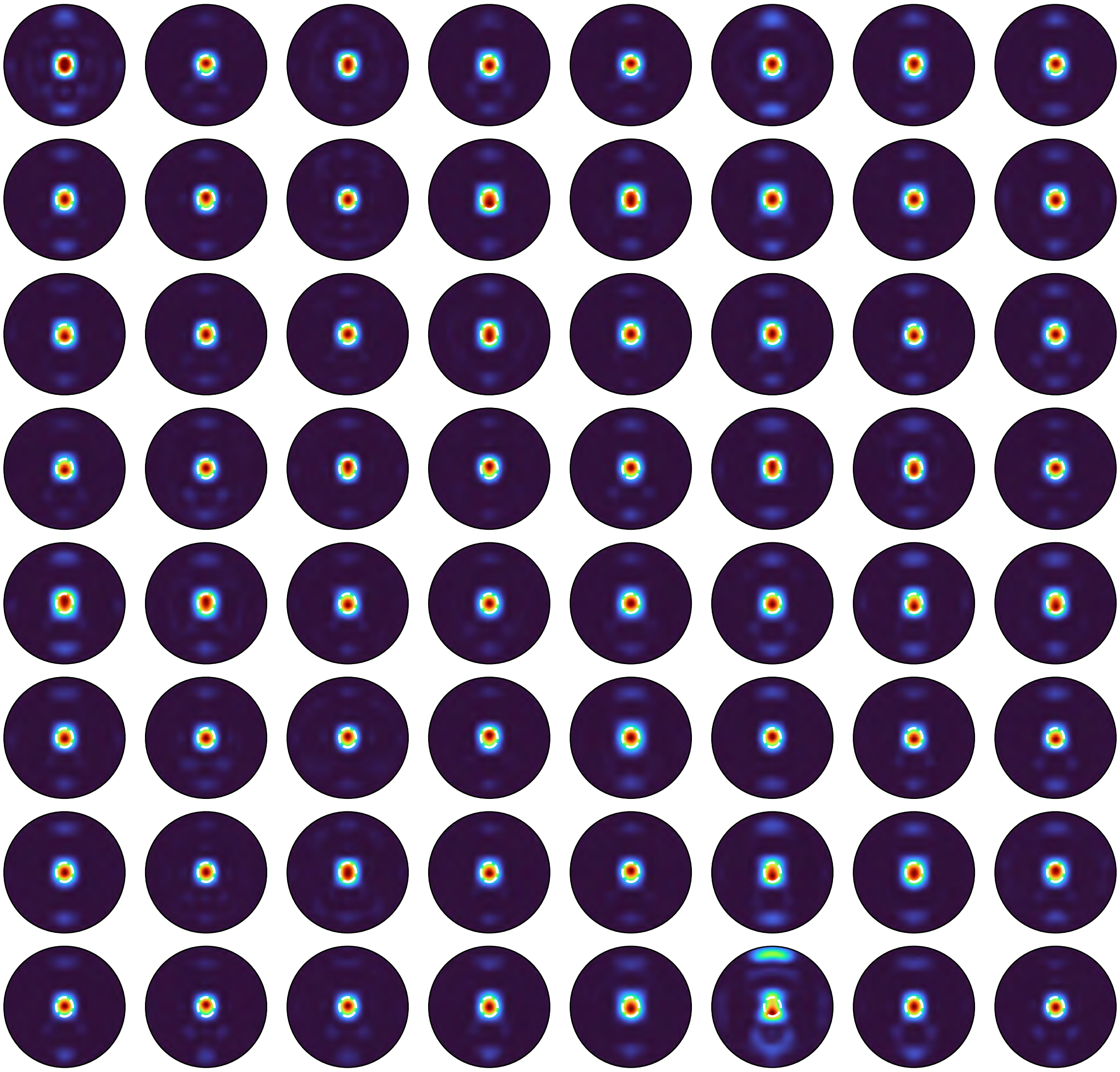

Figure 3-16: Far-field profiles (as in Fig. 3-15) for inverse-designed $L3$ arrays. Each cavity in an 8×8 array emits vertically with $\eta_0 = 0.86 \pm 0.07$, in quantitative agreement with the simulated result in Fig. 2-10.

Today's noise is tomorrow's calibration is the future's Nobel prize.

Professor Wolfgang Ketterle, MIT 8.422 (2007).

4

Microcavity Thermal Noise Limits

Abstract

We present a joint theoretical and experimental analysis of thermo-refractive noise in high quality factor (Q), small mode volume (V) optical microcavities. Analogous to well-studied stability limits imposed by Brownian motion in macroscopic Fabry-Perot resonators, we show that microcavity thermo-refractive noise gives rise to a mode volume-dependent maximum effective quality factor. State-of-the-art fabricated microcavities are found to be within one order of magnitude of this bound. By measuring the first thermodynamically-limited frequency noise spectra of wavelength scale high-Q/V silicon photonic crystal cavities, we confirm the assumptions of our theory, demonstrate a broadband sub-$\mu\mathrm{K}/\sqrt{\mathrm{Hz}}$ temperature sensitivity, and unveil a new technique for discerning sub-wavelength changes in microcavity mode volumes. To illustrate the immediate implications of these results, we show that thermo-refractive noise limits the optimal performance of recently-proposed room temperature, all-optical qubits using cavity-enhanced bulk material nonlinearities.[1]

---

[1] This chapter was adapted from [87]. I thank Gregory Moille (NIST) and Kartik Srinivasan (NIST) for their associated "Viewpoint" [134] in the American Physical Society's *Physics* newsletter, which provides another interesting perspective summary of the work. I also thank Mark Dykman (MSU), Guanhao Huang (EPFL), and Tobias Kippenberg (EPFL) for their useful feedback and discussions.

4.1 How Good is Good?

If you tell any professional scientist or engineer that something is “good”, their answer should always be the same: “relative to what?” This was the question that we faced after fabricating and measuring the devices in Chapter 3. Sure, they were among the highest-Q/V microcavities ever fabricated, but was that “good?” In other words, how do today’s best optical cavities stack up against fundamental performance limits? Amazed by the continual improvement of experimental microcavities, I began investigating this question. These studies led a surprising result: energy and temperature fluctuations in small volumes, a classic problem in statistical mechanics, can significantly affect the performance of practical optical devices. This realization also demonstrates a more general point — that pushing *engineering* problems towards their fundamental limits (i.e. the goal of this thesis) can lead to surprising *scientific* discoveries completely unrelated to the original engineering goals. I will dedicate the next two chapters to explaining these discoveries — and their reciprocal impacts on future *technologies* — before returning to the development of the PhC-SLM in Chapter 6.

4.2 The Noise-Volume Tradeoff

Room temperature, high-quality factor (Q) optical cavities enable the investigation of new physical phenomena by enhancing light-matter interaction [135], shaping electromagnetic modes [136], and modifying the vacuum photon density of states [137]. However, these advantages come with an often forgotten cost — interaction with a thermally equilibrated confining medium inherently injects noise into the optical mode in accordance with the fluctuation-dissipation theorem (FDT) [138]. Macroscopic resonators (Fig. 4-1a), such as those implemented in gravitational wave interferometers, minimize this interaction by supporting a large mode volume $\tilde{V} \gg 1$ in vacuum, where $\tilde{V} = V/(\lambda/n)^3$ for the volume V of a λ-wavelength optical mode confined in a refractive index n. The surprising realization that the sensitivity of these ∼km-long cavities can still be limited by Brownian motion in few µm-thick mirror coatings [139, 140] has spurred interest in low-noise mirror coatings [141], grating-based mirrors [142, 143], and the fundamental limits of macroscopic cavities in the presence of thermal fluctuations [144–146].

Here, we consider the opposite case: optical microcavities (Fig. 4-1b) [85], whose small mode volumes ($\tilde{V} \sim 1$) have facilitated single molecule label-free sensing [147], high-repetition rate frequency combs [148, 149] for frequency synthesis [150], spectroscopy [151], and astronomy [152], enhanced coupling for atom-photon interfaces [153–155], and low-energy (down to single-photon level) nonlinear interactions [80]. These microcavity-enhanced nonlinearities even reveal new directions in physical science [156]: experimental demonstrations of non-Hermitian phenomena [157], topological enhancement [158, 159], synchronization [160], and chaotic dynamics [161]

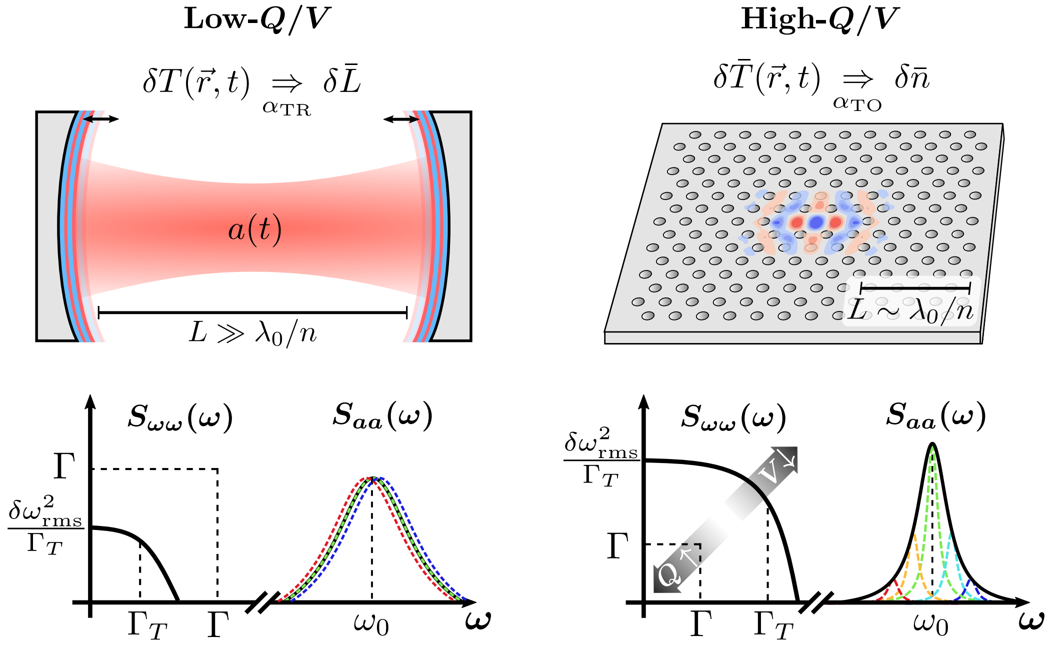

Figure 4-1: Comparison of thermo-refractive noise (TRN) in macroscopic resonators and microcavities. Mode-averaged temperature fluctuations $\delta\bar{T}$ in large cavities induce refractive index noise $\delta\bar{n}$ (and thus pathlength changes $\delta\bar{L}$) due to the mirrors' non-zero thermo-optic coefficient $\alpha_{\mathrm{TR}} = \mathrm{d}n/\mathrm{d}T$. The large mode volume V reduces $\delta\bar{T}$, yielding a narrowband resonant frequency noise spectrum $S_{\omega\omega}(\omega)$ and an rms resonant frequency fluctuation $\delta\omega_{\mathrm{rms}} \ll \Gamma$, the cavity half-linewidth. This non-dominant thermal noise inhomogeneously broadens the intracavity field spectrum $S_{aa}(\omega)$. Decreasing V increases both the magnitude $\delta\omega_{\mathrm{rms}}$ and bandwidth Γ_T of TRN, while increasing the resonator quality factor $Q = \omega_0/2\Gamma$ causes both quantities to exceed Γ. TRN therefore becomes a dominant source of homogeneous broadening in wavelength-scale high-Q/V microcavities, leading to thermal dephasing and reduced resonant excitation efficiency of the cavity field $a(t)$.

are just a few recent examples. However, shrinking mode confinement towards the near-diffraction-limited volumes offered by microcavities significantly amplifies fundamental temperature fluctuations $\langle \delta T^2 \rangle \propto 1/V$ [162]. These small volume temperature fluctuations are a classic problem in statistical mechanics [163], and their exact nature was heavily debated [164–166] until initial measurements were reported in the 1990s [167]. Temperature noise has since been studied in diverse contexts including high-energy collisions [168], molecular dynamics [169], spin ensembles [170], and state-of-the-art electron- [171] or graphene-based nanocalorimeters [172]. In optics, the associated refractive index fluctuations, so called "thermo-refractive noise" (TRN), have been studied extensively in fiber-based lasers and interferometers [173–176]. In recent years, TRN has emerged as a principal source of resonant frequency noise in various dielectric microcavity geometries including microspheres [177], whispering-gallery mode resonators [178, 179], ring resonators [180], and photonic crystal (PhC) cavities [181]. TRN has also recently been shown to limit the stability of integrated lasers [182, 183] and microcavity frequency combs [184].

To date, microcavity TRN has only been considered in a pertubative regime, where the resulting rms resonant frequency fluctuation $\delta\omega_{\mathrm{rms}} \propto 1/\sqrt{V}$ is much less than the loaded cavity linewidth $2\Gamma = \omega_0/Q$. For sufficiently high Q and small V, this assumption becomes invalid. Continued improvements in microcavity performance — yielding $Q > 10^7$, $\tilde{V} \sim 1$ through fabrication advances [76] and $Q \sim 10^5$, $\tilde{V} \sim 10^{-3}$ using novel sub-wavelength dielectric features [78] — thus raises a simple question: when will fundamental thermal noise limit the performance of high-Q/V microcavities?

Here, we answer this open question by deriving general bounds for optical microcavity performance in the presence of TRN and find that current photonic crystal and whispering gallery mode (WGM) devices are within one order of magnitude of this bound. We verify our theory by measuring TRN as the dominant noise source in high-Q/V PhC cavities and demonstrate the ability to distinguish between sub-wavelength mode volumes ($\tilde{V} < 1$) using fundamental noise spectra. To our knowledge, these are the first spectrally-resolved measurements of a near-diffraction-limited optical mode operating at the thermal noise limit. We believe that our devices' unique combination of micron-scale spatial localization with a broadband temperature sensitivity comparable to state-of-the-art room-temperature optical thermometers will enable new directions in thermal physics and non-equilibrium thermodynamics [185, 186]. As an example of the immediate impact of our formalism, we analyze the implications for an outstanding goal in quantum photonics: all-optical qubits using cavity-enhanced bulk material nonlinearities [187]. Since thermal noise is found to limit the qubit coherence, we propose and analyze coherent thermo-optic noise cancellation as one potential avenue towards continued developments in low-noise, high-Q/V microcavities. Together, these results reveal the importance of thermal noise in state-of-the-art optical resonators, inform design choices to minimize its impact on device performance, and motivate new research directions to violate the proposed bounds.

4.3 Basic Formalism

As schematically illustrated in Fig. 4-1, fundamental stochastic temperature fluctuations $\delta T(\vec{r}, t)$ within a cavity confining medium of refractive index n and thermo-optic coefficient $\alpha_{\mathrm{TR}} = \mathrm{d}n/\mathrm{d}T$ drive a mode-averaged refractive index change $\delta\bar{n}(t) = \alpha_{\mathrm{TR}}\delta\bar{T}(t)$. For an optical mode completely confined in dielectric, the resulting resonance shift $\delta\omega(t) = -\omega_0\alpha_{\mathrm{TR}}\delta\bar{T}(t)/n$ follows from first-order perturbation theory [18]. For now, we neglect temperature-induced deformations of the cavity, as the thermo-elastic coefficient of common dielectrics is typically two orders of magnitude smaller than α_{TR} [178]. Resonant enhancement of these mechanical effects over a narrow bandwidth is possible; however, we are primarily interested in the broadband noise performance.

In the presence of TRN, the steady-state rotating-frame intra-cavity field amplitude is

$$\tilde{a}(t) = \sqrt{\Gamma}\tilde{s}_{\mathrm{in}} \int_{-\infty}^{t} \mathrm{d}t' e^{-(i\Delta+\Gamma)(t-t')+i\int_{t'}^{t}\mathrm{d}t''\delta\omega(t'')} \tag{4.1}$$

for a loaded amplitude decay rate Γ and critically-coupled static drive $\tilde{s}_{\mathrm{in}}$ detuned by Δ from the cavity resonance. The associated statistical moments can be computed using the moment-generating properties of the characteristic functional $\langle e^{i\int_{t'}^{t}\delta\omega(t'')dt''}\rangle$, which in the case of zero-mean Gaussian noise only requires the autocorrelation $\langle\delta\omega(t)\delta\omega(t+\tau)\rangle = (\omega_0\alpha_{\mathrm{TR}}/n)^2\langle\delta\bar{T}(t)\delta\bar{T}(t+\tau)\rangle$ [188, 189]. The latter autocorrelation of temperature fluctuations can be computed from the heat equation

$$\frac{\partial}{\partial t}\delta T(\vec{r},t) + D_T\nabla^2\delta T(\vec{r},t) = F_T(\vec{r},t) \tag{4.2}$$

in a medium of thermal diffusivity D_T driven by a Langevin forcing term $F_T(\vec{r},t)$ which satisfies the FDT. As we will illustrate for slab PhC cavities, Eqn. 4.2 can be solved analytically for specific geometries; however, for generality we follow the approach of Ref. [190] and enforce a single-mode decay approximation by introducing a phenomenological thermal decay rate

$$\Gamma_T = D_T\frac{\int\left[\nabla\left(\epsilon(\vec{r})|\vec{E}(\vec{r})|^2\right)\right]^2\mathrm{d}^3\vec{r}}{\int\epsilon(\vec{r})^2|\vec{E}(\vec{r})|^4\mathrm{d}^3\vec{r}} \tag{4.3}$$

evaluated for the envelope of intracavity energy density. This form of Γ_T is chosen for consistency with $\langle\delta\bar{T}^2\rangle = k_BT_0^2/c_VV_T$, the well-known statistical mechanics result for temperature fluctuations in a volume V_T of specific heat capacity c_V at thermal equilibrium with a bath temperature T_0 [163]. Averaging Eqn. 4.2 over the optical mode profile, we then find

$$\frac{\mathrm{d}}{\mathrm{d}t}\delta\bar{T}(t) + \Gamma_T\delta\bar{T}(t) = \bar{F}_T(t), \tag{4.4}$$

leading to the solution

$$\langle\delta\omega(t)\delta\omega(t+\tau)\rangle = \underbrace{\left(\frac{\omega_0}{n}\alpha_{\mathrm{TR}}\right)^2\frac{k_BT_0^2}{c_VV_T}}_{\delta\omega_{\mathrm{rms}}^2}e^{-\Gamma_T|\tau|}, \tag{4.5}$$

where the thermal mode volume

$$V_T = \frac{\left[\int \epsilon(\vec{r})|\vec{E}(\vec{r})|^2 \mathrm{d}^3\vec{r}\right]^2}{\int \epsilon(\vec{r})^2|\vec{E}(\vec{r})|^4 \mathrm{d}^3\vec{r}} \tag{4.6}$$

is the common Kerr nonlinear mode volume found by solving Eqn. 4.2 in a homogeneous medium [177, 191]. For a three-dimensional mode with a Gaussian-shaped energy density distribution, V_T is larger than the standard Purcell mode volume $V = \int \epsilon|\vec{E}|^2\mathrm{d}^3\vec{r}/\max\{\epsilon|\vec{E}|^2\}$ by a factor of $2\sqrt{2}$.

Combining Eqns. 4.1 and 4.5, we can solve for the statistical moments of the driven cavity amplitude $\tilde{a}(t)$ as a function of the primary parameters V_T and Γ_T. The results are dervied in Sec. 4.4 and discussed in Sections 4.7 and 4.8. Here, however, we consider a simplified example of free cavity evolution, which demonstrates the basic techniques and the cavity behavior in two limiting regimes. In this case, the amplitude autocorrelation $\langle \tilde{a}(t)\tilde{a}^*(t+\tau)\rangle \sim \langle e^{-i\int_t^{t+\tau}\delta\omega(t')dt'}\rangle e^{-\Gamma\tau} = F(\tau)e^{-\Gamma\tau}$ can be simplified by evaluating the dephasing function

$$\begin{aligned} F(\tau) &= \exp\left[-\int_0^\tau d\tau'(\tau-\tau')\langle\delta\omega(t)\delta\omega(t+\tau)\rangle\right] \\ &= \exp\left[\left(\frac{\delta\omega_{\mathrm{rms}}}{\Gamma_T}\right)^2\left(1-\Gamma_T\tau - e^{-\Gamma_T\tau}\right)\right], \end{aligned} \tag{4.7}$$

where we have implemented the previously described characteristic functional properties with the frequency noise statistics of Eqn. 4.5. For sufficiently large V_T (corresponding to a slow Γ_T) and small Q as assumed in previous analyses, the cavity resonance is quasistatic over the photon decay period and shifts by much less than a cavity linewidth over time. In this perturbative limit (Fig. 4-1a), $\Gamma_T\tau \ll 1$ over the cavity ringdown time. We can therefore expand $e^{-\Gamma_T\tau}$ in Eqn. 4.7 to second order, yielding $\langle \tilde{a}(t)\tilde{a}^*(t+\tau)\rangle \sim e^{-\Gamma\tau}e^{-\delta\omega_{\mathrm{rms}}^2\tau^2/2}$. The associated lineshape, given by the Fourier transform of $\langle \tilde{a}(t)\tilde{a}^*(t+\tau)\rangle$ via the Wiener–Khinchin theorem, is thus the original Lorentzian with a small inhomogeneous Gaussian broadening due to TRN. Simply put, TRN limits the cavity stability without substantially altering the intracavity dynamics.

However, as the thermal mode volume V_T shrinks, $\delta\omega_{\mathrm{rms}}$ and Γ_T increase until they eventually exceed Γ (Fig. 4-1b). In this high-Q/V limit, the resonant frequency $\omega_0(t)$ directly tracks the temperature noise over the relevant timescales (i.e. the frequency noise in Eqn. 4.5 is effectively δ-correlated), leading to a homogeneous broadening of the resonance that dephases the intracavity field. Inserting the associated limit $\Gamma_T\tau \gg 1$ into Eqn. 4.7, we find $\langle \tilde{a}(t)\tilde{a}^*(t+\tau)\rangle \sim e^{-(\Gamma+\delta\omega_{\mathrm{rms}}^2/\Gamma_T)\tau}$ corresponding to the broadened linewidth $2\Gamma + 2\delta\omega_{\mathrm{rms}}^2/\Gamma_T \approx 2\delta\omega_{\mathrm{rms}}^2/\Gamma_T$.

Our analysis focuses on the transition to this high-Q/V limit. Specifically, we derive general solutions to Eqn. 4.1 for arbitrary TRN powers and bandwidths to calculate mode volume-dependent maximum “effective” cavity quality factors Q_{eff} that describe the fundamental limits of microcavity stability and coherence. Whereas the simple free evolution model presented in this section reveals the essential physics of the extreme low- and high-Q/V cases, our latter generalized solutions are broadly applicable to any highly-confined dielectric microcavity, including, microspheres [177], micropillars [192], ring resonators [180], microtoroids [193], PhC cavities [181], microdisks [194], vertical Fabry-Perot cavities [195], and more.

4.4 Complete Thermo-Refractive Noise Theory

While the development of ultrahigh-performance optical resonators has only recently warranted its study within optical systems, stochastic temperature fluctuations are a fundamental concept in thermodynamics [163]. Assuming Boltzmann statistics within a finite volume V with specific heat capacity c_V at temperature T, we find

$$\langle \delta T^2 \rangle = \frac{k_B T^2}{c_V V}. \tag{4.8}$$

In optical microcavities, V approaches diffraction limited volumes leading to temperature fluctuations that significantly impact the resonance stability in materials with a temperature-dependent refractive index.

Here, we derive the associated thermo-refractive noise (TRN) spectrum in an optical microcavity under the single-mode approximation described in Sec. 4.3. Using this approximation, the intracavity field statistics are derived. In the typical perturbative limit where the rms frequency fluctuation is much smaller than the loaded cavity linewidth ($\delta\omega_{\text{rms}} \ll 2\Gamma_l$), we use perturbation theory to solve for the evolution of the cavity field $a(t)$ and the associated noise spectrum $S_{aa}(t)$. We also provide general solutions for the first and second statistical moments of $a(t)$, which are used Secs. 4.7 and 4.8 to derive “effective” quality factors in the presence of thermal noise. The solution for $S_{aa}(t)$ in the limiting case of high-Q cavities — where the thermal decay rate $\Gamma_T \gg \Gamma_l$ and the frequency noise can be assumed to be white — is also provided. Finally, we compare the single-mode noise spectrum to that derived from a formal solution to heat diffusion in an infinite two dimensional slab, which we found to most accurately model the specific geometry of the photonic crystal microcavities in our experiments.

A few notes on convention: 1) we derive two-sided angular frequency noise spectra $S_{\omega\omega}(\omega)$, but plot one-sided frequency spectra $S_{\text{ff}}(f) = 2S_{\omega\omega}(2\pi f)/2\pi = S_{\omega\omega}(2\pi f)/\pi$ for experimental measurements to conform with the common conventions of the gravitational wave community; 2) temporal coupled mode theory decay rates Γ_i are amplitude decay rates; the associated quality factors are therefore defined as $Q_i = \omega_0/2\Gamma_i$.

4.4.1 Microcavity TRN Statistics

To first order, the change in resonant frequency under a permittivity perturbation $\delta\epsilon(\vec{r},t)$ can be expressed as

$$\frac{\delta\omega(t)}{\omega_0} = -\frac{1}{2}\frac{\int_{\delta\epsilon}\delta\epsilon(\vec{r},t)|\vec{E}(\vec{r})|^2\mathrm{d}^3\vec{r}}{\int\epsilon|\vec{E}(\vec{r})|^2\mathrm{d}^3\vec{r}} \approx -\frac{1}{V_{\text{eff}}}\frac{\int_{\delta n} n\,\delta n(\vec{r},t)|\vec{E}(\vec{r})|^2\mathrm{d}^3\vec{r}}{\max\{\epsilon|\vec{E}(\vec{r})|^2\}}$$

where we have made the approximation $\delta\epsilon \approx 2n\ \delta n$ and introduced the standard mode volume

$$V_{\text{eff}} = \frac{\int\epsilon(\vec{r})|\vec{E}(\vec{r})|^2\mathrm{d}^3\vec{r}}{\max\{\epsilon(\vec{r})|\vec{E}(\vec{r})|^2\}}. \tag{4.9}$$

The change in refractive index $\delta n(\vec{r},t)$ is directly proportional to temperature change $\delta T(\vec{r},t)$, with the thermo-optic coefficient $\alpha_{TO} = dn/dT$ serving as the constant of proportionality. We therefore find

$$\frac{\delta\omega(t)}{\omega_0} = -\frac{1}{V_{\text{eff}}}\frac{\int_{\delta n}\alpha_{\text{TO}}\delta T(\vec{r},t)n|\vec{E}(\vec{r})|^2\mathrm{d}^3\vec{r}}{\max\{\epsilon|\vec{E}(\vec{r})|^2\}}. \tag{4.10}$$

Alternatively, Eqn. 4.9 can be evaluated for a uniform, mode averaged temperature change $\delta\bar{T}(t)$ assuming complete confinement of the mode within a homogeneous medium. This approach yields

$$\frac{\delta\omega(t)}{\omega_0} = -\frac{1}{n}\alpha_{\text{TO}}\delta\bar{T}(t). \tag{4.11}$$

Comparing Eqns. 4.10 and 4.11, we find

$$\delta\bar{T}(t) = \frac{1}{V_{\text{eff}}}\frac{\int\delta T(\vec{r},t)\epsilon(\vec{r})|\vec{E}(\vec{r})|^2\mathrm{d}^3\vec{r}}{\max\{\epsilon|\vec{E}(\vec{r})|^2\}}. \tag{4.12}$$

Eqn. 4.11 can now be solved using the mode averaged temperature change, whose evolution is derived from the heat equation (given a thermal diffusivity D_T)

$$\frac{\partial\delta T(\vec{r},t)}{\partial t} - D_T\nabla^2\delta T = F_T(\vec{r},t) \tag{4.13}$$

driven by a thermal Langevin source $F_T(\vec{r},t)$ with the statistics [196]

$$\langle F_T(\vec{r}_1,t_1)F_T^*(\vec{r}_2,t_2)\rangle = \frac{2D_Tk_BT_0^2}{c_V}\delta(t_1-t_2)\vec{\nabla}_{\vec{r}_1}\cdot\vec{\nabla}_{\vec{r}_2}[\delta(\vec{r}_1-\vec{r}_2)] \tag{4.14}$$

that satisfy the fluctuation-dissipation theorem. Averaging over the mode, we find the approximation

$$\frac{\mathrm{d}(\delta\bar{T}(t))}{\mathrm{d}t} + \Gamma_T \delta\bar{T}(t) = \bar{F}_T(t), \tag{4.15}$$

where Γ_T is introduced as a phenomenological thermal decay rate whose form will be chosen later to ensure the form of $\langle \delta\bar{T}^2 \rangle$ matches the canonical result from statistical mechanics (Eqn. 4.8). In analog with $\delta\bar{T}(t)$, the mode averaged thermal force $\bar{F}_T(t)$ is

$$\bar{F}_T(t) = \frac{1}{V_{\text{eff}}} \frac{\int F_T(\vec{r},t)\epsilon(\vec{r})|\vec{E}(\vec{r})|^2 \mathrm{d}^3\vec{r}}{\max\{\epsilon|\vec{E}(\vec{r})|^2\}}. \tag{4.16}$$

The steady-state solution of Eqn. 4.15,

$$\delta\bar{T}(t) = \int_{-\infty}^{t} \bar{F}(t') e^{-\Gamma_T(t-t')} \mathrm{d}t', \tag{4.17}$$

can then be used to find the corresponding statistics of the temperature fluctuation at equilibrium (i.e. long t):

$$\langle \delta\bar{T}(t)\delta\bar{T}(t+\tau) \rangle = \int_{-\infty}^{t} \mathrm{d}t' \int_{-\infty}^{t+\tau} \mathrm{d}t'' \langle \bar{F}_T(t')\bar{F}_T(t'') \rangle e^{-\Gamma_T(t-t')} e^{-\Gamma_T(t+\tau-t'')}. \tag{4.18}$$

The result requires the autocorrelation of $\bar{F}_T(t)$, which is readily evaluated using the mode averaged form of Eqn. 4.16:

$$\langle \bar{F}_T(t)\bar{F}_T^*(t+\tau) \rangle = \underbrace{\frac{2D_T k_B T_0^2}{c_V V_{\text{eff}}^2} \frac{\int \mathrm{d}^3\vec{r} \left[\vec{\nabla}\left(\epsilon(\vec{r})|\vec{E}(\vec{r})|^2\right)\right]^2}{(\max\{\epsilon|\vec{E}(\vec{r})|^2\})^2}}_{\mathcal{R}_{\bar{F}_T\bar{F}_T}(0)} \delta(\tau) = \mathcal{R}_{\bar{F}_T\bar{F}_T}(0)\delta(\tau).$$

Inserting this result into Eqn. 4.18 along with the change of variables $t'' \to t' + \tau'$ yields

$$\langle \delta\bar{T}(t)\delta\bar{T}(t+\tau) \rangle \approx \frac{\mathcal{R}_{\bar{F}_T\bar{F}_T}(0)}{2\Gamma_T} e^{-\Gamma_T|\tau|}. \tag{4.19}$$

Correspondence with Eqn. 4.8 therefore requires

$$\frac{\mathcal{R}_{\bar{F}_T\bar{F}_T}(0)}{2\Gamma_T} = \frac{k_B T_0^2}{c_V V} \Rightarrow \mathcal{R}_{\bar{F}_T\bar{F}_T}(0) = \frac{2k_B T_0^2 \Gamma_T}{c_V V}. \tag{4.20}$$

Comparing Eqn. 4.20 to Eqn. 4.19 then lends a calculable form of the decay rate Γ_T:

$$\Gamma_T = D_T \frac{\int \mathrm{d}^3\vec{r} \left[\vec{\nabla} \left(\epsilon(\vec{r}) |\vec{E}(\vec{r})|^2 \right) \right]^2}{\int \mathrm{d}^3\vec{r} \epsilon(\vec{r})^2 |\vec{E}(\vec{r})|^4}. \tag{4.21}$$

Combining Eqns. 4.19, 4.20, and 4.21 with the first order perturbation theory relationship $\delta\omega_0(t) \approx -(\omega_0/n)\alpha_{\mathrm{TO}}\delta\bar{T}(t)$ lends the desired autocorrelation of the cavity resonance frequency

$$\langle \delta\omega(t)\delta\omega(t+\tau) \rangle \approx \delta\omega_{\mathrm{rms}}^2 e^{-\Gamma_T|\tau|}, \tag{4.22}$$

for the rms resonant frequency fluctuation

$$\delta\omega_{\mathrm{rms}} = \frac{\omega_0 \alpha_{\mathrm{TO}}}{n} \sqrt{\frac{k_B T_0^2}{c_V V_T}}. \tag{4.23}$$

4.4.2 Derivation of the Thermal Mode Volume

The same correspondence to Eqn. 4.8 can be used to solve for the thermal mode volume V_T [177]. For completeness, we recapitulate this derivation. In an infinite homogeneous medium, we can solve Eqn. 4.13 using Fourier modes instead of introducing the the phenomenological parameter Γ_T, yielding

$$\delta T(\omega, \vec{k}) = \frac{F(\omega, \vec{k})}{i\omega + D_T |\vec{k}|^2}. \tag{4.24}$$

Taking the temperature mode average in Eqn. 4.12 and inverse Fourier transforming yields

$$\delta\bar{T}(t) = \frac{1}{(2\pi)^4 V_{\mathrm{eff}}} \int \mathrm{d}^3\vec{r} \frac{\epsilon |\vec{E}(\vec{r})|^2}{\max\{\epsilon |\vec{E}(\vec{r})|^2\}} \int \mathrm{d}\omega \; e^{-i\omega t} \int \mathrm{d}^3\vec{k} \; e^{i\vec{k}\cdot\vec{r}} \frac{F(\omega, \vec{k})}{i\omega + D_T |\vec{k}|^2}. \tag{4.25}$$

Using the frequency-space autocorrelation of the Langevin driving force (compare Eqn. 4.19) [197],

$$\langle F(\omega_1, \vec{k}_1) F^*(\omega_2, \vec{k}_2) \rangle = (2\pi)^4 \frac{2 k_B T_0^2 D_T}{c_V} |\vec{k}|^2 \delta(\vec{k}_1 - \vec{k}_2) \delta(\omega_1 - \omega_2), \tag{4.26}$$

we can then solve for the autocorrelation of $\delta\bar{T}$:

$$\begin{aligned} \langle \delta\bar{T}(t) \delta\bar{T}^*(t+\tau) \rangle = & \frac{(\max\{\epsilon |\vec{E}(\vec{r})|^2\})^{-2}}{(2\pi)^3 V_{\mathrm{eff}}^2} \frac{k_B T_0^2}{c_V} \\ & \times \int \mathrm{d}^3\vec{k} \; e^{-D_T |\vec{k}|^2 \tau} \left| \int \mathrm{d}^3\vec{r} \; \epsilon(\vec{r}) |\vec{E}(\vec{r})|^2 e^{i\vec{k}\cdot\vec{r}} \right|^2. \end{aligned} \tag{4.27}$$

Eqn. 4.27 must equal Eqn. 4.8 for $\tau = 0$, which reveals the final solution for the thermal mode volume V_T:

$$V_T = \frac{(2\pi)^3 V_{\text{eff}}^2 (\max\{\epsilon|\vec{E}(\vec{r})|^2\})^2}{\int \mathrm{d}^3\vec{k}\ \left|\int \mathrm{d}^3\vec{r}\ \epsilon(\vec{r})|\vec{E}(\vec{r})|^2 e^{i\vec{k}\cdot\vec{r}}\right|^2} = \frac{V_{\text{eff}}^2 (\max\{\epsilon|\vec{E}(\vec{r})|^2\})^2}{\int \mathrm{d}^3\vec{r}\ \epsilon(\vec{r})^2|\vec{E}(\vec{r})|^4} = \frac{V_{\text{eff}}^2}{V_{\text{eff}}^{(2)}} \tag{4.28}$$

where

$$V_{\text{eff}}^{(2)} = \frac{\int \mathrm{d}^3\vec{r}\ \epsilon(\vec{r})^2|\vec{E}(\vec{r})|^4}{\max\{\epsilon^2|\vec{E}|^4\}}. \tag{4.29}$$

This result matches Gorodetsky's original result [177] with the exception of different normalization conditions.

4.4.3 Comparison to Multimode Decay in a 2D PhC Slab

Under the single-mode approximation derived in the preceding sections, Eqn. 4.22 implies a Lorentzian TRN spectrum

$$S_{\omega\omega}(\omega) = \left(\frac{\omega_0}{n}\alpha_{\text{TO}}\right)^2 \frac{k_B T_0^2}{c_V V_T} \frac{2\Gamma_T}{\Gamma_T^2 + \omega^2}. \tag{4.30}$$

As noted in Sec. 4.3, this approximate spectrum can be evaluated for any optical microcavity (photonic crystals, microtoroids, microbottles, ring resonators, micropillars, microdisks, and so on) independent of its exact confining geometry. This allows us to derivethe general noise limits in Sec. 4.4.4. If a particular experimental system is of interest, we can verify the accuracy of this approximation by solving the stochastic heat equation (Eqn. 4.13) for that particular cavity geometry. Here, since we measure TRN in high-Q/V_{eff} 2D slab photonic crystal cavities (see Sec. 4.6), we demonstrate this evaluation for a Gaussian mode confined within an infinite two dimensional slab. The heat equation in this case lends logarithmically — as opposed to exponentially — decaying temperature fluctuations in time.

For a slab of thickness w lying atop the xy plane, the local temperature change $\delta T(\vec{r}, t) = \sum_n T_n(\vec{r}_\parallel, t)\phi_n(z)$ can be expanded in terms of the out-of-plane eigenfunctions $\phi_n(z) = \cos(n\pi z/w)$ assuming insulating boundary conditions on the top and bottom of the slab. The stochastic heat equation then simplifies to the form

$$\frac{\partial T_n(\vec{r}_\parallel, t)}{\partial t} = D_T\left[\nabla^2 - (n\pi/w)^2\right] T_n(\vec{r}_\parallel, t) + \frac{1}{w}\int \phi_n^*(z) F_T(\vec{r}, t)\mathrm{d}z. \tag{4.31}$$

If assume a two-dimensional Gaussian mode profile

$$\epsilon(\vec{r})|\vec{E}(\vec{r})|^2 = \begin{cases} \frac{1}{2\pi\sigma^2} e^{-|\vec{r}_\parallel|^2/2\sigma^2} & 0 < z < w \\ 0 & \text{else} \end{cases}, \tag{4.32}$$

all $n \neq 0$ terms in the temperature expansion have zero contribution to the mode-averaged temperature fluctuation (Eqn. 4.12) of interest, which involves the integral $\int \phi_n(z)dz$. Eqn. 4.31 then simplifies to the two-dimensional form

$$\frac{\partial T(\vec{r}_\parallel, t)}{\partial t} = D_T \nabla^2 T(\vec{r}_\parallel, t) + F_T^\parallel(\vec{r}_\parallel, t), \tag{4.33}$$

where we have dropped the $n = 0$ subscript and introduced a modified fluctuation $F_T^\parallel(\vec{r}_\parallel, t)$ with statistics

$$\begin{aligned}\langle F_T^{\parallel *}(\vec{r}_\parallel, t) F_T^\parallel(\vec{r}^{\,\prime}_\parallel, t')\rangle &= \frac{1}{w^2}\int \mathrm{d}z \int \mathrm{d}z' \phi_0^*(z)\phi_0(z')\langle F_T^*(\vec{r}, t) F_T(\vec{r}^{\,\prime}, t')\rangle \\ &= \frac{1}{w}\frac{2D_T k_B T_0^2}{c_V}\delta(t - t')\vec{\nabla}_{\vec{r}_\parallel} \cdot \vec{\nabla}_{\vec{r}^{\,\prime}_\parallel}\delta(\vec{r}_\parallel - \vec{r}^{\,\prime}_\parallel). \end{aligned} \tag{4.34}$$

Comparing Eqns. 4.33 and 4.34 to their three-dimensional analogs (Eqns. 4.13, 4.14), we see that projecting onto the $n = 0$ subspace reduces the finite-thickness slab to an infinite two-dimensional problem where F_T is scaled by $w^{-1/2}$. We can then apply the techniques of Sec. 4.4.2 (expansion in Fourier normal modes) to solve for the spectrum of temperature (and therefore resonant frequency) fluctuations. Without inverse Fourier transforming frequency, the autocorrelation of Eqn. 4.25 gives

$$\begin{aligned} S_{\omega\omega}^{\mathrm{mm}}(\omega) &= 2\left(\frac{\omega_0}{n}\alpha_{\mathrm{TO}}\right)^2 \frac{k_B T_0^2}{w c_V}\int \frac{D_T k_\parallel^2}{(D_T k_\parallel^2)^2 + \omega^2}|\epsilon E^2(k_\parallel)|^2 \mathrm{d}^2 k_\parallel \\ &= \left(\frac{\omega_0}{n}\alpha_{\mathrm{TO}}\right)^2 \frac{k_B T_0^2}{2\pi w c_v D_T} \underbrace{\int_0^\infty \frac{x}{x^2 + (\omega\sigma^2/D_T)^2} e^{-x}\mathrm{d}x}_{I_{\mathrm{mm}}(\omega\sigma^2/D_T)} \end{aligned} \tag{4.35}$$

with the change of variables $(k_\parallel \sigma)^2 \to x$. Note that we treat the effect of patterned holes in our experimental structures through a reduced thermal conductivity, and therefore thermal diffusivity, as a function of the slab porosity (see Sec. 4.6 for further detail). We can compare this result with the single-mode approximation, which (by evaluating Eqns. 4.21, 4.28 for the Gaussian mode profile in Eqn. 4.32) gives the thermal mode volume $V_T = 4\pi w \sigma^2$, decay rate $\Gamma_T = \frac{D_T}{\sigma^2}$, and noise spectrum

$$S_{\omega\omega}^{\mathrm{sm}}(\omega) = \left(\frac{\omega_0}{n}\alpha_{\mathrm{TO}}\right)^2 \frac{k_B T_0^2}{2\pi w c_v D_T} \underbrace{\frac{1}{1 + (\omega\sigma^2/D_T)^2}}_{I_{\mathrm{sm}}(\omega\sigma^2/D_T)}. \tag{4.36}$$

As expected, the integral $\int_{-\infty}^{\infty} S_{\omega\omega}\mathrm{d}\omega/2\pi$ of either spectra yields

$$\langle \delta\omega^2 \rangle = (\omega_0 \alpha_{\mathrm{TO}}/n)^2 \langle \delta T^2 \rangle = (\omega_0 \alpha_{\mathrm{TO}}/n)^2 k_B T_0^2 / c_V V_T$$

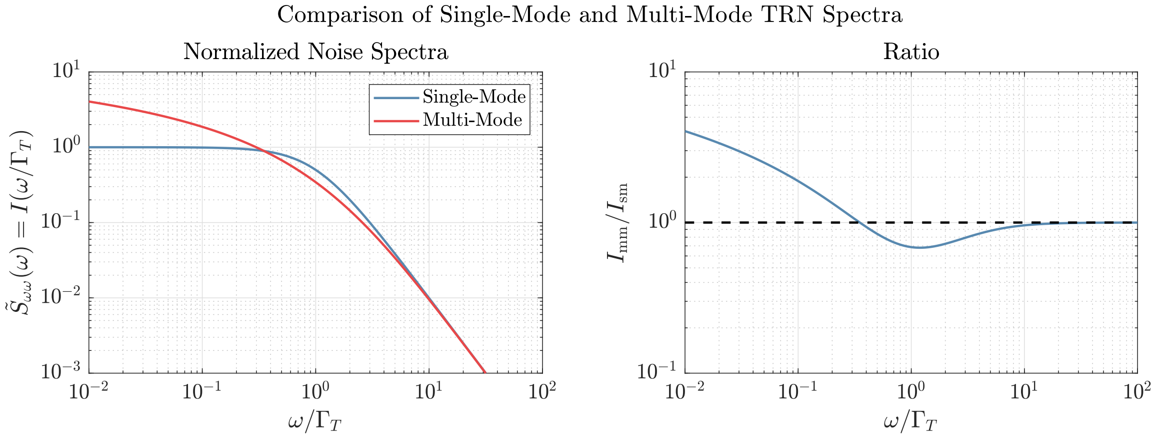

Figure 4-2: Normalized noise spectra $\tilde{S}_{\omega\omega}(\omega) = I(\omega/\Gamma_T)$ for single-mode (Eqn. 4.36) and multimode (Eqn. 4.35) TRN in an infinite slab of finite thickness.

in correspondence with Eqn. 4.8. Fig. 4-2 plots each normalized spectrum for comparison along with the ratio $I_{\mathrm{mm}}/I_{\mathrm{sm}}$. These results show that the single-mode approximation undershoots at low frequency $\omega \ll \Gamma_T$, slightly overshoots at intermediate frequencies $\omega \sim \Gamma_T$, and converges to the multimode spectrum at high frequencies $\omega \gg \Gamma_T$. We further note that the error of the multimode spectrum increases at low frequencies for any finite volume system: in our experiment, for example, the multimode estimate does not account for low frequency heat transfer through the underlying oxide around the released membrane. Thus, in the range of frequencies of interest (i.e. near the thermal cutoff frequency $\Gamma_T = D_T/\sigma^2$), single-mode thermal decay is an appropriate simplifying assumption that allows the thermal noise spectrum to be well-approximated irrespective of the cavity's exact geometry.

4.4.4 Derivation of Driven Cavity Dynamics

To determine the practical impact of thermo-refractive noise on microcavity dynamics, we now consider the case of a cavity driven by a monochromatic laser with frequency ω_L. Intuitively, we would expect that the large (relative to the cavity linewidth), fast (relative to the cavity decay time) stochastic deviations of the resonance frequency in the high-Q/V_{eff} limit would restrict the maximum intensity in the cavity, as a narrow linewidth laser would no longer always be on resonance with the fluctuating cavity resonance. A mode volume-dependent maximum "effective" quality factor describing the stored energy should result. A similar effective quality factor could be derived if the coherence of the intracavity field — rather than the stored energy alone — is also of interest.

To prove these suppositions, we solve the driven temporal coupled mode theory relation

$$\frac{\mathrm{d}a(t)}{\mathrm{d}t} = \left[i\omega_0(t) - \Gamma_l\right]a(t) + \sqrt{2\Gamma_c}s_{\mathrm{in}}(t), \tag{4.37}$$

for the cavity field $a(t)$, where $\omega_0(t) = \omega_0 + \delta\omega(t)$ is the instantaneous resonant frequency, $\Gamma_l = \omega_0/2Q_l$ is the amplitude decay rate of a corresponding to a loaded quality factor Q_l, and Γ_c is the amplitude coupling rate of the drive field $s_{\mathrm{in}}(t) = \tilde{s}_{\mathrm{in}}e^{i\omega_L t} +$ c.c., detuned from resonance by $\Delta = \omega_L - \omega_0$. In the presence of TRN, $\delta\omega(t)$ is non-Markovian, zero-mean Gaussian noise with the autocorrelation given by Eqn. 4.22. Solving with an integrating factor and introducing the slowly varying cavity amplitude $\tilde{a}(t) = a(t)e^{-i\omega_L t}$ in a reference frame co-rotating with the drive frequency ω_L, we find

$$\tilde{a}(t) = \sqrt{2\Gamma_c}\tilde{s}_{\mathrm{in}}\int_{-\infty}^{t}\mathrm{d}t' e^{-(i\Delta+\Gamma_l)(t-t')}e^{i\int_{t'}^{t}\mathrm{d}t''\delta\omega(t'')}. \tag{4.38}$$

Since the steady state solution is desired, we assume that the integration starts at $t = -\infty$ such that the system has no "memory" of the initial conditions. Using Eqn. 4.38, we can compute $\langle\tilde{a}(t)\rangle$ and $\langle|\tilde{a}(t)|^2\rangle$, the mean cavity field amplitude and stored energy, respectively. In certain limiting cases, the noise spectrum $S_{aa}(\omega)$ of the intra-cavity field can also be derived.

Cavity Spectrum in the Perturbative Limit

One of these limiting cases is the perturbative regime commonly studied in the literature for low-Q/V_{eff} cavities, wherein $\delta\omega_{\mathrm{rms}} \ll \Gamma_l$. In this case, $\tilde{a}(t)$ and $\delta\omega(t)$ — described by (c.f. Eqn. 4.15)

$$\frac{\mathrm{d}\,\delta\omega(t)}{\mathrm{d}t} = -\Gamma_T\delta\omega(t) + \delta\omega_{\mathrm{rms}}\sqrt{2\Gamma_T}W(t) \tag{4.39}$$

for a Wiener process $W(t)$ with $\langle W(t)W(t')\rangle = \delta(t-t')$ — can be expanded in orders of $\delta\omega_{\mathrm{rms}}\sqrt{2\Gamma_T}$. The zeroth- and first-order evolution equations (with subscripts 0 and 1, respectively) are

$$\frac{\mathrm{d}\tilde{a}_0(t)}{\mathrm{d}t} = [i(\delta\omega_0(t) - \Delta) - \Gamma_l]\tilde{a}_0(t) + \sqrt{2\Gamma_c}\tilde{s}_{\mathrm{in}} \tag{4.40}$$

$$\frac{\mathrm{d}\tilde{a}_1(t)}{\mathrm{d}t} = [i(\delta\omega_0(t) - \Delta) - \Gamma_l]a_1(t) + i\delta\omega_1(t)\tilde{a}_0(t) \tag{4.41}$$

$$\frac{\mathrm{d}\delta\omega_0(t)}{\mathrm{d}t} = -\Gamma_T\delta\omega_0(t) \tag{4.42}$$

$$\frac{\mathrm{d}\delta\omega_1(t)}{\mathrm{d}t} = -\Gamma_T\delta\omega_1(t) + \delta\omega_{\mathrm{rms}}\sqrt{2\Gamma_T}W(t). \tag{4.43}$$

Solving in the frequency domain yields

$$\tilde{a}_1(\omega) = \frac{\sqrt{2\Gamma_c}\tilde{s}_{\mathrm{in}}}{\Gamma_l + i\Delta}\frac{i\delta\omega_{\mathrm{rms}}\sqrt{2\Gamma_T}W(\omega)}{(\Gamma_T - i\omega)[\Gamma_l + i(\omega+\Delta)]}, \tag{4.44}$$

corresponding to the frequency spectrum

$$S_{aa}(\omega) = \frac{2\Gamma_c|\tilde{s}_{\mathrm{in}}|^2}{\Gamma_l^2 + \Delta^2}\frac{2\Gamma_T\delta\omega_{\mathrm{rms}}^2}{(\Gamma_T^2 + \omega^2)(\Gamma_l^2 + (\omega+\Delta)^2)}. \tag{4.45}$$

The intra-cavity noise spectrum can therefore be approximated as the product of two Lorentzians with spectral widths $2\Gamma_T$ and $2\Gamma_l$. When $\Gamma_T \ll \Gamma_l$, which often coincides with the perturbative limit $\delta\omega_{\mathrm{rms}} \ll \Gamma_l$ for large mode volumes ($\delta\omega_{\mathrm{rms}} \propto V_T^{-1/2}$ and $\Gamma_T \propto V_T^{-2/3}$ for a three-dimensional Gaussian mode), the resonant frequency fluctuations are small and occur over timescales much longer than that of intra-cavity photon decay. TRN thus leads to a weak inhomogeneous broadening of the resonant mode that can often be neglected for common applications of low-Q/V_{eff} optical cavities. Gravitational wave interferometry [140, 197] and ultra-stable optical frequency references [198, 199] are two notable exceptions that have led to significant interest in perturbative TRN.

General Derivation for $\langle\tilde{a}(t)\rangle$

Our work focuses on the transition to non-perturbative TRN in high-Q/V_{eff} microcavities, where we are interested in general solutions for the statistical moments of Eqn. 4.38 in the presence of TRN. Specifically, $\langle\tilde{a}(t)\rangle$ provides insight into thermal noise-induced dephasing while $\langle\tilde{a}^2(t)\rangle$ lends a bound on the maximum allowable energy storage.

The expected intra-cavity field amplitude

$$\langle\tilde{a}(t)\rangle = \sqrt{2\Gamma_c}\tilde{s}_{\mathrm{in}}\int_{-\infty}^{t}\mathrm{d}t' e^{-(i\Delta+\Gamma_l)(t-t')}\langle e^{\int_{t'}^{t}\mathrm{d}t'' i\delta\omega(t'')}\rangle \tag{4.46}$$

follows directly from Eqn. 4.38, where the average on the right-hand side has a similar form to the characteristic functional [189]

$$\Phi[k(t)] = \langle e^{i\int k(t)f(t)\mathrm{d}t}\rangle = \frac{\int e^{i\int k(t)f(t)\mathrm{d}t}P[f(t)]\mathcal{D}f(t)}{\int P[f(t)]\mathcal{D}f(t)}, \tag{4.47}$$

a normalized average of $e^{i\int k(t)f(t)\mathrm{d}t}$ along the paths $f(t)$ with respective probabilities $P[f(t)]$. For the special case of Gaussian noise, the moment-generating properties of the characteristic functional allow Eqn. 4.47 to be simplified to

$$\Phi[k(t)] = e^{i\int k(t)M(t)\mathrm{d}t}e^{-1/2\int\mathrm{d}t\int\mathrm{d}t' k(t)k(t')\langle f(t)f(t')\rangle}, \tag{4.48}$$

which is characterized by two parameters only: 1) the mean path $M(t)$, and the autocorrelation of the noise $f(t)$, $\langle f(t)f(t+t')\rangle$. Comparing Eqn. 4.46 to Eqn. 4.47, we find $k(t'') = \begin{cases} 1 & t' < t'' < t \\ 0 & \text{else} \end{cases}$ and $f(t) = \delta\omega(t'')$. Since $\langle \omega_0(t)\rangle = 0$,

$$\begin{aligned} \Phi &= \exp\left[-\frac{1}{2}\int_{t'}^{t} \mathrm{d}t_2' \int_{t'}^{t} \mathrm{d}t_2'' \delta\omega_{\mathrm{rms}}^2 e^{-\Gamma_T|t_2''-t_2'|}\right] \\ &= \exp\left[\frac{\delta\omega_{\mathrm{rms}}^2}{\Gamma_T^2}\left(1 - \Gamma_T(t-t') - e^{-\Gamma_T(t-t')}\right)\right]. \end{aligned} \tag{4.49}$$

The above form, combined with the change of variable $\tilde{\tau} = (\delta\omega_{\mathrm{rms}}/\Gamma_T)^2 e^{-\Gamma_T(t-t')}$, simplifies to

$$\langle \tilde{a}(t)\rangle = \frac{\sqrt{2\Gamma_c}\tilde{s}_{\mathrm{in}}}{\Gamma_T} e^{(\delta\omega_{\mathrm{rms}}/\Gamma_T)^2} \left(\frac{\delta\omega_{\mathrm{rms}}}{\Gamma_T}\right)^{2\left[\frac{-i\Delta-\Gamma_l-\frac{\delta\omega_{\mathrm{rms}}^2}{\Gamma_T}}{\Gamma_T}\right]} \int_0^{(\delta\omega_{\mathrm{rms}}/\Gamma_T)^2} \tilde{\tau}^{\frac{i\Delta+\Gamma_l+\frac{\delta\omega_{\mathrm{rms}}^2}{\Gamma_T}}{\Gamma_T}-1} e^{-\tilde{\tau}} \mathrm{d}\tilde{\tau}, \tag{4.50}$$

which is in the form of the lower incomplete Gamma function

$$\gamma_l(s,x) = \int_0^x \tilde{\tau}^{s-1} e^{-\tilde{\tau}} \mathrm{d}\tilde{\tau}. \tag{4.51}$$

The final closed-form solution is therefore

$$\langle \tilde{a}(t)\rangle = \frac{\sqrt{2\Gamma_c}\tilde{s}_{\mathrm{in}}}{\Gamma_T} e^{x} x^{-s} \gamma_l(s,x) \tag{4.52}$$

$$x \equiv \left(\frac{\delta\omega_{\mathrm{rms}}}{\Gamma_T}\right)^2 \tag{4.53}$$

$$s \equiv \frac{\Gamma_l + i\Delta}{\Gamma_T} + x. \tag{4.54}$$

To confirm this solution, we can evaluate the limiting case of $\delta\omega_{\mathrm{rms}} \to 0$ ($x \to 0$), corresponding to a noiseless thermal reservoir when $T \to 0$. Using the series expansion of $\gamma_l(s,x)$ in terms of s, x and the complete Gamma function $\gamma_f(z)$, we find

$$\langle \tilde{a}(t)\rangle_{T=0} = \frac{\sqrt{2\Gamma_c}\tilde{s}_{\mathrm{in}}}{\Gamma_T}\frac{\gamma_f(s)}{\gamma_f(s+1)} = \frac{\sqrt{2\Gamma_c}\tilde{s}_{\mathrm{in}}}{\Gamma_T}\left.\frac{1}{s}\right|_{x=0} = \frac{\sqrt{2\Gamma_c}\tilde{s}_{\mathrm{in}}}{\Gamma_l + i\Delta} \tag{4.55}$$

as expected from noiseless temporal coupled mode theory. Assuming critical coupling ($\Gamma_c = \Gamma_l/2$) and resonant excitation ($\Delta = 0$), we find the "effective" quality factor

$$Q_{\mathrm{eff}} = \frac{\omega_0|\langle \tilde{a}(t)\rangle|^2}{2|\tilde{s}_{\mathrm{in}}|^2} = Q_l\left(\frac{\Gamma_l}{\Gamma_T}\right)^2 e^{2x} x^{-2s} \gamma_l^2(s,x) \tag{4.56}$$

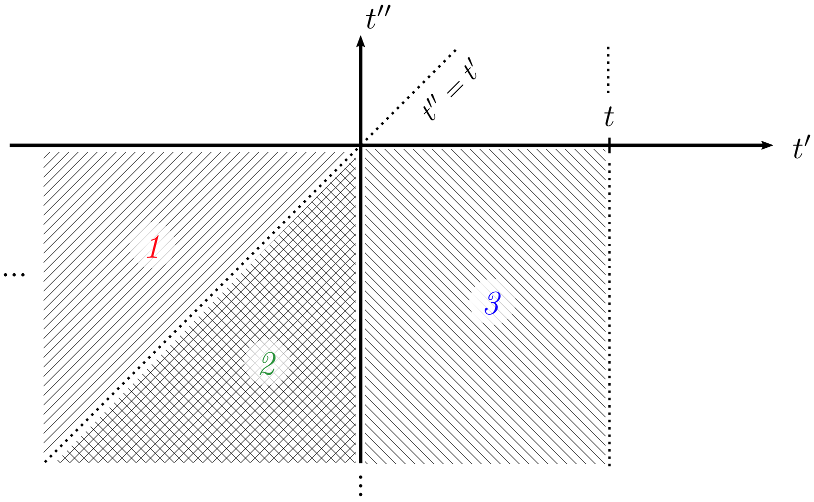

Figure 4-3: The complete region of integration can be divided into three sub-spaces which yield different conditions for $k(t)$.

by analogy to the noiseless result where $Q = \omega_0 |\langle \tilde{a}(t)\rangle|^2_{T=0}/2|\tilde{s}_{\mathrm{in}}|^2$.

We will use this result in Sec. 4.8 to describe dephasing in the qubit limit of cavity nonlinear optics. For a given mode volume, the optimum loaded quality factor $Q_l^{\mathrm{opt}} \approx \omega_0 \Gamma_T / 2\delta\omega_{\mathrm{rms}}^2$ (assuming $\delta\omega_{\mathrm{rms}} \ll \Gamma_T$, which is valid for the range of mode volumes plotted in Fig. 4-10) maximizes the resonant cavity amplitude: lower quality factors incur excess loss, whereas higher quality factors allow the qubit to "explore" a larger region of the phase space, thereby reducing the integrated cavity amplitude. Intuitively, the resulting maximum amplitude $|\langle \tilde{a}(t)\rangle|$ increases with increasing mode volume due to the reduced magnitude of temperature fluctuations.

General Derivation for $\langle \tilde{a}^2(t)\rangle$

Solving for $\langle \tilde{a}(t)^2\rangle$ generally follows the same procedure, and reveals a limit on the allowable intra-cavity optical energy in the presence of TRN. Starting from Eqn. 4.38, the amplitude correlation takes the form

$$\langle \tilde{a}(t)\tilde{a}^*(0)\rangle = 2\Gamma_c |\tilde{s}_{\mathrm{in}}|^2 \int_{-\infty}^{t} \mathrm{d}t' e^{-(i\Delta+\Gamma_l)(t-t')} \int_{-\infty}^{0} \mathrm{d}t'' e^{-(i\Delta-\Gamma_l)t''} \langle e^{\int_{t'}^{t} i\delta\omega(t_2)\mathrm{d}t_2 - \int_{t''}^{0} i\delta\omega(t_2)\mathrm{d}t_2}\rangle. \tag{4.57}$$

Following the method of [188], the average can be expressed in the form of Eqn. 4.47,

$$\langle e^{\int_{t'}^{t} i\delta\omega(t_2)\mathrm{d}t_2 - \int_{t''}^{0} i\delta\omega(t_2)\mathrm{d}t_2}\rangle = \langle e^{i\int_{-\infty}^{\infty} k(t_2)\delta\omega(t_2)\mathrm{d}t_2}\rangle, \tag{4.58}$$

by appropriately defining $k(t)$. As illustrated in Fig. 4-3, the dependence of $k(t_2)$ upon t', t'', and t differs in three sectors of the region of integration. Simple diagrams in each of the three scenarios can be used to find a closed form for $k(t)$:

$$k(t_2) = \begin{cases} \text{sign}(t'' - t'), & \begin{array}{l} t' < 0 \text{ and} \\ \min(t', t'') \leq t_2 \leq \max(t', t'') \end{array} \\ 1, & \begin{array}{l} (t' < 0 \text{ and } 0 \leq t_2 \leq t) \text{ or} \\ (t' > 0 \text{ and } t' \leq t_2 \leq t) \end{array} \\ -1, & t' > 0 \ \& \ t'' \leq t_2 \leq 0 \\ 0, & \text{else.} \end{cases} \tag{4.59}$$

This definition allows us to rewrite the autocorrelation as

$$\begin{aligned} \mathcal{R}_{aa}(t) = \langle \tilde{a}(t)\tilde{a}^*(0)\rangle^* = 2\Gamma_c|\tilde{s}_{\text{in}}|^2 \int_{-\infty}^{t} \mathrm{d}t' e^{(i\Delta-\Gamma_l)(t-t')} \int_{-\infty}^{0} \mathrm{d}t'' e^{(i\Delta+\Gamma_l)t''} \\ \times \exp\left[-\frac{1}{2}\int_{-\infty}^{\infty} \mathrm{d}t_2' \int_{-\infty}^{\infty} \mathrm{d}t_2'' k(t_2')k(t_2'')\delta\omega_{\text{rms}}^2 e^{-\Gamma_T|t_2'-t_2''|}\right]. \end{aligned} \tag{4.60}$$

While a general solution to the full autocorrelation in Eqn. 4.60 appears intractable, we can find $\langle|\tilde{a}|^2\rangle = \langle|\tilde{a}(0)|^2\rangle$ by evaluating Eqn. 4.60 at $t = 0$ (thereby eliminating integration region #3 in Fig. 4-3), which yields

$$\begin{aligned} \langle|\tilde{a}|^2\rangle =& 2\Gamma_c|\tilde{s}_{\text{in}}|^2 \int_{-\infty}^{0} \mathrm{d}t' e^{(i\Delta+\Gamma_l)t'} \int_{-\infty}^{0} \mathrm{d}t'' e^{(-i\Delta+\Gamma_l)t''} \\ & \times \exp\left[\left(\frac{\delta\omega_{\text{rms}}}{\Gamma_T}\right)^2 \left(1 - \Gamma_T|t''-t'| - e^{-\Gamma_T|t''-t'|}\right)\right]. \end{aligned} \tag{4.61}$$

Note that the integral in Region 1 or Region 2 is nearly the same – exchanging t' and t'' in either region returns the integral for the other region, but conjugates $i\Delta$. Therefore, we focus on evaluating Eqn. 4.61 in Region 1 ($t'' > t'$), and then generalize this result to the other region by taking the complex conjugate. In Region 1, the substitution $\tilde{\tau} = (\delta\omega_{\text{rms}}/\Gamma_T)^2 \exp\left[-\Gamma_T(t''-t')\right]$ gives

$$\begin{aligned} \langle|\tilde{a}(0)|^2\rangle_1 &= 2\Gamma_c|\tilde{s}_{\text{in}}|^2 \int_{-\infty}^{0} \mathrm{d}t' e^{2\Gamma_l t'} \frac{e^x}{\Gamma_T} x^{-s'} \int_{xe^{\Gamma_T t'}}^{x} \tilde{\tau}^{s'-1} e^{-\tilde{\tau}} d\tilde{\tau} \\ &= 2\Gamma_c|\tilde{s}_{\text{in}}|^2 \frac{e^x}{\Gamma_T} x^{-s'} \int_{-\infty}^{0} \mathrm{d}t' e^{2\Gamma_l t'} \left[\gamma_l(s', x) - \gamma_l(s', xe^{\Gamma_T t'})\right] \end{aligned} \tag{4.62}$$

where $x = (\delta\omega_{\text{rms}}/\Gamma_T)^2$ and $s' = (\delta\omega_{\text{rms}}^2/\Gamma_T - \Gamma_l + i\Delta)/\Gamma_T$. The first term can be directly evaluated, while the second can be simplified with integration by parts using the relationship

$$\frac{\partial\gamma_l(s', x)}{\partial x} = x^{s'-1}e^{-x}. \tag{4.63}$$

With a second substitution $\tilde{\tau}_2 = xe^{\Gamma_T t'}$ we find

$$\begin{aligned}
\langle|\tilde{a}(0)|^2\rangle_1 &= 2\Gamma_c|\tilde{s}_{\text{in}}|^2\frac{e^x}{\Gamma_T}x^{-s'}\left[\frac{\gamma_l(s',x)}{2\Gamma_l} - \frac{x^{-\frac{2\Gamma_l}{\Gamma_T}}}{\Gamma_T}\int_0^x \tilde{\tau}_2^{\frac{2\Gamma_l}{\Gamma_T}-1}\gamma_l(s',\tilde{\tau}_2)\mathrm{d}\tilde{\tau}_2\right] \\
&= 2\Gamma_c|\tilde{s}_{\text{in}}|^2\frac{e^x}{\Gamma_T}x^{-s'}\left\{\frac{\gamma_l(s',x)}{2\Gamma_l} - \frac{x^{-\frac{2\Gamma_l}{\Gamma_T}}}{\Gamma_T}\left(\frac{\Gamma_T}{2\Gamma_l}\right)\right. \\
&\quad \left.\times\left[\tilde{\tau}_2^{\frac{2\Gamma_l}{\Gamma_T}}\gamma_l(s',\tilde{\tau}_2) + \gamma_u(s'+\frac{2\Gamma_l}{\Gamma_T},\tilde{\tau}_2)\right]_{\tilde{\tau}_2=0}^{\tilde{\tau}_2=x}\right\} \qquad (4.64)
\end{aligned}$$

where $\gamma_u(s',x)$ is the upper incomplete Gamma function defined by

$$\gamma_u(s',x) = \int_x^\infty \tau^{s'-1}e^{-\tau}d\tau. \qquad (4.65)$$

Evaluating the final terms, the result simplifies nicely to

$$\langle|\tilde{a}(0)|^2\rangle_1 = \frac{|\tilde{s}_{\text{in}}|^2}{\Gamma_T}\left(\frac{\Gamma_c}{\Gamma_l}\right)e^x x^{-(s'+\frac{2\Gamma_l}{\Gamma_T})}\gamma_l(s'+\frac{2\Gamma_l}{\Gamma_T},x). \qquad (4.66)$$

To find the complete result, we simply add the second term in Eqn. 4.61 to find

$$\begin{aligned}
\langle|\tilde{a}|^2\rangle &= \frac{|\tilde{s}_{\text{in}}|^2}{\Gamma_T}\left(\frac{\Gamma_c}{\Gamma_l}\right)e^x\left[x^{-s}\gamma_l(s,x) + x^{-s^*}\gamma_l(s^*,x)\right] && (4.67) \\
x &\equiv \left(\frac{\delta\omega_{\text{rms}}}{\Gamma_T}\right)^2 && (4.68) \\
s &\equiv \frac{\Gamma_l + i\Delta}{\Gamma_T} + x. && (4.69)
\end{aligned}$$

Note the similarity to Eqns. 4.52-4.54. Once again, we must ensure that our solution corresponds to the noiseless result expected when $\delta\omega_{\text{rms}} \to 0$. Using the series expansion of $\gamma_l(s,x)$, we find

$$\begin{aligned}
\langle|\tilde{a}|^2\rangle_{T=0} &= \frac{|\tilde{s}_{\text{in}}|^2}{\Gamma_T}\left(\frac{\Gamma_c}{\Gamma_l}\right)\left[\frac{\gamma_f(s|_{x=0})}{\gamma_f(s|_{x=0}+1)} + \frac{\gamma_f(s^*|_{x=0})}{\gamma_f(s^*|_{x=0}+1)}\right] \\
&= \frac{|\tilde{s}_{\text{in}}|^2}{\Gamma_T}\left(\frac{\Gamma_c}{\Gamma_l}\right)\left[\frac{\Gamma_T}{\Gamma_l+i\Delta} + \frac{\Gamma_T}{\Gamma_l-i\Delta}\right] \\
\langle|\tilde{a}|^2\rangle_{T=0} &= \frac{2\Gamma_c|\tilde{s}_{\text{in}}|^2}{\Delta^2+\Gamma_l^2} \qquad (4.70)
\end{aligned}$$

as expected. Similar to the solution for $\langle\tilde{a}(t)\rangle$, we define the effective quality factor

$$Q_{\text{eff}} = \frac{\omega_0\langle|\tilde{a}|^2\rangle}{2|\tilde{s}_{\text{in}}|^2} = \frac{\omega_0}{2\Gamma_T}e^x x^{-s}\gamma_l(s,x) \tag{4.71}$$

for resonant excitation ($\Delta = 0$) and critical coupling ($\Gamma_c = \Gamma_l/2$).

As opposed to the non-monotonic scaling of the mean field amplitude $|\langle\tilde{a}(t)\rangle|$ with Q_l, the stored energy $\langle|\tilde{a}(t)|^2\rangle$ increases monotonically with increasing Q_l. This is intuitively described in Sec. 4.7: continuing to increase Q_l decreases the cavity linewidth until Q_{eff} is saturated by mode volume-dependent thermal noise in the high-Q_l/V_{eff} regime. Finally, we note that the maximum energy storage (although not necessarily the maximum intensity, which also depends on the mode volume) is a achieved with large mode volumes due to reduced thermo-optic noise.

Cavity Spectrum in the White Noise Limit

The complete field autocorrelation in Eqn. 4.60 simplifies considerably in the high-Q_l limit where $\Gamma_T \gg \Gamma_l$, as the cavity resonant frequency $\omega_0(t)$ can be assumed to directly track the temperature noise over the relevant timescales. The frequency noise is then effectively delta-correlated in time, and the aforementioned — albeit tedious — "integration by regions" technique can then be similarly applied to solve for the field noise spectrum $S_{aa}(\omega)$. A more intuitive approach to this solution is though adiabatic elimination of $\omega_0(t)$'s dynamics following the procedure in [200]. Converting the optical field and resonant frequency evolution equations (Eqns. 4.37, 4.39) into stochastic differential equations yields

$$\mathrm{d}\tilde{a}(t) = \left\{\left[i(\delta\omega(t) - \Delta) - \Gamma_l\right]\tilde{a}(t) + \sqrt{2\Gamma_c}\tilde{s}_{\text{in}}\right\}\mathrm{d}t \tag{4.72}$$

$$\mathrm{d}\delta\omega(t) = -\Gamma_T\delta\omega(t)\mathrm{d}t + \delta\omega_{\text{rms}}\sqrt{2\Gamma_T}\mathrm{d}W(t) \tag{4.73}$$

for both Itô and Stratonovich forms since the frequency noise is additive ($\delta\omega_{\text{rms}}\sqrt{2\Gamma_T}$ is constant). In the limit $\Gamma_T \to \infty$, we can adiabatically eliminate the resonant frequency dynamics, yielding a steady state value $\delta\omega(t) = \sqrt{2/\Gamma_T}\delta\omega_{\text{rms}}\mathrm{d}W(t)/\mathrm{d}t$. The cavity evolution can then be simplified to

$$\mathrm{d}\tilde{a}_S(t) = \left[(-i\Delta - \Gamma_l)\tilde{a}_S(t) + \sqrt{2\Gamma_c}\tilde{s}_{\text{in}}\right]\mathrm{d}t + \sqrt{\frac{2}{\Gamma_T}}\delta\omega_{\text{rms}}\tilde{a}_S(t)\mathrm{d}W(t) \tag{4.74}$$

$$\mathrm{d}\tilde{a}_I(t) = \left\{\left[-i\Delta - \left(\Gamma_l + \frac{\delta\omega_{\text{rms}}^2}{\Gamma_T}\right)\right]\tilde{a}_I(t) + \sqrt{2\Gamma_c}\tilde{s}_{\text{in}}\right\}\mathrm{d}t + \sqrt{\frac{2}{\Gamma_T}}\delta\omega_{\text{rms}}\tilde{a}_I(t)\mathrm{d}W(t) \tag{4.75}$$

in Stratonovich and Itô forms, respectively. Applying the Itô rule $(\mathrm{d}W(t))^2 = \mathrm{d}t$ to the latter, we can solve for the steady-state moments

$$\langle \tilde{a}(t) \rangle = \frac{\sqrt{2\Gamma_c}\tilde{s}_{\mathrm{in}}}{[\Gamma_l + \delta\omega_{\mathrm{rms}}^2/\Gamma_T] + i\Delta} \tag{4.76}$$

$$\langle |\tilde{a}(t)|^2 \rangle = \frac{2\Gamma_c \left(1 + \delta\omega_{\mathrm{rms}}^2/\Gamma_T\Gamma_l\right) |\tilde{s}_{\mathrm{in}}|^2}{\left[\Gamma_l + \delta\omega_{\mathrm{rms}}^2/\Gamma_T\right]^2 + \Delta^2} \tag{4.77}$$

which by comparison to Eqn. 4.55 and Eqn. 4.70 immediately reveals a thermal broadening $2\Gamma_l \to 2\Gamma_l + 2\delta\omega_{\mathrm{rms}}^2/\Gamma_T$ of the microcavity linewidth. We can also derive an equation of motion for the autocorrelation $R_{aa}(\tau) = \langle \tilde{a}(t)\tilde{a}^*(t+\tau) \rangle$,

$$\frac{\mathrm{d}}{\mathrm{d}\tau} R_{aa}(\tau) = \left[i\Delta - \left(\Gamma_l + \frac{\delta\omega_{\mathrm{rms}}^2}{\Gamma_T} \right) \right] R_{aa}(\tau) + \sqrt{2\Gamma_c}\tilde{s}_{\mathrm{in}} \langle \tilde{a}(t) \rangle. \tag{4.78}$$

Solving Eqn. 4.78 subject to the $\tau = 0$ conditions of Eqn. 4.77, we find

$$R_{aa}(\tau) = \frac{2\Gamma_c |s_{\mathrm{in}}|^2}{\left[\Gamma_l + \delta\omega_{\mathrm{rms}}^2/\Gamma_T\right]^2 + \Delta^2} \left[\frac{\delta\omega_{\mathrm{rms}}^2}{\Gamma_T \Gamma_l} e^{\left(i\Delta - \Gamma_l - \delta\omega_{\mathrm{rms}}^2/\Gamma_T\right)\tau} + 1 \right], \tag{4.79}$$

corresponding to the optical noise spectrum

$$S_{aa}(\omega) = \frac{\Gamma_c}{\Gamma_l} \frac{2\delta\omega_{\mathrm{rms}}^2 |s_{\mathrm{in}}|^2/\Gamma_T}{\left[\Gamma_l + \delta\omega_{\mathrm{rms}}^2/\Gamma_T\right]^2 + \Delta^2} \frac{2(\Gamma_l + \delta\omega_{\mathrm{rms}}^2/\Gamma_T)}{(\Gamma_l + \delta\omega_{\mathrm{rms}}^2/\Gamma_T)^2 + (\omega + \Delta)^2}. \tag{4.80}$$

Eqn. 4.80 evaluated in the perturbative limit $\delta\omega_{\mathrm{rms}} \ll \Gamma_l$ coincides with the low-frequency ($\omega \ll \Gamma_T$) limit of the previous perturbative spectrum (Eqn. 4.45).

4.5 Experimental TRN in PhC Cavities

Combined, these general solutions characterize the evolution of a microcavity field in the presence of TRN. We will use them shortly (in Secs. 4.7 and 4.8) to evaluate the coherence and energy storage limits of high-Q/V cavities. Before pursuing these goals, we first measured the noise spectrum of high-Q/V PhC cavities to experimentally verify the fundamental assumptions of our TRN model. The single-mode thermal decay approximation made in Eqn. 4.15 implies the decay rate of Eqn. 4.21 and the spectral density of cavity resonant frequency in Eqn. 4.30. This result is commonly used as a simplifying assumption for temperature fluctuations [167, 190]; however, it is not immediately clear that the single-mode approximation holds in the case of small mode volume optical microcavities, where the characteristic length scales of the near diffraction-limited optical mode ($\sim\lambda/n$) can approach that of the phonon mean free path [201]. In absence of any experimental data in the literature to verify the assumption, we constructed an experiment to measure thermo-refractive noise in high-

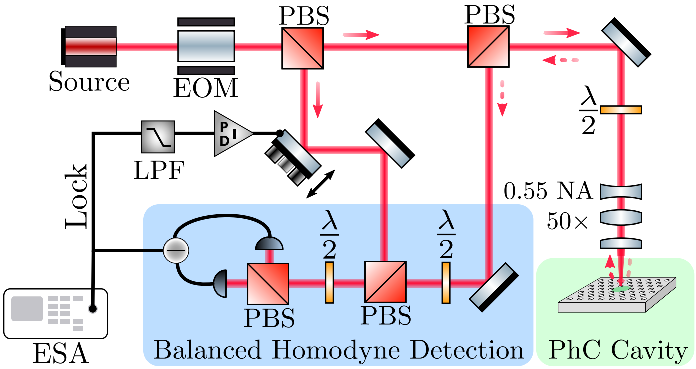

Figure 4-4: Simplified setup schematic for TRN measurements. A shot noise-limited, balanced homodyne detector (a) is locked to the phase quadrature of the cavity reflection signal and records the spectrum of resonant frequency fluctuations.

Q_l/V_{eff} silicon photonic crystal cavities. The experiment also allows us to compare measured TRN with the spectra derived from our multimode theory (Sec. 4.4.3).

As shown in Fig. 4-4, our setup uses a Mach-Zehnder interferometer to measure the phase of a cavity reflection signal via balanced homodyne detection. A variable beamsplitter separates the emission from an amplified tunable infrared laser into local oscillator (LO) and cavity input paths, which are passively balanced to minimize laser frequency noise coupling. A $\lambda/2$-plate rotates the input signal polarization by 45° relative to the dominant cavity polarization axis such that the cavity reflection can be isolated from any specular reflection from the sample using a polarizing beamsplitter (PBS) [202]. The sample stage is temperature controlled to better than 10 mK using a Peltier plate and feedback temperature controller. A balanced, shot noise-limited photodetector measures the homodyne signal from the recombined cavity reflection and LO, and the result is recorded on an electronic spectrum analyzer (ESA). By actively locking to the phase quadrature of the homodyne signal with a piezo-controlled mirror, TRN-induced cavity frequency noise is detected as frequency-resolved voltage noise. To calibrate the spectrum, we inject a known phase noise with an electro-optic modulator (EOM) whose modulation efficiency is measured by sideband fitting [203]. Before discussing the results in Sec. 4.6, I will first describe calibration procedures, review the complete experiment layout, and analyze other possible noise sources in Sec. 4.5.

4.5.1 Complete Experimental Setup

A more detailed version of the experimental setup is provided in Fig. 4-5. The setup consists of a typical polarized light microscope, where the signal reflected from a PhC cavity is measured with balanced homodyne detection.

The homodyne detector is balanced by zeroing the DC component of the ho-

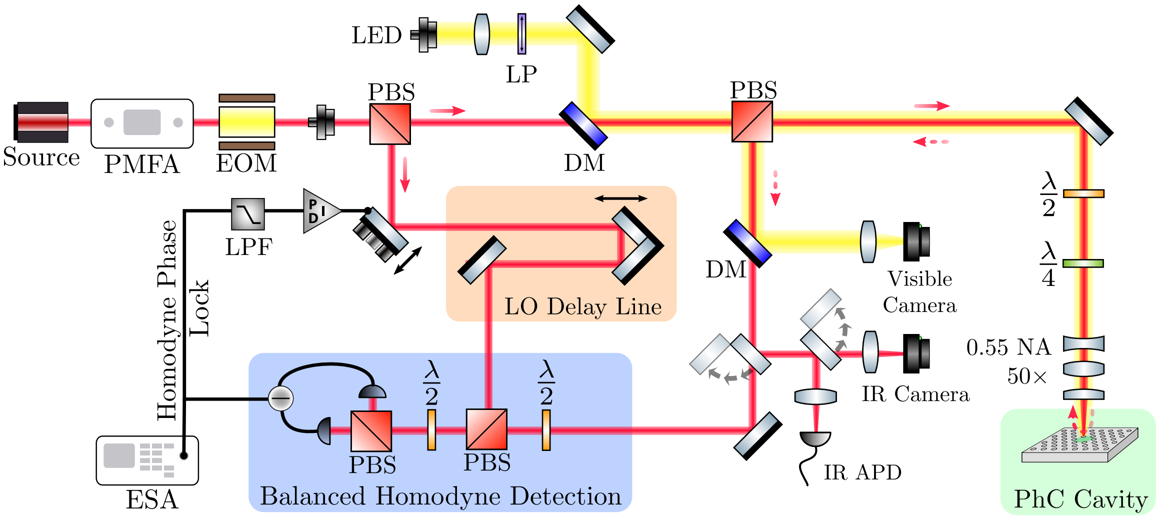

Figure 4-5: Schematic of the setup built to measure TRN in photonic crystal cavities. An amplified (PriTel PMFA) continuous wave laser (Santec TSL-710) is separated into a local oscillator and cavity signal by a polarizing beamsplitter (PBS). The LO line is passively path-length matched to the cavity signal using a tunable retroreflector delay line. The cavity signal is combined with a linearly polarized (LP) white light source (LED) using a dichroic mirror (DM) and is reflected from a PhC cavity rotated 45° from the incident polarization (adjustable with a half-wave plate, $\lambda/2$), which allows the cavity signal to be isolated from the specular reflection using a PBS. A quarter-wave plate ($\lambda/4$) allows the specular reflection to be extracted for comparison to the cavity-only reflection. The reflected illumination light is separated and imaged onto a silicon CCD. The cavity signal can be directed with flip-mirrors towards an IR camera for imaging, an IR avalanche photodetector (ThorLabs PDB410C 10 MHz InGaAs APD) to collect low-noise reflection spectra, or towards the balanced homodyne detector. For the latter, a balanced photodetector (ThorLabs PDB480C-AC 1.6 GHz InGaAs p-i-n Photodetector) measures the homodyne signal from the recombined cavity reflection and local oscillator, and the result is recorded on an electronic spectrum analyzer (ESA; Agilent N9010A EXA Signal Analyzer). The DC signal extracted from a low-pass filter (LPF) is used as the feedback signal for a digital PID controller which stabilizes the signal-LO phase difference by actuating a piezo-actuated mirror. An electro-optic modulator (EOM) provides a known phase noise which can be used to calibrate the frequency noise of the PhC cavity. The sample stage is temperature-stabilized to $\Delta T < 0.01$ K using a peltier plate and a feedback temperature controller.

modyne signal with a digital PID feedback controller connected to a piezo-actuated mirror. In this configuration, the homodyne voltage signal

$$v_h \sim |\tilde{a}_{\mathrm{LO}}||\tilde{a}_{\mathrm{cavity}}|\delta\phi_{\mathrm{cavity}}(t) \tag{4.81}$$

for a local oscillator signal $\tilde{a}_{\mathrm{LO}}$ is directly proportional to the cavity amplitude $|\tilde{a}_{\mathrm{cavity}}|$ and to phase fluctuations $\delta\phi_{\mathrm{cavity}}(t)$ resulting from the stochastic resonant frequency. An electronic spectrum analyzer is used to measure the power spectral density S_{vv} of this homodyne voltage signal.

4.5.2 Phase Noise Calibration

The resonant frequency noise spectral density $S_{\omega\omega}$ can then be determined from S_{vv} using the absolute calibration technique discussed in Refs. [203, 204]. For example, consider a Mach-Zehnder interferometer with input power P_{in} and splitting ratio η_h, which creates the in-phase local oscillator and cavity input signals

$$\tilde{a}_{\mathrm{LO}} = \sqrt{\eta_H P_{\mathrm{in}}} \qquad\qquad \tilde{a}_{\mathrm{in}} = \sqrt{(1-\eta_H)P_{\mathrm{in}}}. \tag{4.82}$$

Assuming resonant drive ($\Delta = \omega_L - \omega_0 = 0$) for a cavity with input/output power coupling rate Γ_c, total loss rate Γ_l, and a perturbative resonant frequency noise $\delta\omega(t)$, the output cavity signal is then

$$\tilde{a}_{\mathrm{out}} = \sqrt{(1-\eta_H)P_{\mathrm{in}}}\frac{2\Gamma_c - \Gamma_l}{\Gamma_l + i\delta\omega(t)}, \tag{4.83}$$

yielding a homodyne detection voltage

$$\begin{aligned} v_h(t) &\approx 2G_c|\tilde{a}_{\mathrm{LO}}||\tilde{a}_{\mathrm{out}}|\delta\phi_{\mathrm{cavity}}(t) \\ &\approx -2G_c\sqrt{\eta_H(1-\eta_H)}P_{\mathrm{in}}\frac{2\Gamma_c-\Gamma_l}{\Gamma_l^2}\delta\omega(t) \end{aligned} \tag{4.84}$$

for a detector conversion gain G_c. The final frequency noise spectral density

$$S_{vv}^{\delta\omega} \approx \underbrace{4G_c^2\eta_H(1-\eta_H)\left(\frac{2\Gamma_c-\Gamma_l}{\Gamma_l^2}\right)^2 P_{\mathrm{in}}^2}_{K_{\mathrm{expt}}} S_{\omega\omega} = K_{\mathrm{expt}}S_{\omega\omega} \tag{4.85}$$

is therefore a function of various experimental constants and cavity coupling parameters.

However, the value of K_{expt} can be exactly determined by injecting a known phase noise $\delta\phi(t) = \phi_m(V_p)\cos(\omega_m t)$ into the interferometer with an electro-optic modulator driven with an electrical tone with frequency ω_m and peak voltage V_p. Under the same experimental conditions, the local oscillator and cavity input signals are

$$\tilde{a}_{\mathrm{LO}} = \sqrt{\eta_H P_{\mathrm{in}}} e^{i\phi_m(V_p)\cos(\omega_m t)} \tag{4.86}$$

$$\tilde{a}_{\mathrm{in}} = \sqrt{(1-\eta_H) P_{\mathrm{in}}} e^{i\phi_m(V_p)\cos(\omega_m t)}. \tag{4.87}$$

With a small enough modulation depth $\phi_m(V_p) = \pi V_p / V_\pi$ (and therefore a small enough drive voltage V_p relative to the half-wave voltage V_π), the local oscillator can be approximated to first order as

$$\tilde{a}_{\mathrm{LO}} \approx \sqrt{\eta_H P_{\mathrm{in}}} \left(1 + i\phi_m(V_p)\cos(\omega_m t)\right). \tag{4.88}$$

Similarly, assuming $\omega_m \ll \Gamma_l$ (as is the case in our experiment), the cavity response yields the output signal

$$\tilde{a}_{\mathrm{out}} \approx \sqrt{(1-\eta_H) P_{\mathrm{in}}} \frac{2\Gamma_c - \Gamma_l}{\Gamma_l} \left[1 + i\phi_m(V_p) \left(\cos(\omega_m t) + \frac{\omega_m}{\Gamma_l} \sin(\omega_m t) \right) \right]. \tag{4.89}$$

The homodyne signal

$$v_h(t) \approx 2G_c \sqrt{\eta_H (1-\eta_H)} P_{\mathrm{in}} \frac{2\Gamma_c - \Gamma_l}{\Gamma_l^2} \omega_m \phi_m(V) \sin(\omega_m t) \tag{4.90}$$

corresponds to a power spectral density

$$S_{vv}^{\delta\phi_m} \approx \underbrace{4G_c^2 \eta_H (1-\eta_H) \left(\frac{2\Gamma_c - \Gamma_l}{\Gamma_l^2} \right)^2 P_{\mathrm{in}}^2}_{K_{\mathrm{expt}}} \omega_m^2 S_{\phi\phi}\big|_{\omega=\omega_m}, \tag{4.91}$$

which, similar to $S_{vv}^{\delta\omega}$, is directly proportional to K_{expt}. K_{expt} can therefore be eliminated to yield an absolute calibration for the resonant frequency noise spectral density:

$$S_{\omega\omega} \approx \frac{S_{vv}^{\delta\omega}}{K_{\mathrm{expt}}} \approx \frac{\omega_m^2 S_{\phi\phi}\big|_{\omega=\omega_m}}{S_{vv}^{\delta\phi_m}\big|_{\omega=\omega_m}} S_{vv}^{\delta\omega}. \tag{4.92}$$

This result can be simplified by evaluating the phase spectral density

$$\begin{aligned} S_{\phi\phi}(\omega) &= \int_{-\infty}^{\infty} \phi_m^2(V_p) \langle \cos(\omega_m t)\cos(\omega_m(t+\tau)) \rangle e^{-i\omega\tau} \mathrm{d}\tau \\ &= \frac{\phi_m^2(V_p)}{2} \left[\frac{1}{2}\delta(\omega - \omega_m) + \frac{1}{2}\delta(\omega + \omega_m) \right]. \end{aligned} \tag{4.93}$$

The spectrum analyzer convolves the δ-functions with the intermediate frequency filter function $F(\omega)$, which is normalized such that $F(0) = \frac{1}{\mathrm{ENBW}}$ [203], where the effective noise bandwidth $\mathrm{ENBW} = \eta_{\mathrm{F}}\mathrm{RBW}$ for a resolution bandwidth RBW and a filter shape-dependent $\eta_{\mathrm{F}} \approx 1$. Therefore, the measured noise spectral density evaluated at the modulation frequency ω_m becomes

$$S_{\phi\phi}(\omega = \omega_m) = \frac{\phi_m^2(V_p)}{4} F(\omega) * \delta(\omega - \omega_m) = \frac{\phi_m^2(V_p)}{4 \cdot \mathrm{ENBW}}. \tag{4.94}$$

Using this result, the calibration term in Eqn. 4.92 can be simplified to a final form

$$S_{\omega\omega}(\omega) = \frac{\omega_m^2 \phi_m^2(V_p)}{4\eta_F \cdot \mathrm{RBW}} \frac{S_{vv}^{\delta\omega}(\omega)}{S_{vv}^{\delta\phi_m}(\omega_m)} \tag{4.95}$$

that agrees with Eqn. 20 of Ref. [203].

Electo-optic Phase Modulator Calibration

Eqn. 4.95 demonstrates that the calibrated frequency noise can be readily obtained by comparing the recorded RF power spectral density $S_{vv}^{\delta\omega}(\omega)$ to the calibration PSD $S_{vv}^{\delta\phi_m}(\omega_m)$ (which corresponds to a known phase spectral density) for a given calibration frequency $\omega_m/2\pi$ and spectrum analyzer RBW. The ENBW correction factor η_F is a function of various spectrum analyzer settings (see Ref. [205] for example), and is therefore measured by comparing the noise marker amplitude (dBm/$\sqrt{\mathrm{Hz}}$) to the measured PSD divided by the RBW. This technique yields $\eta_F \approx 1.057$, which is approximately equal to the value given in Ref. [205] assuming typical spectrum analyzer settings.

The only remaining unknown parameter required for calibration is the peak-voltage-dependent modulation depth $\phi_m(V_p)$ of the phase modulator, which can be determined with a sideband fitting technique as shown in Fig. 4-6. An electro-optic phase modulator (EOM) is embedded in one arm of an unbalanced Mach-Zehnder interferometer, yielding a homodyne signal

$$v_h \propto \sum_n J_n(\phi_m) \cos(n\omega_m t) \tag{4.96}$$

for a modulation frequency ω_m. The power spectrum observed on the spectrum analyzer therefore consists of a periodic sequence of spectrum analyzer filter functions $F(\omega - n\omega_m)$ at frequencies $\omega_n = n\omega_m$ with powers proportional to $J_n^2(\phi_m)$. Fitting the sideband powers (relative to the $n = 1$ sideband, as the $n = 0$ peak is inaccessible on the AC-coupled spectrum analyzer) via a least-squares regression yields $\phi_m(V_p)$ for any peak drive voltage V_p. Fig. 4-6(a) illustrates the result for $\lambda = 1550$ nm and $V_p = 2.24$ V, where the Bessel functions evaluated at $\phi_m \approx 0.6\pi$ rad (red points) are well fitted to the measured (blue curve) peak amplitudes. After repeating the experiment for multiple values of V_p, a linear fit (Fig. 4-6(b)) gives the modulation

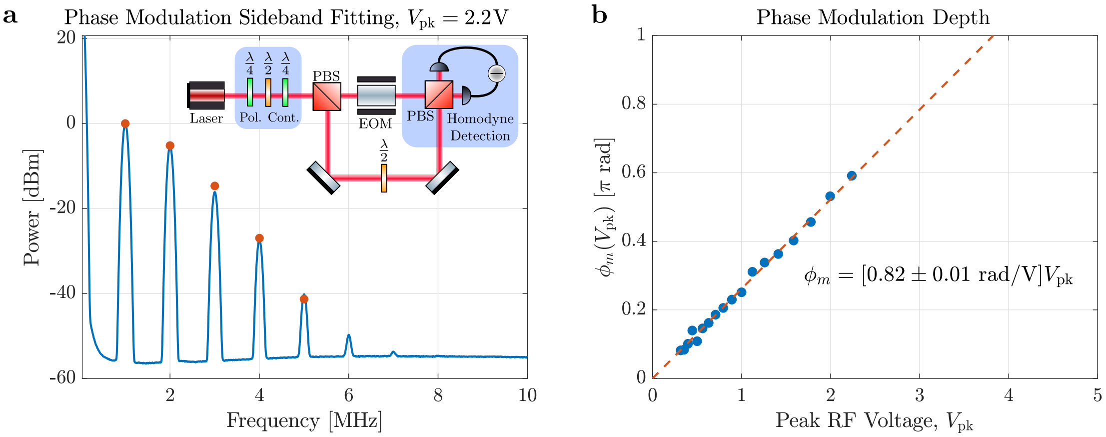

Figure 4-6: Measurement of phase modulator modulation depth $\phi_m(V_p)$ at $\lambda = 1550$ nm. A balanced homodyne measurement is performed on the output of a Mach-Zehnder interferometer with the electro-optic modulator (EOM) in one arm, yielding spectra similar to that of (a). The sideband amplitudes are fitted to find the modulation depth at each peak drive voltage V_p, and a linear fit is applied to find the modulation efficiency. The measured value $\phi_m/V_p = 0.82 \pm 0.01$ rad/V corresponds to a half-wave voltage $V_\pi = 3.83$ V.

efficiency

$$\eta_{\mathrm{mod}} = \left.\frac{\phi_m}{V_p}\right|_{\lambda_0=\lambda_{\mathrm{cal}}} = 0.82 \pm 0.01 \text{ rad/V} \tag{4.97}$$

corresponding to a half-wave voltage $V_\pi = 3.75$ V (roughly in line with the manufacturer quoted value of 3.17 V) at the calibration wavelength.

Note that the DC phase of the fiber interferometer in this experiment was allowed to drift while the measurement was averaged on a timescale much longer than that of the drift – a standard technique [206] which only affects the total power of the homodyne signal, not the relative magnitude of the sidebands.

Balanced Homodyne Detector Characterization

Using the measured EOM modulation efficiency, the calibrated thermo-refractive noise measurements in Fig. 4-8 were obtained by measuring the cavity reflection with the stabilized homodyne detector in Fig. 4-5. We confirmed that the balanced photodetection was shot noise limited (with 10 dB of shot noise clearance) for frequencies greater than ∼100 kHz and balanced the interferometer arms to well within 1 mm – over an order of magnitude shorter than the expected cavity delay (∼cm). This was achieved by tuning a retroreflector-based delay line while observing pulse delays from a picosecond fiber laser on both interferometer paths.

4.5.3 Photonic Crystal Cavity Sample Details

The $L3$ and $L4/3$ photonic crystal cavities were fabricated by Applied Nanotools foundry via electron-beam patterning and dry-etching of 220 nm-thick undoped silicon-on-insulator wafers with a 2 μm-thick buried oxide layer. To suspend the devices, the buried oxide was subsequently released via a 60 second timed wet etch in 49% hydrofluoric (HF) acid. The designs were adapted from Refs. [62, 88]. As shown in Fig. 4-8, superimposed gratings were added to improve vertical coupling efficiency. The gratings are formed via periodic hole radii perturbations ranging from $\Delta r = 0 \to 0.05r$ at a period equal to twice the lattice constant a (c.f. Sec. 2.1). Although devices with quality factors as large as 400,000 were measured for small values of Δr, the results presented in Fig. 4-8 use $\Delta r = 0.05r$, which significantly improves collection efficiency into our fiber-coupled detector.

4.5.4 Summary of Experimental Parameters

Table 4.1 summarizes the various experimental parameters used to generate the data and fit parameters shown in Fig. 4-8. Note that the expected thermal diffusivity is based on thermal conductivity measurements in thin silicon films [201] and the hole lattice porosity ϕ [207]. The porosity $\phi = 3\pi r^2/(3\sqrt{3}a^2/2 - 3\pi r^2)$ — calculated as the ratio of hole area $3\pi r^2$ (assuming a hole radius r) to material area within a hexagonal unit cell of a lattice with lattice constant a — reduces the thin film diffusivity to $D_T \approx D(1-\phi)/(1+\phi)$ [207]. This "restricted" diffusivity is used to calculate the expected decay rates in Fig. 4-8.

4.5.5 Comparison of Other Noise Sources

Should TRN dominate the frequency noise spectrum for the experimental parameters in Sec. 4.5.4? After all, a number of other stochastic processes can also produce resonant frequency noise. Here we consider two such sources: 1) multi-photon absorption leading to photothermal shot noise from free carrier recombination, and 2) self phase modulation. Both noise sources evaluated at their respective nonlinear thresholds — as an estimate of the "worst case" maximum noise levels — are found to be more than one order of magnitude weaker than TRN. Since the cavity is measured well within the linear regime, we find that TRN dominates both other contributions combined, thus further confirming our experimental measurements.

Multi-Photon Absorption

Multi-photon absorption (MPA) within the resonator leads to a free carrier population that stochastically recombines, producing random local heating analogous to fundamental thermo-refractive noise. Considering this similarity, we can analyze the

Parameter	**Symbol**	**Value**	**Source**
Temperature	T	295.68 K	Measured
Si Refractive Index	n_{Si}	3.48	[208]
Si Thermo-optic Coefficient	$\alpha_{\mathrm{TO}}^{\mathrm{Si}}$	1.8×10^{-4} K^{-1}	[208]
Si Specific Heat	c_V^{Si}	1.64 J/cm^3·K	[201]
Si Thermal Conductivity	κ_{Si}	70 W/m·K	[201]
Si Thermal Diffusivity (thin film)	D^{Si}	0.43 cm^2/s	κ/c_V
Lattice Porosity	ϕ	$\{0.29, 0.26\}$	Calculated
Patterned Thermal Diffusivity	$D_{\mathrm{T}}^{\mathrm{Si}}$	$\{0.23, 0.25\}$ cm^2/s	$D^{\mathrm{Si}}(1-\phi)/(1+\phi)$ [207]
Resonant Wavelength	λ_0	$\{1559.3, 1551.5\}$ nm	Measured
Quality Factor	Q_l	{168,000, 163,000}	Measured
Phase Modulator Efficiency	η_{mod}	0.821 rad/V	Measured (1550 nm)
ESA Noise Correction Factor	η_F	1.057	Measured
Mode Confinement Factor	γ_{Si}	$\{0.96, 0.95\}$	Simulated
Mode Volume	$\tilde{V}_{\mathrm{eff}}$	$\{0.95, 0.32\}$	Simulated
Thermal Mode Volume	$\tilde{V}_T$	$\{3.92, 1.51\}$	Simulated (Eqn. 4.28)

Table 4.1: Parameters used for calibrating the noise spectrum and computing or fitting Γ_T and V_T. Independent values n for $L3$ and $L4/3$ microcavities are listed as $\{n_{\mathrm{L3}}, n_{\mathrm{L4/3}}\}$ for cavity-dependent parameters. The mode confinement factor $\gamma_{\mathrm{Si}} \sim 1$ confirms the validity of Eqn. 4.95, which assumes complete confinement of the mode in silicon.

MPA photothermal shot noise by redefining the statistics of the mode averaged temperature driving force $\bar{F}_T(t)$ in Eqn. 4.15. The mean rate of intra-cavity k-photon absorption is [60]

$$\langle r_{k\mathrm{PA}} \rangle = \frac{\beta_k}{k\hbar\omega_0} I_{\mathrm{pk}}^k V_{k\mathrm{PA}}, \tag{4.98}$$

where $I_{\mathrm{pk}} = c|\tilde{a}|^2/2nV_{\mathrm{eff}}$ is the peak intensity of the stored energy $|\tilde{a}|^2$, β_k is the k-photon absorption coefficient, c is the speed of light, and

$$V_{k\mathrm{PA}} = \int_{\mathrm{dielectric}} |\vec{E}(\vec{r})|^{2k} \mathrm{d}^3 r / \max\{|\vec{E}(\vec{r})|^{2k}\}. \tag{4.99}$$

Note that we assume that the heating produced by the photoexcited free carriers is local (i.e. no carrier diffusion). The variance of $\bar{F}_T(t)$ is then determined from the temperature change expected from the variance of MPA events within an infinitesimally small time (a Poisson process), yielding the autocorrelation

$$\langle \bar{F}^*_{T,k}(t)\bar{F}_{T,k}(t')\rangle = \frac{k\hbar\omega_0}{c_V^2 V_T^2}\beta_k I^k_{\text{pk}} V_{k\text{PA}}\delta(t-t'). \tag{4.100}$$

Following the method of Sec. 4.4.1, we arrive at the spectral density

$$S^{k\text{PA}}_{\omega\omega}(\omega) = \left(\frac{\omega_0}{n}\alpha_{\text{TO}}\right)^2 \frac{k\hbar\omega_0}{c_V^2 V_T^2}\beta_k I^k_{\text{pk}} V_{k\text{PA}} \frac{1}{\Gamma_T^2+\omega^2}, \tag{4.101}$$

which can be evaluated for any intra-cavity stored energy. Here, we consider I_{pk} at the nonlinear threshold, i.e. the peak intensity for a linewidth resonance shift $|\langle\Delta\omega\rangle|/2\Gamma_l = \alpha_{\text{TO}}\langle\Delta T_{k\text{PA}}\rangle Q_l/n = 1$. The threshold intensity can therefore be derived from the steady state value of Eqns. 4.15, which lends the average temperature change

$$\langle\Delta T_{k\text{PA}}\rangle = \frac{k\hbar\omega_0\langle r_{k\text{PA}}\rangle}{c_V V_T \Gamma_T} = \frac{\beta_k I^k_{\text{pk}} V_{k\text{PA}}}{c_V \Gamma_T V_T}. \tag{4.102}$$

Substituting this result into the spectral density equation assuming two-photon absorption as the dominant process (true for our silicon cavities driven at ∼1550 nm), we can simplify to the final result

$$S^{\text{2PA,threshold}}_{\omega\omega}(\omega) = \frac{\omega_0^2\alpha_{\text{TO}}}{n}\frac{\hbar\omega_0}{Q_l c_V V_T}\frac{2\Gamma_T}{\Gamma_T^2+\omega^2}. \tag{4.103}$$

This result is plotted in Fig. 4-7 assuming the experimental parameters of our devices listed in Table 4.1. Comparing with Eqn. 4.36, we find $S^{\text{2PA,threshold}}_{\omega\omega}/S^{\text{TRN}}_{\omega\omega} = (n/Q_l\alpha_{\text{TO}}T)(\hbar\omega_0/k_BT)$, which accounts for the factor of ∼10 weaker maximum photothermal shot noise in our devices as shown in Fig. 4-7. We operate with an input power much lower than the nonlinear threshold power (such that $\langle\Delta\omega_{\text{2PA}}\rangle \ll \Gamma_l$), so the experimental photothermal shot noise is substantially weaker than the maximum value calculated here.

Kerr Self Phase Modulation

When confined in a $\chi^{(3)}$ nonlinear material, Poissonian fluctuations of the mean intracavity photon number impart self phase modulational (SPM) noise on the resonant frequency. From first-order perturbation theory, the Kerr index change $\delta n(\vec{r}) = 3\chi^{(3)}\epsilon(\vec{r})|\vec{E}(\vec{r})|^2/8\epsilon_0 n^3$ results in a resonant frequency shift

$$\left(\frac{\delta\omega(t)}{\omega_0}\right)_{\text{Kerr}} = -\frac{3\chi^{(3)}}{4\epsilon_0 n^4 V_{\text{Kerr}}}\delta|\tilde{a}(t)|^2 \tag{4.104}$$

where ϵ_0 is the free space permittivity, $|\tilde{a}(t)|^2$ is the stored energy, and the Kerr mode volume V_{Kerr} is equal to the thermal mode volume V_T [209]. When driven with a

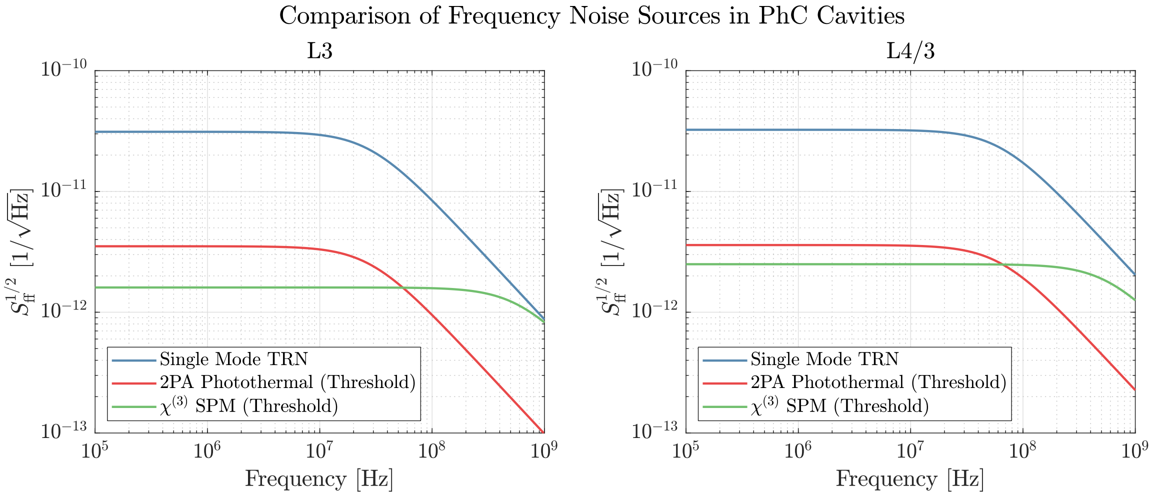

Figure 4-7: Approximate spectrum of microcavity noise sources for the experimental parameters in Table 4.1. Note that $S_{\mathrm{ff}}^{1/2}$ is plotted as a fractional stability (units $1/\sqrt{\mathrm{Hz}}$ to aid comparison with cavity stabilization literature. Noises from two-photon absorption (2PA) and self phase modulation (SPM) at their respective nonlinear threshold powers — which approximates the maximum noise level — are still smaller than TRN.

classical source, the intra-cavity energy autocorrelation

$$\langle \delta|\tilde{a}(t)|^2 \delta|\tilde{a}(t')|^2\rangle = \frac{2\Gamma_c}{\Gamma_l^2} e^{-\Gamma_l|t-t'|}\hbar\omega_0\langle|\tilde{s}_{\mathrm{in}}|^2\rangle \tag{4.105}$$

can derived from temporal coupled mode theory assuming a constant pump power $\langle|\tilde{s}_{\mathrm{in}}|^2\rangle$ coupled at rate Γ_c to a cavity with composite amplitude decay rate Γ_l. The corresponding resonant frequency autocorrelation can then be used to compute the noise spectral density

$$S_{\omega\omega}^{\mathrm{SPM}}(\omega) = \left(\frac{3\chi^{(3)}}{4\epsilon_0 n^4 V_T}\right)^2 \left(\frac{4\Gamma_c/\Gamma_l}{\Gamma_l^2+\omega^2}\right)\hbar\omega_0^3\langle|\tilde{s}_{\mathrm{in}}|^2\rangle. \tag{4.106}$$

Similar to the multi-photon absorption case, we evaluate this result at the nonlinear threshold $\langle\Delta\omega_{\mathrm{Kerr}}\rangle/2\Gamma_l = 1$ for a conservative estimate of the associated noise. The final result is

$$S_{\omega\omega}^{\mathrm{SPM,threshold}}(\omega) = \left(\frac{3\chi^{(3)}}{4\epsilon_0 n^4 V_T Q_l}\right)\left(\frac{2\Gamma_l}{\Gamma_l^2+\omega^2}\right)\hbar\omega_0^3. \tag{4.107}$$

Even at the threshold power, Fig. 4-7 shows that the SPM noise is over an order of magnitude weaker than TRN.

4.6 Measurement Results

Having fully described the theory and experiment in the preceding sections, we can now get to the juicy stuff — seeing if their results match up in practice. Fig. 4-8 shows the resulting measurements for two released (air-clad) silicon PhC cavities: the common $L3$ cavity [88] and the recently-proposed "$L4/3$" cavity [62]. Fabricated cavities yield high quality factors (up to $Q \approx 400{,}000$ at $\lambda_0 \approx 1550$ nm) with efficient vertical coupling [92]. The variation of Purcell mode volume — $\tilde{V} = (0.95,\ 0.32)$ for simulated $L3$ and $L4/3$ cavities, respectively — also allows us to confirm the expected volume-dependence of TRN. Whereas a direct reflection from the sample surface (green trace) adds little additional noise to the LO background (blue), we observe broadband noise from either cavity's reflection (orange). The calibration tone is visible at 200 MHz and we attribute the resonance at ∼15 MHz to optomechanical coupling from the fundamental flexural mode of the suspended membrane [210]. In the corrected cavity noise curve (red), we have subtracted the LO shot noise and accounted for attenuation due to the finite cavity linewidth. As expected, the wavelength-scale mode volumes yield a spectral density of resonant frequency fluctuations $S_{\mathrm{ff}}(f)$ with nearly two orders of magnitude larger amplitude and bandwidth compared to previous results in microspheres [177] and ring resonators [180]. The corrected $L4/3$ noise spectra in Fig. 4-9 also confirm that the measurement is invariant across the range of acceptable input powers, which is limited below by the homodyne locking stability and above by the onset of nonlinear effects leading to excess noise.

The measured noise spectra show excellent agreement with numerical simulations based on a modified version of the fluctuation-dissipation theorem for thermo-refractive noise [211], which is further described in Chapter 5. The multimode model derived in Sec. 4.4.3 is similarly well-fitted to the data and yields the fit parameters

$$\{\tilde{V}_T^{\mathrm{L3}}, \Gamma_T^{\mathrm{L3}}/2\pi, \tilde{V}_T^{\mathrm{L4/3}}, \Gamma_T^{\mathrm{L4/3}}/2\pi\} = \{3.4 \pm 0.3, 28 \pm 1\ \mathrm{MHz}, 1.4 \pm 0.1, 80 \pm 3\ \mathrm{MHz}\}$$

that compare favorably with the expected values ($\{3.9, 29\ \mathrm{MHz}, 1.5, 84\ \mathrm{MHz}\}$) from Eqn. 4.6 (evaluated numerically from the finite element method-simulated mode profiles) and Eqn. 4.3. In Eqn. 4.3, we assume a two-dimensional Gaussian mode and reduced thermal diffusivity $D_T = D(1-\phi)/(1+\phi)$ for the patterned slab with porosity ϕ compared to the unpatterned thin film diffusivity D [201, 207]. As predicted, the reduced mode volume of the $L4/3$ cavity increases the bandwidth and spectral density of thermal fluctuations. These observations thereby illustrate a new technique for evaluating the mode volume of fabricated optical resonators using fundamental quantities as opposed to complex invasive techniques, such as near-field scanning optical microscopy [78].

As expected from the multimode thermal description in Sec. 4.4.3, the noise spectra of the proposed single-mode approximation (Eqn. 4.5) underestimate the measured noise of both devices at low frequencies $\omega \ll \Gamma_T$, but accurately approximate S_{ff} in the range of frequencies of interest (near and above the cutoff frequency Γ_T)

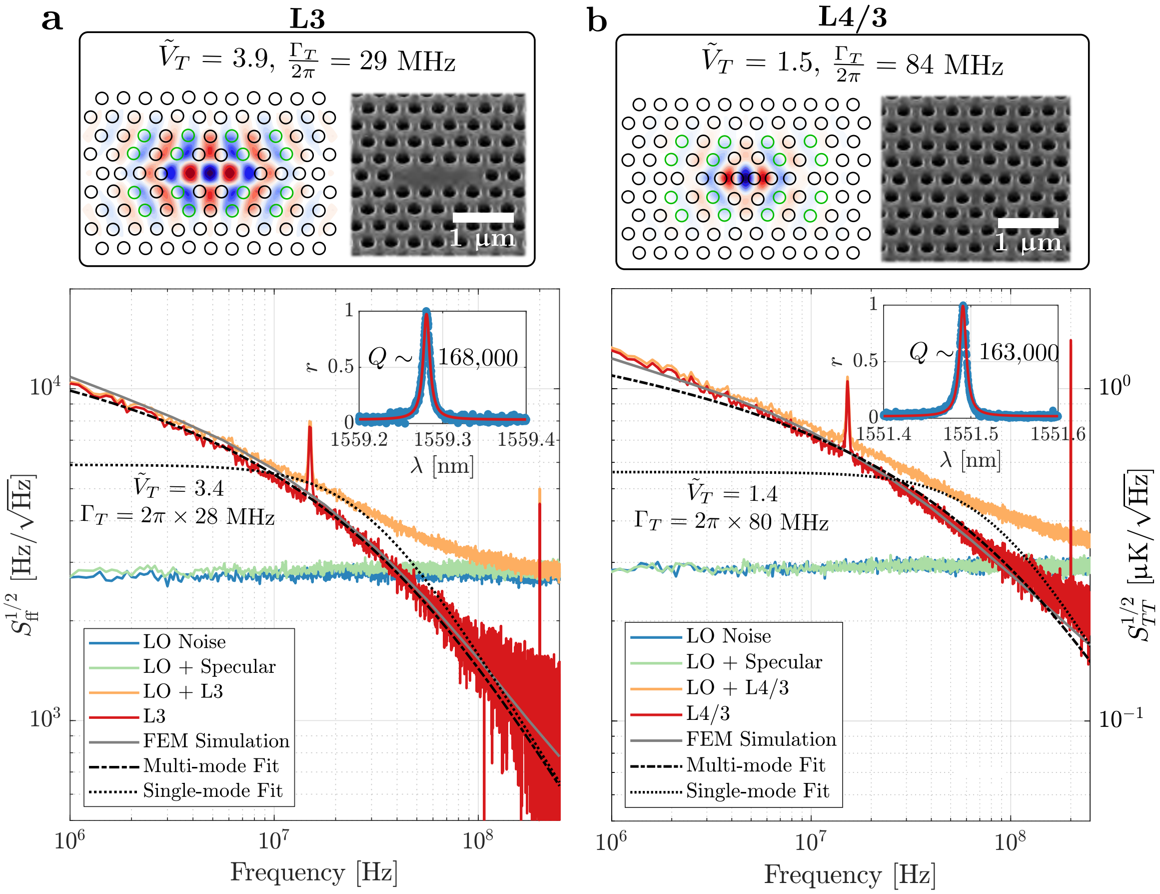

Figure 4-8: Calibrated measurement of thermo-refractive noise (TRN) in high-Q/V silicon PhC cavities. The finite difference time domain (FDTD) simulated mode profiles, thermal mode volume $\tilde{V}_T$ (Eqn. 4.6), and thermal decay rate Γ_T (Eqn. 4.3) of the $L3$ and $L4/3$ devices tested are shown in the top panels. The radii of the green holes are increased by up to 5% to form superimposed gratings which improve vertical coupling efficiency (Sec. 2.1). The measured spectral density of cavity resonant frequency and temperature noise — $S_{\mathrm{ff}}(f)$ and $S_{\mathrm{TT}}(f)$, respectively — (red) for $L3$ (a) and $L4/3$ (b) cavities are compared to noise from a specular reflection off the sample surface, finite-element method (FEM) simulations of cavity TRN, as well as single- and multi-mode fits. The listed multimode fit parameters agree with the predicted values in the top panels. Inset reflection spectra of each device reveal quality factors on the order of 10^5, which compare favorably with the FDTD computed values (1.7×10^5 and 1.6×10^5 for the $L4/3$ and $L3$, respectively). Micrographs of the fabricated designs are also inset.

and conserve the integrated frequency noise $\langle \delta\omega_{\mathrm{rms}}^2 \rangle$. Our results indicate that TRN is the dominant noise source in high-Q/V resonators, and validate the suitability of a single-mode approximation to describe the spectrum of frequency fluctuations in

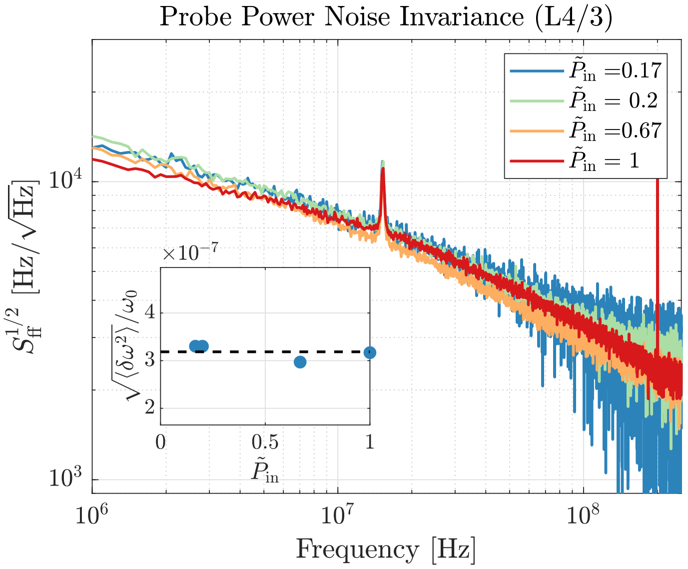

Figure 4-9: Comparison of corrected $L4/3$ cavity frequency noise spectra at various input powers $\tilde{P}_{\text{in}}$ normalized to the maximum value for the dataset. The rms fractional frequency fluctuation $\sqrt{\langle\delta\omega^2\rangle}/\omega_0$ is computed from the integrated noise over the plotted measurement bandwidth and plotted in the inset as a function of $\tilde{P}_{\text{in}}$. No significant power scaling or deviation from the mean value (black dashed line) is observed, indicating that noise contributions from nonlinear effects can be neglected.

general microcavity geometries. To our knowledge, these measurements are the first demonstration of broadband, wavelength-scale cavity readout at the thermodynamic limit. The corresponding temperature sensitivity, $S_{TT}^{1/2} \sim 300$ nK/$\sqrt{\text{Hz}}$ as shown in Fig. 4-8, is within one order of magnitude of room-temperature records set by multimode WGM thermometers [212, 213]. Compared to those state-of-the-art sensors, our PhC devices occupy six orders of magnitude less area and offer three orders of magnitude larger bandwidth. We expect this unique combination of micron-scale spatial resolution and broadband, thermodynamically-limited readout to enable new directions in thermal physics.

Specific applications aside, the lengthy (over a year...) process of achieving agreement between the theoretical, computational, and experimental results in Fig. 4-8 taught me about the scientific method: approaching a problem a different direction exposes flaws in others, and ultimately leads to greater physical insight. Seeing the three aforementioned techniques produce overlapping results in Fig. 4-8 was one of the greatest joys and achievements of this thesis.

4.7 Microcavity Q/V Limits

After experimentally verifying the TRN model, we can now use it to estimate the fundamental performance limits of room temperature microcavities. As described in Section 4.3, TRN broadens the cavity linewidth to $2\Gamma_{\text{eff}}$ according to the cavity mode volume V_T and thermal decay rate Γ_T. The associated quality factor $Q_{\text{eff}} = \omega_0/2\Gamma_{\text{eff}}$ is therefore bound to a maximum value indicative of the resonance stability, which in turn determines the fidelity of integrated optical frequency references or synthesizers [150], the minimum resolvable resonance shift in microcavity sensors [214], and the spectral purity of microcavity lasers [215]. We also specifically consider the quality factor to mode volume ratio Q_{eff}/V, which is proportional to the peak intracavity intensity and therefore of particular significance for cavity nonlinear optics [209] and enhanced sensitivity to point-like defects [60].

The effective quality factor $Q_{\text{eff}} = \omega_0\langle|\tilde{a}(t)|^2\rangle/2|\tilde{s}_{\text{in}}|^2$ of interest in this case can alternatively be viewed as the ratio of intracavity energy $\langle|\tilde{a}(t)|^2\rangle$ to energy input per cycle $2|\tilde{s}_{\text{in}}|^2/\omega_0$ in a resonantly excited, critically-coupled cavity. Under the same conditions, solving Eqn. 4.1 for $\langle|\tilde{a}(t)|^2\rangle$ subject to the noise autocorrelation of Eqn. 4.5 yields (per the derivation in Sec. 4.4.4)

$$\frac{Q_{\text{eff}}}{\tilde{V}} = \frac{\omega_0}{2\Gamma_T\tilde{V}} e^x x^{-s} \gamma_l(s,x) \tag{4.108}$$

where γ_l is the lower incomplete Gamma function, $x = (\delta\omega_{\text{rms}}/\Gamma_T)^2$, and $s = \Gamma/\Gamma_T + x$. Intuitively, decreasing the cavity linewidth 2Γ well below the broadened linewidth has little impact: the prolonged energy storage offsets the reduced excitation rate of the rapidly shifting resonance, leaving the intracavity energy unaltered. Q_{eff} is maximized in this limiting case. The corresponding upper bound of Eqn. 4.108 at $T = 300$ K is plotted for various material systems in Fig. 4-10 as a function of $\tilde{V}$ assuming a three-dimensional Gaussian-shaped mode in a homogeneous three- or two-dimensional confining medium. In the latter case, the decay rate $\Gamma_T = 3\pi D_T/V^{2/3}$ decreases by a factor of $3\sqrt{2}V^{1/3}$ to account for the restricted dimensionality of thermal diffusion.

In the joint limit $(\delta\omega_{\text{RMS}},\ \Gamma) \ll \Gamma_T$, valid for sufficiently high-Q, low V cavities, Eqn. 4.108 simplifies to $Q_{\text{eff}}^{\max} = \omega_0\Gamma_T/2\delta\omega_{\text{rms}}^2$, thereby recovering the broadened linewidth $2\delta\omega_{\text{rms}}^2/\Gamma_T$ derived in Section 4.3. $Q_{\text{eff}}^{\max}$ then scales as $V^{1/3}$ in a homogeneous medium, indicating that larger mode volumes reduce the integrated thermo-optic noise, as expected. For this reason, recent ultra-high-Q ($Q > 10^8$) integrated resonators have been specifically designed with $\tilde{V} \gg 1$ to limit TRN [194, 224]. Alternatively, Fig. 4-10 illustrates the advantage of reducing V to maximize $Q_{\text{eff}}^{\max}/V$. Further optimization of sub-wavelength cavities [78, 225] could therefore improve the intensity enhancement achievable in room temperature devices towards the open goal of microcavity-based quantum nonlinear optics.

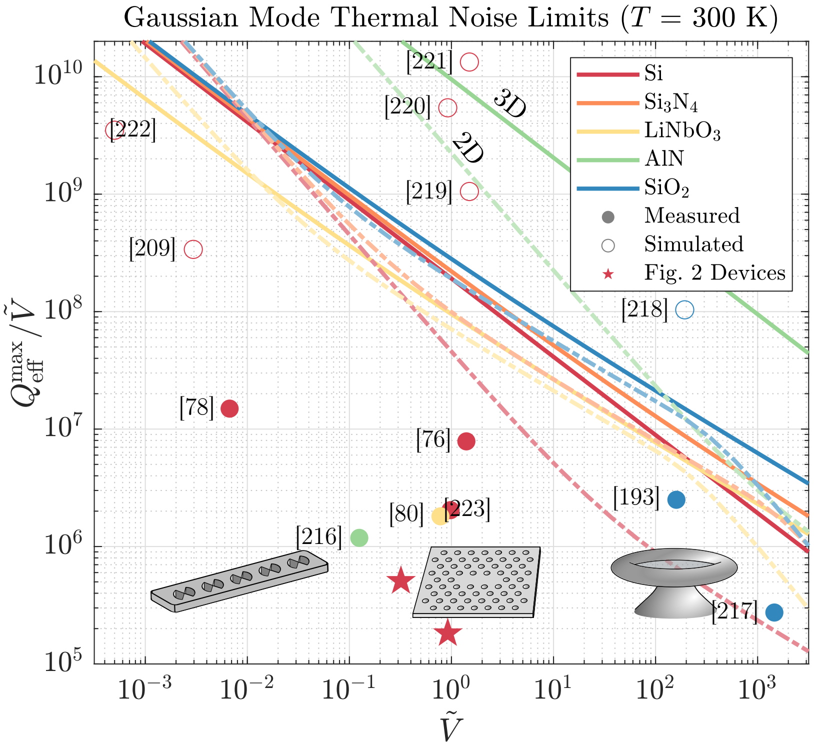

Figure 4-10: Thermal noise-limited room temperature quality factor to mode volume ratios ($Q_{\mathrm{eff}}^{\mathrm{max}}/\tilde{V}$) for the materials considered in Sec. 4.7.1 assuming a Gaussian-shaped mode at $\lambda_0 = 1550$ nm admitting thermal diffusion in two or three dimensions (dash-dot and solid lines, respectively). These limits are compared our devices as well as other fabricated and proposed microcavities. Insets illustrate typical confinement geometries for the range of $\tilde{V}$ listed.

4.7.1 Comparison of TRN in Various Materials

Surprisingly, the $Q_{\mathrm{eff}}^{\mathrm{max}}/\tilde{V}$ limits of several common materials in Fig. 4-10 lie within an order of magnitude. As shown in Table 4.2, this observed invariance can be attributed to a inverse relationship between the thermo-optic coefficient and thermal diffusivity in common materials. Yet this relationship is not fundamental: aluminum nitride, for example, is shown to outperform all other plotted materials by over an order of magnitude due to its simultaneously large thermal conductivity and small thermo-optic coefficient. This realization demonstrates the importance of material choice when designing state-of-the-art high-Q/V_{eff} resonators.

4.7.2 Beyond the Projected Q/V Limit

While our review of high-Q/V cavities (Fig. 4-10) in various materials shows that all fabricated cavities obey the projected bounds, silicon PhC slab cavities [76] and

Material	**Index** n	**TO coeff.** α_{TO} [K^{-1}]	**Density** ρ [g/cm^3]	**Heat capacity** c_V [J/g·K]	**Thermal diffusivity** D_T [cm^2/s]
Si	3.48	1.8×10^{-4}	2.32	0.7	0.8
GaAs	3.38	2.35×10^{-4}	5.32	0.35	0.31
InP	3.16	2×10^{-4}	4.81	0.31	0.37
Si$_3$N$_4$	1.99	2.5×10^{-5}	4.65	0.7	0.02
LiNbO$_3$	2.21	3.2×10^{-5}	5.32	0.63	7×10^{-3}
AlN	2.19	3×10^{-5}	3.23	0.6	1.47

Table 4.2: Material properties used to calculate the thermal noise limits in Fig. 4-10. Aluminum nitride is the only material listed with a favorable thermo-optic coefficient *and* thermal diffusivity.

silica microtoroids [193] lie within an order of magnitude of the thermal noise limit. Furthermore, various simulated devices [218–221] exceed the limit; their practical realization will thus require low-temperature operation — where temperature fluctuations and the thermo-optic coefficient are both suppressed [226] — or novel noise suppression techniques. We introduce one candidate solution — coherent thermo-optic noise cancellation — in the next chapter (Chapter 5).

4.8 Implications for All-Optical Qubits

These proposed thermal noise limits have practical impact for future devices. Chief among the applications driving the pursuit for high-Q/V cavities is quantum information. Within the past few years, numerous proposals [227–231] have explored the feasibility of photonic microcavity-based quantum gates using strong photon-photon interactions mediated by bulk material nonlinearities. Driven by recent developments in high-Q/V microcavities [78, 86] and thin film nonlinear optical materials, current experiments are approaching 1% [232] of this so called "qubit limit of cavity nonlinear optics" [187] where single photon nonlinearities outpace cavity losses. Strong emitter-based single photon nonlinearities in high-Q/V cavities are also a promising route towards optically addressable qubits, but rely on precise coupling to single atoms [233], ions [155], quantum dots [234], or defect centers [235]. We therefore focus our analysis on emitter-free, all-optical qubits using bulk nonlinearities. These techniques promise room temperature operation — the requisite hallmark for connecting distant nodes in future quantum networks [236] — by leveraging the relative immunity of optical photons to thermal noise. While this insensitivity is granted by Planck's Law, we have shown here that through the thermo-refractive effect, temperature fluctuations can significantly impact light in a high-Q/V resonator. For coherent processes, TRN-induced dephasing of the field amplitude $\tilde{a}(t)$ must be considered in addition to the previously discussed stability and intracavity energy limitations in

Section 4.7. We therefore solved for $\langle \tilde{a}(t) \rangle$ in the presence of TRN (Sec. 4.4.4). This result corresponds to an effective quality factor $Q_{\text{eff}} = \omega_0 |\langle \tilde{a}(t) \rangle|^2 / 2 |\tilde{s}_{\text{in}}|^2$ in a resonant, critically-coupled cavity, yielding

$$Q_{\text{eff}} = \frac{\omega_0}{2\Gamma_{\text{eff}}} = Q \left(\frac{\Gamma}{\Gamma_T} \right)^2 e^{2x} x^{-2s} \gamma_l^2(s, x) \tag{4.109}$$

for the previously defined x, s. Eqn. 4.109 describes the coherence of the intracavity field, and is synonymous with the dephasing time $T_2^* = 1/\Gamma_{\text{eff}} = 2Q_{\text{eff}}/\omega_0$ commonly considered for quantum emitters [237].

We can compare Γ_{eff} to a nonlinear coupling rate g between qubit basis states with the simple figure of merit FOM $= g/2\Gamma_{\text{eff}}$, which intuitively corresponds to the number of qubit operations that can be completed prior to decay or dephasing[2]. For bulk $\chi^{(3)}$ and $\chi^{(2)}$ nonlinearities, the coupling rate g is a function of material parameters and mode volumes [238]. For more information, see Refs. [187, 229]. The procedure is to first derive the classical equations of motion for fields in nonlinear oscillators and then to quantize them, deriving the Hamiltonian and the single-photon coupling strength. In classical cavity electrodynamics, a cavity field can be expressed as a sum of resonant modes

$$E(\vec{x}, t) = \sum_{\omega} C_\omega \big(A_\omega(t) E_\omega(\vec{x}) e^{-i\omega t} + \text{c.c.} \big) \tag{4.110}$$

where $C_\omega = \sqrt{\hbar\omega/2\epsilon_0}$ and $\hbar$, ω, and ϵ_0 are Planck's constant, the resonant frequency, and the vacuum permittivity, respectively. The modes E_ω satisfy the Helmholtz equation $\nabla \times (\nabla \times E_\omega) = (n^2\omega^2/c^2) E_\omega$ in a medium of refractive index n given the speed of light c. This is a generalized eigenvalue equation and the resulting solutions can be orthogonalized: $\int n^2 E^*_{\omega'} E_\omega \mathrm{d}^3\vec{r} = c^2 \int B^*_{\omega'} B_\omega \mathrm{d}^3\vec{r} = \delta_{\omega'\omega}$. With this normalization, we find that the electromagnetic energy density in the cavity is $U = \sum_\omega \hbar\omega |A_\omega|^2$. Therefore, A_ω is the normalized field operator, where $|A_\omega|^2$ gives the number of photons in the mode E_ω.

Nonlinear interactions can be treated as perturbations because the nonlinearity is weak on the order of a single optical cycle. The Helmholtz equation acquires a nonlinear polarization $P = \epsilon_0(\chi^{(2)} : E^2 + \chi^{(3)} : E^3 + \ldots)$, which can be integrated to give perturbations to the equations of motion for A_ω [239]:

$$\nabla \times (\nabla \times E) + \frac{n^2}{c^2}\frac{\partial^2 E}{\partial t^2} = -\frac{1}{c^2}\frac{\partial^2 (P/\epsilon_0)}{\partial t^2} \tag{4.111}$$

$$\Rightarrow \frac{\mathrm{d}A_\omega}{\mathrm{d}t} = \frac{i\omega}{2C_\omega} \int E_\omega(\vec{x})^* \Big[\frac{P(\vec{x}, t)}{\epsilon_0} \Big]_\omega e^{i\omega t} \mathrm{d}^3\vec{r} \tag{4.112}$$

---

[2] I thank Ryan Hamerly for deriving the qubit figures of merit evaluated here for comparison to TRN-limited microcavity performance

4.8.1 Kerr ($\chi^{(3)}$) Interaction

In the $\chi^{(3)}$ case, we have a cavity with a single resonant mode E_ω. The polarization term due to the Kerr interaction is $P = \epsilon_0\chi^{(3)} : (C_\omega A_\omega E_\omega e^{-i\omega t} + \text{c.c.})^3$. This gives rise to the equation of motion $\dot{A}_\omega = -i\chi|A_\omega|^2 A_\omega$, where

$$\chi = -\frac{3\hbar\omega^2\chi^{(3)}}{4n^4\epsilon_0}\frac{1}{V_{\text{Kerr}}}, \qquad V_{\text{Kerr}} \equiv \frac{\left(\int n^2|E_\omega|^2 \mathrm{d}^3\vec{r}\right)^2}{\int_* n^4|E_\omega|^4\mathrm{d}^3\vec{r}}, \tag{4.113}$$

The integral $\int(\ldots)\mathrm{d}^3\vec{r}$ is taken over all space, while $\int_*(\ldots)\mathrm{d}^3\vec{r}$ is restricted to the nonlinear material. Quantizing the field to satisfy the commutation relations $[\hat{A}_\omega, \hat{A}_\omega^\dagger] = 1$ this equation of motion can be generated from the Hamiltonian:

$$H_{\text{Kerr}} = \frac{1}{2}\chi\hat{A}_\omega^\dagger\hat{A}_\omega^\dagger\hat{A}_\omega\hat{A}_\omega \tag{4.114}$$

As an open quantum system, the field interacts with a bath through Lindblad dissipation terms, in this case $L = \sqrt{2\Gamma}A_\omega$, where $\Gamma = \omega/2Q$. The figure of merit for strong coupling is:

$$\text{FOM}_{\chi^{(3)}} = \frac{\chi}{2\Gamma} = \underbrace{\frac{3\pi\hbar c}{2n\epsilon_0}\frac{\chi^{(3)}}{\lambda^4}}_{K_\chi}\frac{Q}{\tilde{V}_{\text{Kerr}}} \tag{4.115}$$

In the strong coupling regime $g/2\Gamma \gg 1$, the intensity-dependent refractive index leads to an anharmonicity of Fock state energies that decouples the qubit basis (zero and one photon states) from higher energy states [187].

4.8.2 Second-order ($\chi^{(2)}$) Interaction

Alternatively, bulk $\chi^{(2)}$ nonlinearities can mediate coupling between doubly resonant first- and second-harmonic qubit basis states. The coupling rate $g = \omega_0 K_\epsilon/\tilde{V}_{\text{shg}}^{1/2}$ then describes the frequency of Rabi oscillations between a single photon in the second-harmonic mode and two photons at the fundamental frequency [227, 240, 241]. In this case, we have two fields at frequencies $(\omega, 2\omega)$. The polarization term is: $P = \epsilon_0\chi^{(2)} : (C_\omega A_\omega E_\omega e^{-i\omega t} + C_{2\omega}A_{2\omega}E_{2\omega}e^{-2i\omega t} + \text{c.c.})^2$. This gives rise to the following equations:

$$\dot{A}_{2\omega} = -\frac{1}{2}\epsilon A_\omega^2, \quad \dot{A}_\omega = \epsilon A_{2\omega}A_\omega^* \tag{4.116}$$

where

$$\epsilon = \frac{\omega\sqrt{\hbar\omega/\epsilon_0}}{n^3 V_{\text{shg}}^{1/2}}\chi^{(2)}, \tag{4.117}$$

$$V_{\text{shg}} = \frac{\left(\int n^2|E_{2\omega}|^2 \mathrm{d}^3\vec{r}\right)\left(\int n^2|E_\omega|^2\mathrm{d}^3\vec{r}\right)^2}{\left|\int_* n^3 E_{2\omega}^* E_\omega E_\omega \mathrm{d}^3\vec{r}\right|^2} \tag{4.118}$$

in the case that $\vec{E}$ and $\vec{P}$ are aligned (otherwise ϵ is reduced by a geometric factor).

As before, we can quantize the fields $\hat{A}_\omega$, $\hat{A}_{2\omega}$ and derive a Hamiltonian corresponding to Eqs. (4.116). As an open quantum system, there will also be Lindblad dissipation terms $\Gamma_1 = \omega/2Q_1$, $\Gamma_2 = 2\omega/2Q_2$:

$$H = \epsilon\frac{\hat{A}_{2\omega}^\dagger\hat{A}_\omega\hat{A}_\omega - \hat{A}_\omega^\dagger\hat{A}_\omega^\dagger\hat{A}_{2\omega}}{2i}, \tag{4.119}$$

$$L_1 = \sqrt{2\Gamma_1}\,A_\omega, \tag{4.120}$$

$$L_2 = \sqrt{2\Gamma_2}\,A_{2\omega}. \tag{4.121}$$

The figure of merit for strong coupling again is expressed as a ratio of the coupling rate ϵ to the loss rate. Here there are two loss channels, and a common approach is to take the geometric mean of the two (a choice motivated by the limit $Q_2 \ll Q_1$, in which the $\chi^{(2)}$ interaction can be adiabatically eliminated to a $\chi^{(3)}$ one with $\chi/\Gamma \propto \epsilon^2/\Gamma_1\Gamma_2$). Thus we set the figure of merit to be:

$$\text{FOM}_{\chi^{(2)}} = \frac{\epsilon}{2\bar{\Gamma}} = \frac{\epsilon}{2\sqrt{\Gamma_1\Gamma_2}} = \underbrace{\sqrt{\frac{\pi\hbar c}{n^3\epsilon_0}\frac{\chi^{(2)}}{\lambda^2}}}_{K_\epsilon}\,\frac{\sqrt{Q_1 Q_2}}{\tilde{V}_{\text{shg}}^{1/2}} \tag{4.122}$$

Assuming an equal amplitude decay rate Γ (quality factor Q) for both modes, $\text{FOM}_{\chi^{(2)}} \propto Q/V_{\text{shg}}^{1/2}$ and strong coupling again requires $g/2\Gamma \gg 1$.

4.8.3 Room Temperature Silicon Qubits?

The resulting figures of merit

$$\text{FOM}_{\chi^{(3)}} = K_\chi\frac{Q_{\text{eff}}}{\tilde{V}_{\text{Kerr}}} \qquad \text{FOM}_{\chi^{(2)}} = K_\epsilon\frac{Q_{\text{eff}}}{\tilde{V}_{\text{shg}}^{1/2}} \tag{4.123}$$

are plotted in Fig. 4-11 for Gaussian-shaped modes in silicon assuming the parameters listed in Table 4.3. Similar figures of merit are applicable to high-fidelity single photon sources [238, 241]. While silicon's centrosymmetric structure precludes an intrinsic $\chi^{(2)}$ nonlinearity, we assume the intrinsic $\chi^{(3)}$ nonlinearity can create an electric-field

Parameter	**Symbol**	**Value**	**Source**
$\chi^{(3)}$ Nonlinear Index	n_2	1.2×10^{-13} cm^2/W	[243, Sec. 11]
$\chi^{(3)}$ FOM Constant	K_χ	8.7×10^{-11}	Eqn. 4.115
$\chi^{(2)}$ (DC E-Field Induced)	$\chi^{(2)}$	40 pm/V	[242]
$\chi^{(2)}$ FOM Constant	K_ϵ	1.3×10^{-7}	Eqn. 4.122
Thermo-optic Coefficient	$\alpha_{\mathrm{TO}}^{\mathrm{Si}}$	1.8×10^{-4} K^{-1}	[208]
Thermal Diffusivity	D^{Si}	0.8 cm^2/s	[201]

Table 4.3: Silicon material properties assumed to calculate the qubit figures of merit at $\lambda_0 = 2.3$ µm and $T = 300$K.

induced $\chi^{(2)} = 3\chi^{(3)}E_{\mathrm{dc}}$ near the breakdown dc electric field E_{dc} [242].

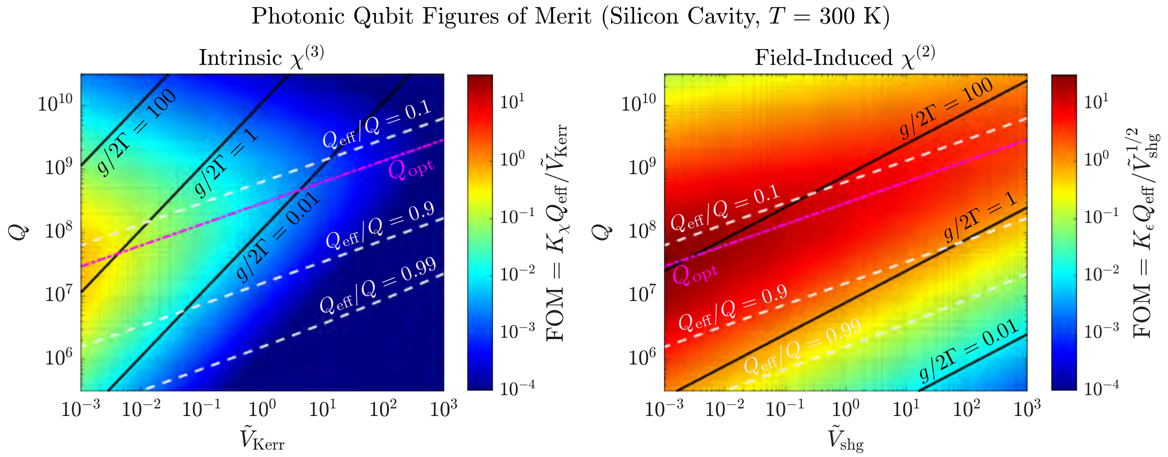

Figure 4-11: Performance of room temperature all-optical qubits using bulk $\chi^{(3)}$ (left) or electric field-induced $\chi^{(2)}$ (right) nonlinearities in silicon microcavities as a function of loaded cavity quality factor Q at $\lambda_0 = 2.3$ µm and the relevant normalized nonlinear mode volume $\tilde{V}$ ($\tilde{V}_{\mathrm{Kerr}} = \tilde{V}_T$ and $\tilde{V}_{\mathrm{shg}}$, assumed to be equal to $\tilde{V}_T$, for $\chi^{(3)}$ and $\chi^{(2)}$, respectively) . The figure of merit (FOM) — the ratio of qubit coupling rate g to the composite decay and thermal dephasing rate $2\Gamma_{\mathrm{eff}} = \omega_0/Q_{\mathrm{eff}}$ — is largest for strong coupling ($g/2\Gamma \gg 1$) and weak dephasing ($Q_{\mathrm{eff}} \approx Q$). These competing characteristics yield an optimum quality factor $Q = Q_{\mathrm{opt}}$ for any $\tilde{V}$. Three dimensional thermal diffusion in a homogeneous medium is assumed.

An ideal qubit operates well within the strong coupling regime with minimal dephasing. In the presence of TRN, increasing Q/V improves the former at the cost of the latter, leading to the observed mode volume-dependent optimum loaded quality factor $Q_{\mathrm{opt}} \approx \omega_0\Gamma_T/2\delta\omega_{\mathrm{rms}}^2$. Fig. 4-11 also illustrates a relative performance advantage for $\chi^{(2)}$ devices in silicon, as strong coupling can be achieved at lower quality factors. For example, the peak $\mathrm{FOM}_{\chi^{(2)}} \sim 10$ is three orders of magnitude greater than $\mathrm{FOM}_{\chi^{(3)}}$ assuming $Q = Q_{\mathrm{opt}}$ and $\tilde{V}_{\mathrm{Kerr}} = \tilde{V}_{\mathrm{shg}} = 1$. Although small $\tilde{V}_{\mathrm{shg}}$ — which as illustrated in Eqn. 4.118 involves maximizing the nonlinear overlap function between two co-localized cavity modes — is generally more difficult to achieve than small $\tilde{V}_{\mathrm{Kerr}}$ [244], $\mathrm{FOM}_{\chi^{(2)}} \propto \tilde{V}_{\mathrm{shg}}^{-1/2}$ also demonstrates more favorable scaling at larger mode volumes.

4.9 Summary & Outlook

Ultimately, understanding the fundamental stability and coherence limits of optical microcavities relies on the proper characterization of thermo-optic noise. Towards this end, we have presented a general theory for thermo-refractive noise in optical microcavities, discussed the resulting practical limitations on future integrated photonic components, and highlighted design choices that optimize device performance in its presence. We experimentally verified our model by measuring the dominant effect of temperature fluctuations in high-Q/V silicon PhC cavities, which demonstrated the viability of optical microcavities as high-spatial-resolution temperature probes operating at the fundamental thermal noise limit. Our results show that non-perturbative TRN ultimately limits the achievable quality factor in small mode volume cavities and that experimental devices have neared this fundamental bound. Violating the observed tradeoff between mode volume and thermo-optic noise stands as an exciting avenue for future investigation, and is the subject of discussion for our next chapter.

5

Beyond the Thermal Noise Limit

Abstract

This limits derived in Chapter 4 have immediate implications for an array of applications. As an example, we specifically explored optical quantum computing and showed that microcavity thermal noise limits the coherence of recently proposed all-optical qubits. Here, to overcome these limitations, we propose and evaluate a noise cancellation technique that coherently suppresses thermally-driven frequency fluctuations, thereby enabling continued development in quantum optics, precision sensing, and low-noise integrated photonics. Our optimized design reduces the impact of thermal fluctuations by over one order of magnitude at low frequencies by coherently canceling thermo-refractive and thermo-elastic noises.

5.1 Revisiting the Noise-Volume Tradeoff

Small mode volume optical microcavities reveal new possibilities in photonics, including chip-scale optical frequency synthesizers [150], Purcell-enhanced nanolasers with large modulation bandwidths [245], strong atom-photon [246] and photon-phonon [247] coupling, photon-level nonlinear interactions [80], and single molecule sensors with high spatial selectivity [147]. In an effort to extend these applications, recent research has focused on reducing the mode volume V of optical cavities while maintaining high quality factor [78, 209]. Unfortunately, decreasing V comes with a fundamental cost: enhanced thermal noise from statistical temperature fluctuations.[1] As

---

[1] While the integrated photonics community is quick to jump to the assumption of "shot-noise-limited" readout, other noise sources *will* eventually dominate as the input power increases (i.e.

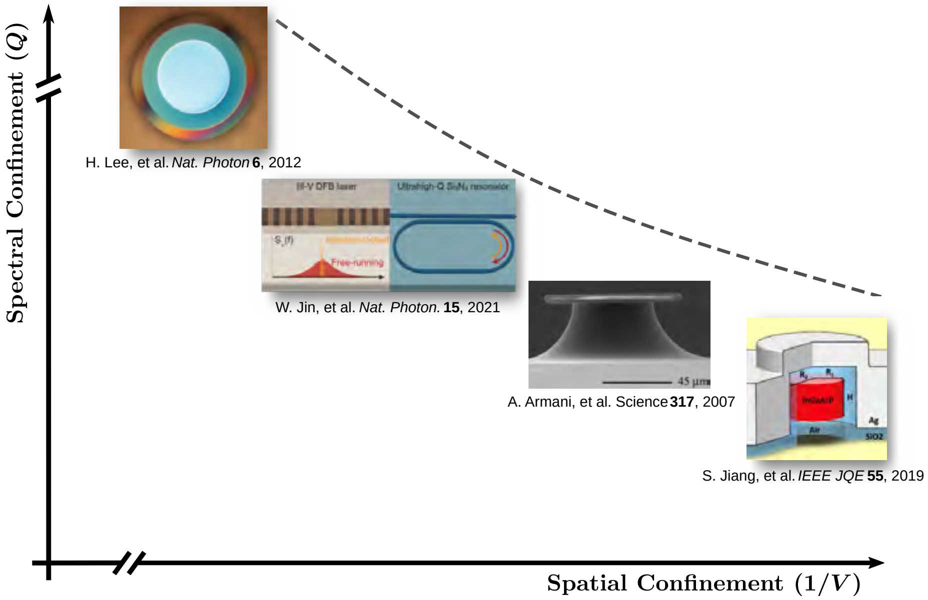

Figure 5-1: The noise-volume tradeoff facing integrated optical resonators. In light of the volume-dependent noise derived in Chapter 4, we see that the observed Q-V tradeoff drawn previously in Fig. 1-5 is indeed fundamental. As a result, billion qauality-factor integrated resonators [194] and Hz-class lasers [183] are centimeter-scale. Conversely, nanolasers [182] are inherently noisy and resonant biosensors [147] sacrifice spatial-resolution for sensitivity.

illustrated by Fig. 5-1, which the resulting thermal broadening yields wavelength-scale ultra-high-Q resonators [194], narrow-linewidth lasers [249], and high-performance optical qubits thermodynamically forbidden. Breaking this fundamental "noise-volume tradeoff" in optical microcavities would lift our proposed Q/V limits and could enable quantum noise-limited readout of diffraction-limited optical modes, thereby unveiling new possibilities in physics.[2] A chip-scale resonator with a strain sensitivity rivaling that of initial 40 meter LIGO prototypes in a twelve order of magnitude smaller form-factor would not be out of the question.

Active cavity stabilization is one candidate solution; however, the limited speed of control loops and tuning mechanisms has restricted the noise rejection bandwidth of previous demonstrations to few hundred Hz [212]. Passive feedback noise rejection via photo-thermal backaction [190] — resonance detuning-dependent laser heating that counteracts temperature fluctuations — has also been experimentally demonstrated

---

measurement imprecision noise decreases [248]).

[2] Analogous developments for gravitational wave interferometers, such as the integration of cryogenic, single-crystal silicon mirrors in LIGO (operated at 123K, where the silicon's coefficient of thermal expansion is zero), offer similar prospects [250]. I thank Evan Hall (MIT) and the MIT LIGO team for their feedback on these proposals.

[184], but the noise reduction scales with $\Gamma_T^{-1/2}$ and therefore becomes ineffective for small cavities. The requirement for large intracavity also amplifies extraneous noise sources (such as photothermal shot noise as described in Sec. 4.5.5). Finally, neither feedback-based technique can suppress fluctuations in the high-Q/V regime where the rate of resonant frequency fluctuations exceeds that of cavity leakage.

5.2 Coherent Thermo-Optic Noise Cancellation

To overcome these limitations, we propose and analyze coherent thermo-optic (TO) noise cancellation as an avenue towards the open goal of broadband thermal noise suppression. This technique stems from an analogous proposal for thermal noise reduction in mirror coatings [141, 162, 251–253]. As illustrated in Fig. 5-2, when the uniform temperature of a thickness t coating is raised by δT, the increase in phase accumulation $\delta\phi = 2\pi t\,\delta n/\lambda = 2\pi t\,\alpha_{\mathrm{TR}}\delta T/\lambda$ from an increase in refractive index δn can be offset by the coating expansion $\delta t = t\alpha^L_{\mathrm{TE}}\delta T$ *towards* the incident beam provided the linear coefficient of thermal expansion α^L_{TE} and α_{TR} have the same sign.

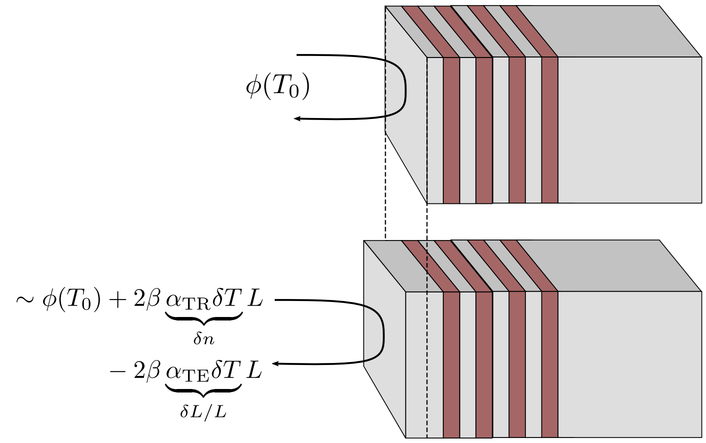

Figure 5-2: Concept for coherent thermo-optic noise cancellation in dielectric Bragg mirrors. A change in temperature δT leads to two effects that vary the original reflection phase ϕ at equilibrium temperature T_0: 1) the optical penetration depth into the dielectric stack varies due to temperature-dependent indices of refraction; and 2) the point of reflection is modified due to thermal expansion. The factor β accounts for the nonuniform lateral intensity of the reflected field [254]. If the coefficients of thermal expansion and thermo-refraction (α_{TE} and α_{TR}, respectively) have the same sign (as is the case for typical dielectrics), both effects can coherently cancel.

In a microcavity, this relationship is reversed. Intuitively, we expect thermo-optic noise to be minimized when the normalized thermo-elastic (TE) frequency shift $\delta\tilde{\omega}_{\mathrm{TR}} = \delta\omega_{\mathrm{TE}}/\omega = -\alpha^L_{\mathrm{TE}}\delta T$ of a freely expanding cavity equals that of the thermo-

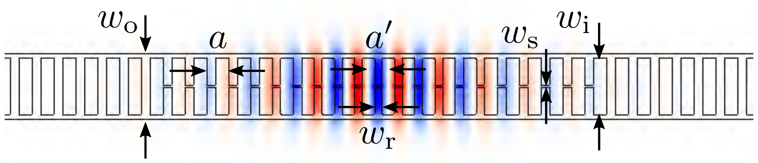

Figure 5-3: Baseline athermal "ladder" PhC design (adapted from [256]). The Q-optimized cavity with $\{a, a', w_o, w_i, w_s\} = \{647\,\text{nm},\ 0.914a,\ 3a,\ 0.85w_o,\ 0\}$ and thickness $t = 3a$ is formed by quadratically tapering the lattice constant a to a' over the inner twelve periods with a constant "rung" duty cycle $\eta_r = w_r/a = 0.4$.

refractive (TR) effect, $\delta\tilde{\omega}_{\mathrm{TR}} = -\alpha_{\mathrm{TR}}\delta T/n$, leading to the athermal condition

$$\frac{\alpha^L_{\mathrm{TE}}}{\alpha_{\mathrm{TR}}} = -\frac{\gamma}{n} \tag{5.1}$$

for the energy confinement fraction $\gamma \in (0, 1]$ of the optical mode in the dielectric. Eqn. 5.1 can be satisfied by tuning γ provided α^L_{TE} and α_{TR} are of comparable magnitude with opposite sign. Whereas we previously assumed $|\alpha^L_{\mathrm{TE}}/\alpha_{\mathrm{TR}}| \ll 1$ for common dielectrics, these two requirements are remarkably well satisfied by a range of polymers. Given their weak electronic effects, the thermo-refractive and thermo-elastic coefficients are nearly entirely dictated by their temperature-dependent density, which allows the ratio of thermo-optic coefficients to be accurately approximated by the Clausius-Mossotti relation $\alpha^L_{\mathrm{TE}}/\alpha_{\mathrm{TR}} \approx -(n^2+2)(n^2-1)$ [255]. In polymethylmethacrylate (PMMA, $n = 1.48$), for example, $\gamma = 0.83$ enables steady-state athermal operation. Upon realizing this, I was surprised to find that our group had previously demonstrated high-Q/V polymer "ladder" cavity designs [256], schematically illustrated in Fig. 5-3, that were well-suited for TO noise cancellation.

5.3 A Fluctuation-Dissipation Theorem Perspective

But does steady-state athermal behavior imply complete broadband TO noise cancellation? Unfortunately the answer is no, which we will illustrate with the computational form of the FDT used to simulate TRN in Sec. 4.6 [139, 211]. As illustrated in Fig. 5-4, the total TO resonance shift

$$\delta\tilde{\omega}_{\mathrm{TO}} = \int \underbrace{[g_{\mathrm{TR}}(\vec{r}) + g_{\mathrm{TE}}(\vec{r})]}_{g_{\mathrm{TO}}(\vec{r})} \delta T(\vec{r})\mathrm{d}^3\vec{r}, \tag{5.2}$$

i.e. the spatial average of temperature fluctuations $\delta T(\vec{r})$ weighted by $g_{\mathrm{TO}}(\vec{r})$, is calculated at frequency ω_i by driving the entropy S (conjugate to δT) with a harmonic, perturbative heat source $\delta Q_{\mathrm{TO}}(\vec{r}, t) = T\delta S(\vec{r}, t) = TQ_0 g_{\mathrm{TO}}(\vec{r})\cos(\omega_i t)$, where Q_0 is a constant of proportionality. The resulting spectrum of *fluctuations*,

$$S_{\omega\omega}(\omega_i) = \frac{2k_B T}{\pi \omega_i^2 Q_0^2} W_{\text{diss}}, \tag{5.3}$$

at the equilibrium temperature T is then computed from the time-averaged ($\langle\cdot\rangle$) power *dissipation* [211]

$$W_{\text{diss}} = \int \frac{\kappa}{T} \langle [\nabla \delta T(\vec{r}, t)]^2 \rangle \mathrm{d}^3\vec{r} \tag{5.4}$$

due to irreversible heat flow from the resulting harmonic temperature profile $\delta T(\vec{r}, t)$ in a material with thermal conductivity κ. We obtain the functional form of the TR and TE contributions to the composite TO weight function $g_{\text{TO}}(\vec{r}) = g_{\text{TR}}(\vec{r}) + g_{\text{TE}}(\vec{r})$ by placing the associated first-order perturbation theory results [18, 257] into the form of Eqn. 5.2:

$$\delta\tilde{\omega}_{\text{TR}} \approx \int_{\Omega} \underbrace{-\alpha_{\text{TR}}(\vec{r}) n^2 |\vec{E}(\vec{r})|^2}_{g_{\text{TR}}(\vec{r})} \delta T(\vec{r})\ \mathrm{d}^3\vec{r} \tag{5.5}$$

$$\delta\tilde{\omega}_{\text{TE}} \approx \int_{\partial\Omega} \underbrace{-\frac{\alpha_{\text{TE}}^L h(\vec{r})}{4(n^2-1)^{-1}} \left[|\vec{E}_{\parallel}(\vec{r})|^2 + \frac{|\vec{D}_{\perp}(\vec{r})|^2}{n^2} \right]}_{g_{\text{TE}}(\vec{r})} \delta T(\vec{r})\ \mathrm{d}^2\vec{r}. \tag{5.6}$$

Here, $\vec{E}_{\parallel}$ ($\vec{D}_{\perp}$) is the electric (electric displacement) field parallel (perpendicular) to the cavity boundary $\partial\Omega$, $h(\vec{r})$ is the dielectric thickness between between neighboring boundaries, and we assume a normalized mode $\int n^2 |\vec{E}|^2 \mathrm{d}^3\vec{r} = 1$. We also note that Eqn. 5.6 is only valid for sufficiently low frequencies $\omega \ll D_T / \max\{h(\vec{r})\}^2$ such that $\delta T(\vec{r})$ is approximately uniform throughout the dielectric between neighboring boundaries. We therefore see that TRN is associated with an energy-density-dependent volumetric heat source $\delta Q_{\text{TR}}(\vec{r}) = T Q_0 g_{\text{TR}}(\vec{r})$, whereas TE noise is associated with a surface heat source $\delta Q_{\text{TE}}(\vec{r}) = T Q_0 g_{\text{TE}}(\vec{r})$ that depends on the field intensity and mechanical displacement amplitude of the dielectric boundary.

To summarize, the following procedure is used to compute the thermo-optic noise spectrum of a cavity: (1) the harmonic heat sources of Eqns. 5.5, 5.6 are injected into the cavity at the frequency of interest ω; (2) the harmonic temperature distribution is computed via finite element simulations with a frequency-domain thermal eigensolver; (3) the noise level (Eqn. 5.3) is calculated from the the loss associated with the harmonic temperature distribution (Eqn. 5.4); (4) steps (1)-(3) are repeated for each ω of interest.

Given this formulation, we immediately see that the TO noise cannot be *completely* canceled at all frequencies due to the spatial mismatch between the heat sources,

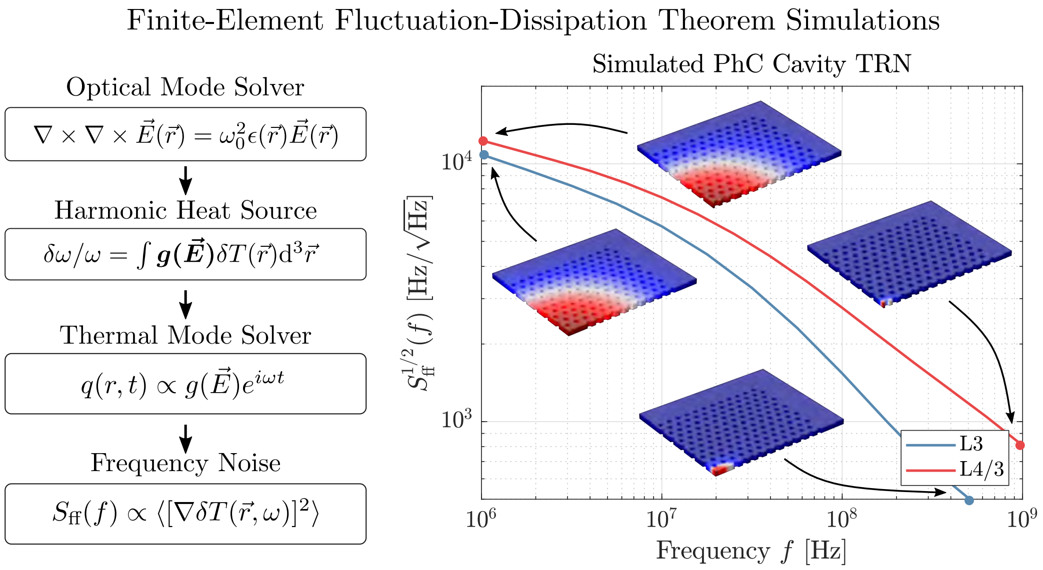

Figure 5-4: Overview (left) and results (right, for the cavities designs measured in Fig. 4-8) of finite-element fluctuation-dissipation theorem (FDT) simulations [211]. All symbols are defined in the text. In Levin's computational form of the FDT, a harmonic heat source $q = ge^{i\omega t}$ (for the weighing factor g relating temperature fluctuations to resonant frequency shifts — generates a harmonic temperature profile δT. The irreversible *dissipation* from heat transfer drives the *fluctuation*, which can be computed from the temperature profile δT. Repeating this process at any frequency ω of interest yields the thermal noise curves shown on the right-hand panel. Insets show the harmonic temperature profiles which are broad at low frequency due to thermal diffusion but approach the optical mode shape (for the case of thermo-refractive noise, where g is proportional to the mode's energy density) at high frequency.

which invariably leads to irreversible heat flow and the associated noise. However, our analysis reveals two intuitive design principles to maximize the coherence between anti-correlated TR and TE sources, thereby minimizing the total TO noise: I: the cavity boundaries should be placed near high-intensity regions of the cavity mode to maximize the spatial overlap between TR and TE sources; and II: we intuitively expect that the amplitude of the harmonic temperature profile, and thereby the TO noise, should be minimized if the total added heat $Q_{\mathrm{TO}} = \int_\Omega \delta Q_{\mathrm{TR}}(\vec{r})\ \mathrm{d}^3\vec{r} + \int_{\partial\Omega} \delta Q_{\mathrm{TE}}(\vec{r})\ \mathrm{d}^2\vec{r}$ is zero. This is true away from the sources at sufficiently low frequencies, where thermal diffusion effectively "masks" the exact source locations, and is actually equivalent to the athermal condition of Eqn. 5.1.

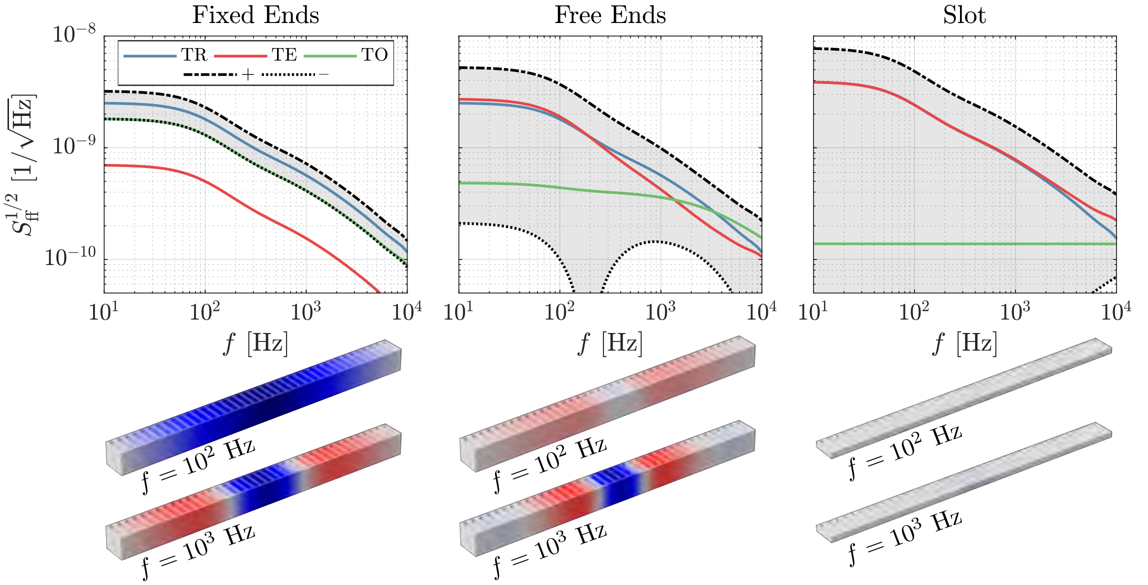

Figure 5-5: Evaluation of coherent thermo-optic noise cancellation with an athermal polymer (PMMA) microcavity. Finite element fluctuation-dissipation simulations are conducted with a Q-optimized design driven by anti-correlated volumetric and boundary heat sources corresponding to thermo-refractive (TR) and thermo-elastic (TE) noise, respectively. The composite thermo-optic (TO) frequency noise spectrum $S_{\mathrm{ff}} \propto [\nabla \delta T(\vec{r}, f)]^2$ is computed from the resulting harmonic temperature profiles $\delta T(\vec{r})$ (bottom) and is bounded by the coherent (−) and incoherent (+) sum of TR and TE contributions (shaded region). From left to right, the three simulated devices have fixed endpoints, free endpoints, and fixed endpoints with a sub-wavelength center slot of width w_s. As visually depicted by the reduced $\delta T(\vec{r})$ at low frequencies, the slot geometry (with optimized parameters $\{a, a', w_o, w_i, w_s, t, \eta_r\} = \{697\text{ nm},\ 0.874a,\ 3a,\ 0.85w_o,\ 10\text{ nm},\ 0.8a,\ 0.6\}$) provides optimal noise cancellation. Note that temperature color scales in the bottom panels are normalized to the fixed-end case to facilitate comparison.

5.4 Intuitive Design Rules and Optimization

Guided by these two simple principles, we optimized the coherent TO noise cancellation of the PMMA ladder cavity in Fig. 5-5. Our baseline design yields $Q = 3 \times 10^5$, $\tilde{V} = 2.6$, and $\gamma = 0.75$ — approximately 10% away from the athermal confinement condition. However, the beam ends are assumed to be fixed for support, which restricts lateral thermal expansion (which then primarily affects the width and thickness of the beam, as well as the width of individual "rungs") and leads to a dominant TR effect as shown by the individual TR and TE noise spectra in Fig. 5-5. If both heat sources are simultaneously simulated, the resulting TO noise resembles the coherent combination of the individual contributions, i.e. the noise amplitudes subtract as desired. However, as depicted by the associated harmonic temperature profiles in Fig. 5-5(b), the achievable noise reduction is modest owing to the dominant amplitude of the TR source near the center, high-intensity region of the cavity mode.[3]

According to criterion II it is evident that the TE source must be amplified to improve the noise cancellation. Freeing the cavity ends achieves this goal by enabling isotropic expansion, but violates the criterion I: expansion along the beam length amplifies boundary displacements and the associated TE heat source away from the TR source maximum at the cavity center, thereby minimizing the spatial overlap between the two heat sources. As a result, TO noise suppression is again limited despite the nearly equal TR and TE noise contributions (center panel of Fig. 5-5).

To simultaneously co-locate the heat sources and magnify the TE effect, we instead propose placing a thin air "slot" through the ladder rungs at the center of the cavity as shown in the final (right-most) panel of Fig. 5-5. In the original design, expansion along the ladder rung length displaces the side rail boundary, where the cavity field is weak. The modified design's narrow slot moves this displacement boundary to the center of the beam (the "half-rungs" expand to fill the gap), where the cavity field and TR heat source are maximized. We then thin the beam to satisfy criterion II within 1% and re-design the cavity defect region to maximize Q. The final optimized design supports a high-Q/V resonance ($Q = 6 \times 10^4$, $\tilde{V} = 0.75$) that suppresses fundamental thermal noise by over an order of magnitude at low frequencies. The temperature profiles in Fig. 5-5(e) graphically evidence this cancellation and suggest again that the achievable suppression is limited by the imperfect coherence of the two spatially-resolved heat sources.

This intuition-driven optimization is a first proof-of-concept demonstration of broadband, coherent cancellation of fundamental thermodynamic fluctuations in a microcavity. While the achievable noise reduction our trial structure is relatively limited, the design is based on simple principles that can be readily extended to other designs, materials, and optimization techniques. For example, the interdisciplinary thermo-optical design of high-Q/V, low-noise resonators requires structural modifications that are well suited to recent developments in topological optimization of subwavelength integrated photonics [225, 258, 259]. The coherent thermo-optic cancellation scheme can also be applied other materials beyond polymers, such as CMOS-compatible titanium dioxide (TiO_2) [260] or perovskites [261] with negative thermo-optic coefficients. Our preliminary results thus motivate an exciting new research avenue into novel noise abatement schemes in pursuit of ultra-high-Q/V

---

[3] At higher frequencies, the thermo-elastic and thermo-refractive noises appear to converge to a similar amplitude; however, these high-frequency results must be interpreted with care: above ~10 kHz, the assumption of uniform temperature between boundaries (required in Eqn. 5.6) is no longer valid. Ideally, the thermo-elastic displacement at high frequency should be a function of the averaged temperature between boundaries; however, this form seems incompatible with Levin's form of the FDT.

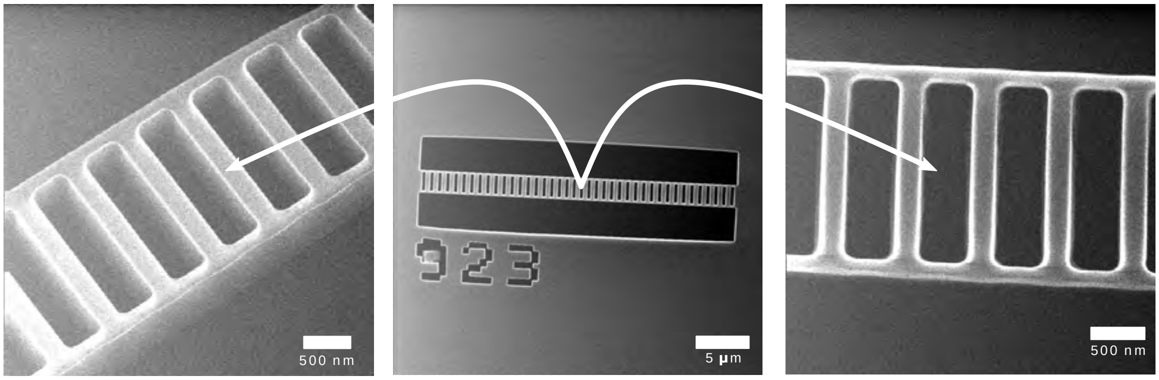

Figure 5-6: Helium-ion microscope pictures of a fabricated PMMA photonic crystal nanobeam cavity, corresponding to the “fixed-end" design in Fig. 5-5.

cavities beyond our the thermal noise limit.

5.5 Outlook and Initial Experimental Progress

These proof-of-concept simulations demonstrate the feasibility of the coherent thermo-optic cancellation scheme, which can also be applied to other materials beyond polymers, such as CMOS-compatible titanium dioxide (TiO_2) and perovskites with negative thermo-optic coefficients. Experimentally, we have fabricated “fixed-end” designs (Fig. 5-6) with $Q > 10^4$ and an effective thermo-optic coefficient $\alpha_{\mathrm{TO}}^{\mathrm{eff}} \approx -1.1\times 10^{-4}/\mathrm{K}$ (Fig. 5-7); future fabrication optimization is planned to achieve athermal operation. Together, these preliminary results motivate an exciting new research avenue into novel noise abatement schemes in pursuit of ultra-high-Q/V cavities beyond our proposed thermal noise limits.

We hope that our proposal and analysis of one possible solution — coherent thermo-optic noise cancellation — towards low-noise, high-Q/V integrated optical devices further motivates this field of research. Ultimately, these advances will be necessary to achieve the performance required for future developments in optical quantum information processing, cavity optomechanics, precision optical sensing, and beyond.

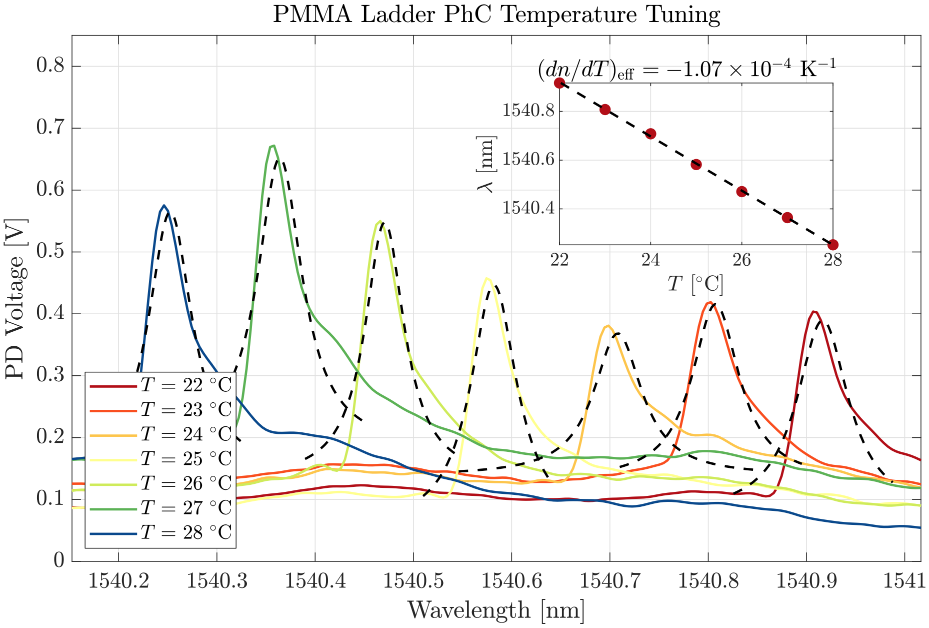

Figure 5-7: Linescans of the cavity imaged in Fig. 5-6 (measured as a function of sample mount temperature T) reveal a quality factor $Q \sim 10,000$ at the expected resonant wavelength λ. The resonance blue-shifts as temperature increases, indicating that thermo-refractive effects dominate as expected. An “effective” thermo-optic coefficient $\mathrm{d}n/\mathrm{d}T$ can be extracted via a linear fit to the resonant wavelength as a function of T.

6

Cavity Array Post-Fabrication Trimming

Abstract

Having completed our investigation of thermal noise in single microcavities, we now return to the proposed SLM application, which requires coherent operation between multiple cavities. We therefore invented a fully automated, parallel "holographic trimming" technique that aligns the resonant wavelength of microcavities with picometer precision. Previous beamforming approaches have avoided high-quality-factor (Q) resonators, as alignment to a common operating wavelength requires scalable, precise, and low-loss trimming —– an unsolved challenge. Our automated holographic trimming method uses structured laser illumination to grow thermal oxide on selected devices in parallel, resulting in a picometer-order wavelength uniformity between 64 wavelength-scale microcavities with a mean $Q > 10^5$. Notably, this record wavelength uniformity corresponds to sub-atomic length-scale structural uniformity between each device.

6.1 Fabrication Disorder

In addition to the overlapping far-field emission profiles shown in Fig. 3-16, programmable multimode interference requires each cavity to operate near a common resonant wavelength λ_0. For sufficiently high-Q resonators, this tolerance cannot be solely achieved through optimized fabrication since $\mathcal{O}(\text{nm})$ fabrication fluctuations translate to $\mathcal{O}(\text{nm})$ resonant wavelength variations [113, 114].

Our prototype 8×8 arrays of $L3$ cavities (chosen to optimally balance requirements on Q, V, directive emission, and fabrication tolerance) typically span a $\sim$3 nm

Technique [Year]	**Cavity Type**	N	$\boldsymbol{\Delta\lambda_0^{\text{p-p}}}$ **[pm]**	$\langle Q\rangle$	**In situ?**	**Par-allel?**
“Holographic” oxidation [2022]	**Si PhC**	**64**	**13**	2×10^5	**Y**	**Y**
Germanium implantation [2021]	Si ring [262]	58	32	4×10^3	Y	N
Laser-annealed cladding [2020]	Si ring [263]	2	20*	2×10^4	Y	N
Boron implantation [2019]	Si ring [264]	4	15	5×10^3	Y	N
Electron-beam irradiation [2018]	Si PhC [265]	4	400	3×10^5	N	N
Photo-electro-chemical etching [2017]	GaAs disk [266]	5	200*	2×10^4	Y	N
Annealed cladding [2016]	Si ring [267]	5	90*	3×10^3	Y	N
Ultraviolet irradiation [2014]	a-Si ring [268]	4	45	8×10^3	Y	N
Post-fabrication etching [2013]	GaAs PhC [269]	18	100*	3×10^4	N	Y
Photochromatic thin-film [2011]	GaAs PhC [270]	3	340	8×10^3	Y	N
Anodic oxidation [2006]	GaAs PhC [271]	2	100*	5×10^3	N	N

Table 6.1: Comparison of microcavity array trimming techniques. Estimated values are marked with a *. $\Delta\lambda_{\text{p-p}}$ = peak-to-peak wavelength error; $\langle Q\rangle$ = mean quality factor.

peak-to-peak wavelength variation (given $\sigma_\lambda \approx 0.6$ nm), corresponding to hundreds of linewidths for the target $Q \sim 10^5$. Correcting this inhomogeneity requires automated, low-loss, and picometer-precision resonance trimming, which remains an open goal. The previous techniques detailed in Table 6.1 — including ex-situ structural modifications [269, 271, 272], solution-immersed photoelectrochemical etching [266], or lossy ion implantation [262, 273] — fail to simultaneously satisfy these requirements.

6.2 “Holographic” Thermal Oxidation

Of the techniques reviewed in Table 6.1, laser-assisted thermal oxidation is a notable standout offering low-loss single-device trimming with micron-order spatial resolution [74, 75], albeit with limited speed and controllability (to date). The basic idea is illustrated in Fig. 6-1b-c: a focused visible laser heats a silicon slab in an oxygen environment to a temperature near its melting point ($T \approx 1700$K), causing a surface reaction that grows oxide at the membrane's surface. Since silicon is consumed by the reaction, the effective structural parameters (hole radius r and slab thickness t) are modified and the resonant wavelength blue-shifts.[1]

---

[1] Even though the membrane expands during the oxidation process (the molar volume of silicon dioxide is greater than that of silicon), the blue-shift associated with the consumption of silicon outweighs the red-shift of oxide growth.

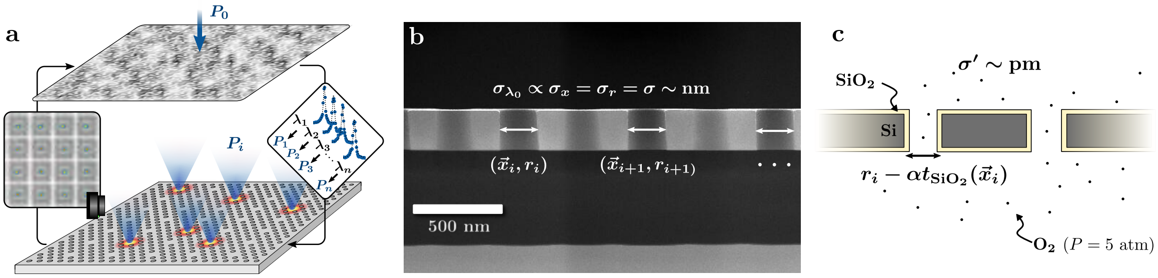

Figure 6-1: Parallel, fully-automated, and low-loss microcavity "holographic trimming" via structured laser oxidation. In each iteration of the trimming loop (a), a weighted Gerchberg-Saxton algorithm distributes a visible trimming laser with power P_0 to powers $\{P_i\}$ at desired cavities based on the measured resonant wavelength λ_i of each cavity. A few nm-thick layer of thermal oxide grows at each optical focus (photographed spots in the inset cavity array image), reducing the as-fabricated standard deviation in hole parameters $\sigma \sim$ nm (b,c) and permanently shifting the targeted resonances. The process is accelerated in a high-pressure ($P \sim 5$ atm) oxygen environment.

We implemented two solutions to address the limitations of previous thermal oxidation-based trimming implementations: 1) accelerated oxidation in a high-pressure oxygen chamber with in-situ characterization; and 2) "holographic" distribution of the trimming laser to simultaneously trim multiple devices. In each iteration of the automated trimming loop (Fig. 6-1a), the resonant wavelengths $\{\lambda_i\}$ are measured and a subset T of N devices is selected to maximize the total trimming distance $N(\min_T\{\lambda_i\} - \lambda_t)$ to a target wavelength λ_t.

6.2.1 High-Power Liquid Crystal SLM Setup

Each cavity in T is then targeted by a visible laser using the SLM setup in Fig. 6-2. A liquid crystal on silicon (LCOS) SLM actively distributes a high-power, continuous-wave visible laser to target devices during the cavity trimming procedure. The input laser was tunably attenuated with a motorized half-wave plate (preceding a PBS) and subsequently expanded to overfill the LCOS aperture. The LCOS SLM was reimaged onto the objective BFP (as confirmed by imaging with L2 in place) using two lenses (L4, L5) with focal lengths chosen to optimally match the imaged SLM and objective pupil dimensions. As discussed in Sec. 6.2.2, phase retrieval-computed holograms then evenly distribute power to an array of focused spots on the sample when the mechanical, flip mirror shutter is opened. Photographs of the LCOS SLM setup with watt-class power handling are shown in Fig. 6-3.

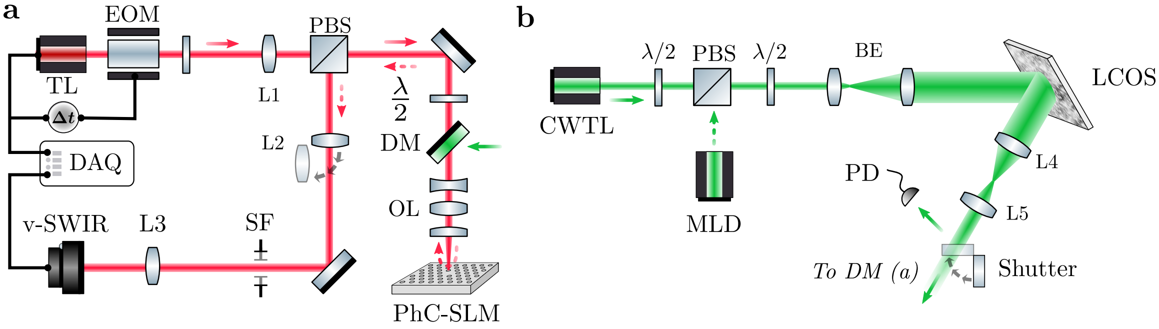

Figure 6-2: Setup for microcavity trimming via structured laser illumination. By adding a dichroic mirror (DM) to the characterization setup described in Sec. 2.5.1 (a), a structured visible laser (b) can be joined with the probe beam for in situ trimming. The same holographic distribution technique can be used with a nanosecond-class modulated laser diode (MLD) for high-speed on-off switching experiments (Sec. 7.2). CWTL: continuous-wave trimming laser (Coherent Verdi V18); MLD: modulated laser diode (Hubner Cobolt or PicoLAS LDP); BE: 5× visible beam expander; LCOS: high-power liquid crystal SLM (Santec SLM-300); L4: 300 mm; L5: 250 mm; PD: photo-detector

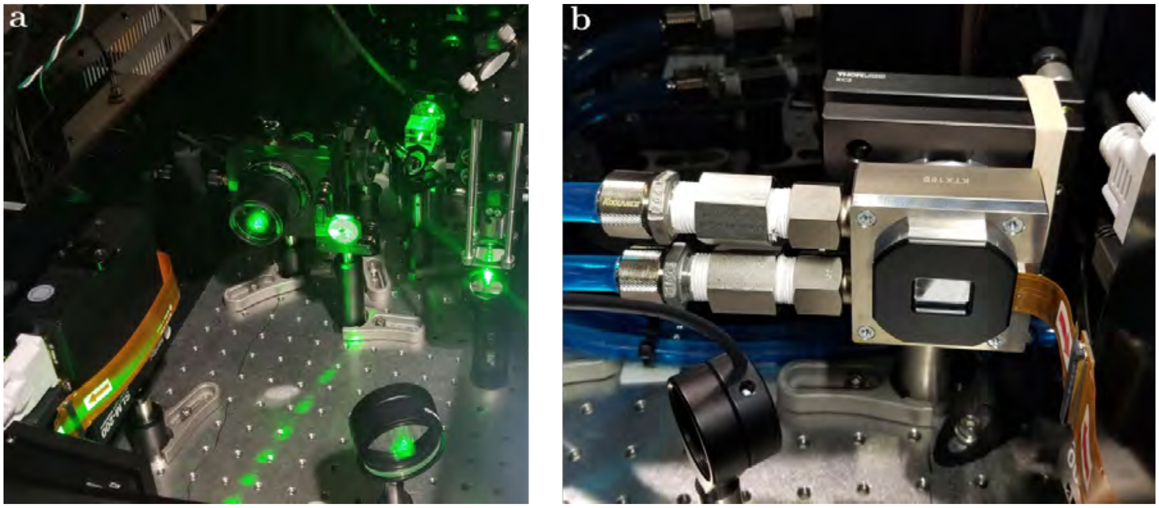

Figure 6-3: Experimental trimming setup (a) featuring a liquid-cooled, high-power LCOS SLM (b). The beam expander, SLM, and lens L4 (see Fig. 6-2) are visible in (a); lens L5 located on the main table (visible in Fig. 2-8) after the periscope.

6.2.2 Optical Focus Array Generation: The `slm-suite` Toolbox

To generate the phase masks required to evenly distribute the trimming laser to targeted cavities, we developed an open-source, GPU-accelerated experimental holography software package that implements fixed-phase, weighted Gerchberg-Saxton (WGS) phase retrieval algorithms.[2] Using camera feedback, the algorithm can generate thousands of near-diffraction-limited foci with ∼1% peak-to-peak power uniformity and single-camera-pixel-order location accuracy within a few iterations (i.e. less than a second; typically limited by the LCOS SLM refresh rate).

Features

`slm-suite` simplifies the creation of high-uniformity, arbitrary-geometry optical focus arrays using various phase retrieval algorithms. The package features:

1. Automated wavefront calibration routines that measure the Fourier-plane source amplitude and phase using a super-pixel interference technique to compensate for aberrations along the SLM imaging train [274]

2. Various graphical processing unit (GPU)-accelerated Gerchberg-Saxton (GS) algorithms that use the measured source constraints (1) to produce optimized spot array phase masks [275–277]

3. Automated affine transformations between grating wave vectors applied to the SLM and image-space coordinates (i.e. camera pixels) by projecting and detecting a GS-computed spot array

4. Camera-based feedback of measured spot amplitudes at known (calibrated) locations into phase retrieval algorithms to improve the uniformity of image-space spot arrays

5. Automated evaluation metrics to monitor diffraction efficiency, spot amplitude and position tolerance, and spot quality.

6. Simplified hardware interface and control.

After calibration, high-uniformity optical foci can be generated at arbitrary image plane locations specified by the user. For example, Fig. 6-4 shows a 10 × 10 spot array with ∼1% power uniformity and sub-micron placement accuracy formed on a 10 × 10 cavity array during the trimming procedure of Section 6.2.4.

---

[2] slm-suite. `https://github.mit.edu/cpanuski/qp-slm`. The package is currently avaliable to MIT affiliates only; however, at the time of writing, we are completing final formatting to transition to a fully open-source `python` package.

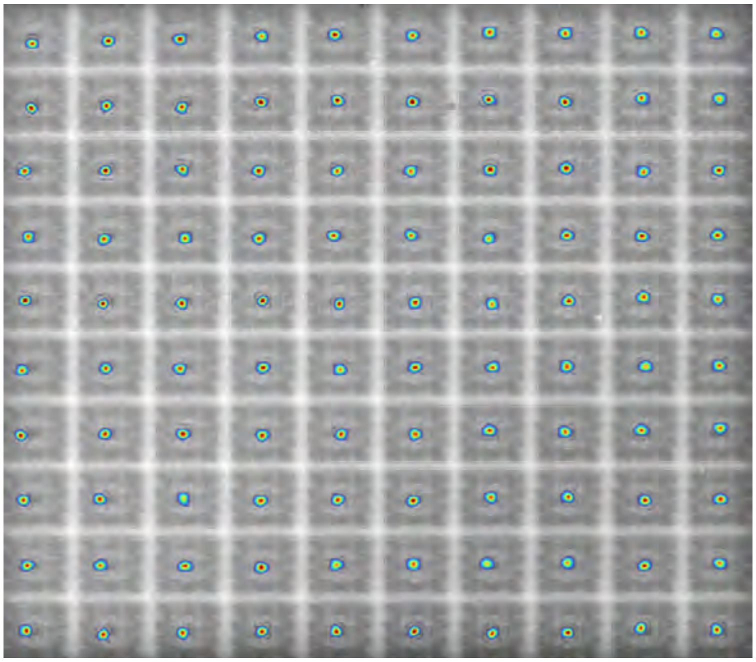

Figure 6-4: Overlaid images of 10×10 cavity (grey) and trimming spot (color) arrays demonstrating the $\ll$ μm placement accuracy and percent-order power uniformity of weighted Gerchberg-Saxton phase retrieval with experimental camera feedback.

6.2.3 High-Pressure Thermal Oxidation

The holographically-targeted pixels are then laser-heated with a computed exposure power and duration (based on the current trimming rates, resonance locations, and other array characteristics) to grow thermal oxide at the membrane surface. For thin oxide layers, the consumption of silicon during the reaction with ambient oxygen permanently blueshifts the cavity resonance in proportion to the oxide thickness $t_{\mathrm{SiO_2}}$ (Fig. 6-1b) [75]. Per the Deal-Grove model, the rate-limiting diffusion of oxygen through the grown oxide increases with oxygen pressure — a well-known technique (high-pressure thermal oxidation, or “HIPOX”) in microelectronics fabrication [278]. We therefore oxidize our samples in pure oxygen with partial pressure $P_{\mathrm{O_2}} = 5$ bar. Fig. 6-5 shows the chamber design and setup, which enables $\mathrm{d}\lambda_0/\mathrm{d}t \approx 0.1$ nm/s resonance trimming rates over record wavelength ranges $\Delta\lambda_0 > 20$ nm (Fig. 6-6).

After each trimming exposure, we remeasure the resonance statistics and recycle the loop until all devices are aligned within a set tolerance about λ_t. As we will detail in the following section, the trimming algorithm also accounts for long-term moisture adsorption to the membrane surface, thermal cross-talk, and trimming rate variations.

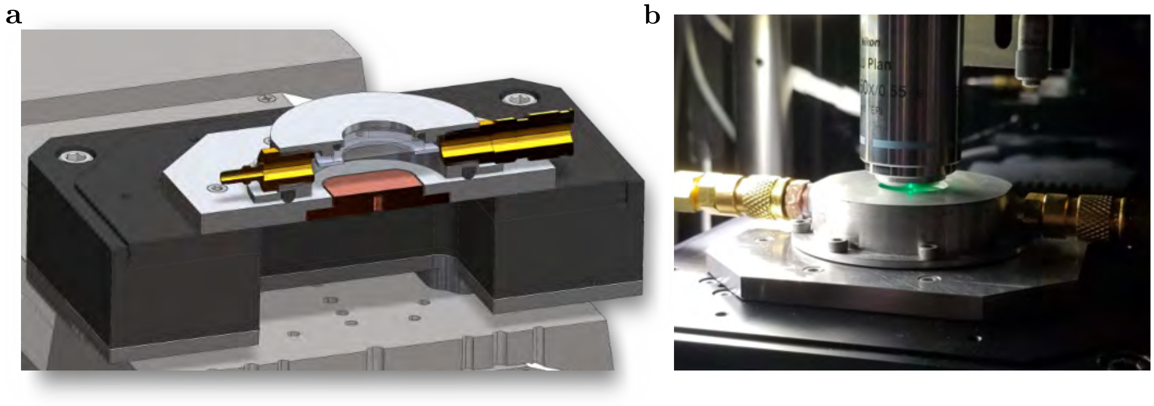

Figure 6-5: Custom chamber designed (a) and built (b) for high-pressure oxidation. The chamber is mounted to the sample stages of the characterization setup (Fig. 2-8), and optical access is provided by a 1"-diameter, 1.2 mm-thick N-BK7 precision ($\lambda/10$) window. This window limits the ultimate chamber pressure to ~10 atm (as confirmed by accidental destructive testing).

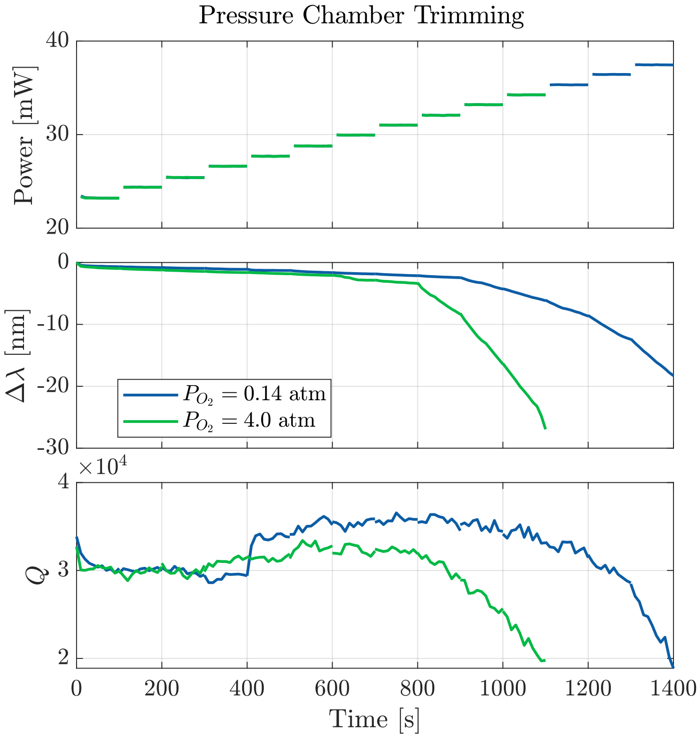

Figure 6-6: Wavelength and quality factor trends as a function of incident visible laser power, demonstrating accelerated trimming with increased oxygen partial pressure P_{O_2}.

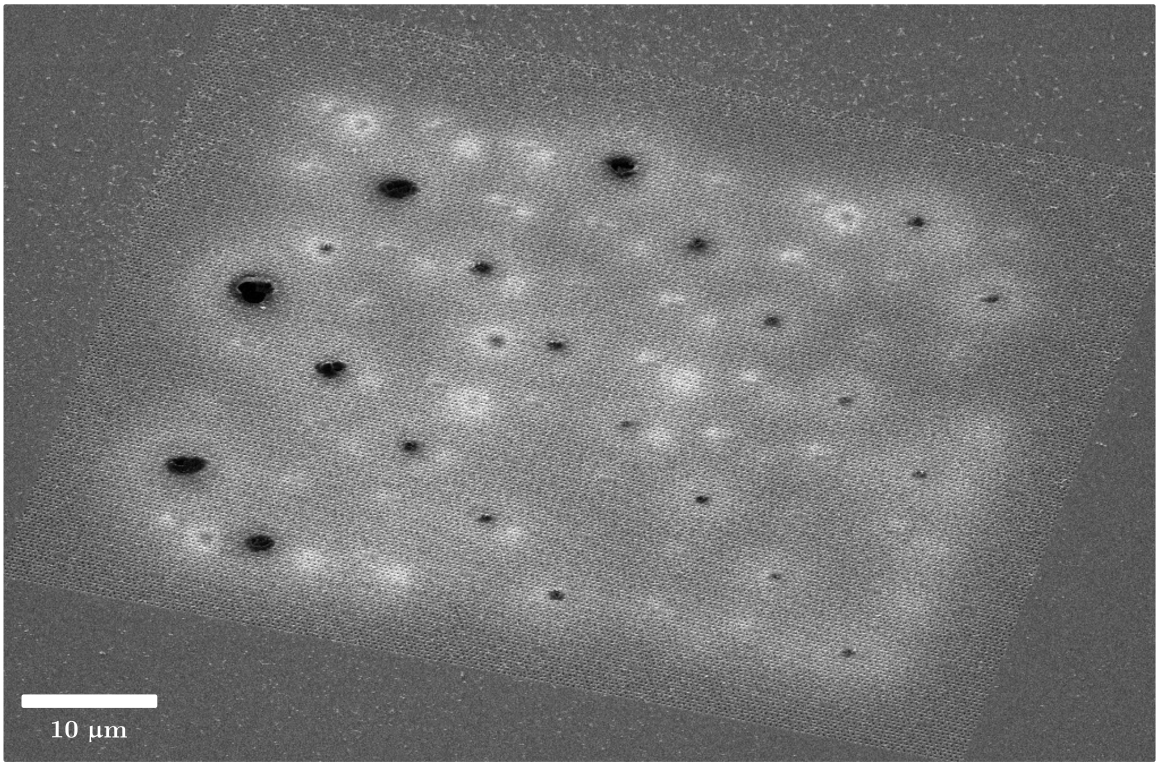

Figure 6-7: Helium-ion micrograph of a 10 × 10 cavity array damaged during the trimming process. Since high-speed oxidation requires operation at temperatures approaching the melting point of silicon, precision control of the trimming laser is required to avoid damage.

6.2.4 Parallel Trimming Algorithm

Without precision power control, timing, and resonance monitoring, the PhC cavity arrays can easily be damaged during the holographic trimming process as shown in Fig. 6-7. We therefore developed and implemented a control algorithm (Fig. 6-8) to align high-Q microcavities in parallel.

The main loop of the trimming process consists of device selection, hologram setup, parallel laser oxidation, and resting intervals. The algorithm monitors two resonant wavelengths: the instantaneous wavelength λ_i and the steady-state wavelength λ_0. Initially $\lambda_i = \lambda_0$; however, focusing high-power (~10 mW) visible light onto the cavity (as required to sufficiently heat the PhC membrane for thermal oxidation) causes a temporary blueshift $\Delta\lambda_0$ due to the desorption of moisture attached to hydrophilic hydroxyl surface terminations. For any target rest wavelength λ_t, we therefore trim devices to an instantaneous wavelength $\lambda_i = \lambda_t - \Delta\lambda_0$ that relaxes over $\mathcal{O}$(minute) timescales to $\lambda_i = \lambda_0 = \lambda_t$ as moisture re-adsorbs to the surface. In practice, the stability and estimation of the "overtune" $\Delta\lambda_0$ limit the uniformity and scale of the trimming process, respectively.

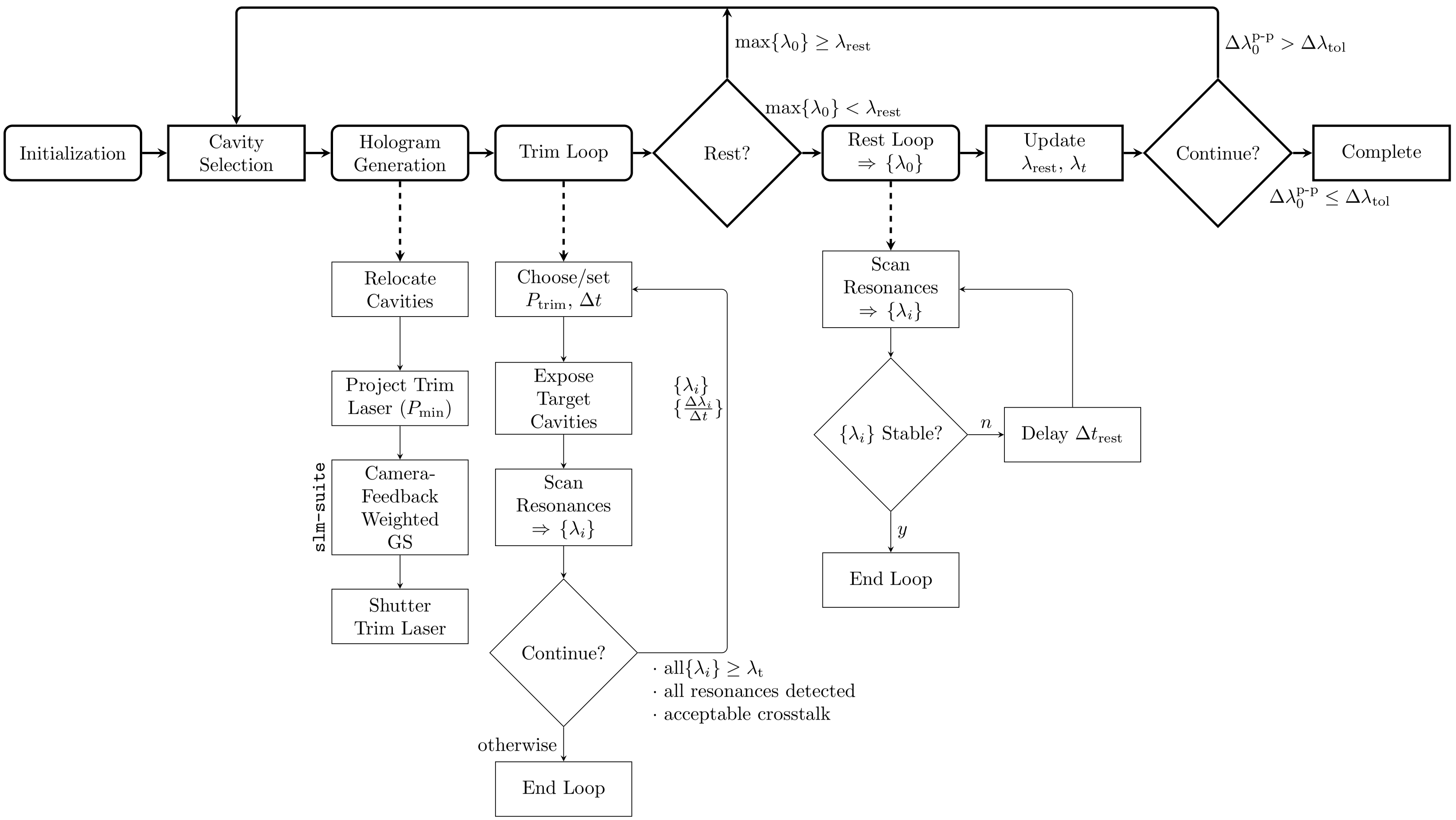

Figure 6-8: Flowchart of the holographic trimming algorithm. Trimming holograms are formed with weighted Gerchberg-Saxton (GS) algorithms and projected onto desired cavities for duration Δt with power P_{trim}. Alternating trimming and resonance readout periods continue until the instantaneous wavelength λ_i of any targeted cavity blueshifts past the target wavelength λ_t. Thereafter, a new set of target cavities is selected and trimmed. This selection and trimming sub-loop continues until all resonant wavelengths $\{\lambda_0\}$ are below the "rest" wavelength λ_{rest}, at which point trimming is halted and the resonances are continuously monitored at readout interval Δt_{rest}. When the resonances are sufficiently stable (redshifting from moisture adsorption to the silicon membrane is arrested), the total "rehydration" redshift $\Delta\lambda_0$ of each cavity is updated to better estimate the true resonant wavelength $\lambda_0 \approx \lambda_i + \Delta\lambda_0$ from the instantaneous wavelengths $\{\lambda_i\}$ during trimming. The entire process terminates when the peak-to-peak static resonant wavelength uniformity $\Delta\lambda_0^{\text{p-p}}$ drops below the desired tolerance $\Delta\lambda_{\text{tol}}$.

After initializing the cavity locations, scanning the device resonances, and calibrating the SLM (Section 6.2.2), a spot array targeting every cavity (Fig. 6-4, for example) is projected on the membrane for a short (few second) duration. Monitoring the resonances at fixed intervals $\Delta t \approx 10$ s until λ_i stabilizes to the rest wavelength λ_0 gives an initial estimate $\Delta\lambda_0 = \lambda_0 - \min\{\lambda_i\}$ for the overtune parameter of each cavity. We also update the target wavelength $\lambda_t = \min\{\lambda_0\}$ and rest wavelengths before continuing the trimming procedure. To update $\Delta\lambda_0$, we periodically conduct this same "rest loop" when λ_0 of each cavity is below an algorithmically chosen checkpoint wavelength λ_{rest}.

As described in Section 6.2, a subset of N cavities is then selected to maximize the total possible trimming distance to λ_t. The number of targeted cavities neighboring each untargeted cavity is also limited to reduce crosstalk. A spot array is then formed to evenly distribute the trimming laser to the selected devices. After confirming that the location accuracy and power uniformity of the array are within tolerance, we alternate exposure and readout intervals to grow thermal oxide with in situ monitoring. The laser power is progressively increased to reach a desired, wavelength-uniformity-dependent trimming rate. As evidenced by Fig. 6-6, the rate is relatively power-independent until reaching a threshold power. We detect and save these threshold powers for use when selecting the initial exposure power in each trimming loop.

The trimming sub-loop continues until the estimated λ_0 of any targeted cavity crosses λ_t. New cavities are then selected, targeted, and trimmed until a rest period is triggered. We developed a graphical interface (Fig. 2-1) to monitor the trimming process and array uniformity. When the peak-to-peak wavelength uniformity at the end of a rest period is below the user-defined tolerance λ_{tol}, the process is terminated.

6.3 Record-Uniformity Trimmed Microcavity Arrays

Fig. 6-10 (left) demonstrates the results of this trimming procedure applied to our prototype 8×8 pixel PhC-SLM. Prior to trimming, the hyperspectral near-field reflection image shows the large (> 200 linewidths for the mean quality factor $\langle Q\rangle = 1.6\times 10^5$) resonant wavelength variation between the otherwise spatially uniform and high-fill resonant modes. For any wavelength in this range, typically only a single device is resonantly excited — thereby preventing simultaneous coherent operation of the array.

Conversely, holographic trimming reduces the wavelength standard deviation and peak-to-peak spread by $> 100\times$ to $\sigma_\lambda = 2.5$ pm and $\Delta\lambda_0^{\text{p-p}} = 1.3\Gamma = 13$ pm, respectively, enabling all 64 devices to be resonantly excited at a common operating wavelength (Fig. 6-10, right). Since σ_λ is directly related to the corresponding hole radius and placement variability (σ_r and σ_h, respectively) with an $\mathcal{O}(1)$ design-dependent constant of proportionality, the thermal oxide homogenizes the effective dimensions of

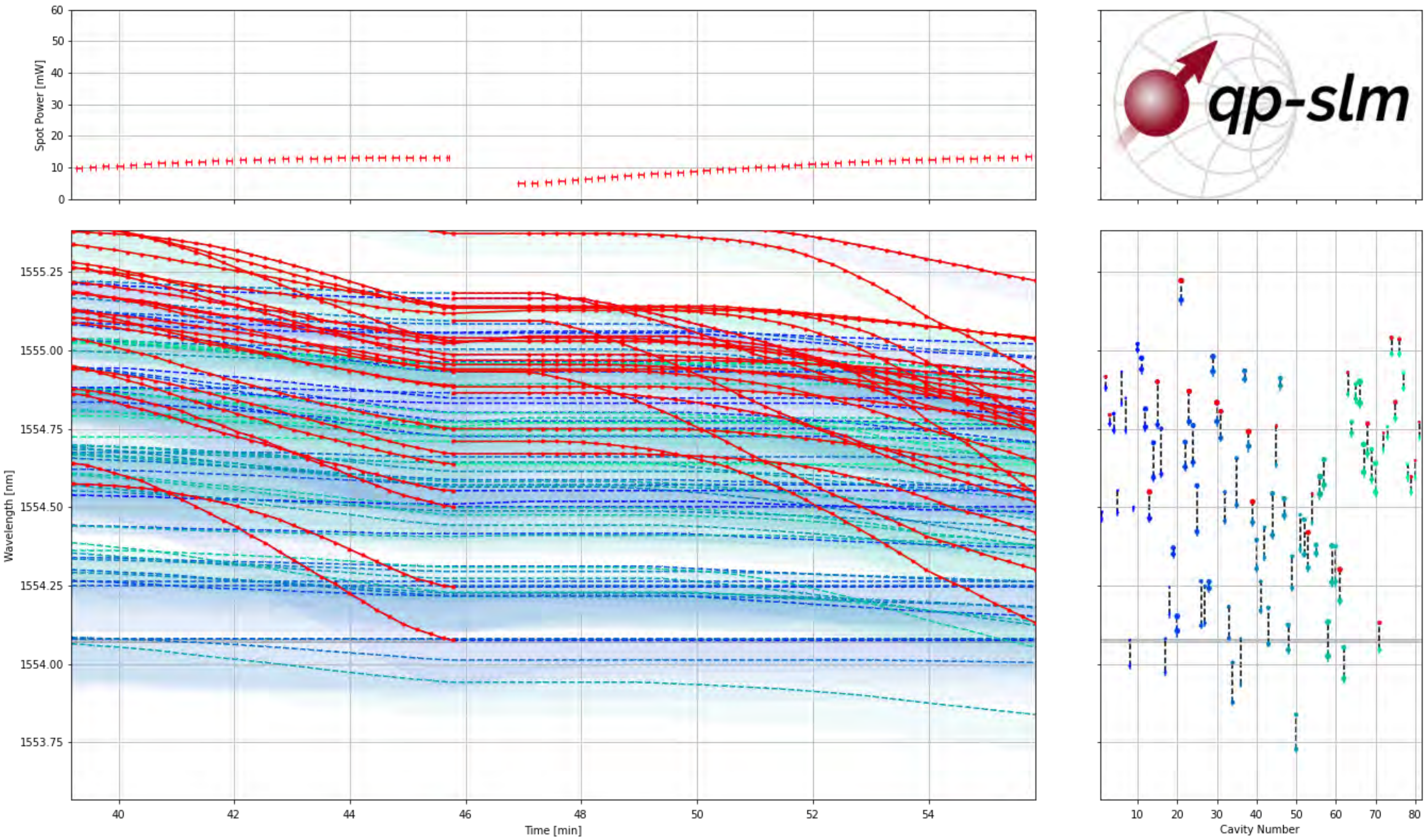

Figure 6-9: Software developed for massively parallel microcavity post-fabrication trimming using commercial SLMs. We developed `qp-slm`, a GPU-accelerated software package to generate dynamic optical focus arrays, and projected these patterns onto the optical cavity array. By varying the power (top) at desired "target" cavities (wavelength traces highlighted in red), the wavelength of each device can be selectively trimmed (center, right). We measure the resonances in parallel after each trimming step to estimate the rest wavelengths λ_0 (top dot of each device in the right panel; the lower dot indicates the instantaneous wavelength λ_i). Using this data, the optimized trimming algorithm chooses devices to tune and eventually converges on a chosen target wavelength.

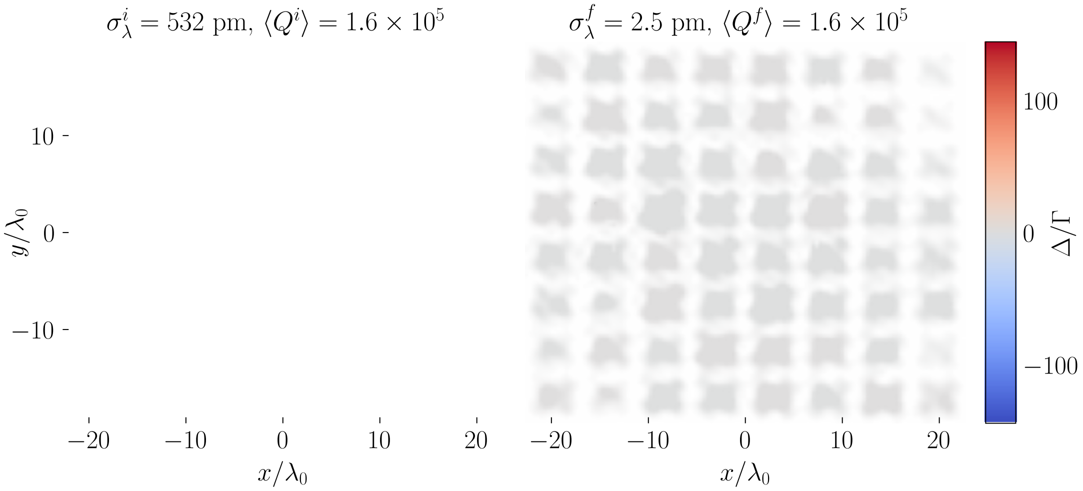

Figure 6-10: Record uniformity, high-finesse microcavity arrays. Initial and final near-field hyperspectral reflection images (color-coded by each device's wavelength normalized detuning Δ/Γ) show the $> 100\times$ reduction in resonant-wavelength standard deviation to $\sigma_\lambda = 2.5$ pm without affecting the mean quality factor $Q > 10^5$. The effective dimensions of the final array (d) are thus homogenized to $\sigma' \sim$ pm length-scales by oxidation.

each microcavity to the picometer scale. The mean quality factor and near-field reflection profile of the array remain largely unmodified throughout the process. Fig. 6-11, a micrograph of an exemplary trimmed array, depicts variable oxide growth at each cavity site as required to homogenize the array.

To our knowledge, these results are the first demonstration of parallel, non-volatile microcavity trimming. The achievable scale is currently limited by environmental factors that could be overcome with stricter process control as described in Sec. 6.2.4. Even without these improvements, the current uniformity, scale, and induced loss outperform the corresponding metrics of the previous techniques reviewed in Table 6.1, paving the way towards scalable integrated photonics with high-Q resonators.

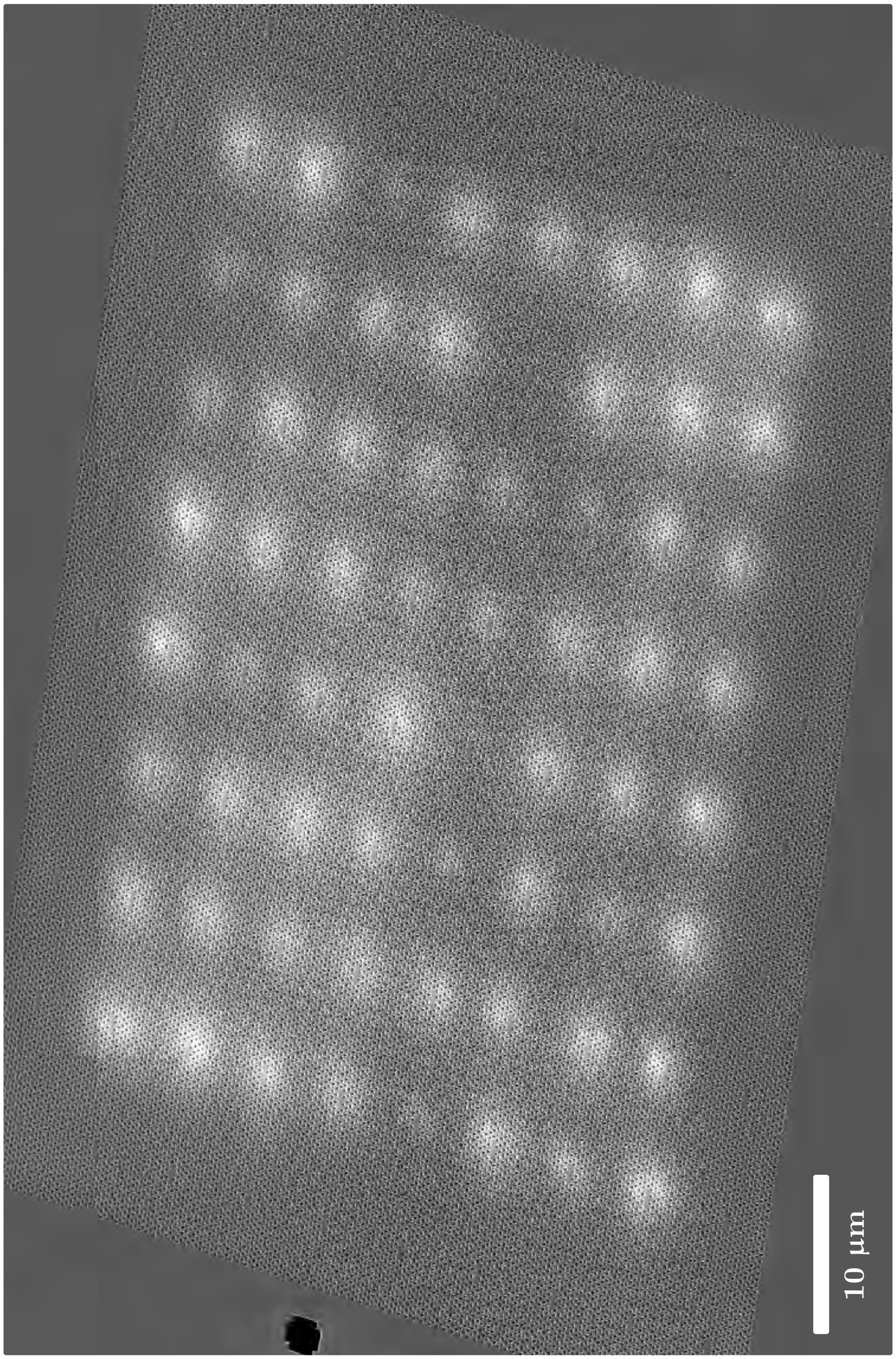

Figure 6-11: Helium-ion micrograph of a 8 × 8 PhC cavity array after post-fabrication trimming to picometer-order resonant wavelength standard deviation. Bright areas reveal regions of local oxide growth.

The two outstanding innovations of the fifth decade of this century were the jet plane and the computer. A jet plane can go one hundred times as fast as a man can run. A computer can go ten thousand times as fast as a man can compute. LIGHTNING will go ten million times as fast.

H. H. Campaigne (*NSA*, ~1958)

7

Full-DoF Spatial Light Modulation

Abstract

Ironically, the *NSA*'s *Lightning* project — seeking make a gigahertz-clock-rate electronic computer — stalled the pursuit of high-speed spatial light modulation and display technology [279]. Half a century later, this chapter revisits that open goal. From first-principles considerations of the "ideal" SLM, we propose and demonstrate a high-speed control system that eliminates metal wiring. By applying emerging "multimodal visible light communications" technology to control each microcavity, this approach avoids electrical interference and scale limits (wires for every device in a 2D array of area A cannot always be routed through the perimeter, which scales as $\sqrt{A}$). We specifically show that µLED arrays, an active research topic for augmented and virtual reality displays, enable high-speed (ns timeframe), low-power (fJ switching energy) control over coherent optical circuits.

7.1 Static Far-Field Characterization

Once trimmed to within a linewidth, a coherent field $E_\mathrm{i}(\vec{r}, t)$ incident on the PhC-SLM couples into and is reflected by each resonator, producing a paraxial far-field output [109]

$$E_\mathrm{r}(\vec{k}, t) = S(\vec{k}) \sum_{m,n} r\{\Delta_{mn}(t)\} E_\mathrm{i}(\vec{r}_{mn}, t) e^{j\vec{k}\cdot\vec{r}_{mn}} \tag{7.1}$$

that can be dynamically controlled within the single-element scattering profile $S(\vec{k})$ by setting the detuning $\Delta_{mn}(t)$ (and therefore the near-field reflection coefficient

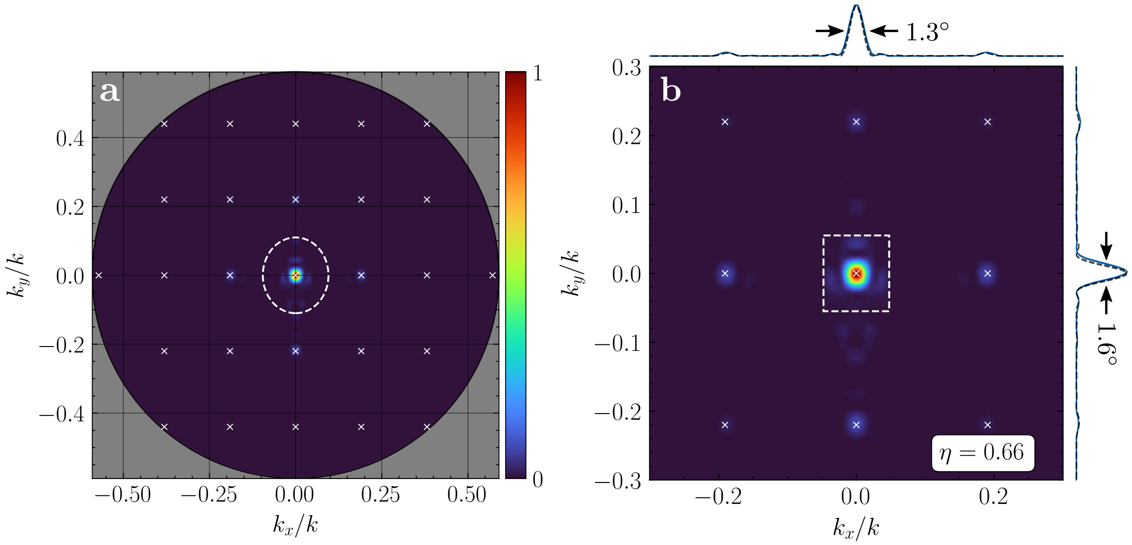

Figure 7-1: High-efficiency scattering from a trimmed microcavity array. The far-field intensity profiles (over the entire objective NA in the left panel, and zoomed to the zero-order region of interest in the right panel), half-maximum beam widths, and zero-order diffraction efficiency η_0 (integrated within the dashed white box) of a 8×8 trimmed array are provided with horizontal and vertical cross-sectional profiles (blue traces) compared to those of an array of uniform apertures with 80% linear fill (black, dashed).

$r(\Delta)$) of each resonator. Experimentally, we measure the intensity pattern $|E_r(\vec{k})|^2$ on the back focal plane of a microscope objective above the PhC-SLM (using the single-device characterization setup in Sec. 2.5.1) and optically program $\Delta_{mn}(t)$ via photo-excited free carriers.

Without any control input ($\Delta_{mn} \approx 0$), Fig. 7-1 shows the static far-field intensity pattern $|E_r(\vec{k}|^2$ of a widefield-illuminated (i.e. $E_i(\vec{r}) \approx E_i$) 8×8 trimmed array with $\{Q\} = 1.85 \times 10^5$ and $\sigma_\lambda = 5$ pm at $\lambda = 1562$ nm. The inverse-designed cavity unit cells minimize scattering into undesired diffraction orders, producing a high-efficiency ($\eta_0 = 0.66$) zero-order beam with the expected 1.3° and 1.6° horizontal and vertical beamwidths given the $42.0\lambda \times 36.4\lambda$ aperture size. The cross-sectional beam profiles are well matched to those of uniform apertures with width $w = 0.8\lambda$, suggesting an 80% effective linear fill of the array. This extracted value agrees with the observed zero-order efficiency and the array's physical design (each $16a \times 16a$ cavity offering near-unity fill was padded to $20a \times 20a$ with unoptimized holes to prevent coupling to adjacent cells).

7.2 All-Optical Switching

After confirming the static performance of the array, we conducted optical switching experiments with two sources: an incoherent µLED array and a pulsed visible laser. Before characterizing either source, we first developed an analytic model for all-optical switching in slab-type PhC cavities to estimate the required tuning energy.

7.2.1 Analytic Model for Slab Switching

After absorption in a semiconductor slab, a control pulse produces a refractive index change

$$\delta n(\vec{r},t) = -\alpha_c N(\vec{r},t) + \alpha_t T(\vec{r},t) \tag{7.2}$$

proportional to the photo-excited carrier density N and induced temperature change T through the plasma dispersion and thermo-refractive effects, respectively. The thermo-refractive coefficient $\alpha_t = \mathrm{d}n/\mathrm{d}T$ and empirical free-carrier "scattering volume" $\alpha_c = -\mathrm{d}n/\mathrm{d}N$ are typically both positive such that the two effects counteract one another. The evolution of δT and N are governed by the diffusion equations

$$\frac{\partial N(\vec{r},t)}{\partial t} = \nabla \cdot (D_c \nabla N) - \frac{N}{\tau} + g(\vec{r},t) \tag{7.3a}$$

$$\frac{\partial T(\vec{r},t)}{\partial t} = \nabla \cdot (D_t \nabla T) + q(\vec{r},t) \tag{7.3b}$$

given the thermal diffusivity D_t and assuming ambipolar diffusion of carriers with lifetime τ and diffusivity D_c. Over relevant timescales $t > w^2/D_c$ in a w-thick uniform slab, vertical diffusion can be neglected to yield solutions

$$N(\vec{r},t) = g(\vec{r},t) *_{\vec{r},t} G(\vec{r}, 2D_c t) e^{-t/\tau} \tag{7.4a}$$

$$T(\vec{r},t) = q(\vec{r},t) *_{\vec{r},t} G(\vec{r}, 2D_t t) \tag{7.4b}$$

expressed as convolutions ($*$) of the inhomogeneous sources $g(\vec{r},t)$ and $q(\vec{r},t)$ with the two-dimensional Green's function

$$G(\vec{r},\sigma^2) = \frac{1}{2\pi w \sigma^2} \exp\left\{-\frac{|\vec{r}|^2}{2\sigma^2}\right\}. \tag{7.5}$$

All variables are considered uniform along the vertical axis; $\vec{r}$ in our notation thus corresponds only to transverse coordinates in the slab plane. We specifically consider solutions to Eqns. 7.4 in response to a focused, square-wave Gaussian control pulse with beam waist $2\sigma_p$, pulse-width T, and pulse (photon) energy E (E_0) absorbed into the cavity with efficiency η_{abs}. The results can be considerably simplified with the conservative (i.e. underestimating plasma dispersion at short timescales $t \lesssim \tau$), albeit crude, assumption of instantaneous carrier diffusion to the diffusion length

$\sqrt{D_c\tau}$. This method decouples carrier decay and diffusion to yield the carrier density

$$N(\vec{r},t) = N_0(t)G(\vec{r}, 2D_c\tau + \sigma_p^2) \tag{7.6}$$

with time-dependent total population

$$N_0(t) = \eta_{\text{abs}}\frac{\tau}{T}\frac{E}{E_0}\begin{cases}(1-e^{-t/\tau}), & t \le T \\ e^{-t/\tau}(e^{T/\tau}-1), & t > T.\end{cases} \tag{7.7}$$

The recombination of each carrier pair releases the bandgap energy E_g back into the slab with volumetric heat capacity c_v, yielding the source

$$q(\vec{r},t) = -\left(\frac{\partial N}{\partial t}\right)_{\text{decay}}\frac{E_g}{c_v} = \frac{N(\vec{r},t)}{\tau}\frac{E_g}{c_v} \tag{7.8}$$

that produces the temperature profile

$$T(\vec{r},t) = \frac{E_g}{c_v\tau}N_0(t) *_t G(\vec{r}, 2D_t t + 2D_c\tau + \sigma_p^2). \tag{7.9}$$

Note that we neglect additional initial heating from above-band absorption.

Given sufficiently small $|\delta n|$, the resulting linewidth-normalized resonance shift

$$\tilde{\Delta}(t) = \Delta(t)/\Gamma = -Q\int\frac{\delta n}{n}(\vec{r},t)|\vec{E}(\vec{r})|^2 \mathrm{d}^3\vec{r} \tag{7.10}$$

for the electric field profile $\vec{E}(\vec{r})$ with normalization ($\int|\vec{E}(\vec{r})|^2\mathrm{d}^3\vec{r} = 1$) is well-approximated by first-order perturbation theory [18]. We consider a Gaussian-shaped mode envelope $|\vec{E}|^2 = G(\vec{r},\sigma_0)$ fully-confined with uniform transverse amplitude within the high-index slab.

Since Eqn. 7.9 must be evaluated numerically, we assume a constant temperature change $T(\vec{r},t) = T(0,t)$ across the mode — valid for typical experimental regimes of interest where $\sigma_0 \ll 2D_t t + 2D_c\tau + \sigma_p$ — to avoid the additional integration in Eqn. 7.10. The overlap between the optical mode and the static free carrier profile, on the other hand, can be analytically evaluated to yield the combined result

$$\begin{aligned}\tilde{\Delta}(t) = &\frac{\alpha_c}{n}N_0(t)\frac{\sigma_0^2}{2D_c\tau + \sigma_p^2 + \sigma_0^2}\left(\frac{Q}{V}\right) \\ &- Q\frac{\alpha_t}{n}\frac{E_g}{c_v\tau}N_0(t) *_t G(0, 2D_t t + 2D_c\tau + \sigma_p^2)\end{aligned} \tag{7.11}$$

for the cavity mode volume $V = \int\epsilon|E|^2\mathrm{d}^3\vec{r}/\max\{\epsilon|E|^2\} = 2\pi w\sigma_0^2$. Since the reflected signal directly tracks the cavity amplitude in cross-polarization, the normalized

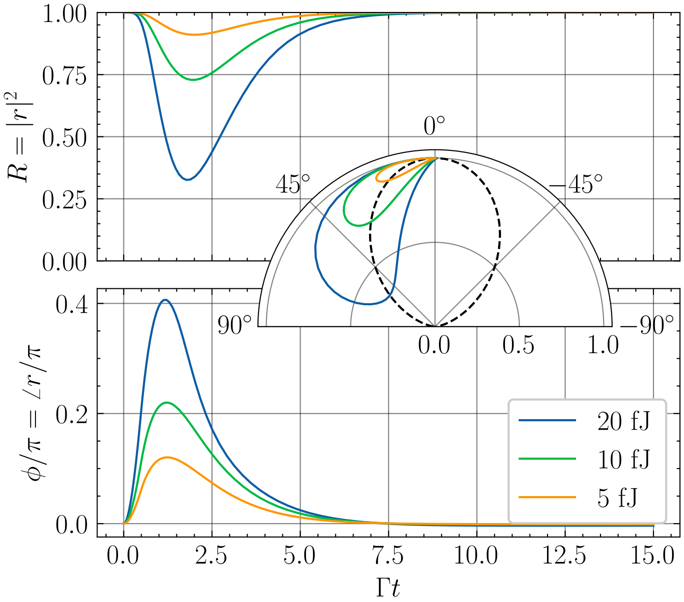

Figure 7-2: Estimated normalized reflection coefficient $r(t) = \sqrt{R(t)}e^{j\phi(t)}$ as a function of switching energy for the parameters in Table 7.1. Insets: same results in polar form for comparison to the Lorentzian reflection profile $r(\Delta) = 1/(1+j\Delta)$ of a cavity under cross-polarized excitation with static detuning Δ (black dashed line).

reflectivity

$$r(t) = \int_0^t \mathrm{d}t' e^{-\Gamma(t-t')-i\int_t^{t'}\mathrm{d}t''2\Delta(t'')} \tag{7.12}$$

is finally found by numerically integrating the cavity evolution as dictated by coupled mode theory [109] (c.f. Eqn. 4.38).

Fig. 7-2 plots the switching characteristics for the parameters in Table 7.1. Free-carrier dispersion dominates the response for the nanosecond-order timescales of interest followed by a slow (µs-order), weak ($|\tilde{\Delta}| \ll 1$) thermal rebound. The three order-of-magnitude timescale difference effectively decouples the two modulation mechanisms. Note that the true reflection coefficient deviates from the Lorentzian response of a quasi-static cavity due to the fast (relative to the cavity decay rate Γ) carrier dynamics. These results indicate that a SLM with 10^6 pixels operating with $\omega_s > 2\pi \times 100$ MHz could be realized with $\mathcal{O}$(watt) optical control power.

7.2.2 Experimental Setup

To experimentally reconstruct the expected complex, time-varying reflection coefficients, we combined the homodyne setup used for thermal noise measurements (Fig. 4-4) with the updated wide-field characterization setup in Fig. 2-8. The resulting shot-noise-limited balanced homodyne detection setup in Fig. 7-3a-b enables

Parameter	**Value**	**Source**
n_{Si}	3.48	[208]
E_g	1.12 eV	[208]
α_t	1.8×10^{-4} K^{-1}	[208]
c_v	1.64 J/cm^3·K	[87]
D_t	0.26 cm^2/s	[87]
α_c	8×10^{-9} µm^3	[280] (Linearized)
D_c	19 cm^2/s	[61]
τ	1 ns	[61]
λ_0	1550 nm	Assumed
Q	200,000	Assumed
$\tilde{V}$	0.95	[87]
w	220 nm	Measured
$2\sigma_0$	0.66 µm	$2\sqrt{V/(2\pi w)}$
λ_p	0.53 µm	Assumed
T	0.5 ns	Assumed
$2\sigma_p$	0.22 µm	$\lambda_p/2$
η_{abs}	0.6	FDTD

Table 7.1: Parameters used for the simulated switching results in Fig. 7-2. Pulse parameters were selected to mimic the typical experimental conditions of Sec. 7.3.

complex reflection coefficient measurements with greater than >3 dB shot-noise clearance below 1 GHz. A photograph of the updated setup is shown in Fig. 7-4.

Signal light reflected from the cavity combines with a path-length-matched (to within ∼mm based on time-delay measurements with a picosecond-class pulsed laser) local oscillator (LO), and both signals are coupled into a balanced detector using anti-reflection coated fibers.[1] The in-phase ($I(t)$) and quadrature ($Q(t)$) components of the cavity reflection were sequentially measured by locking to the first and second harmonics of the balanced output in the presence of a piezo-driven LO phase dither. The resonant, cross-polarized cavity reflection R and phase shift ϕ are then reconstructed as

$$R = \frac{[V_p - I(t)]^2 + Q^2(t)}{V_p^2} \qquad \phi = \arctan \frac{Q(t)}{V_p - I(t)} \tag{7.13}$$

by normalizing to the measured peak voltage swing V_p of the interference signal.

---

[1] Anti-reflection coated fibers were crucial to these experiments. Without them, strong LO light reflects from the fiber facet, reflects off the cavity, and re-couples into the fiber. The LO therefore couples to itself in absence of a signal beam, which can be readily observed on a camera.

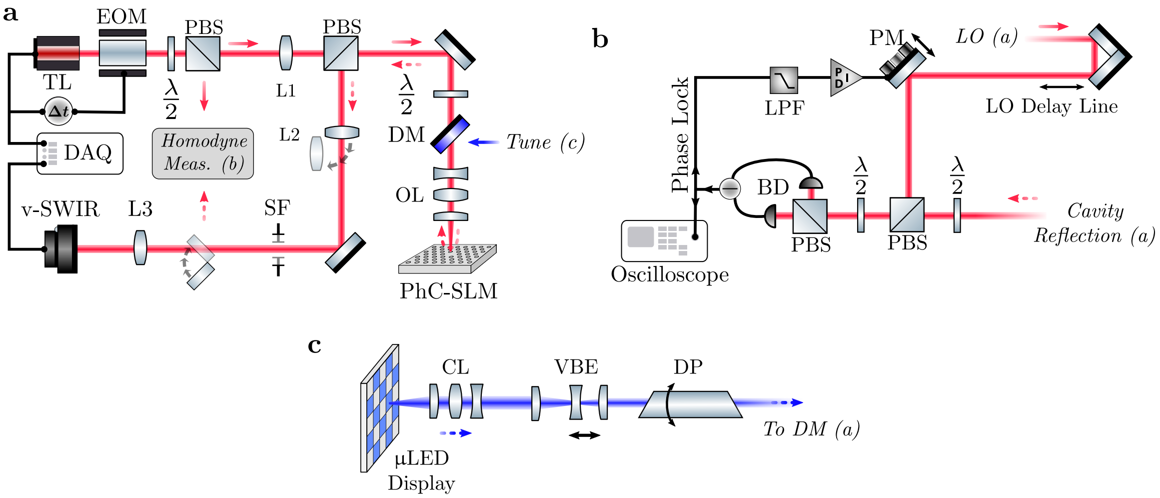

Figure 7-3: Setups for homodyne switching experiments. A balanced homodyne detector (b) is added to the previously described wide-field characterization setup (a; also see Sec. 2.5.1) to characterize µLED- (c) or laser-driven (Fig. 6-2b) all-optical switching. LO: local oscillator; PM: piezo mirror; BD: balanced detector (Thorlabs PDB480C-AC); Phase Lock: TEM LaseLock; LPF: low-pass filter; CWTL: continuous-wave trimming laser (Coherent Verdi V18); MLD: modulated laser diode (Hubner Cobolt or PicoLAS LDP); BE: 5× visible beam expander; LCOS: high-power liquid crystal SLM (Santec SLM-300); L4: 300 mm; L5: 250 mm; PD: photodetector; CL: collection lens (Zeiss Fluar 5×/0.25 NA); VBE: 0.5 × −2× variable beam expander; DP: dove prism. Other labels are described in Fig. 2-8.

7.2.3 Incoherent Switching with a µLED Array

Originally developed for high-bandwidth visible light communication and optically pumped laser arrays, the µLED display (Fig. 7-5) consists of a 16 × 16 array of individually-addressable gallium nitride µLEDs with >150 MHz small-signal bandwidth and ∼10^6 cd/m^2 peak luminances (at 450 nm) flip-chip bonded to high-efficiency CMOS drivers [67, 281].

Optimal Imaging

Using the setup in Fig. 7-3c, we imaged this 100 µm-pitch display with variable demagnification and rotation onto the PhC cavity array. The collection optics in Fig. 7-3c maximize the intensity of a µLED display projected onto the PhC membrane within the constraints of the constant radiance theorem. Assuming a Lambertian emission profile, geometric optics gives the collection efficiency $\eta_c = \alpha_c^2$ for an objective lens (CL) with numerical aperture α_c focused on the µLED display. The projection efficiency η_p through the projection objective (OL, with numerical aperture α_p) depends on the relative pupil sizes of both objectives and can be similarly approximated

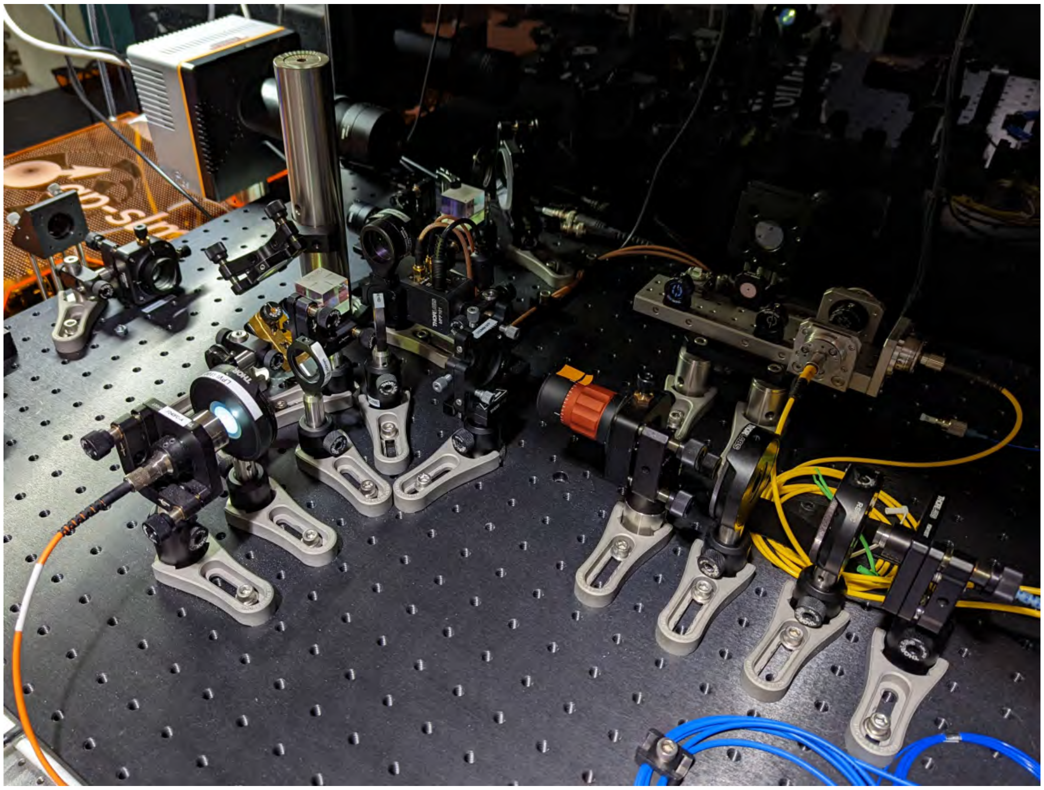

Figure 7-4: Updated setup with conbined widefield readout and homodyne measurement. The fiber-coupled homodyne detector is located in the top-right corner of the setup. By tapping off signal light from the imaging path with a 90:10 beamsplitter, the cavity reflection can be monitored on a camera while locked to the homodyne detector. This feature significantly assists system alignment and monitoring.

from geometric optics. As illustrated in Fig. 7-6, the resulting intensity enhancement $\zeta = \eta_c\eta_p/M^2$ between the source and image (with magnification M) reaches a maximum $\zeta_{\max} = \frac{1}{M^2+(1-\alpha_p^2)/\alpha_p^2}$ when the CL-collimated light overfills the back aperture of OL. The resulting design criteria,

$$\alpha_c > \sqrt{\frac{M^2\alpha_p^2}{(M^2-1)\alpha_p^2+1}}, \tag{7.14}$$

is achieved for our imaging setup with $\alpha_c = 0.25$, $\alpha_p = 0.95$ (specifically chosen to maximize $\zeta_{\max}$), and $M \approx 1/30$. After CL, The overall magnification and rotation are fine-tuned with a variable beam expander and Dove prism, respectively.

Under these optimum illumination conditions, digitally triggering the CMOS drivers enables reconfigurable, binary optical addressing as illustrated by the imaged projections of the μLED onto the PhC-SLM in Fig. 7-7.

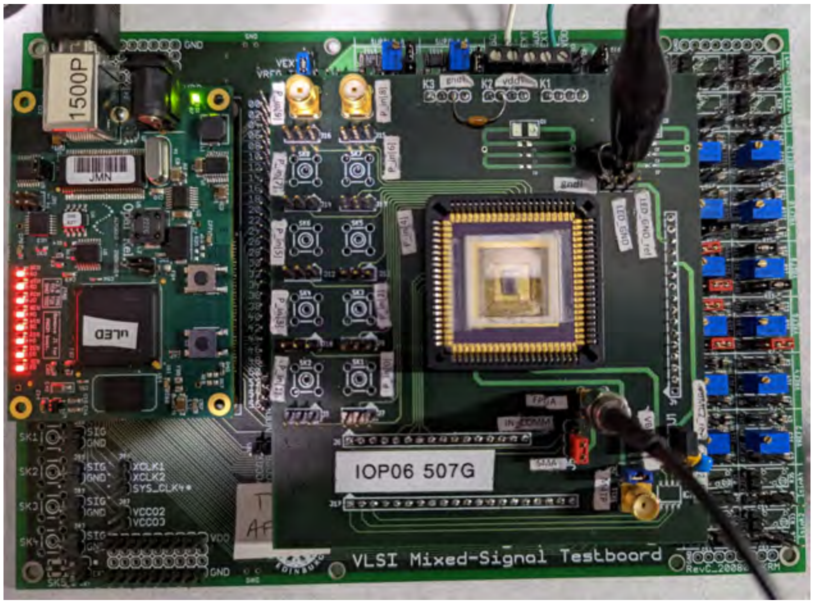

Figure 7-5: A high-speed µLED display developed by our collaborators at the Institute of Photonics. The setup consists of a FPGA signal generator (left), a µLED daughter card (center) with a packaged gallium nitride µLED array (16 × 16 or 10 × 40), and a signal distribution board (background) for communication between all units.

Single-Pixel Switching

We measured the resulting pixel reflection amplitude and phase the locked, shot-noise-limited balanced homodyne detector described in Sec. 7.2.2. Fig. 7-8 depicts the maximum phase shift $\Delta\phi$ as a function of CMOS trigger duration T_{CMOS} and imaged pump energy density $E_{\mu\mathrm{LED}}$. Single-cavity switching is possible with energy densities below 10 fJ/µm^2 (corresponding to ∼100 fJ/µm^2 total energy for our chosen demagnification) and a minimum trigger duration $T_{\mathrm{CMOS}} \approx 5$ ns. Shorter trigger pulses produce output probe pulses with relatively constant widths T_{switch} (due to the µLED fall time) and insufficient energy for high-contrast switching.

7.2.4 Coherent Switching via Pulsed Laser Fan-out

Confining visible pump pulses in space and time to the silicon free-carrier diffusion length (∼ 1µm) and lifetime ($\tau \approx 1$ ns), respectively, would reduce the required switching energy and maximize bandwidth bandwidth. While both metrics are achievable with recent state-of-the-art µLED displays, we demonstrated the expected performance enhancement with a pulsed visible ($\lambda = 515$ nm) laser. Fig. 7-9a shows that — in qualitative agreement with the analytic model of Sec 7.2.1 — 3 dB power reflectivity changes and high-contrast phase modulation are feasible for 5 fJ pump pulses with $T_{\mathrm{switch}} \approx 1$ ns. The achievable modulation bandwidth is limited by two

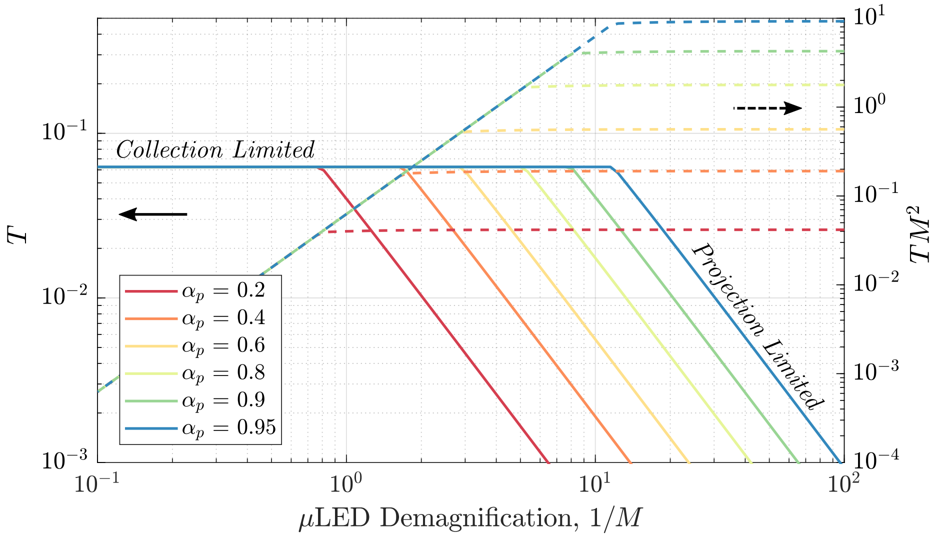

Figure 7-6: Ideal imaging transmission T (solid curves) and intensity enhancement TM^2 (dashed curves) of a Lambertian emitter through two opposing infinity corrected objectives as a function of demagnification $1/M$. The collection objective (with numerical aperture $\eta_c = 0.25$ set to match experiments) serves as a tube lens for the projection objective (numerical aperture η_p). In the "collection limited" regime (collimated light from the collection objective does not fully fill the back aperture of the projection lens), total transmission varies as a function of M but intensity enhancement is variable. We alternatively operate in the "projection limited" regime (collected light overfills the projection lens' back aperture) where $T \propto M^2$ and the constant intensity enhancement increases with η_p, motivating the use of a high-numerical aperture projection lens.

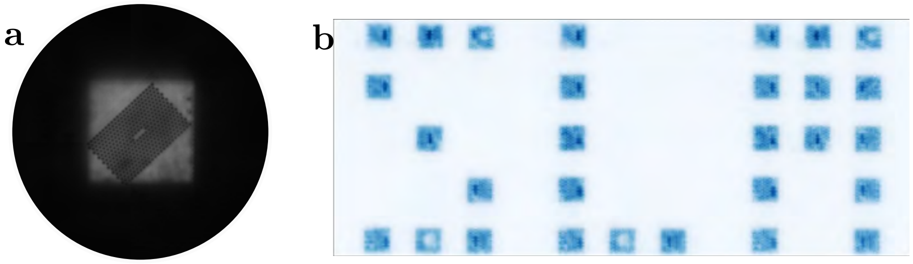

Figure 7-7: Experimental photographs of µLEDs imaged onto single cavities (a) and cavity arrays (b). The width of the demagnified µLEDs is ~10µm and ~3µm in (a) and (b), respectively.

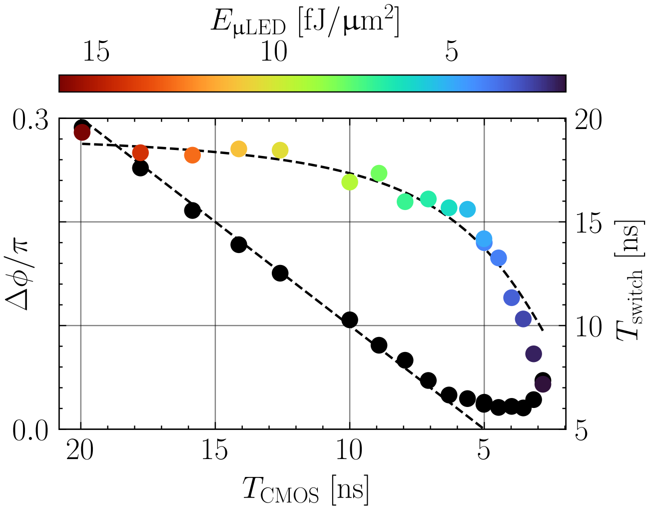

Figure 7-8: Peak phase shift $\Delta\phi$ and half-maximum switching interval T_{switch} produced by pulses from a CMOS-integrated μLED display imaged onto the cavity array as a function of trigger duration T_{CMOS} and pulse energy density $E_{\mu\mathrm{LED}}$.

parameters: the free-carrier lifetime τ and the cavity bandwidth Γ. For full DOF temporal modulation, the physically-limited modulation bandwidth ($\omega = 1/\tau$, in this case) should exceed the limiting optical bandwidth, namely the cavity linewidth Γ. To compare these two timescales in our devices, we measured the normalized small-signal transfer function $T(\omega)$ between a harmonic pump power (produced by a network analyzer-driven amplitude electro-optic modulator) and the output phase-locked homodyne response. The results in Fig. 7-9b match the expected second-order response $T(\omega) = 1/\{[1 + (\omega\tau)^2]\,[1 + (\omega/\pi\Gamma)^2]\}$ for a fitted carrier lifetime $\tau = 1.1$ ns (corresponding to a 150 MHz bandwidth) and the measured $\Gamma = 1.0$ GHz. Complete spatiotemporal modulation therefore requires higher-Q resonators; however, the current regime of operation enables near-complete control over a larger bandwidth $\omega_s = 2\pi \times 135$ MHz $\approx 1/\tau$, i.e. without significantly degrading the carrier-lifetime-limited modulation bandwidth.

7.3 Nanosecond, Femtojoule Spatial Light Modulation

Combining these optimized switching characteristics with the space-bandwidth-limited vertical beaming of each resonator enables multimode programmable optics approaching the fundamental limits of spatiotemporal control. We currently probe the PhC-SLM in a wide-field, cross-polarized setup that produces amplitude-dominant Lorentzian reflection profiles $r(\Delta) \propto 1/(1 + j\Delta)$ regardless of the resonator coupling regime

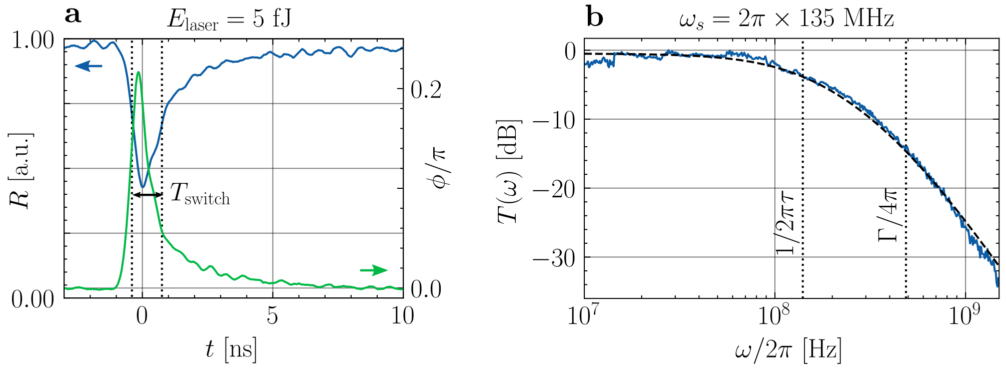

Figure 7-9: (a) Complex reflectivity $r = \sqrt{R}e^{j\phi}$ modulation with femtojoule-order pulse energies E_{laser} from a focused visible laser. (b) Output probe to input visible (pump) power transfer function $T(\omega)$ fit to a second-order response function, yielding a $\omega_s = 2\pi \times 135$ MHz bandwidth limited by the free carrier lifetime $\tau \approx 1.1$ ns and cavity bandwidth $\Gamma \approx 1$ GHz.

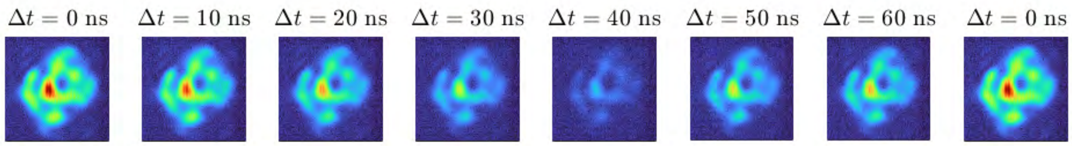

Figure 7-10: Near-field single-cavity reflection images measured via wide-field pump-probe spectroscopy as a function of time delay Δt. Extinction (with μLED switching, in this case) exceeds 10 dB at an optimal delay $\Delta t = 40$ ns.

(cavity emission is isolated from specular reflection). For simplicity, we therefore conducted proof-of-concept demonstrations using the PhC-SLM as an array of high-speed binary amplitude modulators. In this modality, a nanosecond-class pulsed visible laser is passively fanned out to the desired devices. Devices targeted by pump light are detuned far from resonance ($\Delta \gg \Gamma$) and effectively extinguished, whereas unactuated cavities retain their high $\Delta \approx 0$ reflectivity.

We used pump-probe spectroscopy to image these few-nanosecond switching events. Short infrared probe pulses were carved with the electro-optic amplitude modulator (DC biased to an intensity null) in Fig. 7-3 and variably delayed to coincide with the arrival of visible pump light at the PhC membrane, gating probe field transmission to the IR camera. We then measured the near- and far-field reflection as a function of the probe delay to reconstruct switching events with sub-nanosecond time resolution. Fig 7-10 shows near-field images of a single cavity as a function of time delay and Fig. 7-11 plots the resulting far-field intensity profiles $|E_r|^2$ for horizontal and vertical on-off gratings. For a 5 ns probe pulse width, the maximum near-field extinction of targeted cavities (7.4 dB and 9.8 dB for horizontal and vertical gratings, respectively)

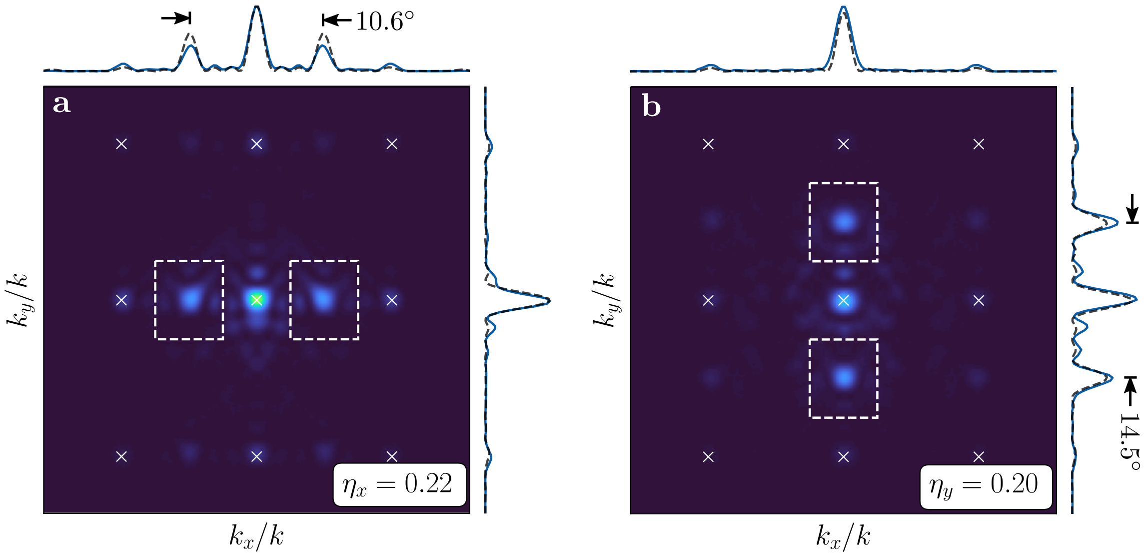

Figure 7-11: Analogous results to Fig. 7-1 for the switched array with an optically-patterned horizontal (vertical) amplitude grating at the maximum extinction time $t_0 + 6$ ns, producing $\pm 1^{\text{st}}$-order diffraction peaks over a 10.6° (14.5°) field-of-view and diffraction efficiency $\eta_x = 0.22$ ($\eta_y = 0.20$).

occurs within a ∼6 ns delay; i.e. just after the pump and probe pulses completely overlap. This minimum probe pulse width is limited by the requirement for high imaging contrast between probe pulses and leakage (due to the imperfect probe modulator extinction) given the instrument-limited trigger repetition rate (∼MHz) and camera integration time.

As expected, light is primarily scattered into first-order diffraction peaks within the $> 10°$ 2D field-of-view of $S(\vec{k})$. The illustrated cross sectional beam profiles are again in close agreement with analytic results for a 80% filled linear array of uniform apertures (black dashed lines). Notably, the total emitted power for the horizontal grating in Fig. 7-11a is a factor of ∼2 *larger* than expected due to a corresponding power increase in unactuated cavities during switching events. We attribute this crosstalk to residual coupling between adjacent cavities and have scaled the associated theory curve accordingly to facilitate pattern comparison. In both cases, the pattern diffraction efficiencies — measured as the fraction of integrated power within the outlined regions in Fig. 7-11 — $(\eta_x, \eta_y) = (0.22, 0.20)$ compare favorably to that of the fitted uniform aperture array (32%). Even with sub-optimal amplitude modulation, these experimental efficiencies exceed those of previous resonator-based experiments due to the near-fully-filled array of our high-directivity PhC antennas [34].

7.4 Performance Comparisons

Table 7.2 compares the PhC-SLM demonstrated here to other actively-controlled, 2D SLMs (Fig. 1-3).

Class [Year]	**Device [Ref]**	$\boldsymbol{N_x \times N_y}$	$\boldsymbol{\Omega_s = \frac{\lambda}{\Lambda_x} \times \frac{\lambda}{\Lambda_y}}$	$\boldsymbol{\zeta}$ **[%]**	$\boldsymbol{\omega_s/2\pi}$ **[Hz]**
EO [2022]	**PhC-SLM**	$\mathbf{8 \times 8}$	$\mathbf{10.6^\circ \times 14.5^\circ}$	**64**	$\mathbf{1.4 \times 10^8}$
EO [2021]	$\chi^{(2)}$ polymer-coated grating [41]	4×4	$0.2^\circ \times 0.2^\circ$	—	5.0×10^7
EO [2019]	$\chi^{(3)}$ plasmonic resonator [40]	4×4	$0.8^\circ \times 1.1^\circ$	20*	1.0×10^9
EO [2017]	Bilayer guided resonators [38]	6×6	$1.3^\circ \times 0.3^\circ$	40*	2×10^8
EO [2011]	$\chi^{(2)}$ polymer-coated grating [25]	4×4	$0.1^\circ \times 0.1^\circ$	18*	8.0×10^5
EO [2005]	MQW micropillar modulators [39]	128×128	$1.3^\circ \times 1.3^\circ$	50	1.3×10^7
Thermal [2018]	Asymmetric Fabry-Perot cavity [34]	6×6	$3.4^\circ \times 3.4^\circ$	59	1.4×10^4
Thermal [2013]	Waveguided phased array [33, 282]	8×8	$9.9^\circ \times 9.9^\circ$	10*	1.1×10^6
MEMS [2019]	Grating phase shifters [27]	160×160	$4.4^\circ \times 4.1^\circ$	85*	5.5×10^4
MEMS [2019]	Piston mirrors [36]	960×540	$3.4^\circ \times 3.4^\circ$	—	2.0×10^4
MEMS [2014]	High-contrast gratings [26]	8×8	$2.7^\circ \times 2.7^\circ$	36*	5.0×10^5
MEMS [2001]	Piston mirrors [35]	256×256	$2.2^\circ \times 2.2^\circ$	86	5.0×10^5
LC [2020]	Plasmonic metasurface [31]	3×3	$0.3^\circ \times 0.3^\circ$	—	2.5×10^1
LC [2019]	“MacroSLM" [30]	1536×1536	$3.0^\circ \times 3.0^\circ$	95	6.0×10^2
LC [1994]	Binary ferroelectric LC [29]	256×256	$2.2^\circ \times 2.2^\circ$	79	8.3×10^3

Table 7.2: Performance comparison of selected active 2D spatial light modulators from Fig. 1-3. Estimated fill factors ζ are marked by a *.

Wavelength-steered devices and switch arrays are omitted to restrict focus to the typical SLM architecture in Fig. 1-2. Notably, while beamsteering with PhC waveguides [54, 283, 284] and laser arrays [285] has recently been demonstrated, our device is the first (to our knowledge) to feature simultaneous emission from a 2D array of individually controllable PhC pixels.

If the theory of making Telescopes could at length be fully brought into Practice, yet there would be certain bounds beyond which Telescopes could not perform. For the air through which we look upon the stars is in perpetual Tremor.

Sir Isaac Newton, *Opticks* (1704).

8

Future Avenues

These proof-of-concept experiments demonstrate near-complete spatiotemporal control of a narrow-band optical field filtered in space and time by an array of wavelength-scale, high-speed resonant modulators. While the general resonant architecture (Fig. 1-2c) is applicable to a range of microcavity geometries and modulation schemes, the combination of our high-Q, vertically-coupled PhC cavities with efficient, all-optical free-carrier modulation achieves (C1-5) with an ultrahigh per-pixel spatiotemporal bandwidth $\nu \approx 5.6$ MHz $\cdot$ sr. This MHz-order modulation bandwidth per aperture-limited spatial mode corresponds to a more than ten-fold improvement over the 2D spatial light modulators reviewed in Fig 1-2b. Our wafer-scale fabrication and parallel trimming offer a direct route towards scaling this performance to spectrally-multiplexed, $\mathcal{O}(\mathrm{cm}^2)$ apertures for exascale interconnects beyond the reach of current electronic systems, thus motivating the continued development of optical addressing and control techniques.

The PhC-SLM opens the door to a number of applications and opportunities, a few of which we are currently pursing and describe here.

High-definition, high-frame-rate holographic displays

For a desired resolution r, holographic displays require $\mathcal{O}(r^4)$ DoF per frame to reconstruct a scalar light field with two transverse coordinates and two angular coordinates. While "visually acceptable" frame rates and resolutions are inaccessible by today's spatial light modulators, the PhC-SLM's large spatiotemporal bandwidth could enable high-definition, high-speed holographic projections. For this application, one key goal is to achieve phase-only modulation with photonic crystal cavities. Sec. 2.3.1 shows that this objective can be achieved with an added backreflector, which enables $> 90\%$

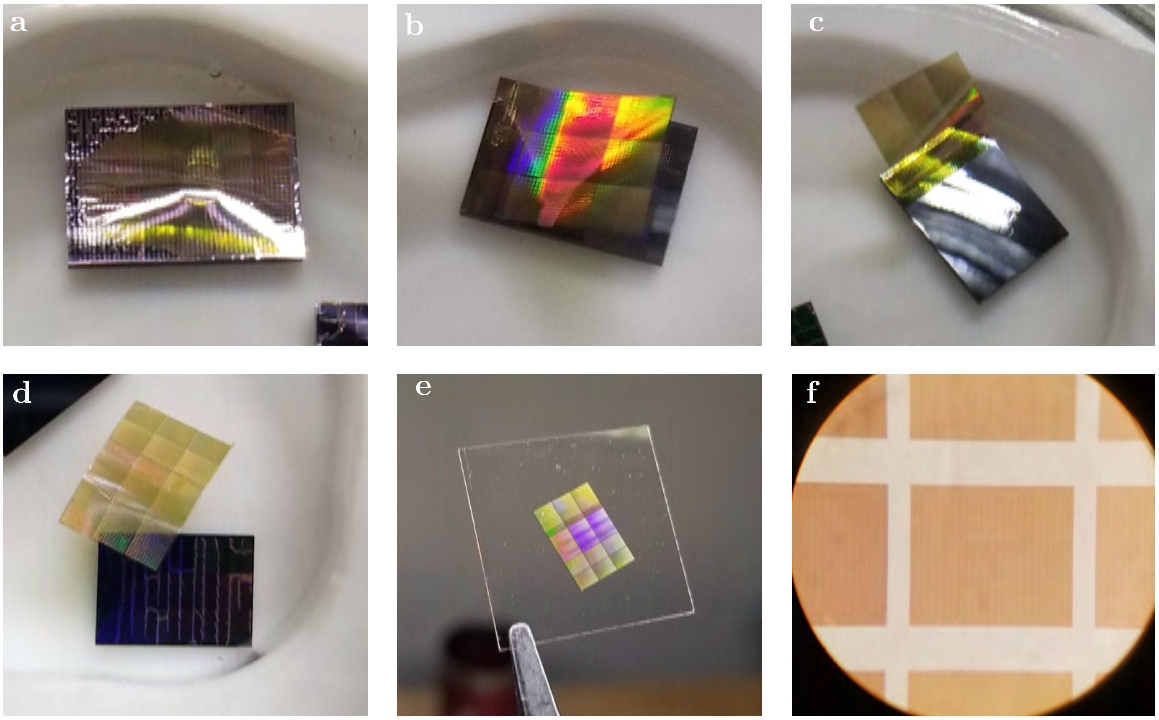

Figure 8-1: Full-die (6 mm × 8.5 mm) membrane release and transfer. A two-hour wet etch in concentrated hydroflouric acid releases the photonic crystal membrane from the SOI substrate (a-d), enabling high-quality transfer to non-native substrates such as a glass slide (e-f).

unidirectional cavity coupling to a Gaussian input. Heterogeneously integrating our cavity arrays onto a mirrored substrate would therefore enable high-efficiency holography (Fig. 2-11) with optimized analog detunings. Similarly, directly integrating our cavity arrays onto a high-bandwidth μLED display would eliminate the external imaging optics and associated design constraints (Fig. 7-7). We are currently pursing numerous experimental avenues for this heteogenous integration: full membrane transfer (Fig. 8-1), transfer printing (Fig. 8-2)[1], and flip-chip integration (Fig. 8-3).

Focal plane array sensors

Operated in reverse, the PhC-SLM also constitutes a hyperspectral sensor that maps patterned index perturbations to magnified field modulations with μm-order spatial resolution, overcoming the limitations of guided-resonance sensors [287] for high-performance, space-constrained imaging in applications from endoscopy to bolometry

---

[1] Professor Michael Strain's group — experts in transfer printing integrated photonic circuits [286] — performed the PhC cavity transfer illustrated here.

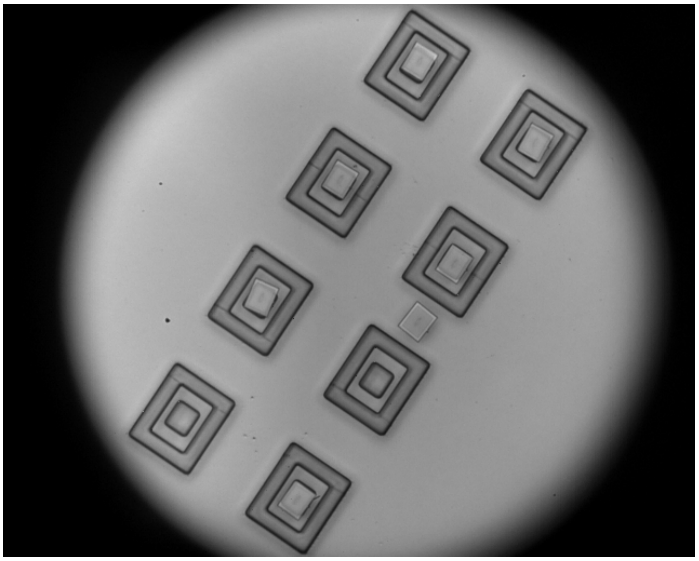

Figure 8-2: Cavity-by-cavity transfer printing onto a mirrored substrate with variable thickness target frames. Initial experiments confirm the ability to sub-select high-uniformity devices sets and transfer to non-native substrates without modifying the array's resonant characteristics.

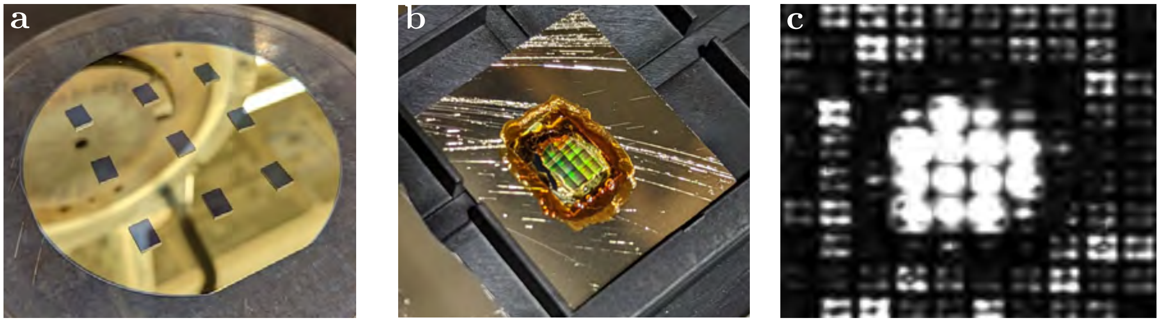

Figure 8-3: Initial phase-only device fabrication via flip chip bonding. The top oxide cladding of the fabricated wafers is polished to the optimal λ-thickness (c.f. Fig. 3-7), covered with a 100 nm-thick gold bond layer, and thermocompression bonded to a gold-plated silicon substrate (a). After substrate removal via back-side grinding and XeF_2 etching (b), the transferred membrane is released with a final timed wet etch. Initial reflectivity measuremnts (c) show intensity enhancement near the released areas at the center of each array.

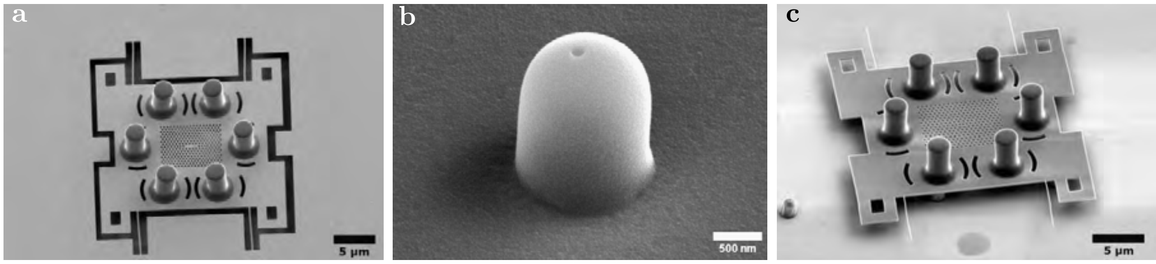

Figure 8-4: Thermal isolation engineering to convert a photonic crystal cavity into an optical bolometer. Pyrolized carbon absorbers are added to increase the pixel responsivity (a). Eggshell-like zirconia pillars with a few-nm-thick sidewall are fabrication (b) to thermally isolate the pixel from from the substrate (c).

[288, 289][2]. Thus, we envision that combining the thermal noise-limited resonance readout demonstrated in Chapter 4 with the wafer-scale photonic crystal fabrication of Chapter 3 will unveil new possibilities for high-performance optically addressed sensor arrays. For example, we are currently evaluating the feasibility of a microcavity-enhanced bolometer to overcome the $1/f$ readout noise inherent in room temperature vanadium oxide bolometers [290].

Our initial fabrication steps shown in Fig. 8-4 have focused on the addition of efficient infrared absorbers as well as thermal isolation engineering to convert our standard photonic crystal cavities into sensitive infrared detectors. Next, we will measure the low-frequency readout noise, responsivity, and overall detectivity for comparison to traditional electrically-mediated bolometers.

"Free-form" spatial light modulation with coupled resonators

The PhC cavities used in our PhC-SLM enable high-Q, diffraction-limited confinement of optical modes, but require precise fabrication and trimming. Alternatively, guided mode resonators (GMRs) provide modest quality factors, can be formed with a defect-free PhC lattice, and are intrinsically vertically coupled [100]. Combined with recent developments in thin film, high-Pockels-coefficient materials such as barium titanate (BTO) and lithium niobate (LN) [291, 292], GMRs enable linewidth-order resonances shifts with low quality factors ($Q \sim 100$) and are a promising solution for low-numerical aperture spatial light modulation.

For example, our proposed implementation consists of 1D or 2D dielectric grating patterned atop an electro-optic (EO) thin film. An underlying CMOS electrode array patterns a spatially varying electric field, which is effectively transduced to local

---

[2] The aforementioned membrane transfer processes are particularly exciting for these applications: for example, one could imagine transfer printing a PhC cavity array onto the end of a multimode fiber for real-time, through-fiber imaging where refractive index perturbations are spatially encoded in the resonance shifts of each microcavity.

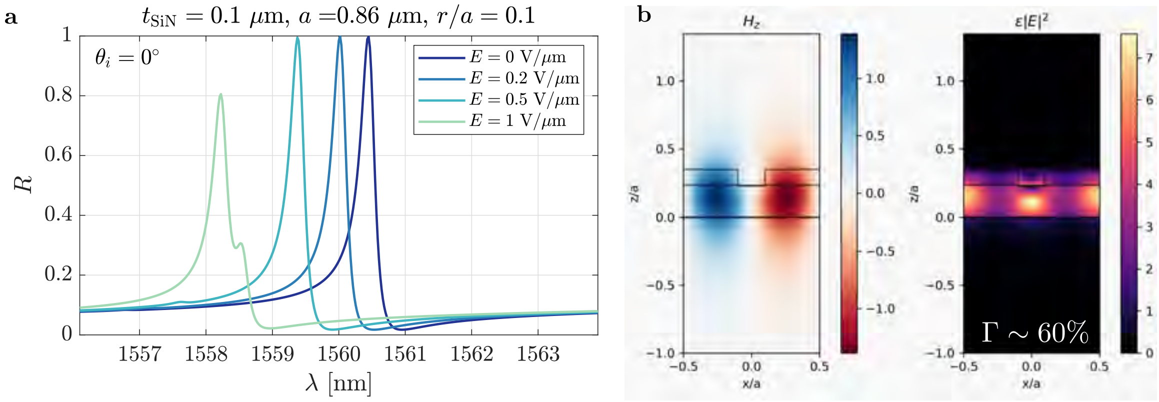

Figure 8-5: Design of an electro-optically controlled guided mode resonance based on silicon nitride on an electro-optic thin film. The optimized reflection spectra (a) demonstrate that linewidth-order wavelength shifts can be achieved with an in-plane electric field $|\vec{E}| < 1\ V/\mu\mathrm{m}$ (a). As illustrate by the field profiles in (b), the large energy confinement ($\Gamma \sim 60\%$) in a high-Pockels-coefficient material (barium titanate, $r_{42} \sim 900$ pm/V) enables near-unity on-off modulation contrast with CMOS-compatible voltages micron-scale pixel pitches.

optical phase shifts by a well-confined, moderate-Q guided mode resonance (GMR). The distributed GMR is intrinsically vertically coupled, features high optical power handling (as highlighted by recent Watt-class surface emitting laser demonstrations [293]), and can be formed with a defect-free, wafer-scale 1D or 2D grating fabricated by interference photolithography. Motivated by these advantages, we optimized and fabricated a simple GMR design consisting of a two-dimensional silicon nitride grating on a uniform unpatterned layer of thin film electro-optic material (Fig. 8-5). We are currently testing these structure.

Fig. 8-5 illustrates the feasibility of modulating the zero-order GMR reflection using a uniformly patterned index perturbation. Due to finite lateral propagation in waveguide mode, however, non-uniform index patterning to achieve a desired reflection profile is more complex [294, 295]. Assuming typical electro-optic materials, dimensions, and CMOS-compatible voltages, the normalized index perturbation $\epsilon = \Delta n/n \sim 10^{-4}$ indicates that significant resonant enhancement is required for appreciable phase shifts. For the large associated quality factors Q, diffraction affects the intracavity light. The GMR no longer acts as a thin local phase plate and the far-field profile is not directly related to the Fourier transform of the near-field control parameters. The central question is then: how many independent modes can be controlled in this free-form planar architecture? Two simple conditions for “independent pixels" based either the Rayleigh length or angular bandwidth associated with the single pixel size indicate that the wavelength-normalized pixel pitch scales with $\sqrt{Q}$ for a vertical resonator, lending minimum pixel sizes $\Lambda \sim \lambda/\sqrt{\epsilon} \sim 100\lambda$ that

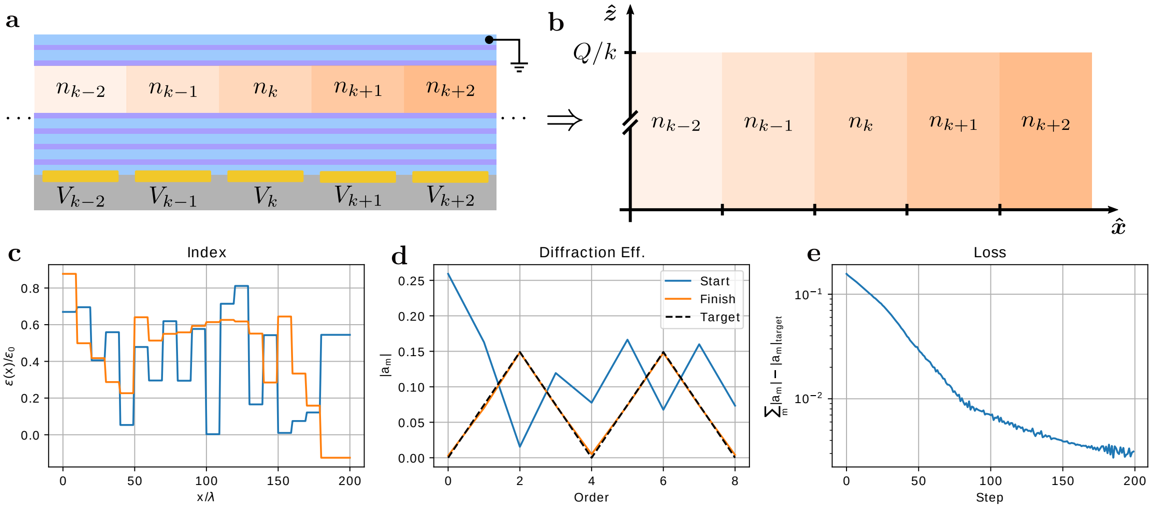

Figure 8-6: Intuitive design and computational optimization of a coupled-resonator SLM. An unfolded one-sided Fabry-Perot cavity (a) with tunable intracavity refractive index — i.e. a traditional etalon with an embedded photonic crystal — can be approximated as a thick grating (b). The far-field emission can then be optimized with automatic differentiation (c-e). The refractive index (c) in each 5λ-wide pixel is optimized (left) in an attempt to mimic a target diffraction efficiency pattern (d). For the assumed maximum index tuning $\Delta n/n = 10^{-2}$, the loss function (e), the Euclidean norm of the amplitude error vector, converges within ∼100 optimization steps.

are an order of magnitude larger than typical backplane electrode lengths $\Lambda \sim 10\lambda$. Controlling these “free-form” devices with inter-pixel coupling is an ongoing research goal.

As a case study, we have considered a vertical Fabry Perot resonator in the opposite “weak perturbation" regime — $\Lambda\sqrt{\epsilon}/\lambda \ll 1$ — as a “thick" grating (Fig. 8-6). By optimizing the intracavity index profile to achieve a desired angular emission profile, we demonstrate the feasibility of low-NA beamsteering using a simple Fabry-Perot resonator despite coupling between adjacent pixels. Our inverse design implementation mirrors other recent results int the literature [296].

Similar considerations are also applicable to an all-optical implementation, where a high-speed display is imaged onto the resonator for arbitrary refractive index patterning. Currently, we are working on a rigorous band theory-based model to describe the fundamental limits of spatial light modulation in similar structures with weak, free-form index perturbations. By reduing the PhC-SLM’s minimum pixel pitch (currently set to minimize coupling between adjacent devices), these results could enable wide field-of-view beamforming with coupled PhC resonators.

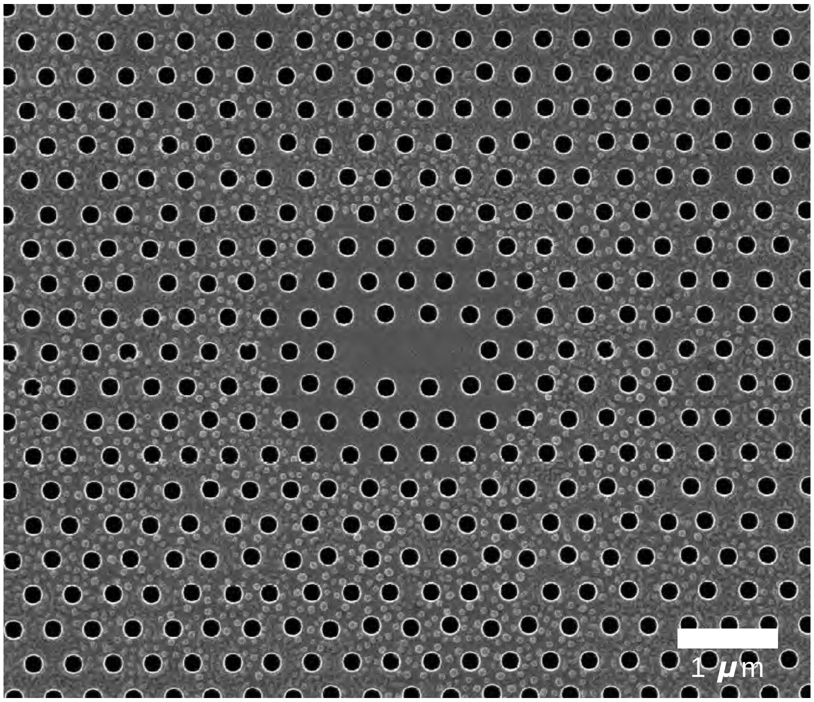

Figure 8-7: Resonator trimming via laser ablation. The micrograph shows that a thin (few-nm-thick) layer of deposited phase change material (Sb_2Se_3) can be removed using the same holographic laser addressing described in Chapter 6.

.

Novel trimming techniques and experiments

In Chapter 6 we demonstrated resonance alignment to a single operating wavelength such that individual pixels could be modulated at high-speed with a μLED display (Chapter 7). In addition, trimming to non-zero static detuning profiles can allow pre-programmed patterns to be steered without external control [16]. Combining these two techniques (fast index perturbation and static resonator detunings) could therefore enable high-speed, three-dimensional optical addressing and imaging. To further improve the wavelength uniformity of trimmed arrays, we are also exploring nonlinear operation wherein thermal effects between adjacent devices "lock" the array to a slightly (red) detuned pump laser.

While the results discussed in this thesis were enabled by thermal oxidation-based trimming, we are actively exploring other (i.e. faster[3]) trimming techniques. Fig. 8-7, for example, illustrates trimming via laser ablation of a deposited phase change

---

[3] Primarily due to environmental factors such as moisture adsorption, a ~10 × 10 array currently takes $\mathcal{O}(10)$ hours to align.

material.[4]

High-speed programmable unitary transformations

As described in Sec. 1.1, programmable optical transformations are ubiquitous in modern science and engineering. The PhC-SLM could therefore have applications to universal linear optics processors [10], optical neural network accelerators (via low-power, high-density unitary transformation of free-space optical inputs [9, 11]), and high-speed adaptive optics for free-space compressive sensing, deep-brain neural stimulation, and real-time scattering matrix inversion in complex media [297, 298]. Moreover, whereas we have so far considered only mode transformations, the PhC-SLM's high-Q/V resonant enhancement suggests the possibility of programming the quantum optical excitations/fields of these modes for applications ranging from multimode squeezed light generation, to multiplexed single photon sources for linear optics quantum computing [12] or deterministic photonic logic [229, 299].

Regardless of the final applications, the results of this thesis push optical measurement, sensing, and control one step closer to their current "fundamental limits". I opened this final chapter with Newton's quote, though, to demonstrate that these limits are ever evolving — an interplay of scientific insight and engineering breakthroughs. We thus hope that our investigations motivate future studies in the ongoing quest to *completely* harness the remarkable complexity of optical fields.

---

[4] I thank Cosmin-Constant Popescu (MIT) and Professor Juejun Hu (MIT) for their collaboration on these efforts.

Bibliography

[1] A. Marsh, "The first transatlantic telegraph cable was a bold, beautiful failure," *IEEE Spectrum*, Oct 2019.

[2] TeleGeography, "The state of the network," 2022.

[3] S. Varughese, S. Edirisinghe, M. Stephens, B. Boyanov, and P. Mertz, "Sdm enabled record field trial achieving 300+ Tbps trans-atlantic transmission capacity," in *Optical Fiber Communication Conference*, pp. M1F–2, Optica Publishing Group, 2022.

[4] B. Dormon, "How the internet works: Submarine fiber, brains in jars, and coaxial cables," May 2016.

[5] C. L. Panuski, I. R. Christen, M. Minkov, C. J. Brabec, S. Trajtenberg-Mills, A. D. Griffiths, J. J. McKendry, G. L. Leake, D. J. Coleman, C. Tran, J. St Louis, J. Mucci, C. Horvath, J. N. Westwood-Bachman, S. F. Preble, M. D. Dawson, M. J. Strain, M. L. Fanto, and D. R. Englund, "A full degree-of-freedom photonic crystal spatial light modulator," *arXiv preprint arXiv:2204.10302*, 2022.

[6] J. P. Gardner, J. C. Mather, M. Clampin, R. Doyon, M. A. Greenhouse, H. B. Hammel, J. B. Hutchings, P. Jakobsen, S. J. Lilly, K. S. Long, *et al.*, "The James Webb Space Telescope," *Space Science Reviews*, vol. 123, no. 4, pp. 485–606, 2006.

[7] A. M. Packer, B. Roska, and M. Häusser, "Targeting neurons and photons for optogenetics," *Nature neuroscience*, vol. 16, no. 7, pp. 805–815, 2013.

[8] J. Demas, J. Manley, F. Tejera, K. Barber, H. Kim, F. M. Traub, B. Chen, and A. Vaziri, "High-speed, cortex-wide volumetric recording of neuroactivity at cellular resolution using light beads microscopy," *Nature Methods*, vol. 18, no. 9, pp. 1103–1111, 2021.

[9] R. Hamerly, L. Bernstein, A. Sludds, M. Soljačić, and D. Englund, "Large-scale optical neural networks based on photoelectric multiplication," *Physical Review X*, vol. 9, no. 2, p. 021032, 2019.

[10] W. Bogaerts, D. Pérez, J. Capmany, D. A. Miller, J. Poon, D. Englund, F. Morichetti, and A. Melloni, "Programmable photonic circuits," *Nature*, vol. 586, no. 7828, pp. 207–216, 2020.

[11] G. Wetzstein, A. Ozcan, S. Gigan, S. Fan, D. Englund, M. Soljačić, C. Denz, D. A. Miller, and D. Psaltis, "Inference in artificial intelligence with deep optics and photonics," *Nature*, vol. 588, no. 7836, pp. 39–47, 2020.

[12] P. Kok, W. J. Munro, K. Nemoto, T. C. Ralph, J. P. Dowling, and G. J. Milburn, "Linear optical quantum computing with photonic qubits," *Reviews of modern physics*, vol. 79, no. 1, p. 135, 2007.

[13] S. Ebadi, T. T. Wang, H. Levine, A. Keesling, G. Semeghini, A. Omran, D. Bluvstein, R. Samajdar, H. Pichler, W. W. Ho, *et al.*, "Quantum phases of matter on a 256-atom programmable quantum simulator," *Nature*, vol. 595, no. 7866, pp. 227–232, 2021.

[14] S. N. Sanders, T. H. Schloemer, M. K. Gangishetty, D. Anderson, M. Seitz, A. O. Gallegos, R. C. Stokes, and D. N. Congreve, "Triplet fusion upconversion nanocapsules for volumetric 3d printing," *Nature*, vol. 604, no. 7906, pp. 474–478, 2022.

[15] L. Streich, J. C. Boffi, L. Wang, K. Alhalaseh, M. Barbieri, R. Rehm, S. Deivasigamani, C. T. Gross, A. Agarwal, and R. Prevedel, "High-resolution structural and functional deep brain imaging using adaptive optics three-photon microscopy," *Nature methods*, vol. 18, no. 10, pp. 1253–1258, 2021.

[16] A. M. Shaltout, V. M. Shalaev, and M. L. Brongersma, "Spatiotemporal light control with active metasurfaces," *Science*, vol. 364, no. 6441, p. eaat3100, 2019.

[17] M. Piccardo, V. Ginis, A. Forbes, S. Mahler, A. A. Friesem, N. Davidson, H. Ren, A. H. Dorrah, F. Capasso, F. T. Dullo, *et al.*, "Roadmap on multimode light shaping," *Journal of Optics*, vol. 24, no. 1, p. 013001, 2021.

[18] J. D. Joannopoulos, S. G. Johnson, and J. N. Winn, *Photonic Crystals: Molding the Flow of Light - Second Edition.* Princeton, 2011.

[19] D. A. Miller, "Fundamental limit to linear one-dimensional slow light structures," *Physical review letters*, vol. 99, no. 20, p. 203903, 2007.

[20] D. Gabor, "Iv light and information," in *Progress in optics*, vol. 1, pp. 109–153, Elsevier, 1961.

[21] G. H. Heilmeier, L. A. Zanoni, and L. A. Barton, "Dynamic scattering: A new electrooptic effect in certain classes of nematic liquid crystals," *Proceedings of the IEEE*, vol. 56, no. 7, pp. 1162–1171, 1968.

[22] Z. Zhang, Z. You, and D. Chu, "Fundamentals of phase-only liquid crystal on silicon (LCOS) devices," *Light: Science & Applications*, vol. 3, no. 10, pp. e213–e213, 2014.

[23] Y.-X. Ren, R.-D. Lu, and L. Gong, "Tailoring light with a digital micromirror device," *Annalen der physik*, vol. 527, no. 7-8, pp. 447–470, 2015.

[24] L. J. Hornbeck, "128× 128 deformable mirror device," *IEEE Transactions on Electron Devices*, vol. 30, no. 5, pp. 539–545, 1983.

[25] C. Greenlee, J. Luo, K. Leedy, B. Bayraktaroglu, R. Norwood, M. Fallahi, A.-Y. Jen, and N. Peyghambarian, "Electro-optic polymer spatial light modulator based on a fabry-perot interferometer configuration," *Optics express*, vol. 19, no. 13, pp. 12750–12758, 2011.

[26] W. Yang, T. Sun, Y. Rao, M. Megens, T. Chan, B.-W. Yoo, D. A. Horsley, M. C. Wu, and C. J. Chang-Hasnain, "High speed optical phased array using high contrast grating all-pass filters," *Optics express*, vol. 22, no. 17, pp. 20038–20044, 2014.

[27] Y. Wang, G. Zhou, X. Zhang, K. Kwon, P.-A. Blanche, N. Triesault, K.-s. Yu, and M. C. Wu, "2D broadband beamsteering with large-scale mems optical phased array," *Optica*, vol. 6, no. 5, pp. 557–562, 2019.

[28] O. Tzang, E. Niv, S. Singh, S. Labouesse, G. Myatt, and R. Piestun, "Wavefront shaping in complex media with a 350 khz modulator via a 1D-to-2D transform," *Nature Photonics*, vol. 13, no. 11, pp. 788–793, 2019.

[29] D. J. McKnight, K. M. Johnson, and R. A. Serati, "256× 256 liquid-crystal-on-silicon spatial light modulator," *Applied Optics*, vol. 33, no. 14, pp. 2775–2784, 1994.

[30] J. H. Marshel, Y. S. Kim, T. A. Machado, S. Quirin, B. Benson, J. Kadmon, C. Raja, A. Chibukhchyan, C. Ramakrishnan, M. Inoue, *et al.*, "Cortical layer–specific critical dynamics triggering perception," *Science*, vol. 365, no. 6453, p. eaaw5202, 2019.

[31] J. Li, P. Yu, S. Zhang, and N. Liu, "Electrically-controlled digital metasurface device for light projection displays," *Nature communications*, vol. 11, no. 1, pp. 1–7, 2020.

[32] R. Fatemi, A. Khachaturian, and A. Hajimiri, "A nonuniform sparse 2D large-fov optical phased array with a low-power pwm drive," *IEEE Journal of Solid-State Circuits*, vol. 54, no. 5, pp. 1200–1215, 2019.

[33] J. Sun, E. Timurdogan, A. Yaacobi, E. S. Hosseini, and M. R. Watts, "Large-scale nanophotonic phased array," *Nature*, vol. 493, no. 7431, pp. 195–199, 2013.

[34] Y. Horie, A. Arbabi, E. Arbabi, S. M. Kamali, and A. Faraon, "High-speed, phase-dominant spatial light modulation with silicon-based active resonant antennas," *Acs Photonics*, vol. 5, no. 5, pp. 1711–1717, 2017.

[35] V. Shrauger and C. Warde, "Development of a high-speed high-fill-factor phase-only spatial light modulator," in *Diffractive and Holographic Technologies for Integrated Photonic Systems*, vol. 4291, pp. 101–108, International Society for Optics and Photonics, 2001.

[36] T. A. Bartlett, W. C. McDonald, and J. N. Hall, "Adapting Texas Instruments DLP technology to demonstrate a phase spatial light modulator," in *Emerging Digital Micromirror Device Based Systems and Applications XI*, vol. 10932, p. 109320S, International Society for Optics and Photonics, 2019.

[37] X. Zhang, K. Kwon, J. Henriksson, J. Luo, and M. C. Wu, "A large-scale microelectromechanical-systems-based silicon photonics LiDAR," *Nature*, vol. 603, no. 7900, pp. 253–258, 2022.

[38] Y.-C. Shuai, D. Zhao, Y. Liu, C. Stambaugh, J. Lawall, and W. Zhou, "Coupled bilayer photonic crystal slab electro-optic spatial light modulators," *IEEE Photonics Journal*, vol. 9, no. 2, pp. 1–11, 2017.

[39] S. Junique, Q. Wang, S. Almqvist, J. Guo, H. Martijn, B. Noharet, and J. Y. Andersson, "GaAs-based multiple-quantum-well spatial light modulators fabricated by a wafer-scale process," *Applied optics*, vol. 44, no. 9, pp. 1635–1641, 2005.

[40] A. Smolyaninov, A. El Amili, F. Vallini, S. Pappert, and Y. Fainman, "Programmable plasmonic phase modulation of free-space wavefronts at gigahertz rates," *Nature Photonics*, vol. 13, no. 6, pp. 431–435, 2019.

[41] I.-C. Benea-Chelmus, M. L. Meretska, D. L. Elder, M. Tamagnone, L. R. Dalton, and F. Capasso, "Electro-optic spatial light modulator from an engineered organic layer," *Nature communications*, vol. 12, no. 1, pp. 1–10, 2021.

[42] S. Chung, H. Abediasl, and H. Hashemi, "A monolithically integrated large-scale optical phased array in silicon-on-insulator CMOS," *IEEE Journal of Solid-State Circuits*, vol. 53, no. 1, pp. 275–296, 2017.

[43] C. V. Poulton, M. J. Byrd, P. Russo, E. Timurdogan, M. Khandaker, D. Vermeulen, and M. R. Watts, "Long-range LiDAR and free-space data communication with high-performance optical phased arrays," *IEEE Journal of Selected Topics in Quantum Electronics*, vol. 25, no. 5, pp. 1–8, 2019.

[44] C. Rogers, A. Y. Piggott, D. J. Thomson, R. F. Wiser, I. E. Opris, S. A. Fortune, A. J. Compston, A. Gondarenko, F. Meng, X. Chen, *et al.*, "A universal 3D imaging sensor on a silicon photonics platform," *Nature*, vol. 590, no. 7845, pp. 256–261, 2021.

[45] Q. Wang, E. T. Rogers, B. Gholipour, C.-M. Wang, G. Yuan, J. Teng, and N. I. Zheludev, "Optically reconfigurable metasurfaces and photonic devices based on phase change materials," *Nature photonics*, vol. 10, no. 1, pp. 60–65, 2016.

[46] Y. Zhang, C. Fowler, J. Liang, B. Azhar, M. Y. Shalaginov, S. Deckoff-Jones, S. An, J. B. Chou, C. M. Roberts, V. Liberman, *et al.*, "Electrically reconfigurable non-volatile metasurface using low-loss optical phase-change material," *Nature Nanotechnology*, vol. 16, no. 6, pp. 661–666, 2021.

[47] Y. Wang, P. Landreman, D. Schoen, K. Okabe, A. Marshall, U. Celano, H.-S. P. Wong, J. Park, and M. L. Brongersma, "Electrical tuning of phase-change antennas and metasurfaces," *Nature Nanotechnology*, vol. 16, no. 6, pp. 667–672, 2021.

[48] E. Arbabi, A. Arbabi, S. M. Kamali, Y. Horie, M. Faraji-Dana, and A. Faraon, "MEMS-tunable dielectric metasurface lens," *Nature communications*, vol. 9, no. 1, pp. 1–9, 2018.

[49] P. C. Wu, R. A. Pala, G. Kafaie Shirmanesh, W.-H. Cheng, R. Sokhoyan, M. Grajower, M. Z. Alam, D. Lee, and H. A. Atwater, "Dynamic beam steering with all-dielectric electro-optic III-V multiple-quantum-well metasurfaces," *Nature communications*, vol. 10, no. 1, pp. 1–9, 2019.

[50] J. Park, B. G. Jeong, S. I. Kim, D. Lee, J. Kim, C. Shin, C. B. Lee, T. Otsuka, J. Kyoung, S. Kim, *et al.*, "All-solid-state spatial light modulator with independent phase and amplitude control for three-dimensional LiDAR applications," *Nature nanotechnology*, vol. 16, no. 1, pp. 69–76, 2021.

[51] G. K. Shirmanesh, R. Sokhoyan, P. C. Wu, and H. A. Atwater, "Electro-optically tunable multifunctional metasurfaces," *ACS nano*, vol. 14, no. 6, pp. 6912–6920, 2020.

[52] T. Kim, P. Bhargava, C. V. Poulton, J. Notaros, A. Yaacobi, E. Timurdogan, C. Baiocco, N. Fahrenkopf, S. Kruger, T. Ngai, *et al.*, "A single-chip optical phased array in a wafer-scale silicon photonics/CMOS 3D-integration platform," *IEEE Journal of Solid-State Circuits*, vol. 54, no. 11, pp. 3061–3074, 2019.

[53] C. V. Poulton, M. J. Byrd, B. Moss, E. Timurdogan, R. Millman, and M. R. Watts, "8192-element optical phased array with 100° steering range and flip-chip CMOS," in *CLEO: Applications and Technology*, pp. JTh4A–3, Optical Society of America, 2020.

[54] H. Ito, Y. Kusunoki, J. Maeda, D. Akiyama, N. Kodama, H. Abe, R. Tetsuya, and T. Baba, "Wide beam steering by slow-light waveguide gratings and a prism lens," *Optica*, vol. 7, no. 1, pp. 47–52, 2020.

[55] Y.-W. Huang, H. W. H. Lee, R. Sokhoyan, R. A. Pala, K. Thyagarajan, S. Han, D. P. Tsai, and H. A. Atwater, "Gate-tunable conducting oxide metasurfaces," *Nano letters*, vol. 16, no. 9, pp. 5319–5325, 2016.

[56] X. Ye, F. Ni, H. Li, H. Liu, Y. Zheng, and X. Chen, "High-speed programmable lithium niobate thin film spatial light modulator," *Optics Letters*, vol. 46, no. 5, pp. 1037–1040, 2021.

[57] D. A. Miller, "Attojoule optoelectronics for low-energy information processing and communications," *Journal of Lightwave Technology*, vol. 35, no. 3, pp. 346–396, 2017.

[58] C. L. Panuski and D. R. Englund, "All-optical spatial light modulators," June 1 2021. US Patent 11,022,826.

[59] R. A. Soref and B. R. Bennett, "Electrooptical effects in silicon," *IEEE journal of quantum electronics*, vol. 23, no. 1, pp. 123–129, 1987.

[60] C. Panuski, M. Pant, M. Heuck, R. Hamerly, and D. Englund, "Single photon detection by cavity-assisted all-optical gain," *Physical Review B*, vol. 99, no. 20, p. 205303, 2019.

[61] T. Tanabe, H. Taniyama, and M. Notomi, "Carrier diffusion and recombination in photonic crystal nanocavity optical switches," *Journal of Lightwave Technology*, vol. 26, no. 11, pp. 1396–1403, 2008.

[62] M. Minkov, V. Savona, and D. Gerace, "Photonic crystal slab cavity simultaneously optimized for ultra-high Q/V and vertical radiation coupling," *Applied Physics Letters*, vol. 111, no. 13, p. 131104, 2017.

[63] Y. Huang, E.-L. Hsiang, M.-Y. Deng, and S.-T. Wu, "Mini-LED, Micro-LED and OLED displays: Present status and future perspectives," *Light: Science & Applications*, vol. 9, no. 1, pp. 1–16, 2020.

[64] J. Lin and H. Jiang, "Development of microLED," *Applied Physics Letters*, vol. 116, no. 10, p. 100502, 2020.

[65] F. Templier, L. Dupré, B. Dupont, A. Daami, B. Aventurier, F. Henry, D. Sarrasin, S. Renet, F. Berger, F. Olivier, *et al.*, "High-resolution active-matrix 10-um pixel-pitch GaN LED microdisplays for augmented reality applications," in *Advances in Display Technologies VIII*, vol. 10556, p. 105560I, International Society for Optics and Photonics, 2018.

[66] C.-J. Chen, H.-C. Chen, J.-H. Liao, C.-J. Yu, and M.-C. Wu, "Fabrication and characterization of active-matrix 960×540 blue GaN-based micro-LED display," *IEEE Journal of Quantum Electronics*, vol. 55, no. 2, pp. 1–6, 2019.

[67] J. Herrnsdorf, J. J. McKendry, S. Zhang, E. Xie, R. Ferreira, D. Massoubre, A. M. Zuhdi, R. K. Henderson, I. Underwood, S. Watson, *et al.*, "Active-matrix GaN micro light-emitting diode display with unprecedented brightness," *IEEE Transactions on Electron Devices*, vol. 62, no. 6, pp. 1918–1925, 2015.

[68] R. X. Ferreira, E. Xie, J. J. McKendry, S. Rajbhandari, H. Chun, G. Faulkner, S. Watson, A. E. Kelly, E. Gu, R. V. Penty, *et al.*, "High bandwidth GaN-based micro-LEDs for multi-Gb/s visible light communications," *IEEE Photonics Technology Letters*, vol. 28, no. 19, pp. 2023–2026, 2016.

[69] Y. Cai, J. I. Haggar, C. Zhu, P. Feng, J. Bai, and T. Wang, "Direct epitaxial approach to achieve a monolithic on-chip integration of a HEMT and a single micro-LED with a high-modulation bandwidth," *ACS applied electronic materials*, vol. 3, no. 1, pp. 445–450, 2021.

[70] N. B. Hassan, F. Dehkhoda, E. Xie, J. Herrnsdorf, M. J. Strain, R. Henderson, and M. D. Dawson, "Ultra-high frame rate digital light projector using chipscale LED-on-CMOS technology," *arXiv preprint arXiv:2111.13586*, 2021.

[71] D. A. Miller, "Optical interconnects to electronic chips," *Applied optics*, vol. 49, no. 25, pp. F59–F70, 2010.

[72] X. Liang and S. G. Johnson, "Formulation for scalable optimization of microcavities via the frequency-averaged local density of states," *Optics express*, vol. 21, no. 25, pp. 30812–30841, 2013.

[73] C. Peng, R. Hamerly, M. Soltani, and D. R. Englund, "Design of high-speed phase-only spatial light modulators with two-dimensional tunable microcavity arrays," *Optics express*, vol. 27, no. 21, pp. 30669–30680, 2019.

[74] H. Lee, S. Kiravittaya, S. Kumar, J. Plumhof, L. Balet, L. H. Li, M. Francardi, A. Gerardino, A. Fiore, A. Rastelli, *et al.*, "Local tuning of photonic crystal nanocavity modes by laser-assisted oxidation," *Applied Physics Letters*, vol. 95, no. 19, p. 191109, 2009.

[75] C. J. Chen, J. Zheng, T. Gu, J. F. McMillan, M. Yu, G.-Q. Lo, D.-L. Kwong, and C. W. Wong, "Selective tuning of high-Q silicon photonic crystal nanocavities via laser-assisted local oxidation," *Optics express*, vol. 19, no. 13, pp. 12480–12489, 2011.

[76] T. Asano, Y. Ochi, Y. Takahashi, K. Kishimoto, and S. Noda, "Photonic crystal nanocavity with a Q factor exceeding eleven million," *Optics express*, vol. 25, no. 3, pp. 1769–1777, 2017.

[77] H. Choi, M. Heuck, and D. Englund, "Self-similar nanocavity design with ultrasmall mode volume for single-photon nonlinearities," *Physical review letters*, vol. 118, no. 22, p. 223605, 2017.

[78] S. Hu, M. Khater, R. Salas-Montiel, E. Kratschmer, S. Engelmann, W. M. Green, and S. M. Weiss, "Experimental realization of deep-subwavelength confinement in dielectric optical resonators," *Science advances*, vol. 4, no. 8, p. eaat2355, 2018.

[79] H. Liang, R. Luo, Y. He, H. Jiang, and Q. Lin, "High-quality lithium niobate photonic crystal nanocavities," *Optica*, vol. 4, no. 10, pp. 1251–1258, 2017.

[80] M. Li, H. Liang, R. Luo, Y. He, J. Ling, and Q. Lin, "Photon-level tuning of photonic nanocavities," *Optica*, vol. 6, no. 7, p. 860, 2019.

[81] M. Li, H. Liang, R. Luo, Y. He, and Q. Lin, "High-Q 2D lithium niobate photonic crystal slab nanoresonators," *Laser & Photonics Reviews*, vol. 13, no. 5, p. 1800228, 2019.

[82] M. Li, J. Ling, Y. He, U. A. Javid, S. Xue, and Q. Lin, "Lithium niobate photonic-crystal electro-optic modulator," *Nature Communications*, vol. 11, no. 1, pp. 1–8, 2020.

[83] C. L. Panuski, *Cavity-assisted all-optical photodetection.* PhD thesis, Massachusetts Institute of Technology, 2019.

[84] J. Goldstein, C. L. Panuski, and D. R. Englund, "Microcavity-enhanced optical bolometer," 2021. US Patent Application, submitted.

[85] K. J. Vahala, "Optical microcavities," *Nature*, vol. 424, no. 6950, pp. 839–846, 2003.

[86] Q. Zhao, L. Zhang, and O. D. Miller, "Minimum dielectric-resonator mode volumes," *arXiv preprint arXiv:2008.13241*, 2020.

[87] C. Panuski, D. Englund, and R. Hamerly, "Fundamental thermal noise limits for optical microcavities," *Physical Review X*, vol. 10, no. 4, p. 041046, 2020.

[88] M. Minkov and V. Savona, "Automated optimization of photonic crystal slab cavities," *Scientific reports*, vol. 4, no. 1, pp. 1–8, 2014.

[89] T. Shibata, T. Asano, and S. Noda, “Fabrication and characterization of an $L3$ nanocavity designed by an iterative machine-learning method,” *APL Photonics*, vol. 6, no. 3, p. 036113, 2021.

[90] R. C. Hansen, “Fundamental limitations in antennas,” *Proceedings of the IEEE*, vol. 69, no. 2, pp. 170–182, 1981.

[91] R. W. Ziolkowski, “Using huygens multipole arrays to realize unidirectional needle-like radiation,” *Physical Review X*, vol. 7, no. 3, p. 031017, 2017.

[92] N.-V.-Q. Tran, S. Combrié, and A. De Rossi, “Directive emission from high-Q photonic crystal cavities through band folding,” *Physical Review B*, vol. 79, no. 4, p. 041101, 2009.

[93] N.-V.-Q. Tran, S. Combrié, P. Colman, A. De Rossi, and T. Mei, “Vertical high emission in photonic crystal nanocavities by band-folding design,” *Physical Review B*, vol. 82, no. 7, p. 075120, 2010.

[94] S. L. Portalupi, M. Galli, C. Reardon, T. Krauss, L. O’Faolain, L. C. Andreani, and D. Gerace, “Planar photonic crystal cavities with far-field optimization for high coupling efficiency and quality factor,” *Optics express*, vol. 18, no. 15, pp. 16064–16073, 2010.

[95] L. Li, H. Choi, M. Heuck, and D. Englund, “Field-based design of a resonant dielectric antenna for coherent spin-photon interfaces,” *Optics Express*, vol. 29, no. 11, pp. 16469–16476, 2021.

[96] Y. Duan, K. C. Chen, D. R. Englund, and M. E. Trusheim, “A vertically-loaded diamond microdisk resonator spin-photon interface,” *Optics Express*, vol. 29, no. 26, pp. 43082–43090, 2021.

[97] L. C. Andreani and D. Gerace, “Photonic-crystal slabs with a triangular lattice of triangular holes investigated using a guided-mode expansion method,” *Physical Review B*, vol. 73, no. 23, p. 235114, 2006.

[98] M. Minkov, I. A. Williamson, L. C. Andreani, D. Gerace, B. Lou, A. Y. Song, T. W. Hughes, and S. Fan, “Inverse design of photonic crystals through automatic differentiation,” *ACS Photonics*, vol. 7, no. 7, pp. 1729–1741, 2020.

[99] W. Zhou, D. Zhao, Y.-C. Shuai, H. Yang, S. Chuwongin, A. Chadha, J.-H. Seo, K. X. Wang, V. Liu, Z. Ma, and S. Fan, “Progress in 2D photonic crystal Fano resonance photonics,” *Progress in Quantum Electronics*, vol. 38, no. 1, pp. 1–74, 2014.

[100] G. Pitruzzello and T. F. Krauss, “Photonic crystal resonances for sensing and imaging,” *Journal of Optics*, vol. 20, no. 7, p. 073004, 2018.

[101] K. Nozaki, T. Tanabe, A. Shinya, S. Matsuo, T. Sato, H. Taniyama, and M. Notomi, "Sub-femtojoule all-optical switching using a photonic-crystal nanocavity," *Nature Photonics*, vol. 4, no. 7, pp. 477–483, 2010.

[102] M. Notomi, E. Kuramochi, and T. Tanabe, "Large-scale arrays of ultrahigh-Q coupled nanocavities," *Nature photonics*, vol. 2, no. 12, pp. 741–747, 2008.

[103] Y. Guo, M. Xiao, Y. Zhou, and S. Fan, "Arbitrary polarization conversion with a photonic crystal slab," *Advanced Optical Materials*, vol. 7, no. 14, p. 1801453, 2019.

[104] S. G. Johnson, S. Fan, P. R. Villeneuve, J. D. Joannopoulos, and L. Kolodziejski, "Guided modes in photonic crystal slabs," *Physical Review B*, vol. 60, no. 8, p. 5751, 1999.

[105] S. G. Johnson and J. D. Joannopoulos, "Block-iterative frequency-domain methods for maxwell's equations in a planewave basis," *Optics express*, vol. 8, no. 3, pp. 173–190, 2001.

[106] J. Vuckovic, M. Loncar, H. Mabuchi, and A. Scherer, "Optimization of the Q factor in photonic crystal microcavities," *IEEE Journal of Quantum Electronics*, vol. 38, no. 7, pp. 850–856, 2002.

[107] S.-H. Kim, S.-K. Kim, and Y.-H. Lee, "Vertical beaming of wavelength-scale photonic crystal resonators," *Physical Review B*, vol. 73, no. 23, p. 235117, 2006.

[108] M. Munsch, N. S. Malik, E. Dupuy, A. Delga, J. Bleuse, J.-M. Gérard, J. Claudon, N. Gregersen, and J. Mørk, "Dielectric GaAs antenna ensuring an efficient broadband coupling between an InAs quantum dot and a gaussian optical beam," *Physical Review Letters*, vol. 110, no. 17, p. 177402, 2013.

[109] H. A. Haus, *Waves and fields in optoelectronics*. Prentice-Hall series in solid state physical electronics, Englewood Cliffs, NJ: Prentice-Hall, 1984.

[110] S. Molesky, Z. Lin, A. Y. Piggott, W. Jin, J. Vucković, and A. W. Rodriguez, "Inverse design in nanophotonics," *Nature Photonics*, vol. 12, no. 11, pp. 659–670, 2018.

[111] W. Ma, Z. Liu, Z. A. Kudyshev, A. Boltasseva, W. Cai, and Y. Liu, "Deep learning for the design of photonic structures," *Nature Photonics*, vol. 15, no. 2, pp. 77–90, 2021.

[112] S. G. Johnson, M. Povinelli, M. Soljačić, A. Karalis, S. Jacobs, and J. Joannopoulos, "Roughness losses and volume-current methods in photonic-crystal waveguides," *Applied Physics B*, vol. 81, no. 2, pp. 283–293, 2005.

[113] Y. Taguchi, Y. Takahashi, Y. Sato, T. Asano, and S. Noda, "Statistical studies of photonic heterostructure nanocavities with an average Q factor of three million," *Optics express*, vol. 19, no. 12, pp. 11916–11921, 2011.

[114] M. Minkov, U. P. Dharanipathy, R. Houdré, and V. Savona, "Statistics of the disorder-induced losses of high-Q photonic crystal cavities," *Optics express*, vol. 21, no. 23, pp. 28233–28245, 2013.

[115] D. Dodane, J. Bourderionnet, S. Combrié, and A. de Rossi, "Fully embedded photonic crystal cavity with $Q = 0.6$ million fabricated within a full-process CMOS multiproject wafer," *Optics express*, vol. 26, no. 16, pp. 20868–20877, 2018.

[116] K. Ashida, M. Okano, T. Yasuda, M. Ohtsuka, M. Seki, N. Yokoyama, K. Koshino, K. Yamada, and Y. Takahashi, "Photonic crystal nanocavities with an average Q factor of 1.9 million fabricated on a 300-mm-wide SOI wafer using a CMOS-compatible process," *Journal of Lightwave Technology*, vol. 36, no. 20, pp. 4774–4782, 2018.

[117] R. Benevides, F. G. Santos, G. O. Luiz, G. S. Wiederhecker, and T. P. M. Alegre, "Ultrahigh-Q optomechanical crystal cavities fabricated in a CMOS foundry," *Scientific reports*, vol. 7, no. 1, pp. 1–6, 2017.

[118] K. Ashida, M. Okano, M. Ohtsuka, M. Seki, N. Yokoyama, K. Koshino, M. Mori, T. Asano, S. Noda, and Y. Takahashi, "Ultrahigh-Q photonic crystal nanocavities fabricated by CMOS process technologies," *Optics Express*, vol. 25, no. 15, pp. 18165–18174, 2017.

[119] W. Xie, M. Fiers, S. Selvaraja, P. Bienstman, J. Van Campenhout, P. Absil, and D. Van Thourhout, "High-Q photonic crystal nanocavities on 300 mm SOI substrate fabricated with 193 nm immersion lithography," *Journal of Lightwave Technology*, vol. 32, no. 8, pp. 1457–1462, 2014.

[120] W. Xie, P. Verheyen, M. Pantouvaki, J. Van Campenhout, and D. Van Thourhout, "Efficient resonance management in ultrahigh-Q 1D photonic crystal nanocavities fabricated on 300 mm SOI CMOS platform," *Laser & Photonics Reviews*, vol. 15, no. 2, p. 2000317, 2021.

[121] E. Schelew, G. W. Rieger, and J. F. Young, "Characterization of integrated planar photonic crystal circuits fabricated by a CMOS foundry," *Journal of Lightwave Technology*, vol. 31, no. 2, pp. 239–248, 2012.

[122] K. K. Mehta, J. S. Orcutt, O. Tehar-Zahav, Z. Sternberg, R. Bafrali, R. Meade, and R. J. Ram, "High-Q CMOS-integrated photonic crystal microcavity devices," *Scientific reports*, vol. 4, no. 1, pp. 1–6, 2014.

[123] C. V. Poulton, X. Zeng, M. T. Wade, J. M. Shainline, J. S. Orcutt, and M. A. Popović, “Photonic crystal microcavities in a microelectronics 45-nm SOI CMOS technology,” *IEEE Photonics Technology Letters*, vol. 27, no. 6, pp. 665–668, 2015.

[124] Y. Ooka, T. Tetsumoto, A. Fushimi, W. Yoshiki, and T. Tanabe, “CMOS compatible high-Q photonic crystal nanocavity fabricated with photolithography on silicon photonic platform,” *Scientific reports*, vol. 5, no. 1, pp. 1–9, 2015.

[125] N. M. Fahrenkopf, C. McDonough, G. L. Leake, Z. Su, E. Timurdogan, and D. D. Coolbaugh, “The AIM Photonics MPW: A highly accessible cutting edge technology for rapid prototyping of photonic integrated circuits,” *IEEE Journal of Selected Topics in Quantum Electronics*, vol. 25, no. 5, pp. 1–6, 2019.

[126] T. Asano, B.-S. Song, and S. Noda, “Analysis of the experimental Q factors ($\sim$1 million) of photonic crystal nanocavities,” *Optics express*, vol. 14, no. 5, pp. 1996–2002, 2006.

[127] S.-H. Kim, J. Huang, and A. Scherer, “From vertical-cavities to hybrid metal/photonic-crystal nanocavities: towards high-efficiency nanolasers,” *JOSA B*, vol. 29, no. 4, pp. 577–588, 2012.

[128] W. L. Barnes, S. A. Horsley, and W. L. Vos, “Classical antennas, quantum emitters, and densities of optical states,” *Journal of Optics*, vol. 22, no. 7, p. 073501, 2020.

[129] D. Yamashita, Y. Takahashi, T. Asano, and S. Noda, “Raman shift and strain effect in high-Q photonic crystal silicon nanocavity,” *Optics Express*, vol. 23, no. 4, pp. 3951–3959, 2015.

[130] T. Begou, F. Lemarchand, F. Lemarquis, A. Moreau, and J. Lumeau, “High-performance thin-film optical filters with stress compensation,” *JOSA A*, vol. 36, no. 11, pp. C113–C121, 2019.

[131] E. Iwase, P.-C. Hui, D. Woolf, A. W. Rodriguez, S. G. Johnson, F. Capasso, and M. Lončar, “Control of buckling in large micromembranes using engineered support structures,” *Journal of Micromechanics and Microengineering*, vol. 22, no. 6, p. 065028, 2012.

[132] H. Sekoguchi, Y. Takahashi, T. Asano, and S. Noda, “Photonic crystal nanocavity with a Q-factor of $\sim$9 million,” *Optics Express*, vol. 22, no. 1, pp. 916–924, 2014.

[133] M. Nakadai, K. Tanaka, T. Asano, Y. Takahashi, and S. Noda, “Statistical evaluation of Q factors of fabricated photonic crystal nanocavities designed by

using a deep neural network," *Applied Physics Express*, vol. 13, no. 1, p. 012002, 2019.

[134] G. Moille and K. Srinivasan, "Small cavities make noisy homes for light," *Physics*, vol. 13, p. 192, 2020.

[135] The LIGO Scientific Collaboration, "GW170817: Observation of Gravitational Waves from a Binary Neutron Star Inspiral," *Physical Review Letters*, vol. 119, no. 16, p. 161101, 2017.

[136] S. P. Yu, J. A. Muniz, C. L. Hung, and H. J. Kimble, "Two-dimensional photonic crystals for engineering atom–light interactions," *Proceedings of the National Academy of Sciences of the United States of America*, vol. 116, no. 26, pp. 12743–12751, 2019.

[137] U. Delić, M. Reisenbauer, K. Dare, D. Grass, V. Vuletić, N. Kiesel, and M. Aspelmeyer, "Cooling of a levitated nanoparticle to the motional quantum ground state," *Science*, vol. 367, pp. 892–895, feb 2020.

[138] H. B. Callen and T. A. Welton, "Irreversibility and Generalized Noise," *Physical Review*, vol. 83, pp. 34–40, jul 1951.

[139] Y. Levin, "Internal thermal noise in the LIGO test masses: A direct approach," *Physical Review D*, vol. 57, no. 2, p. 659, 1998.

[140] The LIGO Scientific Collaboration, "Sensitivity of the Advanced LIGO detectors at the beginning of gravitational wave astronomy," *Physical Review D*, vol. 93, no. 11, pp. 112004–112005, 2016.

[141] G. D. Cole, W. Zhang, M. J. Martin, J. Ye, and M. Aspelmeyer, "Tenfold reduction of Brownian noise in high-reflectivity optical coatings," *Nature Photonics*, vol. 7, no. 8, pp. 644–650, 2013.

[142] D. Heinert, S. Kroker, D. Friedrich, S. Hild, E. B. Kley, S. Leavey, I. W. Martin, R. Nawrodt, A. Tünnermann, S. P. Vyatchanin, and K. Yamamoto, "Calculation of thermal noise in grating reflectors," *Physical Review D*, vol. 88, no. 4, p. 042001, 2013.

[143] S. Kroker, J. Dickmann, C. B. Rojas Hurtado, D. Heinert, R. Nawrodt, Y. Levin, and S. P. Vyatchanin, "Brownian thermal noise in functional optical surfaces," *Physical Review D*, vol. 96, no. 2, p. 022002, 2017.

[144] K. Numata, A. Kemery, and J. Camp, "Thermal-noise limit in the frequency stabilization of lasers with rigid cavities," *Physical Review Letters*, vol. 93, no. 25, p. 250602, 2004.

[145] T. Kessler, T. Legero, and U. Sterr, "Thermal noise in optical cavities revisited," *Journal of the Optical Society of America B*, vol. 29, no. 1, p. 178, 2012.

[146] N. O. Zhadnov, K. S. Kudeyarov, D. S. Kryuchkov, I. A. Semerikov, K. Y. Khabarova, and N. N. Kolachevsky, "On the thermal noise limit of ultrastable optical cavities," *Quantum Electronics*, vol. 48, pp. 425–430, may 2018.

[147] A. M. Armani, R. P. Kulkarni, S. E. Fraser, R. C. Flagan, and K. J. Vahala, "Label-Free, Single-Molecule Detection with Optical Microcavities," *Science*, vol. 317, pp. 783–787, aug 2007.

[148] T. J. Kippenberg, R. Holzwarth, and S. A. Diddams, "Microresonator-based optical frequency combs," *science*, vol. 332, no. 6029, pp. 555–559, 2011.

[149] T. J. Kippenberg, A. L. Gaeta, M. Lipson, and M. L. Gorodetsky, "Dissipative kerr solitons in optical microresonators," *Science*, vol. 361, no. 6402, 2018.

[150] D. T. Spencer, T. Drake, T. C. Briles, J. Stone, L. C. Sinclair, C. Fredrick, Q. Li, D. Westly, B. R. Ilic, A. Bluestone, *et al.*, "An optical-frequency synthesizer using integrated photonics," *Nature*, vol. 557, no. 7703, pp. 81–85, 2018.

[151] A. Dutt, C. Joshi, X. Ji, J. Cardenas, Y. Okawachi, K. Luke, A. L. Gaeta, and M. Lipson, "On-chip dual-comb source for spectroscopy," *Science Advances*, vol. 4, no. 3, p. e1701858, 2018.

[152] E. Obrzud, M. Rainer, A. Harutyunyan, M. H. Anderson, J. Liu, M. Geiselmann, B. Chazelas, S. Kundermann, S. Lecomte, M. Cecconi, *et al.*, "A microphotonic astrocomb," *Nature Photonics*, vol. 13, no. 1, pp. 31–35, 2019.

[153] M. Eichenfield, R. Camacho, J. Chan, K. J. Vahala, and O. Painter, "A picogram- and nanometre-scale photonic-crystal optomechanical cavity," *Nature*, vol. 459, no. 7246, pp. 550–555, 2009.

[154] A. Goban, C. L. Hung, S. P. Yu, J. D. Hood, J. A. Muniz, J. H. Lee, M. J. Martin, A. C. McClung, K. S. Choi, D. E. Chang, O. Painter, and H. J. Kimble, "Atom-light interactions in photonic crystals," *Nature Communications*, vol. 5, p. 3808, 2014.

[155] J. M. Kindem, A. Ruskuc, J. G. Bartholomew, J. Rochman, Y. Q. Huan, and A. Faraon, "Control and single-shot readout of an ion embedded in a nanophotonic cavity," *Nature*, vol. 580, no. 7802, pp. 201–204, 2020.

[156] H. Cao and J. Wiersig, "Dielectric microcavities: Model systems for wave chaos and non-hermitian physics," *Rev. Mod. Phys.*, vol. 87, pp. 61–111, Jan 2015.

[157] Z. Gao, S. T. M. Fryslie, B. J. Thompson, P. S. Carney, and K. D. Choquette, "Parity-time symmetry in coherently coupled vertical cavity laser arrays," *Optica*, vol. 4, pp. 323–329, Mar 2017.

[158] W. Chen, Ş. K. Özdemir, G. Zhao, J. Wiersig, and L. Yang, "Exceptional points enhance sensing in an optical microcavity," *Nature*, vol. 548, no. 7666, pp. 192–196, 2017.

[159] S. Mittal, E. A. Goldschmidt, and M. Hafezi, "A topological source of quantum light," *Nature*, vol. 561, no. 7724, pp. 502–506, 2018.

[160] J. K. Jang, A. Klenner, X. Ji, Y. Okawachi, M. Lipson, and A. L. Gaeta, "Synchronization of coupled optical microresonators," *Nature Photonics*, vol. 12, no. 11, pp. 688–693, 2018.

[161] F. Monifi, J. Zhang, Ş. K. Özdemir, B. Peng, Y.-x. Liu, F. Bo, F. Nori, and L. Yang, "Optomechanically induced stochastic resonance and chaos transfer between optical fields," *Nature Photonics*, vol. 10, no. 6, pp. 399–405, 2016.

[162] M. Evans, S. Ballmer, M. Fejer, P. Fritschel, G. Harry, and G. Ogin, "Thermo-optic noise in coated mirrors for high-precision optical measurements," *Physical Review D*, vol. 78, no. 10, p. 102003, 2008.

[163] L. D. Landau and E. M. Lifshitz, *Statistical Physics.* Elsevier, 1980.

[164] C. Kittel, "Temperature fluctuation: an oxymoron," *Phys. Today*, vol. 41, no. 5, p. 93, 1988.

[165] B. B. Mandelbrot, "Temperature fluctuation: a well-defined and unavoidable notion," *PhT*, vol. 42, no. 1, p. 71, 1989.

[166] M. Falcioni, D. Villamaina, A. Vulpiani, A. Puglisi, and A. Sarracino, "Estimate of temperature and its uncertainty in small systems," *American Journal of Physics*, vol. 79, no. 7, pp. 777–785, 2011.

[167] T. C. Chui, D. R. Swanson, M. J. Adriaans, J. A. Nissen, and J. A. Lipa, "Temperature fluctuations in the canonical ensemble," *Physical Review Letters*, vol. 69, no. 21, pp. 3005–3008, 1992.

[168] L. Stodolsky, "Temperature fluctuations in multiparticle production," *Physical Review Letters*, vol. 75, no. 6, p. 1044, 1995.

[169] J. Hickman and Y. Mishin, "Temperature fluctuations in canonical systems: Insights from molecular dynamics simulations," *Physical Review B*, vol. 94, no. 18, p. 184311, 2016.

[170] T. Jahnke, S. Lanéry, and G. Mahler, “Operational approach to fluctuations of thermodynamic variables in finite quantum systems,” *Physical Review E*, vol. 83, no. 1, p. 011109, 2011.

[171] P. Seifert, X. Lu, P. Stepanov, J. R. Durán Retamal, J. N. Moore, K.-C. Fong, A. Principi, and D. K. Efetov, “Magic-angle bilayer graphene nanocalorimeters: Toward broadband, energy-resolving single photon detection,” *Nano Letters*, vol. 20, no. 5, pp. 3459–3464, 2020.

[172] B. Karimi, F. Brange, P. Samuelsson, and J. P. Pekola, “Reaching the ultimate energy resolution of a quantum detector,” *Nature Communications*, vol. 11, no. 1, pp. 1–6, 2020.

[173] K. Wanser, “Fundamental phase noise limit in optical fibres due to temperature fluctuations,” *Electronics Letters*, vol. 28, pp. 53–54, jan 1992.

[174] R. Moeller and W. Burns, “Observation of thermal noise in a dynamically biased fiber-optic gyro,” *Optics Letters*, vol. 21, no. 3, pp. 171–173, 1996.

[175] S. Foster, A. Tikhomirov, and M. Milnes, “Fundamental thermal noise in distributed feedback fiber lasers,” *IEEE Journal of Quantum Electronics*, vol. 43, no. 5, pp. 378–384, 2007.

[176] L. Duan, “General treatment of the thermal noises in optical fibers,” *Physical Review A*, vol. 86, no. 2, p. 23817, 2012.

[177] M. L. Gorodetsky and I. S. Grudinin, “Fundamental thermal fluctuations in microspheres,” *Journal of the Optical Society of America B*, vol. 21, no. 4, p. 697, 2004.

[178] A. A. Savchenkov, A. B. Matsko, V. S. Ilchenko, N. Yu, and L. Maleki, “Whispering-gallery-mode resonators as frequency references I Fundamental Limitations,” *Journal of the Optical Society of America B*, vol. 24, no. 12, p. 2988, 2007.

[179] J. Lim, A. A. Savchenkov, E. Dale, W. Liang, D. Eliyahu, V. Ilchenko, A. B. Matsko, L. Maleki, and C. W. Wong, “Chasing the thermodynamical noise limit in whispering-gallery-mode resonators for ultrastable laser frequency stabilization,” *Nature Communications*, vol. 8, no. 1, pp. 1–7, 2017.

[180] G. Huang, E. Lucas, J. Liu, A. S. Raja, G. Lihachev, M. L. Gorodetsky, N. J. Engelsen, and T. J. Kippenberg, “Thermorefractive noise in silicon-nitride microresonators,” *Physical Review A*, vol. 99, p. 061801, jun 2019.

[181] K. Saurav and N. Le Thomas, “Probing the fundamental detection limit of photonic crystal cavities,” *Optica*, vol. 4, no. 7, p. 757, 2017.

[182] S. Jiang, S. H. Pan, S. S. Deka, C. Y. Fang, Z. Chen, Y. Fainman, and A. El Amili, "Impact of fundamental temperature fluctuations on the frequency stability of metallo- dielectric nanolasers," *IEEE Journal of Quantum Electronics*, vol. 55, no. 5, p. 2000910, 2019.

[183] W. Jin, Q.-F. Yang, L. Chang, B. Shen, H. Wang, M. A. Leal, L. Wu, M. Gao, A. Feshali, M. Paniccia, *et al.*, "Hertz-linewidth semiconductor lasers using cmos-ready ultra-high-q microresonators," *Nature Photonics*, vol. 15, no. 5, pp. 346–353, 2021.

[184] T. E. Drake, J. R. Stone, T. C. Briles, and S. B. Papp, "Thermal decoherence and laser cooling of kerr microresonator solitons," *Nature Photonics*, vol. 14, p. 480, 2020.

[185] M. Geitner, F. A. Sandoval, E. Bertin, and L. Bellon, "Low thermal fluctuations in a system heated out of equilibrium," *Physical Review E*, vol. 95, no. 3, p. 032138, 2017.

[186] K. Komori, Y. Enomoto, H. Takeda, Y. Michimura, K. Somiya, M. Ando, and S. W. Ballmer, "Direct approach for the fluctuation-dissipation theorem under nonequilibrium steady-state conditions," *Physical Review D*, vol. 97, no. 10, p. 102001, 2018.

[187] H. Mabuchi, "Qubit limit of cavity nonlinear optics," *Physical Review A*, vol. 85, p. 015806, jan 2012.

[188] Y. Zhang, J. Moser, J. Güttinger, A. Bachtold, and M. I. Dykman, "Interplay of driving and frequency noise in the spectra of vibrational systems," *Physical Review Letters*, vol. 113, no. 25, p. 255502, 2014.

[189] R. P. Feynman and A. R. Hibbs, *Quantum Mechanics and Path Integrals*. New York: McGraw-Hill, 1965.

[190] X. Sun, R. Luo, X. C. Zhang, and Q. Lin, "Squeezing the fundamental temperature fluctuations of a high- Q microresonator," *Physical Review A*, vol. 95, no. 2, p. 23822, 2017.

[191] M. Notomi, "Manipulating light with strongly modulated photonic crystals," *Reports on Progress in Physics*, vol. 73, no. 9, p. 096501, 2010.

[192] Y. Zhang and M. Lončar, "Submicrometer diameter micropillar cavities with high quality factor and ultrasmall mode volume," *Optics letters*, vol. 34, no. 7, pp. 902–904, 2009.

[193] T. J. Kippenberg, S. M. Spillane, and K. J. Vahala, "Demonstration of ultra-high- Q small mode volume toroid microcavities on a chip," *Applied Physics Letters*, vol. 85, no. 25, pp. 6113–6115, 2004.

[194] H. Lee, T. Chen, J. Li, K. Y. Yang, S. Jeon, O. Painter, and K. J. Vahala, "Chemically etched ultrahigh-Q wedge-resonator on a silicon chip," *Nature Photonics*, vol. 6, no. 6, pp. 369–373, 2012.

[195] F. Ding, T. Stöferle, L. Mai, A. Knoll, and R. F. Mahrt, "Vertical microcavities with high-q and strong lateral mode confinement," *Physical Review B*, vol. 87, p. 161116, Apr 2013.

[196] V. B. Braginsky, M. L. Gorodetsky, and S. P. Vyatchanin, "Thermodynamical fluctuations and photo-thermal shot noise in gravitational wave antennae," *Physics Letters, Section A: General, Atomic and Solid State Physics*, vol. 264, no. 1, pp. 1–10, 1999.

[197] V. B. Braginsky, M. L. Gorodetsky, and S. P. Vyatchanin, "Thermo-refractive noise in gravitational wave antennae," *Physics Letters, Section A: General, Atomic and Solid State Physics*, vol. 271, no. 5-6, pp. 303–307, 2000.

[198] J. Lim, A. A. Savchenkov, E. Dale, W. Liang, D. Eliyahu, V. Ilchenko, A. B. Matsko, L. Maleki, and C. W. Wong, "Chasing the thermodynamical noise limit in whispering-gallery-mode resonators for ultrastable laser frequency stabilization," *Nature Communications*, vol. 8, no. 1, p. 8, 2017.

[199] W. Zhang, F. Baynes, S. A. Diddams, and S. B. Papp, "Microrod Optical Frequency Reference in the Ambient Environment," *Physical Review Applied*, vol. 12, no. 2, p. 024010, 2019.

[200] C. W. Gardiner, "Adiabatic elimination in stochastic systems. I. Formulation of methods and application to few-variable systems," *Physical Review A*, vol. 29, no. 5, pp. 2814–2822, 1984.

[201] J. Cuffe, J. K. Eliason, A. A. Maznev, K. C. Collins, J. A. Johnson, A. Shchepetov, M. Prunnila, J. Ahopelto, C. M. Sotomayor Torres, G. Chen, and K. A. Nelson, "Reconstructing phonon mean-free-path contributions to thermal conductivity using nanoscale membranes," *Physical Review B*, vol. 91, no. 24, p. 245423, 2015.

[202] M. Galli, S. L. Portalupi, M. Belotti, L. C. Andreani, L. O'Faolain, and T. F. Krauss, "Light scattering and Fano resonances in high-Q photonic crystal nanocavities," *Applied Physics Letters*, vol. 94, no. 7, p. 71101, 2009.

[203] M. L. Gorodetsky, A. Schliesser, G. Anetsberger, S. Deleglise, and T. J. Kippenberg, "Determination of the vacuum optomechanical coupling rate using frequency noise calibration," *Optics Express*, vol. 18, p. 23236, oct 2010.

[204] A. Schliesser, R. Rivière, G. Anetsberger, O. Arcizet, and T. J. Kippenberg, "Resolved-sideband cooling of a micromechanical oscillator," *Nature Physics*, vol. 4, no. 5, pp. 415–419, 2008.

[205] Keysight Technologies, "Spectrum and Signal Analyzer Measurements and Noise," *Application Note 5966*, 2017.

[206] H. Ludvigsen, M. Tossavainen, and M. Kaivola, "Laser linewidth measurements using self-homodyne detection with short delay," *Optics Communications*, vol. 155, pp. 180–186, oct 1998.

[207] A. Jain, Y. J. Yu, and A. J. McGaughey, "Phonon transport in periodic silicon nanoporous films with feature sizes greater than 100 nm," *Physical Review B*, vol. 87, no. 19, p. 195301, 2013.

[208] J. Komma, C. Schwarz, G. Hofmann, D. Heinert, and R. Nawrodt, "Thermo-optic coefficient of silicon at 1550 nm and cryogenic temperatures," *Applied Physics Letters*, vol. 101, no. 4, p. 041905, 2012.

[209] H. Choi, M. Heuck, and D. Englund, "Self-Similar Nanocavity Design with Ultrasmall Mode Volume for Single-Photon Nonlinearities," *Physical Review Letters*, vol. 118, no. 22, p. 223605, 2017.

[210] E. Gavartin, R. Braive, I. Sagnes, O. Arcizet, A. Beveratos, T. J. Kippenberg, and I. Robert-Philip, "Optomechanical coupling in a two-dimensional photonic crystal defect cavity," *Physical Review Letters*, vol. 106, no. 20, p. 203902, 2011.

[211] Y. Levin, "Fluctuation-dissipation theorem for thermo-refractive noise," *Physics Letters, Section A: General, Atomic and Solid State Physics*, vol. 372, pp. 1941–1944, mar 2008.

[212] W. Weng, J. D. Anstie, T. M. Stace, G. Campbell, F. N. Baynes, and A. N. Luiten, "Nano-kelvin thermometry and temperature control: beyond the thermal noise limit," *Physical Review Letters*, vol. 112, no. 16, p. 160801, 2014.

[213] W. Weng, P. S. Light, and A. N. Luiten, "Ultra-sensitive lithium niobate thermometer based on a dual-resonant whispering-gallery-mode cavity," *Optics Letters*, vol. 43, no. 7, pp. 1415–1418, 2018.

[214] T. Lu, H. Lee, T. Chen, S. Herchak, J.-H. Kim, S. E. Fraser, R. C. Flagan, and K. Vahala, "High sensitivity nanoparticle detection using optical microcavities," *Proceedings of the National Academy of Sciences*, vol. 108, no. 15, pp. 5976–5979, 2011.

[215] W. Loh, A. A. Green, F. N. Baynes, D. C. Cole, F. J. Quinlan, H. Lee, K. J. Vahala, S. B. Papp, and S. A. Diddams, "Dual-microcavity narrow-linewidth brillouin laser," *Optica*, vol. 2, no. 3, pp. 225–232, 2015.

[216] W. H. Pernice, C. Xiong, C. Schuck, and H. X. Tang, "High-Q aluminum nitride photonic crystal nanobeam cavities," *Applied Physics Letters*, vol. 100, no. 9, p. 091105, 2012.

[217] J. Zhu, S. K. Ozdemir, Y. F. Xiao, L. Li, L. He, D. R. Chen, and L. Yang, "On-chip single nanoparticle detection and sizing by mode splitting in an ultrahigh-Q microresonator," *Nature Photonics*, vol. 4, no. 1, pp. 46–49, 2010.

[218] S. M. Spillane, T. J. Kippenberg, K. J. Vahala, K. W. Goh, E. Wilcut, and H. J. Kimble, "Ultrahigh-Q toroidal microresonators for cavity quantum electrodynamics," *Physical Review A*, vol. 71, no. 1, p. 013817, 2005.

[219] T. Asano and S. Noda, "Optimization of photonic crystal nanocavities based on deep learning," *Optics Express*, vol. 26, no. 25, p. 32704, 2018.

[220] F. Alpeggiani, L. C. Andreani, and D. Gerace, "Effective bichromatic potential for ultra-high Q-factor photonic crystal slab cavities," *Applied Physics Letters*, vol. 107, no. 26, p. 261110, 2015.

[221] Q. Quan and M. Loncar, "Deterministic design of wavelength scale, ultra-high Q photonic crystal nanobeam cavities," *Optics Express*, vol. 19, p. 18529, sep 2011.

[222] S. Hu and S. M. Weiss, "Design of Photonic Crystal Cavities for Extreme Light Concentration," *ACS Photonics*, vol. 3, no. 9, pp. 1647–1653, 2016.

[223] Y. Lai, S. Pirotta, G. Urbinati, D. Gerace, M. Minkov, V. Savona, A. Badolato, and M. Galli, "Genetically designed l3 photonic crystal nanocavities with measured quality factor exceeding one million," *Applied Physics Letters*, vol. 104, no. 24, p. 241101, 2014.

[224] K. Y. Yang, D. Y. Oh, S. H. Lee, Q. F. Yang, X. Yi, B. Shen, H. Wang, and K. Vahala, "Bridging ultrahigh-Q devices and photonic circuits," *Nature Photonics*, vol. 12, no. 5, pp. 297–302, 2018.

[225] F. Wang, R. E. Christiansen, Y. Yu, J. Mørk, and O. Sigmund, "Maximizing the quality factor to mode volume ratio for ultra-small photonic crystal cavities," *Applied Physics Letters*, vol. 113, no. 24, p. 241101, 2018.

[226] G. Moille, X. Lu, A. Rao, Q. Li, D. A. Westly, L. Ranzani, S. B. Papp, M. Soltani, and K. Srinivasan, "Kerr-microresonator soliton frequency combs at cryogenic temperatures," *Phys. Rev. Applied*, vol. 12, p. 034057, Sep 2019.

[227] M. Heuck, K. Jacobs, and D. R. Englund, "Controlled-Phase Gate Using Dynamically Coupled Cavities and Optical Nonlinearities," *Physical Review Letters*, vol. 124, p. 160501, apr 2020.

[228] M. Heuck, K. Jacobs, and D. R. Englund, "Photon-photon interactions in dynamically coupled cavities," *Phys. Rev. A*, vol. 101, p. 042322, Apr 2020.

[229] S. Krastanov, M. Heuck, J. H. Shapiro, P. Narang, D. R. Englund, and K. Jacobs, "Room-Temperature Photonic Logical Qubits via Second-Order Nonlinearities," *arXiv*, no. 2002.07193v1, 2020.

[230] M. Li, Y.-L. Zhang, H. X. Tang, C.-H. Dong, G.-C. Guo, and C.-L. Zou, "Photon-photon quantum phase gate in a photonic molecule with $\chi^{(2)}$ nonlinearity," *Phys. Rev. Applied*, vol. 13, p. 044013, Apr 2020.

[231] R. Yanagimoto, T. Onodera, E. Ng, L. G. Wright, P. L. McMahon, and H. Mabuchi, "Engineering a kerr-based deterministic cubic phase gate via gaussian operations," *Physical Review Letters*, vol. 124, p. 240503, Jun 2020.

[232] J. Lu, M. Li, C.-L. Zou, A. A. Sayem, and H. X. Tang, "Towards 1% single photon nonlinearity with periodically-poled lithium niobate microring resonators," *arXiv*, no. 2007.07411, 2020.

[233] T. Tiecke, J. D. Thompson, N. P. de Leon, L. Liu, V. Vuletić, and M. D. Lukin, "Nanophotonic quantum phase switch with a single atom," *Nature*, vol. 508, no. 7495, pp. 241–244, 2014.

[234] D. Najer, I. Söllner, P. Sekatski, V. Dolique, M. C. Löbl, D. Riedel, R. Schott, S. Starosielec, S. R. Valentin, A. D. Wieck, *et al.*, "A gated quantum dot strongly coupled to an optical microcavity," *Nature*, pp. 1–1, 2019.

[235] R. E. Evans, M. K. Bhaskar, D. D. Sukachev, C. T. Nguyen, A. Sipahigil, M. J. Burek, B. Machielse, G. H. Zhang, A. S. Zibrov, E. Bielejec, *et al.*, "Photon-mediated interactions between quantum emitters in a diamond nanocavity," *Science*, vol. 362, no. 6415, pp. 662–665, 2018.

[236] S. Wehner, D. Elkouss, and R. Hanson, "Quantum internet: A vision for the road ahead," *Science*, vol. 362, p. 6412, 2018.

[237] A. V. Kuhlmann, J. Houel, A. Ludwig, L. Greuter, D. Reuter, A. D. Wieck, M. Poggio, and R. J. Warburton, "Charge noise and spin noise in a semiconductor quantum device," *Nature Physics*, vol. 9, no. 9, pp. 570–575, 2013.

[238] S. Ferretti and D. Gerace, "Single-photon nonlinear optics with kerr-type nanostructured materials," *Physical Review B*, vol. 85, p. 033303, Jan 2012.

[239] R. W. Boyd, *Nonlinear optics.* Academic press, 2019.

[240] W. T. M. Irvine, K. Hennessy, and D. Bouwmeester, "Strong coupling between single photons in semiconductor microcavities," *Physical Review Letters*, vol. 96, p. 057405, Feb 2006.

[241] A. Majumdar and D. Gerace, “Single-photon blockade in doubly resonant nanocavities with second-order nonlinearity,” *Physical Review B*, vol. 87, p. 235319, Jun 2013.

[242] E. Timurdogan, C. V. Poulton, M. J. Byrd, and M. R. Watts, “Electric field-induced second-order nonlinear optical effects in silicon waveguides,” *Nature Photonics*, vol. 11, no. 3, pp. 200–206, 2017.

[243] R. Hamerly, “Coherent LQG control, Free-Carrier Oscillations, Optical Ising Machines and Pulsed OPO Dynamics,” *arXiv*, no. 1608.07551, 2016.

[244] M. Minkov, D. Gerace, and S. Fan, “Doubly resonant χ (2) nonlinear photonic crystal cavity based on a bound state in the continuum,” *Optica*, vol. 6, no. 8, p. 1039, 2019.

[245] H. Altug, D. Englund, and J. Vučković, “Ultrafast photonic crystal nanocavity laser,” *Nature physics*, vol. 2, no. 7, pp. 484–488, 2006.

[246] J. D. Thompson, T. Tiecke, N. P. de Leon, J. Feist, A. Akimov, M. Gullans, A. S. Zibrov, V. Vuletić, and M. D. Lukin, “Coupling a single trapped atom to a nanoscale optical cavity,” *Science*, vol. 340, no. 6137, pp. 1202–1205, 2013.

[247] M. Aspelmeyer, T. J. Kippenberg, and F. Marquardt, “Cavity optomechanics,” *Reviews of Modern Physics*, vol. 86, no. 4, p. 1391, 2014.

[248] A. A. Clerk, M. H. Devoret, S. M. Girvin, F. Marquardt, and R. J. Schoelkopf, “Introduction to quantum noise, measurement, and amplification,” *Reviews of Modern Physics*, vol. 82, no. 2, p. 1155, 2010.

[249] W. Loh, S. Yegnanarayanan, F. O’Donnell, and P. W. Juodawlkis, “Ultra-narrow linewidth brillouin laser with nanokelvin temperature self-referencing,” *Optica*, vol. 6, pp. 152–159, Feb 2019.

[250] R. X. Adhikari, K. Arai, A. Brooks, C. Wipf, O. Aguiar, P. Altin, B. Barr, L. Barsotti, R. Bassiri, A. Bell, *et al.*, “A cryogenic silicon interferometer for gravitational-wave detection,” *Classical and Quantum Gravity*, vol. 37, no. 16, p. 165003, 2020.

[251] H. Kimble, B. L. Lev, and J. Ye, “Optical interferometers with reduced sensitivity to thermal noise,” *Physical Review Letters*, vol. 101, no. 26, p. 260602, 2008.

[252] M. L. Gorodetsky, “Thermal noises and noise compensation in high-reflection multilayer coating,” *Physics Letters, Section A: General, Atomic and Solid State Physics*, vol. 372, no. 46, pp. 6813–6822, 2008.

[253] T. Chalermsongsak, E. D. Hall, G. D. Cole, D. Follman, F. Seifert, K. Arai, E. K. Gustafson, J. R. Smith, M. Aspelmeyer, and R. X. Adhikari, "Coherent cancellation of photothermal noise in GaAs/$\mathrm{Al_{0.92}Ga_{0.08}As}$ bragg mirrors," *Metrologia*, vol. 53, no. 2, p. 860, 2016.

[254] G. Harry, T. P. Bodiya, and R. DeSalvo, *Optical coatings and thermal noise in precision measurement.* Cambridge University Press, 2012.

[255] Z. Zhang, P. Zhao, P. Lin, and F. Sun, "Thermo-optic coefficients of polymers for optical waveguide applications," *Polymer*, vol. 47, no. 14, pp. 4893–4896, 2006.

[256] X. Gan, H. Clevenson, and D. Englund, "Polymer photonic crystal nanocavity for precision strain sensing," *ACS Photonics*, vol. 4, no. 7, pp. 1591–1594, 2017.

[257] S. G. Johnson, M. Ibanescu, M. A. Skorobogatiy, O. Weisberg, J. D. Joannopoulos, and Y. Fink, "Perturbation theory for maxwell's equations with shifting material boundaries," *Phys. Rev. E*, vol. 65, p. 066611, Jun 2002.

[258] J. S. Jensen and O. Sigmund, "Topology optimization for nano-photonics," *Laser & Photonics Reviews*, vol. 5, no. 2, pp. 308–321, 2011.

[259] P. Cheben, R. Halir, J. H. Schmid, H. A. Atwater, and D. R. Smith, "Subwavelength integrated photonics," *Nature*, vol. 560, no. 7720, pp. 565–572, 2018.

[260] J. Park, S. K. Ozdemir, F. Monifi, T. Chadha, S. H. Huang, P. Biswas, and L. Yang, "Titanium dioxide whispering gallery microcavities," *Advanced Optical Materials*, vol. 2, no. 8, pp. 711–717, 2014.

[261] T. Handa, H. Tahara, T. Aharen, and Y. Kanemitsu, "Large negative thermo-optic coefficients of a lead halide perovskite," *Science Advances*, vol. 5, no. 7, p. eaax0786, 2019.

[262] H. Jayatilleka, H. Frish, R. Kumar, J. Heck, C. Ma, M. N. Sakib, D. Huang, and H. Rong, "Post-fabrication trimming of silicon photonic ring resonators at wafer-scale," *Journal of Lightwave Technology*, vol. 39, no. 15, pp. 5083–5088, 2021.

[263] V. Biryukova, G. J. Sharp, C. Klitis, and M. Sorel, "Trimming of silicon-on-insulator ring-resonators via localized laser annealing," *Optics Express*, vol. 28, no. 8, pp. 11156–11164, 2020.

[264] D. E. Hagan, B. Torres-Kulik, and A. P. Knights, "Post-fabrication trimming of silicon ring resonators via integrated annealing," *IEEE Photonics Technology Letters*, vol. 31, no. 16, pp. 1373–1376, 2019.

[265] S. Han and Y. Shi, “Post-fabrication trimming of photonic crystal nanobeam cavities by electron beam irradiation,” *Optics Express*, vol. 26, no. 12, pp. 15908–15913, 2018.

[266] E. Gil-Santos, C. Baker, A. Lemaître, S. Ducci, C. Gomez, G. Leo, and I. Favero, “Scalable high-precision tuning of photonic resonators by resonant cavity-enhanced photoelectrochemical etching,” *Nature communications*, vol. 8, no. 1, pp. 1–7, 2017.

[267] S. Spector, J. M. Knecht, and P. W. Juodawlkis, “Localized in situ cladding annealing for post-fabrication trimming of silicon photonic integrated circuits,” *Optics Express*, vol. 24, no. 6, pp. 5996–6003, 2016.

[268] T. Lipka, M. Kiepsch, H. K. Trieu, and J. Müller, “Hydrogenated amorphous silicon photonic device trimming by UV-irradiation,” *Optics express*, vol. 22, no. 10, pp. 12122–12132, 2014.

[269] A. H. Atabaki, A. A. Eftekhar, M. Askari, and A. Adibi, “Accurate post-fabrication trimming of ultra-compact resonators on silicon,” *Optics express*, vol. 21, no. 12, pp. 14139–14145, 2013.

[270] T. Cai, R. Bose, G. S. Solomon, and E. Waks, “Controlled coupling of photonic crystal cavities using photochromic tuning,” *Applied Physics Letters*, vol. 102, no. 14, p. 141118, 2013.

[271] K. Hennessy, C. Högerle, E. Hu, A. Badolato, and A. Imamoğlu, “Tuning photonic nanocavities by atomic force microscope nano-oxidation,” *Applied physics letters*, vol. 89, no. 4, p. 041118, 2006.

[272] S. Grillanda, V. Raghunathan, V. Singh, F. Morichetti, J. Michel, L. Kimerling, A. Melloni, and A. Agarwal, “Post-fabrication trimming of athermal silicon waveguides,” *Optics letters*, vol. 38, no. 24, pp. 5450–5453, 2013.

[273] M. M. Milosevic, X. Chen, X. Yu, N. J. Dinsdale, O. Aktas, S. Z. Oo, A. Z. Khokhar, D. J. Thomson, O. L. Muskens, H. M. Chong, *et al.*, “Ion implantation of germanium into silicon for critical coupling control of racetrack resonators,” *Journal of Lightwave Technology*, vol. 38, no. 7, pp. 1865–1873, 2020.

[274] T. Čižmár, M. Mazilu, and K. Dholakia, “In situ wavefront correction and its application to micromanipulation,” *Nature Photonics*, vol. 4, no. 6, pp. 388–394, 2010.

[275] R. Di Leonardo, F. Ianni, and G. Ruocco, “Computer generation of optimal holograms for optical trap arrays,” *Optics Express*, vol. 15, no. 4, pp. 1913–1922, 2007.

[276] F. Nogrette, H. Labuhn, S. Ravets, D. Barredo, L. Béguin, A. Vernier, T. Lahaye, and A. Browaeys, “Single-atom trapping in holographic 2D arrays of microtraps with arbitrary geometries,” *Physical Review X*, vol. 4, no. 2, p. 021034, 2014.

[277] D. Kim, A. Keesling, A. Omran, H. Levine, H. Bernien, M. Greiner, M. D. Lukin, and D. R. Englund, “Large-scale uniform optical focus array generation with a phase spatial light modulator,” *Optics letters*, vol. 44, no. 12, pp. 3178–3181, 2019.

[278] L. N. Lie, R. R. Razouk, and B. E. Deal, “High pressure oxidation of silicon in dry oxygen,” *Journal of The Electrochemical Society*, vol. 129, no. 12, p. 2828, 1982.

[279] B. Gross, *The TVs of Tomorrow.* University of Chicago Press, 2018.

[280] M. Nedeljkovic, R. Soref, and G. Z. Mashanovich, “Free-carrier electrorefraction and electroabsorption modulation predictions for silicon over the 1–14-μm infrared wavelength range,” *IEEE Photonics Journal*, vol. 3, no. 6, pp. 1171–1180, 2011.

[281] S. Zhang, S. Watson, J. J. McKendry, D. Massoubre, A. Cogman, E. Gu, R. K. Henderson, A. E. Kelly, and M. D. Dawson, “1.5 Gbit/s multi-channel visible light communications using CMOS-controlled GaN-based LEDs,” *Journal of lightwave technology*, vol. 31, no. 8, pp. 1211–1216, 2013.

[282] A. Yaacobi, J. Sun, M. Moresco, G. Leake, D. Coolbaugh, and M. R. Watts, “Integrated phased array for wide-angle beam steering,” *Optics letters*, vol. 39, no. 15, pp. 4575–4578, 2014.

[283] D. Vercruysse, N. V. Sapra, K. Y. Yang, and J. Vuckovic, “Inverse-designed photonic crystal circuits for optical beam steering,” *ACS Photonics*, vol. 8, no. 10, pp. 3085–3093, 2021.

[284] T. Tamanuki, H. Ito, and T. Baba, “Thermo-optic beam scanner employing silicon photonic crystal slow-light waveguides,” *Journal of Lightwave Technology*, vol. 39, no. 4, pp. 904–911, 2021.

[285] R. Sakata, K. Ishizaki, M. De Zoysa, S. Fukuhara, T. Inoue, Y. Tanaka, K. Iwata, R. Hatsuda, M. Yoshida, J. Gelleta, *et al.*, “Dually modulated photonic crystals enabling high-power high-beam-quality two-dimensional beam scanning lasers,” *Nature communications*, vol. 11, no. 1, pp. 1–10, 2020.

[286] J. McPhillimy, D. Jevtics, B. J. Guilhabert, C. Klitis, A. Hurtado, M. Sorel, M. D. Dawson, and M. J. Strain, “Automated nanoscale absolute accuracy

alignment system for transfer printing," *ACS applied nano materials*, vol. 3, no. 10, pp. 10326–10332, 2020.

[287] D. Conteduca, I. Barth, G. Pitruzzello, C. P. Reardon, E. R. Martins, and T. F. Krauss, "Dielectric nanohole array metasurface for high-resolution near-field sensing and imaging," *Nature communications*, vol. 12, no. 1, pp. 1–9, 2021.

[288] H. Pahlevaninezhad, M. Khorasaninejad, Y.-W. Huang, Z. Shi, L. P. Hariri, D. C. Adams, V. Ding, A. Zhu, C.-W. Qiu, F. Capasso, and M. J. Suter, "Nano-optic endoscope for high-resolution optical coherence tomography in vivo," *Nature photonics*, vol. 12, no. 9, pp. 540–547, 2018.

[289] M. R. Watts, M. J. Shaw, and G. N. Nielson, "Microphotonic thermal imaging," *Nature Photonics*, vol. 1, no. 11, pp. 632–634, 2007.

[290] J. Goldstein*, C. L. Panuski*, and D. R. Englund, "Thermal infrared detection with an optically-probed photonic crystal bolometer," *In preparation*, 2021.

[291] S. Abel, F. Eltes, J. E. Ortmann, A. Messner, P. Castera, T. Wagner, D. Urbonas, A. Rosa, A. M. Gutierrez, D. Tulli, *et al.*, "Large pockels effect in micro- and nanostructured barium titanate integrated on silicon," *Nature materials*, vol. 18, no. 1, pp. 42–47, 2019.

[292] D. Zhu, L. Shao, M. Yu, R. Cheng, B. Desiatov, C. Xin, Y. Hu, J. Holzgrafe, S. Ghosh, A. Shams-Ansari, *et al.*, "Integrated photonics on thin-film lithium niobate," *Advances in Optics and Photonics*, vol. 13, no. 2, pp. 242–352, 2021.

[293] K. Hirose, Y. Liang, Y. Kurosaka, A. Watanabe, T. Sugiyama, and S. Noda, "Watt-class high-power, high-beam-quality photonic-crystal lasers," *Nature photonics*, vol. 8, no. 5, pp. 406–411, 2014.

[294] I. D. Block, P. C. Mathias, S. I. Jones, L. O. Vodkin, and B. T. Cunningham, "Optimizing the spatial resolution of photonic crystal label-free imaging," *Applied Optics*, vol. 48, no. 34, pp. 6567–6574, 2009.

[295] G. Triggs, M. Fischer, D. Stellinga, M. Scullion, G. Evans, and T. Krauss, "Spatial resolution and refractive index contrast of resonant photonic crystal surfaces for biosensing," *IEEE photonics journal*, vol. 7, no. 3, pp. 1–10, 2015.

[296] P. Thureja, G. K. Shirmanesh, K. T. Fountaine, R. Sokhoyan, M. Grajower, and H. A. Atwater, "Array-level inverse design of beam steering active metasurfaces," *ACS nano*, vol. 14, no. 11, pp. 15042–15055, 2020.

[297] A. P. Mosk, A. Lagendijk, G. Lerosey, and M. Fink, "Controlling waves in space and time for imaging and focusing in complex media," *Nature photonics*, vol. 6, no. 5, pp. 283–292, 2012.

[298] S. Yoon, M. Kim, M. Jang, Y. Choi, W. Choi, S. Kang, and W. Choi, "Deep optical imaging within complex scattering media," *Nature Reviews Physics*, vol. 2, no. 3, pp. 141–158, 2020.

[299] M. Heuck, K. Jacobs, and D. R. Englund, "Controlled-phase gate using dynamically coupled cavities and optical nonlinearities," *Physical review letters*, vol. 124, no. 16, p. 160501, 2020.